Universitat Jaume I, Doctoral School
Doctoral Programme in Sciences

Bulk and Interfacial Engineering to Enhance Photovoltaic Properties of Iodide and Bromide Perovskite Solar Cells

Report submitted in order to be eligible for a doctoral degree awarded by the Universitat Jaume I

Author
Clara Aranda Alonso

Co-Director
Juan Bisquert Mascarell

Co-director
Antonio Guerrero Castillejo

Castelló de la Plana, November 2019

Abstract

Hybrid halide perovskite solar cells (PSCs) have come to the forefront of photovoltaic technology due to their impressive power conversion efficiency (PCE) of up to 24% in lab scale achieved in no more than ten years of research. This high efficiency comes together with great advances regarding large-scale deposition methods and a critical enhancement of device stabilities. However, despite these major achievements, important challenges still remain in the shadows for commercialization of this technology. For example, the environmental impact concerning lead and tin components, the device stability under real operational conditions, numerous gaps regarding the fundamental physics of the material or the complex interactions occurring between the different layers in the complete solar device that are not fully understood.

This thesis addresses issues related with the stability under real operation conditions and those associated with the interfacial interactions. For the first purpose, a robust method to fabricate high efficiency cells at any lab environment was developed through precursor´s formulation engineering. To accomplish the second goal, a clarification of the surface recombination dynamics, aided by optoelectronic and small perturbation techniques, was also provided via interlayer doping. Regarding these targets, two main perovskites materials based in methylammonium lead halides ($MAPbX_3$) were optimized during the course of this thesis: $MAPbI_3$ and $MAPbBr_3$. A wide number of instrumental techniques were also applied for bulk material characterization purposes and to investigate the operational procedures involving the physical dynamics of the cell.

To address the stability issues against atmospheric environments, a deeper understanding of perovskite crystallinity was mandatory. The role of the different precursors during the synthesis process and the control of the structural and chemical defects presented in the final film became crucial. The octahedral coordination chemistry regarding the basic structure of $MAPbI_3$ served as starting point. An intensive study was carried out to clarify the influence of solvents on the formation of lead-halides complexes in solution and the consequences of this influence in the quality of the final perovskite film. This investigation concluded that a competition between solvent molecules and iodine is the responsible of the multi-iodide plumbates formed in solution and these species persist in the films acting as chemical defects that behaves as charge recombination pathways. Absorbance spectroscopy revealed the coordination capability sequence of the usual solvents employed in the perovskite formation: H_2O > dimethylsulfoxide (DMSO) > N,N-dimethylformamide (DMF) > gamma-butyrolactone (GBL). In this series, water presents the strongest coordinative behaviour, due to its high polar character, and GBL the weakest coordinative solvent. The knowledge acquired here was used to develop formation criteria of high efficiency cells prepared under ambient conditions in the presence of moisture. Firstly, the development of reproducible PSCs under dry conditions was carried out via Lewis acid-base adduct of PbI_2, MAI and DMSO that helps with the crystallization. Under ambient conditions, a competition between water and DMSO to coordinate Pb was demonstrated and a balance between DMSO and H_2O concentration was required to control the quality of the films. The DMSO:Pb ratio was adjusted in the perovskite formulation depending on the relative humidity of the ambient (%RH). At high %RH low DMSO:Pb ratios are required to form high crystalline perovskite films. This direct relationship sets the foundations of a universal process to synthesize high crystalline perovskite films, regardless of the environmental moisture

conditions. The resulting devices fabricated with this method showed maximum current densities that approach 23 $mAcm^{-2}$ obtained under 30% RH, leading to a final PCE of ~19%.

The physics of photovoltage (V_{oc}) losses represent one of the areas poorly understood for perovskite solar cells, slowing down the race of higher PCE. Governed by recombination pathways, the reduction of photovoltage losses becomes a major task. The perovskite $MAPbBr_3$ find applications in photo-electrochemistry, tandem solar cells or efficient light emitting diodes (LEDs). With a bandgap of 2.3 eV is an ideal candidate to investigate in depth V_{oc} losses. In fact, the highest reported V_{oc} still representing 0.4 eV loss from the theoretical voltage in the radiative limit. Starting from this point, a high quality $MAPbBr_3$ film was developed to avoid additional recombination pathways related with chemical and structural defects. Then, interfacial doping with lithium salts was demonstrated to be crucial supressing the surface recombination in the complete device. Impedance Spectroscopy measurements coupled with electroluminescence (EL) and photoluminescence (PL) analysis demonstrated the role of Li^+, present at the ESL/perovskite interface, increasing the cation density at the hole accumulation zone. The consequence is an increased size of the space charge layer that reduces the charge transfer radiative recombination, enhancing at the same time the band-to-band radiative recombination as confirmed by PL measurements. This effect allowed to achieve a record photovoltage value for this configuration up to 1.6 V, highlighting the importance of extrinsic cations minimizing photovoltage losses.

Funding

The following sources were resposible for founding the research carried out in this thesis:

- Project: Ayudas para la formación de personal técnico de apoyo en organismos de investigación de la Comunidad Valenciana del Programa Gerónimo Forteza. FPA/2015/093

- Project: Desarrollo de Dispositivos orgánico-inorgánico de bajo coste con perovskitas para la conversión de la energía solar. MAT2013-47912-C3-1-R

- Project: A-Leaf: An artificial leaf. A photoelectrocatalytic cell from abundant materials for suistainable solar production of CO_2-based chemicals and fuels. 732840

- Project: Perovskitas fotovoltaicas estabilzadas de alto rendimiento. MAT2016-76892-C3-1-R

Acknowledgments

En primer lugar, me gustaría agradecer a mis directores, Prof. Juan Bisquert y Dr. Antonio Guerrero, por el apoyo y empuje continuos para conseguir siempre los mejores resultados posibles sacando lo mejor de mí. El aprendizaje tanto en lo académico como en lo personal ha sido mayúsculo gracias en gran parte a ellos.

Quisiera agradecer también al Prof. Francisco Fabregat Santiago por su confianza en mí desde el primer momento, permitiéndome realizar funciones de gestión de laboratorios e instrumentación que sin duda han complementado muy positivamente mi formación como doctoranda. Agradezco además enormemente su apoyo constante, la ayuda prestada y el cariño demostrado en momentos complicados.

La consecución de esta tesis no habría sido posible sin la aportación de compañeros, compañeras y colaboradores. Sandheep Ravishankar y Osbel Almora, por su inestimable ayuda en las cuestiones físicas más complicadas, haciendo posible la consecución de numerosos trabajos conjuntos con entusiasmo y generosidad. Dr. Alexander Kovalenko, por su dedicación a introducirme en el mundo de las perovskitas compartiendo conocimientos y experiencia. Al Dr. Juan Pablo Correa Baena por sus fructíferas enseñanzas y disposición en mi primera visita a EPFL. Al Prof. Christoph Brabec y compañeros del i-MEET de la Universidad de Núremberg por su cálida acogida. Al Dr. Michael Saliba y Dr. Sandy Sánchez del Adolphe Merkel Institute (AMI) de Fribourg por su hospitalidad y constante disposición, inspirando un gran aprendizaje que sin duda ha contribuido a la mejora de esta tesis doctoral.

A Reinaldo y Loles Merchán por su inestimable ayuda en las cuestiones de gestión de laboratorios, haciendo posible lo imposible con su eficacia y profesionalidad. A Javi por su paciencia y buen hacer en los múltiples experimentos con el SEM.

A los buenos amigos, además de compañeros, que han compartido conmigo estos cuatro años de tesis en el INAM y que se han convertido en mi familia de Castellón: Sandheep Ravishankar, Osbel Almora, Ngo Tu Gen, Dr. Isaac Zarazúa, Dr. Miguel García Tecedor, Dra. Elena Más Marzá.

A mis amigas de Chiclana y de la facultad. A Moisés, por todo, por tanto. A mi familia, a Damita, a mis primos, a mi abuela Lola, a mi tío Fernando.

A Agustín, por cada día, por cada sonrisa.

Agradezco infinito a mis hermanas y a mis padres por todo el cariño y apoyo incondicional en cada etapa, por tantísimo, por la fuerza recobrada en cada vuelta a casa que ha hecho de motor para traerme hasta aquí. Por inculcarme el amor por la ciencia y seguir compartiéndolo.

Quisiera por último dedicar mi tesis doctoral a Ana Alonso del Pozo, profesora de mis primeras prácticas de laboratorio en el instituto, quien me enseñó a manejarme entre erlenmeyers y con la que hice mis primeras síntesis químicas. No puedo sentirme más orgullosa por el ejemplo diario de fortaleza inmensa y capacidad que supones para todas y todos quienes te rodean. Gracias Mamá, esta tesis es para ti.

List of publications included in this Thesis

1. Rahimnejad, S.; Kovalenko, A.; Martí-Forés, S.; Aranda, C.; Guerrero, A. Coordination Chemistry Dictates the Structural Defects in Lead Halide Perovskites. *ChemPhysChem*, **2016**, *17*, 2795-2798. Impact Factor 2016: 3.075. DOI: 10.1002/cphc.201600575

2. Aranda, C.; Cristobal, C.; Shooshtari, L.; Li, C.; Huettner, S.; Guerrero, A. Formation Criteria of High Efficiency Perovskite Solar Cells in Ambient Conditions. *Sustainable Energy & Fuels*, **2017**, *1*, 540-547. Impact Factor 2017: Not available. DOI:10.1039/c6se00077k

3. Guerrero, A.; You, J.; Aranda, C.; Kang, Y.Soo; Garcia-Belmonte, G.; Zhou, H.; Bisquert, J.; Yang, Y. Interfacial Degradation of Planar Lead Halide Perovskite Solar Cells. *ACS Nano*, **2016**, *10*, 218-224. Impact Factor 2016: 13.942. DOI: 10.1021/acsnano.5b03687

4. Correa-Baena, J.Pablo; Turren-Cruz, S.H.; Tress, W.; Hagfeldt, A.; Aranda, C.; Shooshtari, L.; Bisquert, J.; Guerrero, A. Changes from Bulk to Surface Recombination Mechanisms between Pristine and Cycled Perovskite Solar Cells. *ACS Energy Letters*, **2017**, *2*, 681-688. Impact Factor 2017:12.277. DOI: 10.1021/acsenergylett.7b00059

5. Aranda, C.; Guerrero, A.; Bisquert, J. Ionic effect enhances light emission and photovoltage of methylammonium lead bromide perovskite solar cell by reduced surface recombination. *ACS Energy Letters*, **2019**, *4*, *741–746.* Impact Factor 2019:12.277. DOI:10.1021/acsenergylett.9b00186

This thesis has been accepted by the co-authors of the publications listed above that have waived the right to present them as part of another PhD thesis.

List of publications not included in this Thesis

1. Almora, O.; Aranda, C.; Zarazua, I.; Guerrero, A.; Garcia-Belmonte, G. Non-capacitive Hysteresis in Perovskite Solar Cells at Room Temperature. *ACS Energy Letters*, **2016**, *1*, 209-215. Impact Factor 2016: Not available. DOI: 10.1021/acsenergylett.6b00116

2. Almora, O.; Aranda, C.; Mas-Marzá, E.; Garcia-Belmonte, G. On Mott-Schottky analysis interpretation of capacitance measurements in organometal perovskite solar cells. *Applied Physics Letters*, **2016**, *109*, 173903. Impact Factor 2016: 3.411. DOI:10.1063/1.4966127

3. Ravishankar, S.; Almora, O.; Echeverría-Arrondo, C.; Ghahremanirad, E.; Aranda, C.; Guerrero, A.; Fabregat-Santiago, F.; Zaban, A.; Garcia-Belmonte, G.; Bisquert, J. Surface Polarization Model for the Dynamic Hysteresis of Perovskite Solar Cells. *The Journal of Physical Chemistry Letters*, **2017**, *8*, 915-921. Impact Factor 2017: 8.709. DOI: 10.1021/acs.jpclett.7b00045

4. Almora, O.; Aranda, C.; Garcia-Belmonte, G. Do Capacitance Measurements Reveal Light-Induced Bulk Dielectric Changes in Photovoltaic Perovskites? *The Journal of Physical Chemistry C*, **2018,** *122*, 13450-13454. Impact Factor 2018: 4.484. DOI: 10.1021/acs.jpcc.7b11703

5. Contreras-Bernal, L.; Aranda, C.; Vallés-Pelarda, M.; Ngo, T.T.; Ramos-Terrón, S.; Gallardo, J.Jesús; Navas, J.; Guerrero, A.; Mora-Seró, I.; Idígoras, J.; Anta, J.A. Homeopathic Perovskite Solar Cells: Effect of Humidity during Fabrication on the Performance and Stability of the Device. *The Journal of Physical Chemistry C*, **2018**, *122*, 5341−5348. ISI Impact Factor 2018: 4.484. DOI: 10.1021/acs.jpcc.8b01558

6. Ravishankar, S.; Aranda, C.; Boix, P.P.; Anta, J.Antonio; Bisquert, J.; Garcia-Belmonte, G. Effects of Frequency Dependence of the External Quantum Efficiency of Perovskite Solar Cells. *The Journal of Physical Chemistry Letters*, **2018**, *9*, 3099-3104. Impact Factor 2018**: 8.709**. DOI: 10.1021/acs.jpclett.8b01245

7. Peng, W.; Aranda, C.; Bakr, O.M.; Garcia-Belmonte, G.; Bisquert, J.; Guerrero, A. Quantification of Ionic Diffusion in Lead Halide Perovskite Single Crystals**.** *ACS Energy Letters*, **2018**, *3*, 1477−1481. Impact Factor 2017:12.277. DOI: 10.1021/acsenergylett.8b00641

8. Bi, Z.; Rodríguez-Martínez, X.; Aranda, C.; San José, E.Pascual; Goñi, A.R.; Campoy-Quiles, M.; Xu, X.; Guerrero, A. Defect Tolerant Perovskite Solar Cells from Blade coated Non-Toxic Solvents. *Journal of Materials Chemistry A*, **2018**, *6*, 19085-19093. Impact Factor 2018: 9.931. DOI: 10.1039/c8ta06771f

9. Suárez, B.; Aranda, C.; Macor, L.; Durantini, J.; Heredia, D.; Durantini, E.N.; Otero, L.; Guerrero, A.; Gervaldo, M. Perovskite solar cells with versatile electropolymerized fullerene as electron extraction layer. *Electrochimica*

Acta, **2018**, *292*, 697-706. Impact Factor 2018: 5.116. DOI: 10.1016/j.electacta.2018.09.196

10. Ravishankar, S.; Aranda, C.; Sanchez, S.; Bisquert, J.; Saliba, M.; Garcia-Belmonte, G. Perovskite Solar Cell Modeling Using Light and Voltage-Modulated Techniques. *The Journal of Physical Chemistry C*, **2019**, 123, 6444-6449. Impact Factor 2019: 4.484. DOI: 10.1021/acs.jpcc.9b011

11. Aranda, C.; Guerrero, A.; Bisquert, J. Crystalline Clear or not: Beneficial and Harmful Effects of Water in Perovskite Solar Cells. *ChemPhysChem,* **2019**, 20, 1–14. Impact Factor 2019: 3.077. DOI: 10.1002/cphc.201900393.

12. Aranda, C.; Bisquert, J.; Guerrero, A. Impedance Spectroscopy of Perovskite/Contact Interface: Beneficial Chemical Reactivity Effect. *Journal of Chemical Physics*, **2019**, 151, 124201. Impact Factor 2019: 2.997. DOI: 10.1063/1.5111925

Appendix

List of abbreviations and acronyms

PSC	Perovskite Solar Cell
DSSC	Dye Sensitizer Solar Cell
V_{oc}	Open Circuit Potential
V_{bi}	Built-in Potential
ESL	Electron Selective Layer
HSL	Hole Selective Layer
J_{sc}	Short-circuit Density Current
IS	Impedance Spectroscopy
EC	Equivalent Circuit
HF	High Frequency
IF	Intermediate Frequency
LF	Low Frequency
EQE	External Quantum Efficiency
OC	Open Circuit
SC	Short Circuit
OCV	Open Circuit Voltage
c-TiO_2	Compact Titanium Dioxide
m-TiO_2	Mesoporous Titanium Dioxide
CIGS	Copper Indium Gallium Selenide
DMF	Dimethylformmamide
DMSO	Dimethylsulfoxide
GBL	Gamma-butyrolactone
DETE	Diethylether
PV	Photovoltaic
PCBM	[6,6]-phenyl-C-61-butyric acid methyl ester
Spiro-OMeTAD	2,2’(7,7’)-tetrakis-(N,N-di-p-methyloxyphenyl-amine)9,9’-spirobifluorene
PEDOTS:PSS	Poly 4-stryrenesulfonate

$MAPbI_3$	Methylammonium Lead Iodide
$MAPbBr_3$	Methylammonium Lead Bromide
MA	Methylammonium
FA	Formammidinium
PL	Photoluminiscence
EL	Electroluminiscence
FF	Fill Factor
CB	Conduction Band
VB	Valence Band
LED	Light Emitting Diode
FR	Forward to Reverse bias
RF	Reverse to Forward bias
j-V	Current density-Voltage
U	Recombination rate
B_{rad}	Bimolecular recombination rate constant
SRH	Shockley-Read-Hall
E_{fn}	Electron Fermi level
E_{fp}	Hole Fermi level
L_d	Diffusion length
Z	Impedance
f	Frequency
n	Electron density
p	Hole density
n_0	Equilibrium electron concentration
p_0	Equilibrium hole concentration
C_{bulk}	Bulk Capacitance
C_s	Surface Capacitance
C_{acc}	Accumulation Capacitance
C_g	Geometrical Capacitance

R_{rec}	Recombination Resistance
R_s	Series Resistance
Z'	Real part of impedance
Z''	Imaginary part of impedance
C_{μ}	Chemical Capacitance
TCO	Transparent Conducting Oxide
FTO	Fluorine-doped Tin Oxide
ϕ	Photon Flux
PEC	Photoelectrochemical
DC	Direct Current
AC	Alternating Current
V_s	Surface Potential
PCE	Photo Conversion Efficiency
WF	Work Function
IQE	Internal Quantum Efficiency
σ	Conductivity
C_{HF}	High Frequency Capacitance
C_{IF}	Intermediate Frequency Capacitance
C_H	Helmholtz Capacitance
$D_{n/p}$	Diffusion coefficient of electrons/holes
$\mu_{n/p}$	Mobility of electrons/holes
R_{LF}	Low Frequency Resistance
R_{IF}	Intermediate Frequency Resistance
R_{HF}	High Frequency Resistance

List of physical constants

q	Electronic charge	1.602×10^{-19} C
$k_B T$	Thermal voltage	0.026 V
h	Planck's constant	6.626×10^{-34} kgm^2s^{-1}
c	Speed of light	3×10^8 ms^{-1}
ϵ_0	Permittivity of vacuum	8.85×10^{-12} Fm^{-1}

Table of contents

Chapter 1

Introduction

Style

This thesis is written in a journal article compilation style format constituted by eight chapters in which the main features of the developed work is described. A literature review is detailed in first place (Chapter 1) to synthesize the state of the art of perovskite technology, raising the issues addressed during the course of this doctoral thesis. The instrumental techniques carried out to solve the raised questions on this research are explained in Chapter 2. A brief summary of the history with respect to their solar energy applications and representative figures of the most important results from them are also exposed. Chapter 3 describes a critical overview of the main research developed, highlighting the context and the significance of the acquired achievements. The last chapters collect the pre-published results as the author´s final manuscript version, including a final section in which the main results are summarised to stablish their relevance and degree of contribution amplifying the knowledge of the field.

1.2. Solar Energy

The use of renewable energy represents the only feasible solution to remediate the global warming provoked by the energy crisis. The grow in energy demand leads to the consumption of fossil sources at an alarming rate, running out in the next 100 - 125 years if used persistently (Fig.1.1). The emissions of Greenhouse Gases (GHG) greatly contribute to aggravate global warming and climate change, which will lead to an environmental calamity worldwide.[1]

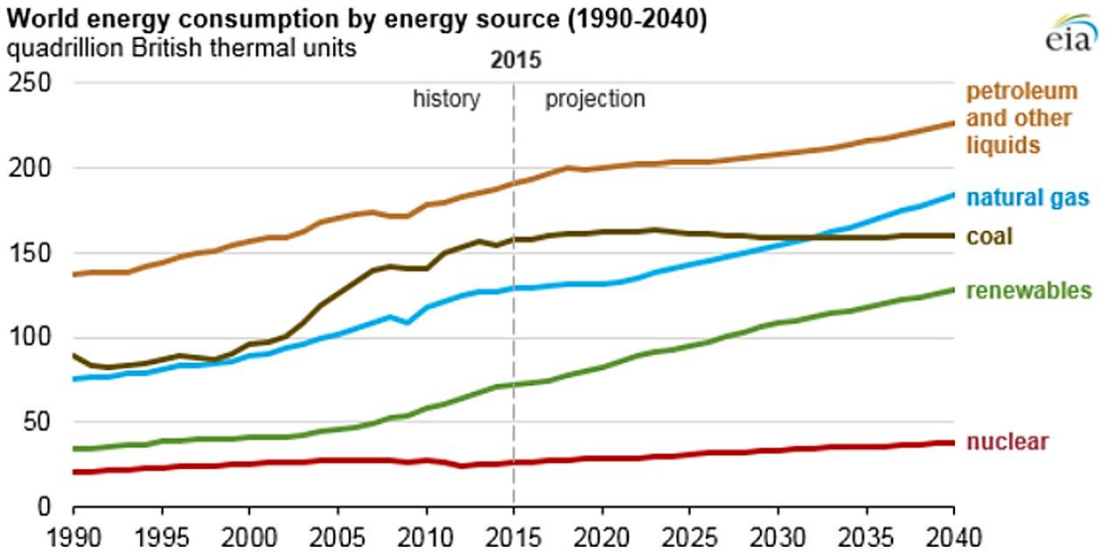

Figure 1.1. World energy consumption between 2015 and the projective for 2040. Data from US Energy Information Administration. International Energy Outlook 2017. Reproduced with permission of Ref.1. Copyright 2017, US Energy Information Administration.

Therefore, an urgent action to reduce carbon emissions and moderate the effects of climate change is mandatory. In 2016, the 21st Conference of Parties of the United Nations Framework Convention on Climate Change established the *Paris Agreement*. The aim is to support the global response to the risk of climate change by keeping a global temperature below 2 degrees Celsius focusing efforts to limit the temperature increase even further to 1.5 degrees. To reach this ambitious goal, a two-thirds reduction in coal power generation is needed by 2030 and then a full phase-out by 2050 according to the Intergovernmental Panel on Climate Change (IPCC).[2]

For this purpose, renewable energy sources appear in the scene as the main weapon to fill the coal gap and to reach the zero-carbon horizon, potentially achieving 90% of the required carbon reductions.[3] In fact, renewable power sources have augmented their inclusion in the energy sector pushing back the role of fossil plants into a secondary position. The result is a steady decrease in global coal plant load factors from 64% in 2006 to 52% in 2016 (Fig.1.2).[4]

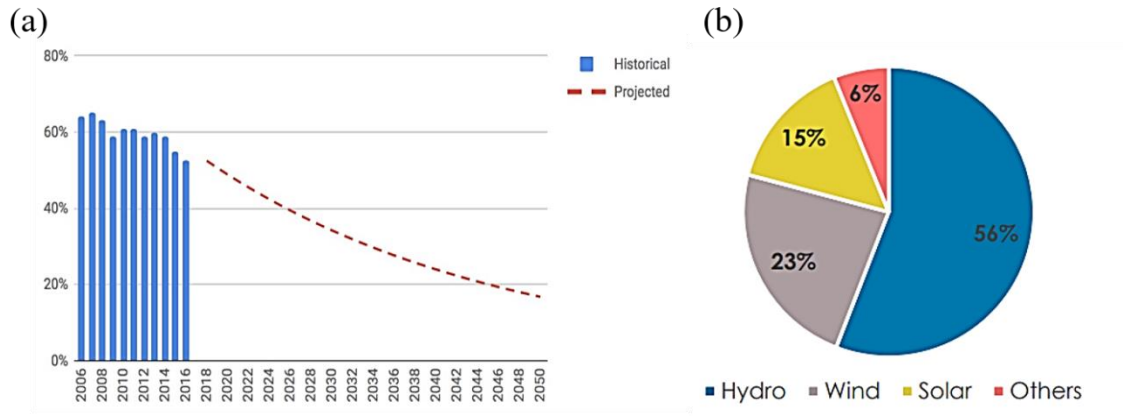

Figure 1.2. (a) Global Coal Plant Load Factor: Historical and Projected. Source of 2006–2016 data: IEA 2017. (b) Renewable generation capacity by energy source, where the 100% corresponds to a 2,006 GW of global generation capacity. Adapted from Ref.2 and Ref.3 respectively. Copyright 2017, Greenpeace and The International Renewable Energy Agency.

As reflected in Fig.1.2b, Solar energy appears as a great contributing factor providing 296 GW of the global renewable power generation.

Currently, solar energy is converted into electricity through two main technologies:

- **Concentrated Solar Power (CSP)**: used to generate electricity in large-scale solar plants, employing a field of mirrors that redirect and concentrate sunrays to a tall thin tower. These rays have the role to heat fluids, producing steam that drives a turbine to generate the electricity. The storing of heat during the night is the main advantage allowing generation of electricity in the absence of sunlight.
- **Photovoltaics (PV) or Solar Cells**: invented in 1954 at Bell Telephone Laboratories, these devices use an absorber material to efficient separate the photogenerated carriers produced by the incident sunlight. An advantage versus CSP plants is that solar PV installations can be configured to provide electricity on a commercial scale or in slighter configurations for mini-grids. In addition, production costs have decreased dramatically in the last years becoming one of the cheapest technique to produce electricity (Fig.1.3).

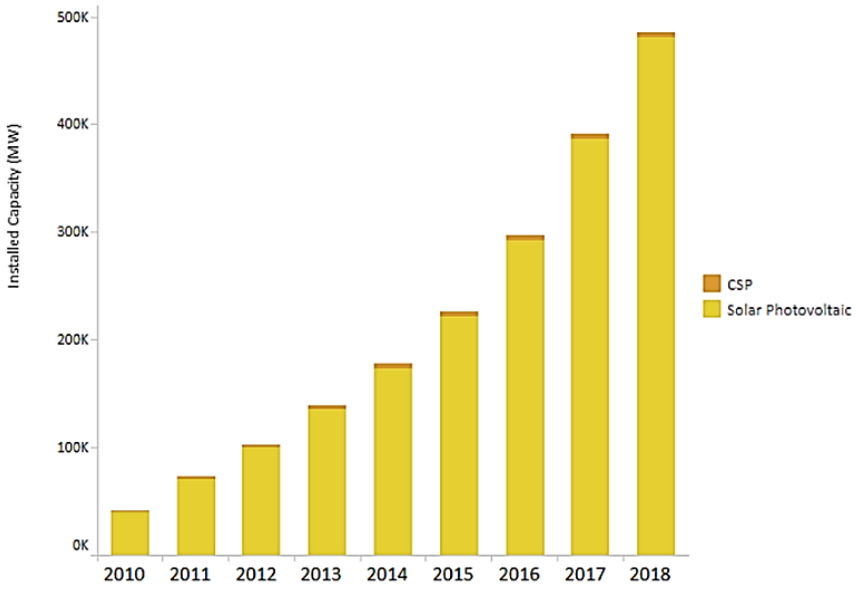

Figure 1.3. Global installed capacity trends of CSP and PV technologies in MW during the last ten years. Adapted from Ref.2 Copyright The International Renewable Energy Agency (IRENA).

The current PV distribution is mostly managed (90%) by crystalline silicon semiconductors solar cells. However, this technology present major disadvantages from many points of view. First of all, silicon is not so efficient absorbing sunlight and semiconductor films must be thick. Secondly, the material is fragile and the necessity of keeping from cracking requires fabrication onto a very heavy piece of glass. Because of these limitations, new photovoltaic materials have emerged. These materials can be divided into three categories attending to the complexity of their structures (Fig.1.4):

- Wafer-based cells including traditional crystalline silicon and alternatives such as gallium arsenide.
- Commercial thin-film cells involving amorphous silicon, cadmium telluride, and copper indium gallium (di)selenide (CIGS).
- Thin-film technologies such organic, quantum dots (QD) and perovskite solar cells.[5]

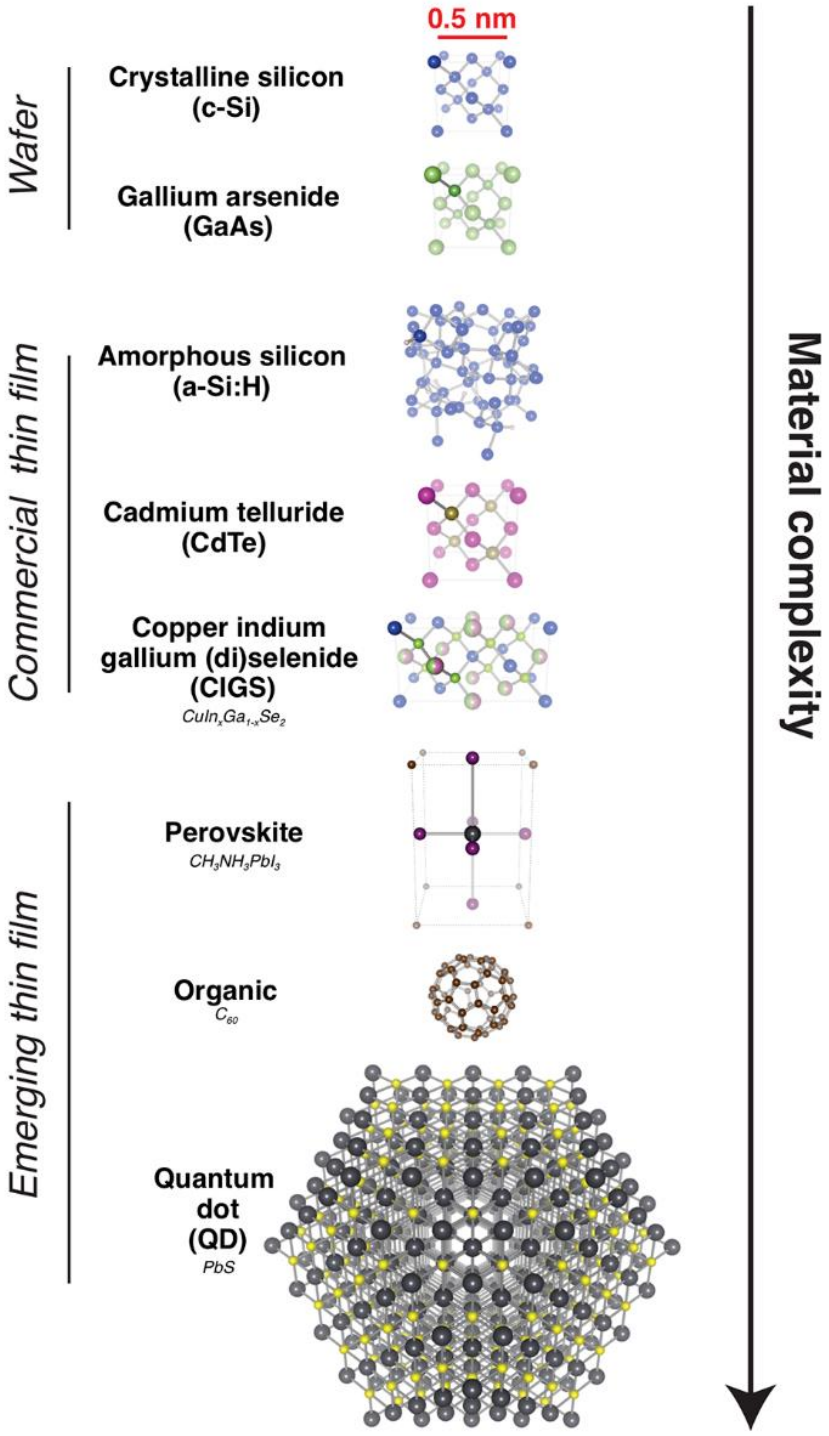

Figure 1.4. Proposed scheme for classifying PV technologies based on material complexity. Reproduced with permission of Ref.5. Copyright 2015, Massachusetts Institute of Technology (MIT).

In this context, perovskite solar cells (PSCs) emerge as the most promising photovoltaic technology. Their chemical structure and optoelectronic characteristics will be described in detail in the following sections.

1.2.1. Perovskite solar cells (PSCs) for photovoltaics

In 2009 Tsutomu Miyasaka and coworkers reported the first hybrid lead halide perovskite compound as light absorber in a dye-sensitized solar cell (DSSC) for solar energy applications. The solar cell showed just a 3.8% of power conversion efficiency (PCE) and completely degraded in a few minutes.[6] Despite these poor photovoltaic performance, the impressive optoelectronic properties of this material lead to an intense effort from the scientific community to push forward the improvement from this starting point. In 2012, the research groups led by Michael Gräetzel, Nam-Gyu Park and Henry Snaith, provided new insights of this technology improving stability and demonstrating the capability of this material to transport electronic charges to the solar cell electrodes, allowing higher PCE to values of 10.9%.[7,8] A wide number of issues were still to resolve to understand the efficiency limit of this type of materials and to increase stability. The nature of charge traps, ion migration, the hysteresis phenomena in the current–voltage curves (*j*-*V*), defects and grain boundaries, represent the main physical and chemical challenges to address that arose over the years. The research efforts to achieve these goals have resulted in an impressive wealth of literature reports and critical findings for this photovoltaic technology. Current best efficiencies have improved up to 24.2% in a single junction perovskite devices for a small lab-scale cells, reported by the Chinese Academy of Sciences in late 2018 and certified by the National Renewable Energy Laboratory (NREL) (Fig.1.5).[9]

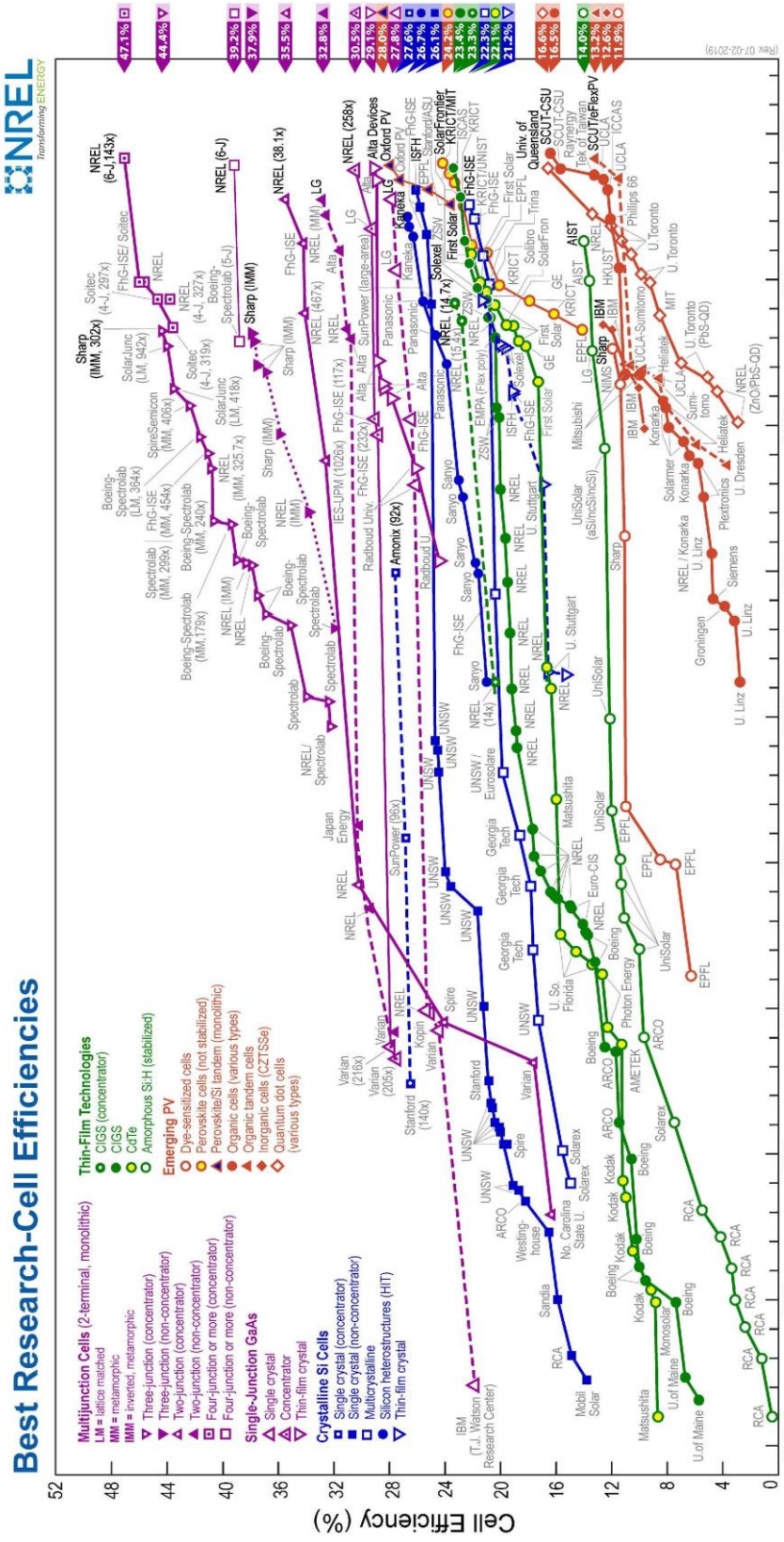

Figure 1.5. Efficiencies evolution of the different PV technologies provided by the National Renewable Energy Laboratory. The impressive rise of the perovskite devices

can be confirmed through the yellow-red circles. Data provided by the National Renewable Energy Laboratory (NREL).

At the same time, large-scale devices (> 1 cm^2) and modules (> 10 cm^2) are acquiring major attention, being developed through compatible deposition techniques as doctor blade coating, screen printing or slot-die coating.[10]

In parallel with the marketable horizon, the single junction devices are giving way to *tandem* or two-junction solar cells. In the case of perovskite/silicon tandem cells, the perovskite material works as a top cell absorbing the high energy region of the solar spectrum, transfering the low energy part to the silicon bottom cell at the same time, achieving extraordinary results. In fact, impressive efficiencies around 28% have been reported for a perovskite/silicon solar tandem cell developed by Oxford PV (Fig.1.5), approaching to the record of 32.8% published by LG Electronics for gallium indium phosphide/gallium arsenide monolithic devices.[9]

In addition to all the mentioned advances, a major application of perovskite solar cells was reported recently: building-integration panels. Saule Technologies has completed a pilot installation of semi-transparent perovskite photovoltaic devices into an office building in Poland.[11] In addition, perovskite-based devices are also contributing to the energy sector as light-emitting diodes (LEDs), detectors, lasers, being involved also in photocatalytic processes.

Yet for all these major achievements, important challenges remain in the shadows. For instance, the toxicity of lead or tin represent a problem for manufacturing panels and the end-of-life cycle, and several groups have been working on the use of non-toxic alternative metal ions.[12] However, the main problem that is actually slowing down the commercialization progress is related with the low stability of the perovskite itself (and as complete device). In addition, reduced stability is connected with the hysteretic behaviour during current density-voltage (*j-V*) measurements and this poses difficulties for standardizing the measurement protocol of PSCs. In fact, dark measurements are carried out with and without encapsulation varying the ambient environment. Under illumination conditions, stability tests use different light sources with and without ultra violet (UV) filter.[13,14,15] This variability during measurements suggest that the standards established by the International Electrotechnical Commission (IEC) for the silicon and inorganic thin-film PV technologies, could be also apply to the PSCs.[16] For this purpose, understanding the degradation mechanism of both perovskite materials and the external contacts during device operation conditions and under real ambient environment becomes mandatory. Nevertheless, remaining gaps still unsolved regarding the fundamental physics of the perovskite material and the interactions of the perovskite material with the other components of the device. Currently, the photocurrent values achieved in latest record efficiencies are close to its practical limit, presenting almost the 100% of their external quantum efficiency (EQE). In the case of photovoltage reported values, however, significant losses continue to occur. These losses are produced by recombination mechanisms, so minimize them becomes mandatory to push forward the power conversion efficiency of PSCs.

The foundations of this thesis lie in line with these remaining issues: 1-Improve understanding of degradation pathways from the point of view of materials synthesis and device configuration and 2-Clarify physical mechanism of recombination and

photovoltage losses. For these purposes, two main formulation perovskites have been optimized: $MAPbI_3$ and $MAPbBr_3$ respectively.

In the following sections, the literature concerning these topics is summarized, taken into account the impressive growing concerning perovskite publications in the latest years.[17]

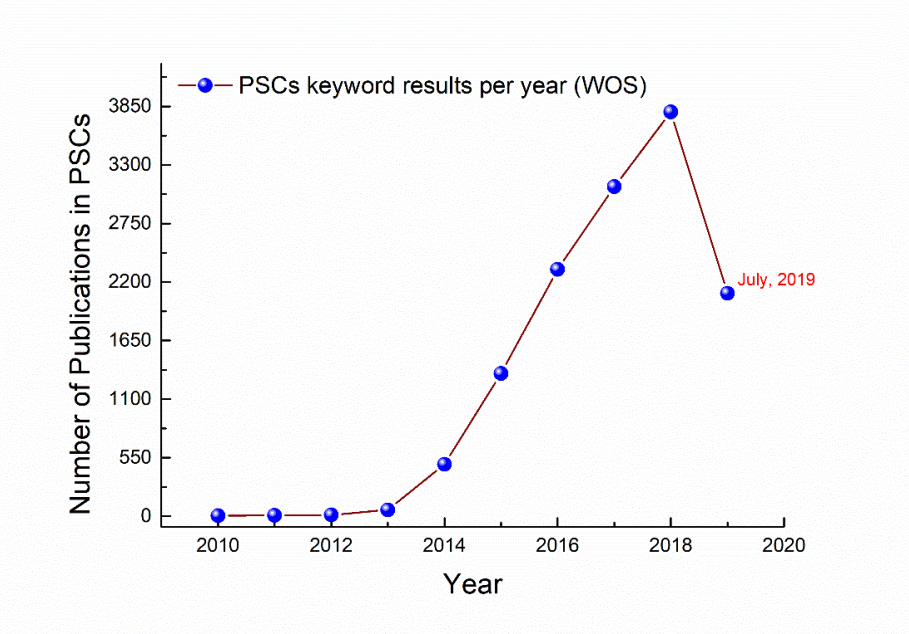

Figure 1.6. Number of publications resulting from the search of "perovskite solar cell" on Web of Science, retrieved on 29/07/2019. The line is a guide for the eye.

1.3. Perovskite Structure: A Coordinative Environment

The term *perovskite* is referred to a wide class of materials with the same type of structure as $CaTiO_3$, mineral discovered by Gustav Rose and named in honour of Lev A. Perovski.[18]

In the general perovskite oxides structure, ABX_3, A and B are cations with different sizes. *A* cation used to be larger than *B* cation, being B six-coordinated by an X-site anion to form a BX_6 octahedron complex. To arrange a three-dimensional (3D) system, the octahedron shares the corners, locating A-site cations in the cavities of the framework. Charge of each cation and anion must be such to preserve the electroneutrality. In the original structure of perovskite, $CaTiO_3$, cation B is a divalent element Ti^{4+}. In the hybrid organic-inorganic perovskites materials the A-site is a monovalent organic amine cation, B a divalent metal (Pb^{2+}, Sn^{2+}) and X an halogen element (Cl^-, Br^-, I^-) or by an extended version associating molecular linkers (azides N_3^-, cyanides CN^- or borohydrides BH_4^-). The divalent metal could also be replaced with mixed monovalent and trivalent metals in order to form the namely *double perovskites* $A_2BB'X_6$ structures (Fig.1.7).[19] The complexity in hybrid perovskite is much higher, with the organic nature of A cation the main responsible to provide useful structural flexibility that cannot be allowed for its completely inorganic counterparts.

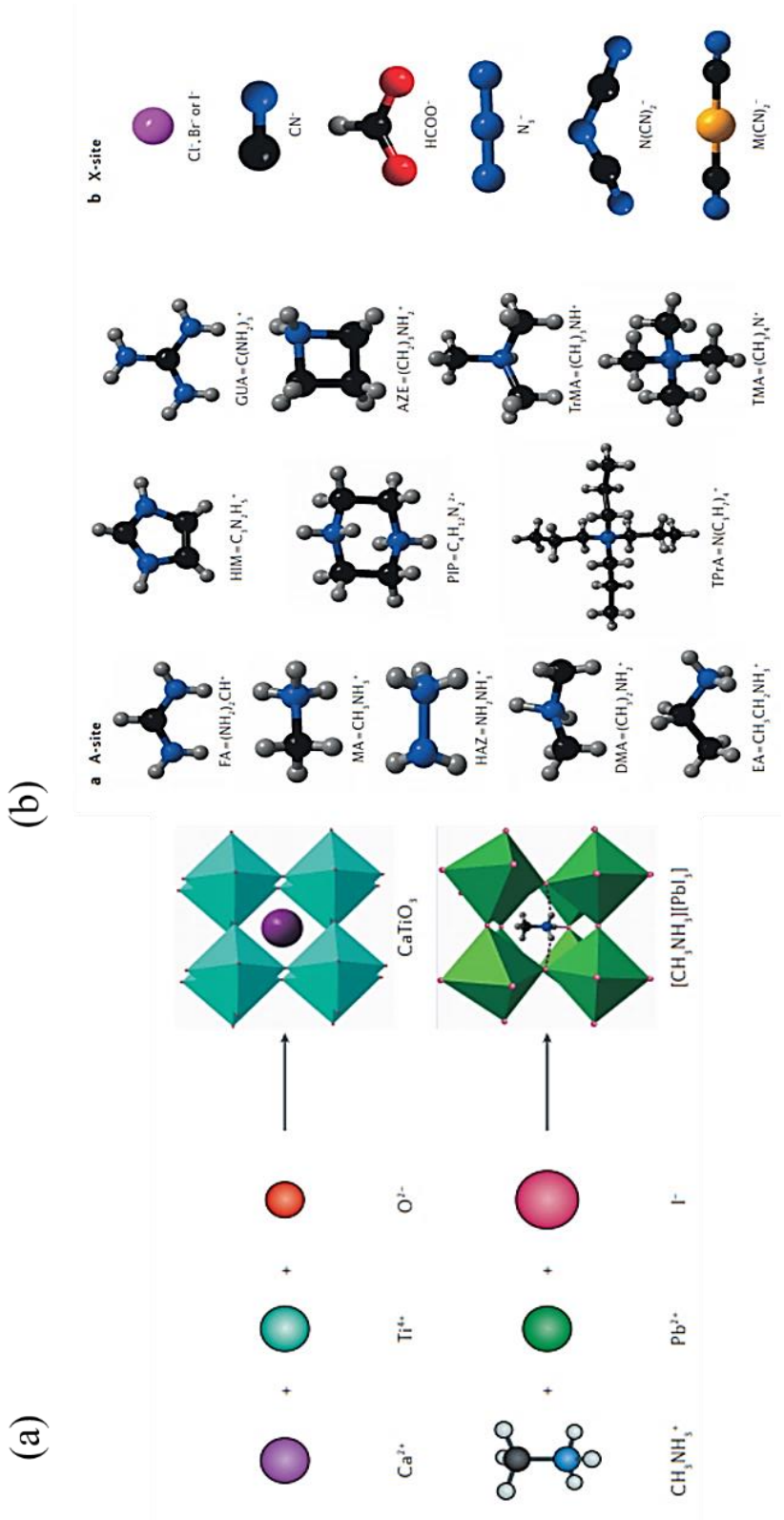

Figure 1.7. (a) Evolution from perovskite oxides to hybrid organic–inorganic perovskites. (b) Variety of A-site and X-site ions tuneable for hybrid perovskites. Adapted with permission of Ref.19. Copyright 2017, Springer Nature Publishing AG.

This great diversity in the chemical composition offers substantial opportunities to perform solar cells with a wide variability of physical properties, making these devices extremely versatile. The capability of tuning the chemistry is governed by the ionic ratio sizes of their components. The Goldschmidt tolerance factor (t) defines which components could match with the perovskite structure without compromising the crystallinity of the material.

$$t = (r_{Aeff} + r_{Xeff})/\sqrt{2}\,(r_B + h_{Xeff}/2) \quad (1)$$

where r_B represents the ionic radio of B-site metal, r_{Aeff} the effective radius of A cation, r_{Xeff} the effective radius of X anion and h_{Xeff} the length of the X molecular ions. The range of the tolerance factor in hybrid-halide perovskites materials goes from 0.8 to 1.0. A tolerance factor of 1 directs a perfect fit and between $0.8 \geq t \leq 1$ perovskites mostly do form. However, below 0.8, perovskites get distorted due to tilting of the BX_6 octahedra, loosing symmetry. Contrary, a $t > 1$ indicates that A cation is too large and generally impedes the formation of the perovskite structure. Coupled with the tolerance factor, another geometric element named as octahedral factor (μ) should be take into account in order to design a stable and useful perovskite material:

$$\mu = r_B/r_X \quad (2)$$

This factor regulates the fit of the B cation into the X_6 octahedron evaluating the compatibility of the A and B cations for the perovskite structure. Plotting t versus μ provides a practical structure map of suitable perovskite materials (Fig 1.8).[20]

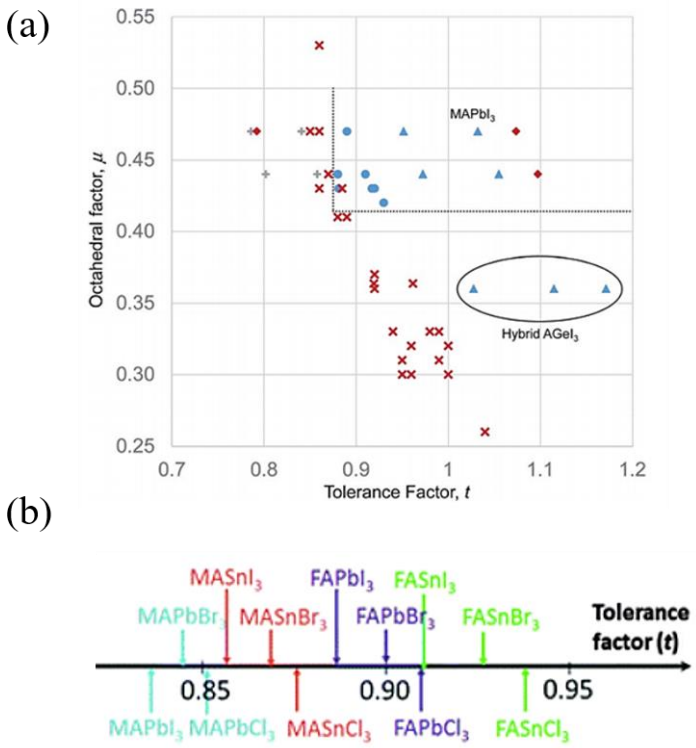

Figure 1.8. (a) Tolerance map for ABI_3 structures. Stable inorganic perovskites are represented by blue dots and hybrid perovskites by blue triangles. Hybrid compounds that

do not form perovskites are marked with red diamonds and inorganic compositions by red crosses. Reproduced with permission of Ref 20. Copyright 2016, The Royal Society of Chemistry. (b) Tolerance factors (t) of a series of halide perovskites. Adapted from Ref 20. Copyright 2016. The Royal Society of Chemistry.

The mentioned octahedral tilting induces consecutive phase transitions between the allotropic phases, following the sequence cubic-tetragonal-orthorhombic with decreasing temperature.

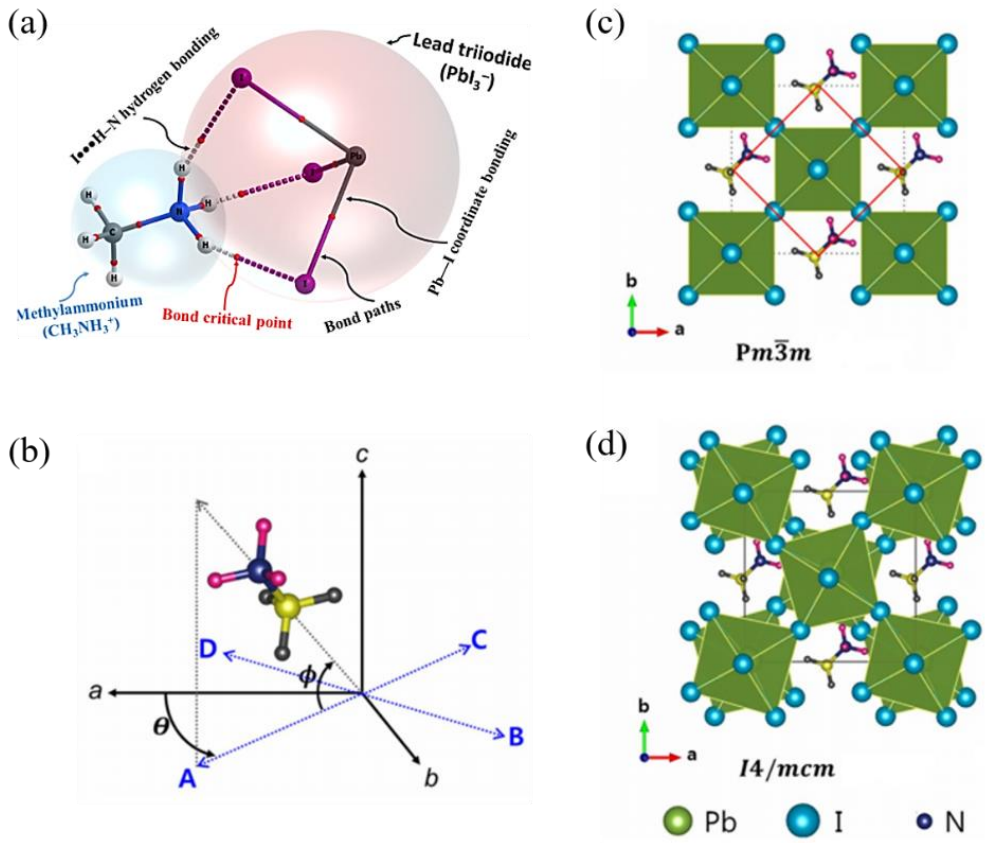

Figure 1.9. (a) Schematic bonding interactions between halides and organic cation. Reproduced with permission of Ref.21 Copyright 2017, Wiley-VHCA AG, Zurich, Switzerland (b) Preferred orientations of the organic MA^+-ion (i.e., C-N bond axis) within the perovskite cavity where A, B, C, and D represent the projection on the a-b plane. (c) Crystal structure of the high-temperature cubic Pm3m phase viewed from the c-axis. (d) Crystal structure of the tetragonal I4/mcm phase viewed from the c-axis. Reproduced with permission of Ref.22 Copyright 2016, Springer Nature Publishing AG

At low temperature (<100 K) an orthorhombic phase (γ) is the predominant structure. At room temperature (160 K) the tetragonal (β) phase appears and is replaced by a more stable cubic phase (α) at higher temperatures (330 K). These transitions influence the thermal stability of the perovskite material, adding great restrictions during the operation process of the cells. In the distorted structures, produced by the octahedral tilting, the lower symmetry incites a reduction in the coordination numbers of the metal B cation, producing the locking of the organic cation, which become well oriented along the high-

symmetry directions of the perovskite crystal (Fig.1.9a, 1.9b).[21,22] Contrary, in the tetragonal and cubic phases (Fig.1.9c, 1.9d), the freedom of rotation and orientation of the A cation leads to magnetic transitions, changes in charge-carriers recombination dynamics, mobility and important changes in the optical bandgaps, as referred by PL evidences (Fig.1.10).[23,24,25]

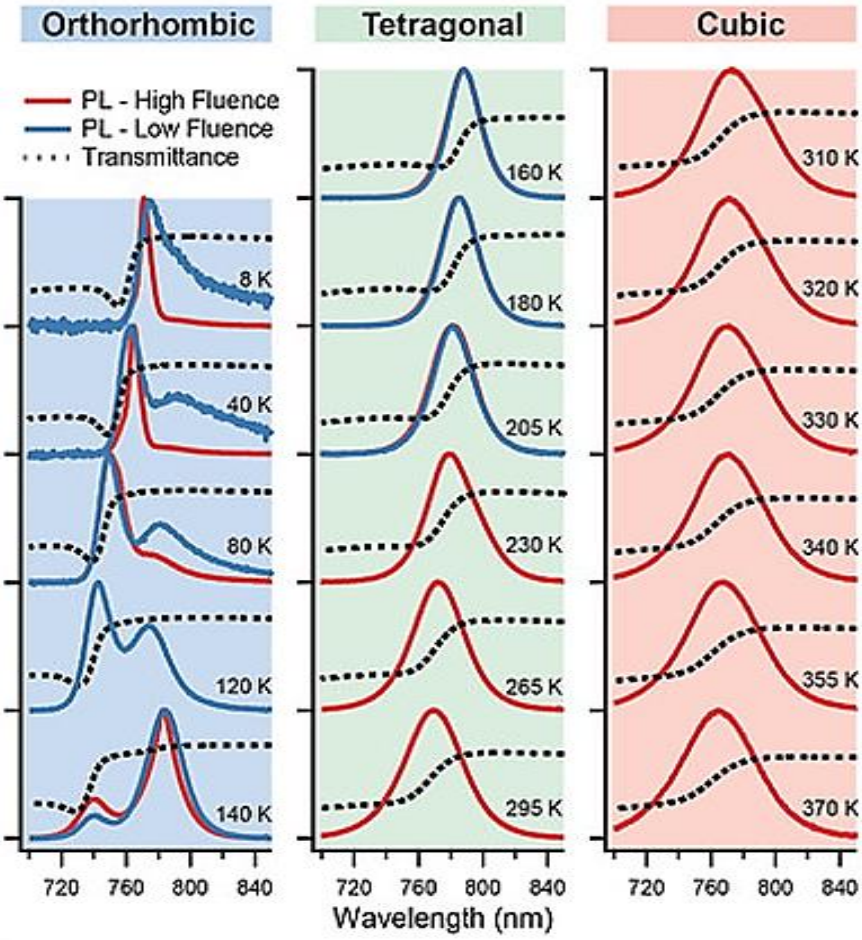

Figure 1.10. Transmittance (dashed lines) and normalized steady-state PL (solid lines) spectra of $MAPbI_3$ measured at temperatures ranging from 8 to 370 K. Black ticks on the y-axis indicate values of 0 and 1 below and above the respective curves. The shading corresponds to the three different phases as labelled at the top of the figure. Reproduced with permission of Ref.23, Copyright 2015, WILEY-VCH Verlag GmbH & Co.

Then, the control of this PbI_6 octahedral tilting in order to enhance stability, can be achieved by adjusting the hydrogen-bonding interactions between the halides and hydrogen atoms bonded to the MA group, which plays a key role in terms of steric size.[26,27,28]

1.3.1. $MAPbI_3$ versus $MAPbBr_3$

To address the stability issues regarding extrinsic and intrinsic factors, two main perovskite formulations have been optimized. For the external issues involving moisture exposure, thin films of the most widely used methylammonium lead iodide formulation ($MAPbI_3$) were optimized by spin-coating for integration into a regular configuration device (n-i-p), with TiO_2 and Spiro-OMeTAD as electron (ESL) and hole (HSL) selective contacts, respectively. To face the intrinsic stability problems related with the ionic dynamic at the interfaces, a methylammonium lead bromide perovskite ($MAPbBr_3$) solar cell was fabricated with high crystalline absorber material also by spin-coating method, with the same ESL and HSL as its iodide counterpart. A comparative analysis regarding the main physical and chemical characteristic properties of each perovskite-based devices is described below.

The chemical, physical and finally optoelectronic properties of solar devices based in methylammonium lead iodide or bromide perovskite materials are a consequence of their respective crystalline structures. In the case of iodide-base material, the tetragonal I4/mcm room-temperature phase is the most common one. Contrary, $MAPbBr_3$ shows a cubic perovskite structure phase $Pm\bar{3}m$ at room temperature (Fig.1.11a and 1.11b). This difference between the preferential crystal space groups is directly related with the ionic radius of I^- and Br^-, which are 2.2 and 1.96 Å, respectively. As mentioned in previous section, the ionic radii relationship between A-site cation, B-site cation and X-site anion, form the criteria for the distortion of the BX_6 octahedron. The smaller X ionic radius, the easier formation of the cubic structure, as long as the Goldsmith factor allows it.

The respective band gaps of both materials are shown in the Fig.1.11c. As can be observed, both present suitable band energies for single-heterojunction solar cells using TiO_2 as ESL due to their higher conduction bands respect to the metal oxide. The energy levels is vaccum are also showed respect to the typical HSL material, Spiro-OMeTAD, suitable to extract holes efficiently for both types of perovskites absorbers.[29]

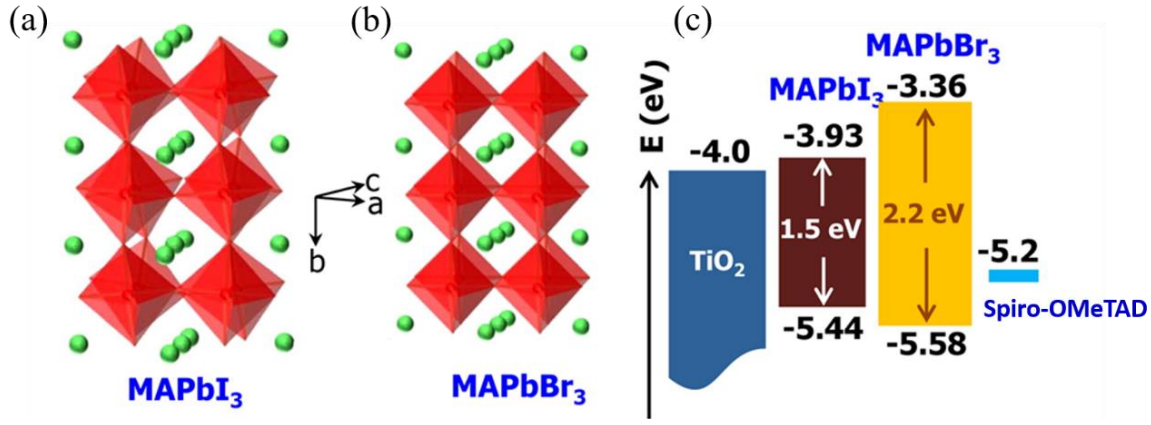

Figure 1.11. Crystal structures and energy levels of $MAPbI_3$ and $MAPbBr_3$ and hybrid heterojunction solar cell configuration. (a) Distorted tetragonal perovskite structure of $MAPbI_3$ at room temperature. (b) Cubic perovskite structure of $MAPbBr_3$ at room temperature. Red: polyhedron $[PbX_6^2]^-$ (X = I, Br); green sphere: CH_3NH_3(= MA). (c) The conduction band (CB) and valence band (VB) of $MAPbI_3$, $MAPbBr_3$, and TiO_2 in eV. Adapted with permission of Ref.29. Copyright 2013, American Chemical Society.

During the process of film fabrication, the PbI_2 precursor is first dissolved in the widely used polar solvent mixture DMF/DMSO. PbI_2 has a layered structure that allows to DMF insert into its structure screening PbI_2 via Pb-O bonding.[30] This intercalation leads to a red-shift of the diffraction plane (001) from 14.8″ to 7.94″ as well as a intercalation of DMSO when this red-shift goes to 9.17″.[31,32,33] When MAI is added and the reaction with PbI_2 starts, a predominant peak at (220) appeared. After the annealing process, the long-range crystalline order increase, leading to grow in the preferential (110) diffraction peak for a tetragonal structure.

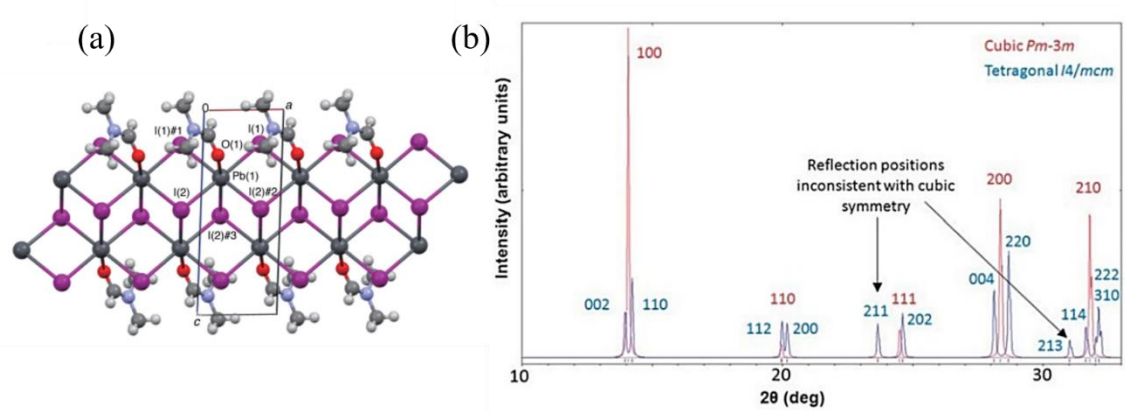

Figure 1.12. (a) DMF insertion into the PbI_2 structure. Reproduced with permission of Ref. 30. Copyright 2014, The Chemical Society of Japan. (b) X-ray diffraction patterns of cubic and tetragonal phase corresponding to bromide and iodide-based perovskite materials. Adapted with permission of Ref.31. Copyright 2013, Royal Society of Chemistry.

Regarding the optical properties, the light emission peaks appear at around 550-580 nm and 780-800 nm for bromide and iodide-base materials respectively, as shown in Fig.1.13a and 1.13b for single crystal structures. The emission peaks corresponding to the different band-gaps associated with each material, being around 2.2 eV in the bromide case and around 1.5 eV in the case of iodide, stablish the premises for the purposes regarding both structures in this thesis.[34] The differences between the photovoltaic performances of these two PSCs are described in the following section in terms of the theoretical maximum efficiency and photovoltage.

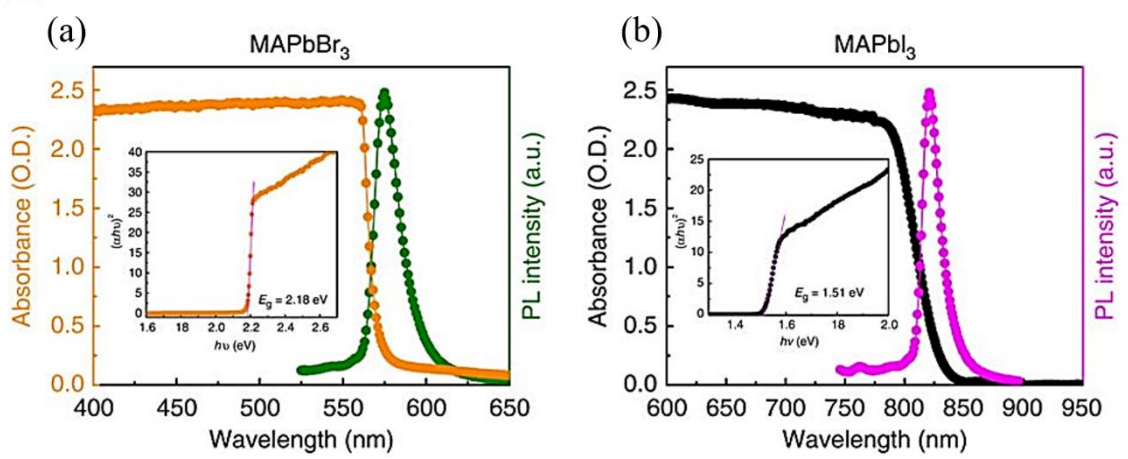

Figure 1.13. Steady-state absorption and photoluminescence of perovskite materials. (a) $MAPbBr_3$ single crystal. (b) $MAPbI_3$ single crystal. Insets: corresponding Tauc plots displaying the extrapolated optical band gaps. Reproduced with permission of Ref.34. Copyright 2015, Springer Nature Publishing AG.

1.4. Device Operation

In this section, the essential physical working mechanisms of a PSC are described. The basic principles regarding the photovoltaic performance based in the diode behaviour is explained in depth. The current density-voltage characteristics are also detailed coupled with the factors limiting the photovoltage. These are described focusing in the recombination processes that govern the phenomena of photovoltage losses, markedly related with the surface recombination and non-radiative recombination dynamics. The role of the external selective contacts through the most widely used mesoscopic regular device configuration (n-i-p) is remarked and the charge separation under the different operation conditions (dark, illumination, polarization) is also analysed, underlying the surface accumulation and recombination phenomena at the ESL/perovskite interface.

1.4.1. Recombination current and radiative limit of V_{oc}

Absorption, generation and recombination are the processes governing the operation mechanisms of a solar cell. Recombination occurs when an electron in the conduction band (CB) that has been excited by the absorption of a photon, returns to the valence band (VB), leading to the loss of mobile photogenerated or injected electronic carriers. This process can take place through three different mechanisms:

- Radiative recombination: also called *band-to-band* recombination with bimolecular characteristic (due to the dependence on both free electron and hole densities). Here, the return to the VB of the excited electron occurs by the emission of a photon with equal energy to the band gap (E_g) of the absorber material.
- Non-radiative recombination:
  - Through trap states, known as monomolecular *Shockley-Read-Hall* (SRH) recombination.
  - Through the kinetic energy (> E_g) transfer between electronic carriers, leading to an excited electron across the gap, also called trimolecular *Auger* non-radiative recombination.[35]

The radiative recombination or band-to-band recombination and Auger non-radiative recombination represent unavoidable processes due to the fundamental functionality of

the solar cell.[36] Contrary, the non-radiative SRH recombination is considered as an avoidable process that could potentially be minimized.

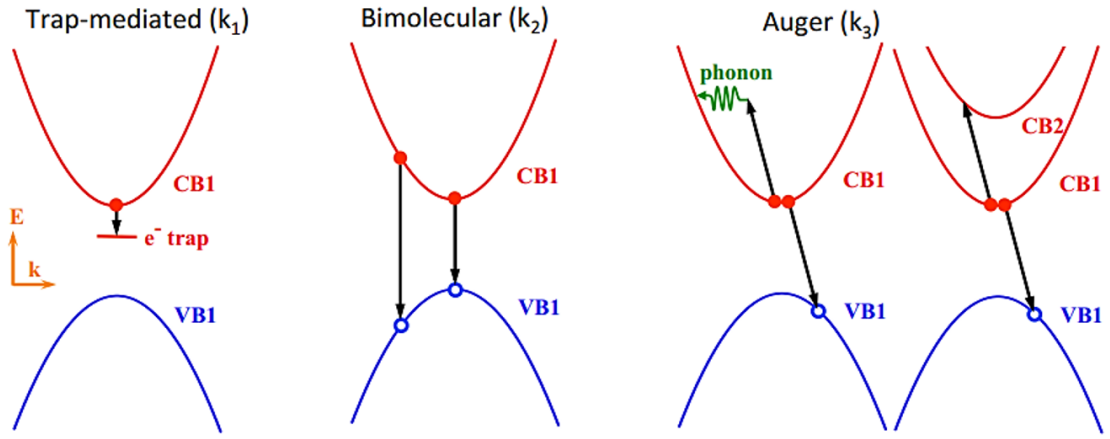

Figure 1.14. Schematic representation of the three different recombination processes. From left to right: non-radiative monomolecular SRH recombination through trap-states; radiative bimolecular band-to-band recombination and non-radiative Auger recombination. Note that k_1, k_2, k_3 are represented as A, B, C in the rate equation below (3). Adapted with permission of Ref.35. Copyright 2016, Annual review of physical chemistry.

The rate equation governing these processes can provide information about the predominant recombination mechanisms and is defined as follows:

$$\frac{dn}{dt} = U_n = An + Bn^2 + Cn^3 \tag{3}$$

where $n(t)$ is the free-charge carrier density and A, B, C represents the rate constants for each process.

A photovoltaic device present a fundamental physical limitation regarding the fact that the solar cell exchanges thermal radiation with its surrounding at the same time that absorbs the solar radiation,[37] and the rate of emission of photons by the solar device should matches with the rate of photon absorption. This allows to a constant concentration of carriers in the material at *steady state*.[38,39] In other words, the probability of absorption of a photon of energy E, a(E), or absorptivity, should be equal to the probability of emission of a photon of energy E, or emissivity ε(E), established by the *detailed balance principle:*

$$a(E) = \varepsilon(E) \tag{4}$$

Both processes have their respective current density associated respect to the equilibrium, dark or illumination conditions.[40]

- Thermal saturation current density, j_0^{th}, due to the absorption of the black body (BB) radiation.
- Photogenerated current density, j_{ph}, due to the absorption of light.
- Recombination current density, j_{rec}, due to the relaxation processes, radiatives and non-radiatives.

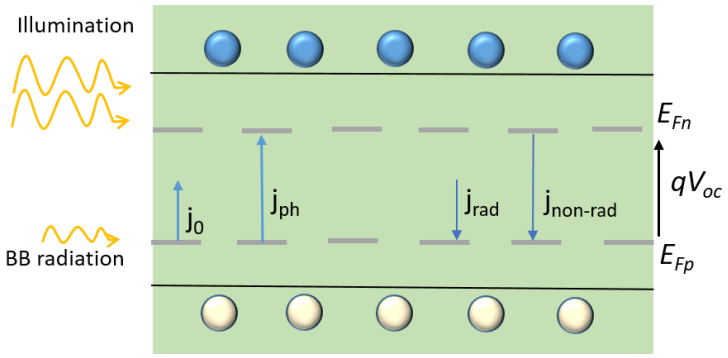

Figure 1.15. Current density associated to the diferent processes taken place both in dark and under illumination conditions. The difference between the Fermi levels on n and p materials, produce the potential difference qV_{oc}.

In thermal equilibrium, that is under dark at zero bias ($V = 0$), the solar device is just affected by the Lambertian black body (BB) radiation (Fig.1.15). This absorbed radiation is emitted at the same rate, due to the detailed balance principle. This emission takes place through *radiative recombination* of the photogenerated carriers (e.g., electrons and holes), by band-to-band mechanisms, described by:

$$U_{rad} = B_{rad} np \tag{5}$$

where B_{rad} is the bimolecular recombination coefficient (cm^3s^{-1}) and np the product of electron and holes densities, which are defined employing the Boltzmann approximation:

$$np = N_C N_V exp\left(\frac{qV_{oc} - E_g}{k_B T}\right) \tag{6}$$

where $N_C N_V$ are the effective densities of states of the conduction and valence band respectively.

In a p-doped material, that is the case of $MAPbI_3$ and $MAPbBr_3$, the process is monomolecular due to the recombination of the minority carriers (electrons):

$$U = B_{rad} N_A (n - n_0) \tag{7}$$

where N_A is the density of acceptors in the p-doped material. The associated recombination current to this process is also described in terms of the detailed balance.

Under dark equilibrium conditions at zero bias (V = 0), the thermal generation parameter, j_0^{th} should be also a measure of recombination in the solar cell and the term j_0^{th} becomes just a *radiative recombination parameter*, in terms of the photovoltaic external quantum efficiency of the solar cell, defined as the ratio of the electron flux to the incoming photon flux:

$$EQE_{PV} = \frac{j(\upsilon)}{q\varphi_{ph}(\upsilon)} \tag{8}$$

Because in dark just the black body (BB) radiation is the only one affecting the solar cell, the radiative recombination parameter reads as follows:

$$j_{0,rad} = \int_0^\infty EQE_{PV}(E)\varphi_{ph}^{bb}(E)dE, \quad (9)$$

where $\varphi_{ph}^{bb}(E)$ is the photon flux of the black body radiation.

This radiative recombination parameter establishes the minimum possible recombination rate for a solar cell. However, not only radiative recombination processes take place during solar cell operation, but also non-radiative mechanisms that increase the rate of recombination, producing additional losses in the photovoltaic performance of the device. Then, the radiative recombination current is lower than the real recombination current under dark equilibrium conditions. Therefore, the total recombination current, or *saturation current* become as:

$$j_0 = \frac{j_{0,rad}}{EQE_{LED}} \quad (10)$$

where EQE_{LED} represents the external quantum efficiency of the solar device operating as a light-emitting diode (LED):

$$EQE_{LED} = \frac{\varphi_{ph}^{out}}{j/q} \quad (11)$$

with φ_{ph}^{out} as the output of emitted photon flux to carriers injected *j/q*.

Under dark but at forward bias conditions, the absorber material is only affected by the BB radiation that generates the flux of thermed electrons, but carriers are injected through the applied bias, leading to a recombination current that can be calculated by the integration of the bimolecular recombination rate across the semiconductor thickness (*d*), resolving as follows:

$$j_{rec} = qdBnp \quad (12)$$

being the saturation current defined as:

$$j_0 = qdBn_i^2 \quad (13)$$

The exponential dependence of recombination current with the voltage is defined as follows:

$$j_{rec} = j_0 e^{qV/mk_BT} \quad (14)$$

where the term m in the exponential part of the equation represents an *ideality factor* introduced to take into account non-ideal behaviours in the solar cell performance. This parameter normally takes values between 1 and 2, and gives an idea of the dominant recombination mechanism governing the system. For an ideal solar cell, the value of the ideal factor is 1 and just radiative band-to-band recombination mechanisms are considered.

Analogy, under illumination conditions, the solar spectra (AM 1.5) irradiates the device producing a photogenerated electrical current density, which can be described also

in terms of EQE_{PV}, taken into account this time the photon flux of the solar spectra, $\varphi_{ph}^{AM1.5}$ instead of the BB radiation:

$$j_{ph} = \int_0^{\infty} EQE_{PV}(E)\varphi_{ph}^{AM1.5}(E)dE \quad (15)$$

1.4.1.1.Current-voltage characteristic and maximum PCE

During normal working conditions, a forward bias is applied at the same time that an incident light arises the device. Assuming ideal external contacts able to extract all the photogenerated carriers, the current balance reads as follows:

$$j = j_{ph} + j_0 - j_{rec} \quad (16)$$

and the exponential dependence of carrier density with the applied voltage is described through its rectifying behaviour by the *Schokley diode equation*:

$$j = j_{ph} - j_0\left(e^{qV/mk_BT} - 1\right) \quad (17)$$

with the corresponding *j-V* curve shape for a diode performance:

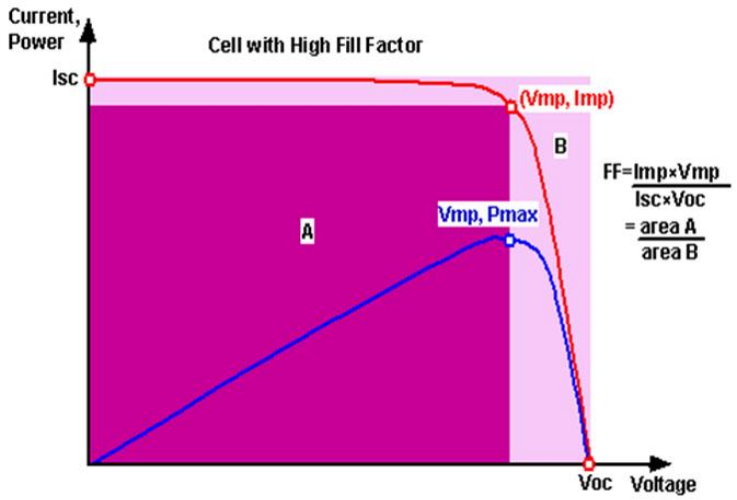

Figure 1.16. Schematic representation of a diode *j-V* curve. The photovoltaic characteristic short-circuit current, I_{sc} and open-circuit potential, V_{oc} are shown. The V_{mp}, P_{max} and I_{mp} are also detailed in red and blue points. The calculation of the FF of the curve is represented as inset in the figure. Copyright PVeducation.org.

If the illumination of the solar device takes place at *open-circuit* conditions, no photogenerated carriers are extracted and the current density balance turn as:

$$j_{ph} = j_0 e^{qV_{oc}/mk_BT} \quad (18)$$

From this relation, seems clear that the maximum value of photovoltage is obtained when the recombination is the minimum possible, represented, as explained before, by the radiative recombination parameter, $j_{0,rad}$. Then, when only radiative phenomena govern

the operation of the solar cell, the open-circuit potential is the maximum and the ideality factor m takes the value 1. The maximum value of the open circuit potential is known as the *radiative limit* of photovoltage:

$$V_{oc}^{rad} = \frac{k_B T}{q} \ln\left(\frac{j_{ph}}{j_{0,rad}}\right) \tag{19}$$

In the case of a real solar cell where non-radiative processes are also involved in the operation mechanistic of the device, the open circuit potential is defined by the saturation current density, j_0 in terms of the EQE_{LED}:

$$V_{oc} = \frac{k_B T}{q} \ln\left(\frac{j_{ph}}{j_{0,rad}} EQE_{LED}\right) \tag{20}$$

Contrary, at $V = 0$, all the photogenerated carriers are extracted and the recombination current equals the dark saturation current. The photocurrent at this condition is termed the *short circuit current density*, j_{sc} that could be described by Eq. 15 when $EQE_{PV}(E) = 1$.

As can be observed in Fig.1.16, the cell power density is defined by the product of the current-voltage and when the applied bias is located between 0-V_{oc}, the solar cell generates the power behaving as the ideal diode and performing the *j-V* curve. At maximum power point, V_m and J_m are the corresponding voltage and current associated with, stablishing the "squareness" of the *j-V* curve by the fill factor term, FF which relates the J_m and V_m terms with respect to the J_{sc} and V_{oc}. Therefore, the maximum efficiency for the solar cell is given by:

$$\eta = \frac{j_{mp} V_{mp}}{\Phi_{E,tot}^{source}} = \frac{J_{sc} V_{oc} FF}{P_s} \tag{21}$$

where P_s is the incident power, established as 100 W cm^{-2}.

If the spectrum is fixed, then only the band gap is the determining factor for η, so for any spectrum exist an optimum band gap for which the efficiency is maximum. Then, for very small or very large band gaps, the photoconversion will be inefficient. Low band gap will leads too small voltage, while the larger band gaps will perform minor photocurrents.

Therefore, the maximum solar conversion efficiency, for an ideal case in which the only recombination mechanisms of hole-electron pair is radiative band-to-band, will be around 33.7% for a p-n junction with a 1.4 eV of band-gap (Fig, 1.17a, 1.17b, 1.17c).[37,38]

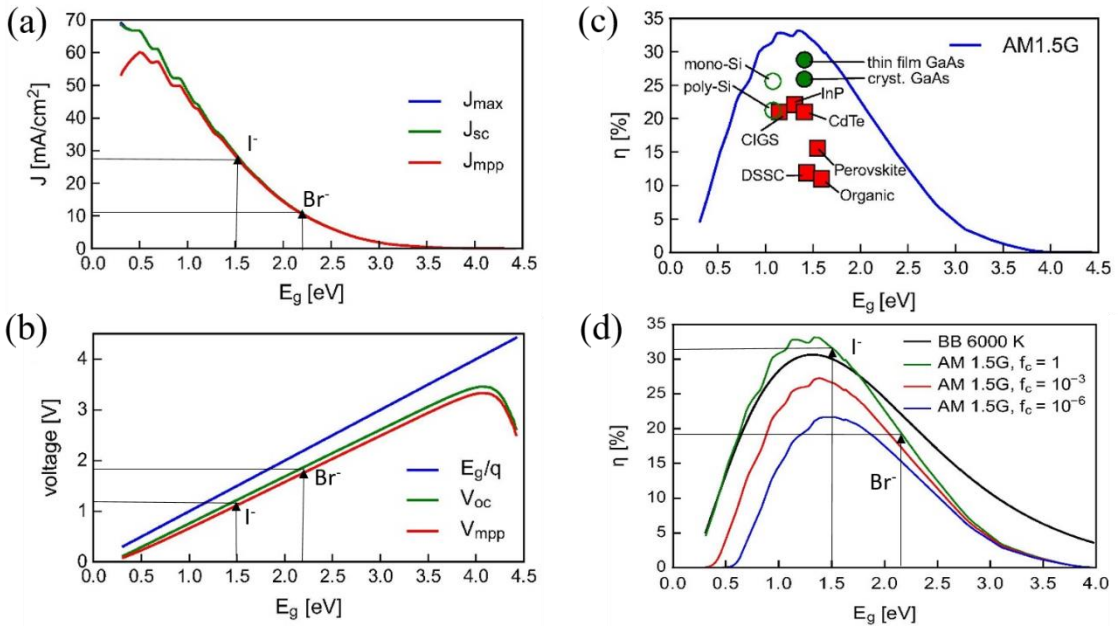

Figure 1.17. (a) Maximum electron–hole generation current density J_{max}, the short circuit current density J_{sc}, and the current density at the maximum power point J_{mpp} calculated for the AM 1.5G spectral irradiance as a function of the band gap energy. (b) Band gap potential $E_{g/q}$, open circuit voltage V_{oc} and maximum power point voltage V_{mpp} as a function of the band gap. (c) Maximum light to electric power conversion efficiency (detailed balance limit) for a solar cell operated at 298.15 K and illuminated with the AM 1.5G spectral irradiance in accordance with standard solar test conditions as a function of the band gap energy. (d) Shockley–Queisser limit for a solar cell with a cell temperature of 300 K, illuminated by a black body (BB) with a surface temperature of 6000 K (black curve) compared to the detailed balance limit for standard solar cell test conditions (Tc = 298.15 K, AM 1.5G). Green curve considering only radiative recombination, non-radiative recombination that is 10^3 (red curve) and 10^6 (blue curve) times stronger than radiative recombination. Adapted with permission of Ref.38. Copyright 2016, Elsevier Ltd.

Then, it can be assumed that for higher efficiencies, we need to move toward higher band-gaps when recombination increases.[38]

Taken these limits into account, in the particular case of iodide and bromide perovskite absorber materials, the highest current density will be achieve through iodide perovskite solar cells, while the maximum photovoltage values will correspond to bromide counterparts.

1.4.2. External selective contacts and charge separation

Efficient charge separation of the generated carriers is needed for a proper photoconversion process in PSCs. This charge separation is provided by introducing a certain amount of asymmetry in the device through which the carriers can travel to the external circuit to produce the electrical work. This asymmetry is provided by the selective contacts, where a p-type and n-type of defects dopes the respective hole and electron selective materials. Since perovskite absorber has been described as an intrinsic

semiconductor, the final architecture corresponds to an n-i-p single heterojunction. Therefore, the electron selective contact (ESL) will extract the carriers with the higher chemical potential (excited state) and the hole selective contact (HSL) the carriers with the lower one (ground state) (Fig.1.18a). In dark conditions without applying bias, the Fermi levels, E_{F0}, equilibrates along the complete device producing a built-in potential V_{bi}. The work functions of the contacts greatly control the open-circuit potential, stablishing the fundamental operating mechanisms of the solar device.

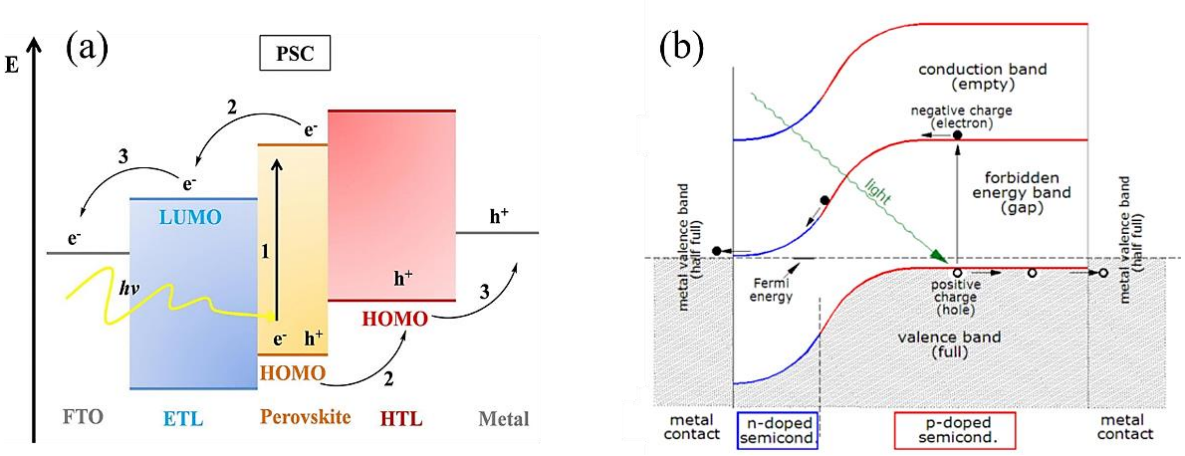

Figure 1.18. (a) Band diagram and genèric operation mechanisms of a PSCs. Reproduced with permision of Ref.34.[41] Copyright 2014, Sprynger. (b) Band diagram showing the drift of the carriers to the n and p materials respectively. Creative Commons Attribution-Share Alike 3.0 Unported.

Several unexpected phenomena related with the charge separation are observed during optoelectronic measures in PSCs. A dynamic evolution of charge distribution, different times domains (*t*) of different processes and the nature of the *j-V* curve, are the main features involving the particularities of the PSCs mechanistic issues. Regarding the *j-V* curves, as mentioned in previous sections, a controversial hysteretic behaviour is observed during measures, being one of the phenomena responsible of slowing down the race to the highest PCE. This behaviour is more or less strong depending on the scan rate, direction of the applied bias and preconditioning treatments.[42] Therefore, the development of a robust measurement protocol that guarantee the reliability of the reported PCE become mandatory, due to the difficulties in the achievement of steady-state conditions. Another important feature frequently observed in PSCs concerning impedance spectroscopy (IS) measures, is a huge capacitance response at low-frequency region.[43,44] The causes of these behaviours have been attributed to chemical and structural defects in the perovskite matrix, traps of electrons and holes and to a redistribution of moving ions (vacancies or interstitials, V_{MA}^{-}; V_{Pb}^{-}; V_{I}^{+}, I^{-}) into the system. However, the slow dynamics observed have been correlated, and supported by several authors, to the slowly moving ions migrating across the system (Fig 1.25b, c).[45]

1.4.2.1.Device architecture: n-i-p heterojunction

In PSCs charge separation is optimized with a single intrinsic heterojunction, p-i-n or n-i-p architecture. The characteristic layered structured is formed by the perovskite light-

harvesting material sandwiched between the external selective layers, ESL and HSL. The sequence in which the selective contacts are disposed with respect to the illumination path, determines the type of device configuration: n-i-p, known as regular configuration, or p-i-n, called as inverted configuration. Therefore, both architectures include a transparent conductive oxide (TCO)–coated glass substrate (fluorine tin oxide, FTO; or indium tin oxide, ITO), an n-type semiconductor as the ESL, the perovskite absorber material, a p-type semiconductor as HSL and a back-contact (metal, TCO, or carbon). In the regular configuration, the ESL is composed by a metal oxide such titanium dioxide TiO_2 or Tin dioxide SnO_2, while the nature of HSL is an organic polymer, normally constituted by 2,2′(7,7′)-tetrakis-(N,N-di-p-methoxyphenyl-amine)9,9′-spirobifluorene (spiro-OMeTAD) or poly(triarlyamine) (PTAA). In contrast, for the p-i-n junction structure, both selective materials are mainly formed by fullerene derivatives and organic materials, such as [6,6]-phenyl-C-61-butyric acid methyl ester (PCBM) and poly(3,4-ethylenedioxythiophene) doped with poly(4-styrenesul-fonate) (PEDOT:PSS), respectively. In both configurations, the light path direction cross the substrate through the TCO-coated glass substrate, and then through the ESL or HSL to be absorbed at the perovskite, leaving the HSL or ESL at the end of the light path with the final back-contact.[46] As it can be observed in Fig.1.19, both, regular and inverted architectures could be also fabricated in tow additional configurations: planar and mesoscopic. However, the usual choice for each other is mesoscopic for n-i-p and planar for p-i-n. This difference will have major implications in terms of charge-accumulation phenomena and will be described in the following sections.

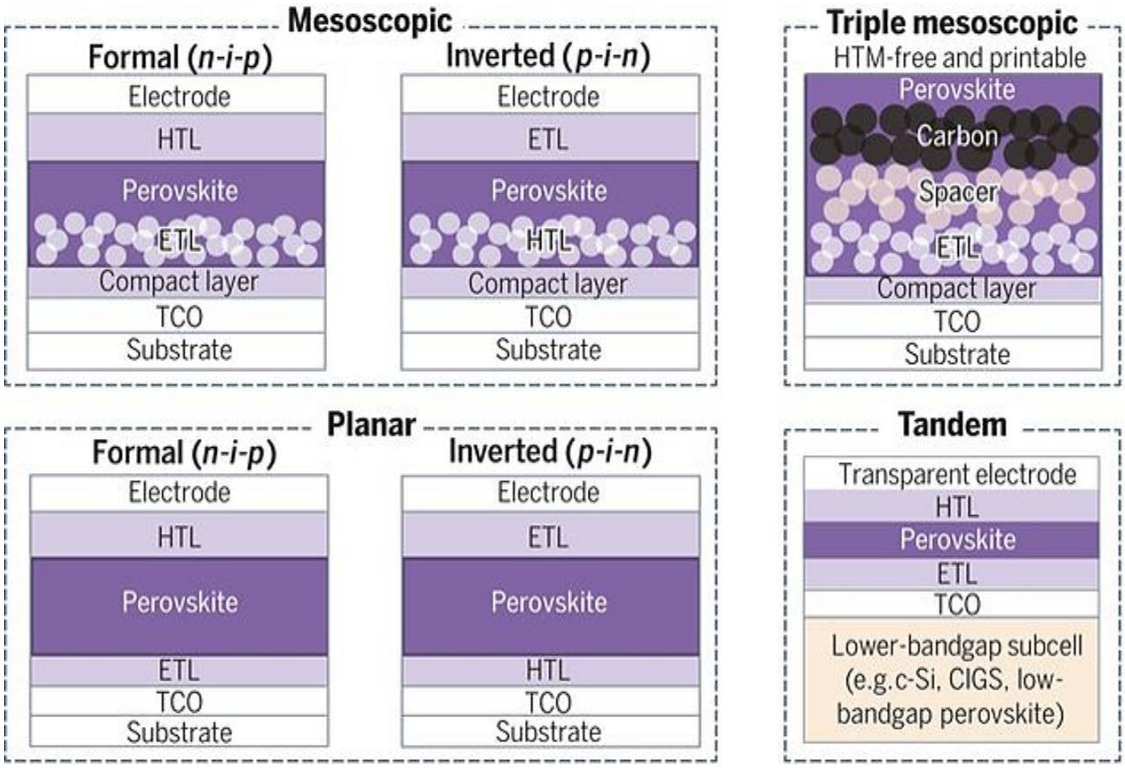

Figure 1.19. Four device configurations of PSCs: mesoscopic structure, planar structure, triple mesoscopic structure, and tandem structure with lower-bandgap sub-cell. Reproduced with permission of Ref.46. Copyright 2018, Science.

In mesoscopic PSCs, developed after investigations of dye-sensitized solar cells, the perovskite absorber sensitizes the mesoporous metal oxide layer (e.g., meso-TiO_2) used as a scaffold, being the most widely used solar structure with the highest efficiencies reported. Triple mesoscopic are also a recent architecture in which the perovskite material is coated onto a triple-layer scaffold, usually made of a screen-printed mesoporous TiO_2 layer, a ZrO_2 spacer layer and a final carbon electrode. A carbon electrode replace here the metal back-contact, avoiding the use of HSL.[47]

The last architecture showed in Fig.1.19 represents the most promising one in terms on multiple junction solar devices. A PSC could be located as a top-cell onto the other PV devices such as silicon, copper indium gallium selenide (CIGS) or low-bandgap perovskites. The result is a tandem solar cell, able to achieve more than competitive results as 26% reported by Oxford PV recently, as mentioned in the previous sections of this thesis. The tandem technology increases the solar efficiency beyond the Shockley-Queisser limit of single-junction devices, stablishing as well an important marketable horizon.[48]

1.4.2.1.1. TiO_2 and Spiro-OMeTAD

Titanium dioxide

Titanium dioxide TiO_2 presents an indirect bandgap and represents the most widely used electron selective material in both planar and mesoscopic architectures of PSCs, acting as a cathode buffer layer due to its n-type nature. Although it can exists in three polymorphs: brookite (orthorhombic), anatase (tetragonal) and rutile (tetragonal); the latter is the thermodynamically most stable phase with a band gap of 3.0 eV, while the anatase phase is the most interesting for the PV applications, with a E_g = 3.15 eV (Fig.1.20a, b).[49] In fact, the solution-based preparation methods for TiO_2 generally shows the anatase phase. This material present high transparency in the visible light (Fig.1.21c), low absorption and high refractive index being firstly optimized for the dye sensitizer solar cells technology (DSSCs). [50,51]

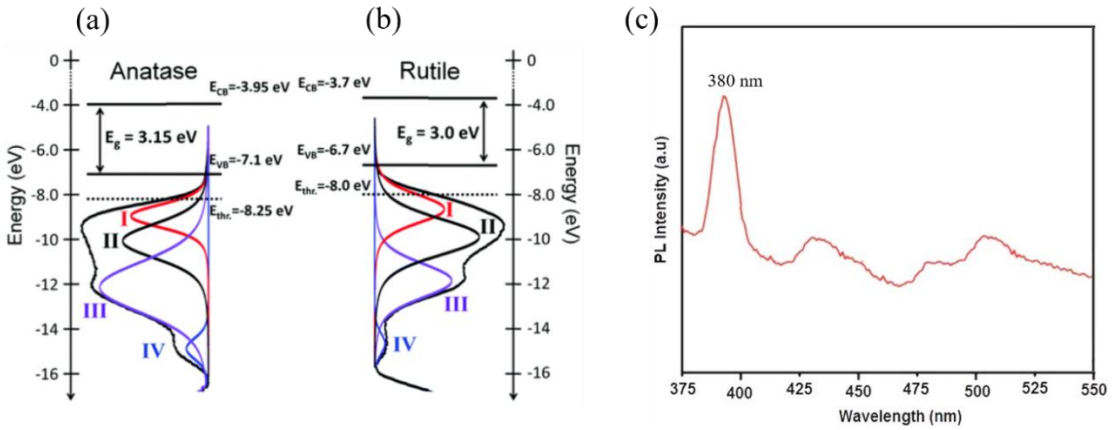

Figure 1.20. (a) Energy levels of two polymorphs of titanium dioxide, anatase and (b) rutile respectively. Adapted with permission of Ref. 49. Copyright 2018, Royal Society of Chemistry. (c) Photoluminiscence spectra of titanium dioxide showing the maximum wavelength at 380 nm. Adapted with permission of Ref.50, Copyright 2016, Materials Research.

The mesoporous TiO_2 film, deposited by spin-coating method onto the compact layer of TiO_2, acts as a scaffold of the perovskite material, being infiltrated by the perovskite solution. However, an important disadvantage is the high density of electronic trap states below conduction band that may affects the charge recombination and charge transport, inducing stability problems that influence the photovoltaic performance.[52] Leijtens et al. proposed a mechanism of UV-induced degradation in organometallic halide PSCs that lies in the excitation of the TiO_2 bandgap, which generates electron-holes pairs. This provokes a recombination of the holes in the valence band with the electrons in the oxygen adsorption sites, desorbing the oxygen molecules. The consequence is the presence of unfilled oxygen vacancies formed at the surface of TiO_2 and free electrons remaining in the conduction band, which can recombine easily with holes from the HSL (Fig.1.21).[53,54]

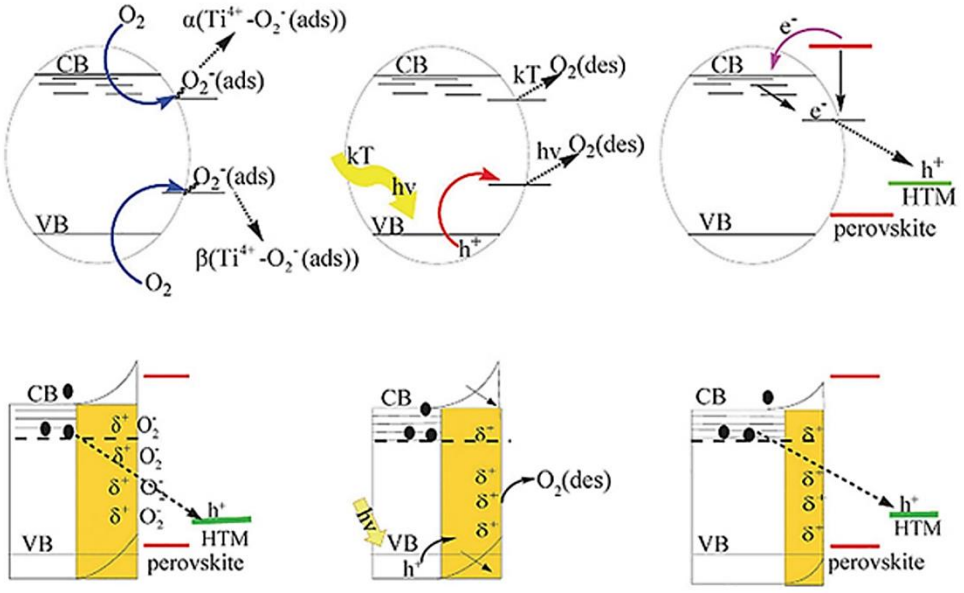

Figure 1.21. Schematic diagrams for the formation of the trap states and depletion area in TiO_2 induced by Oxygen and UV light. Reproduced with permission from Ref. 53. Copyright 2016, Royal Society of Chemistry.

An effective way to reduce the traps states in titanium dioxide is the use of substitutional dopants. The heterojunction of planar TiO_2 architecture was improved by Wojciechowski et. al. employing fullerene derivatives.[55] Alternatively, the PCE and hysteresis behaviour of mesoscopic structures were enhanced with the intercalation of n-dopants and surface treatments with alkaline salts based in lithium, attributing this improving to a better collection and carrier´s transport in iodide-based perovskite solar cells.[56,57] However, in a recent work it was demonstrate the capability of these alkaline-salts treatments reducing surface recombination at the ESL interface, providing evidences of a major impact in photovoltage than in the transport mechanisms in the case of bromide-derivatives.[58] This result will be further described in the following sections as a main part of the work developed during the course of this thesis.

Spiro-OMeTAD

The most widely used HSL in n-i-p mesoscopic architecture is the Spiro-OMeTAD. Its organic nature (Fig.1.22) have been catalogued as one of the main pathways of interfacial degradation of perovskite devices due to the fast oxidation processes under light and oxygen exposure.[59]

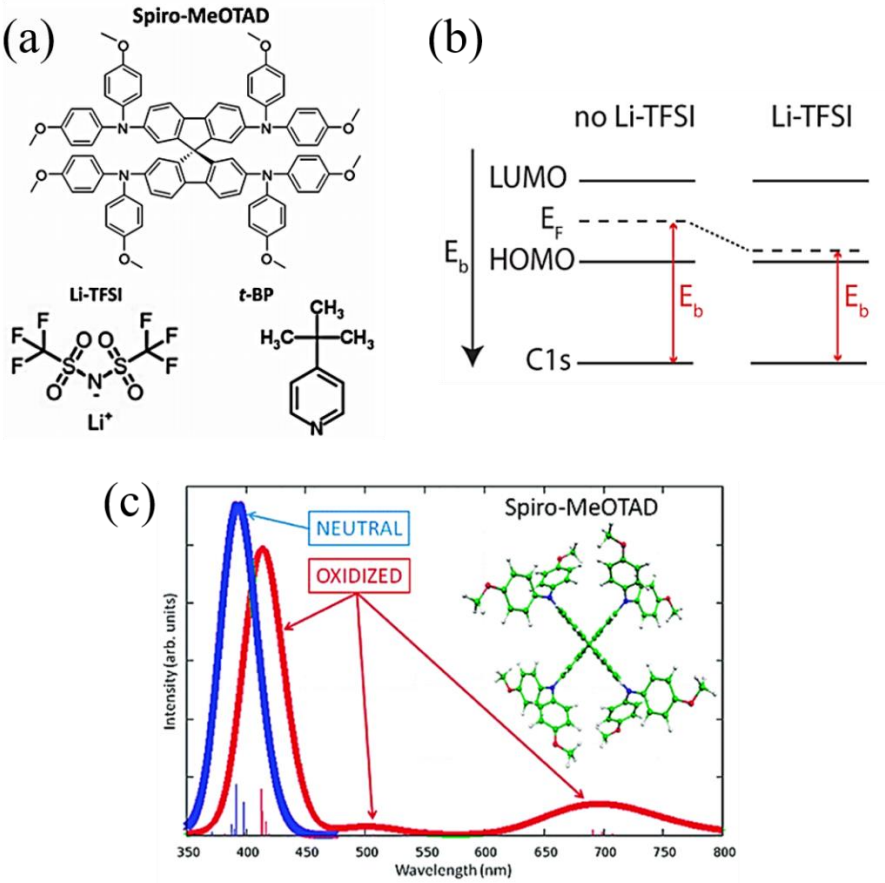

Figure 1.22. (a) Structure of Spiro-OMeTAD and the dopants terc-butylpyridine (tBP) and bis(trifluoromethane)sulfonimide lithium salt (Li-TFSI). Reproduced with permission of Ref.59. Copyright 2015, American Chemical Society. (b) Energy level of pristine Spiro-OMeTAD and doped with Li-TFSI. Reproduced with permission of Ref. 61. Copyright 2012, American Chemical Society. (c) Absorbance spectra for fresh Spiro-OMeTAD and after oxidation. Reproduced with permission of Ref.63. Copyright 2011, American Chemical Society.

In addition, the conductivity of this compound itself is relatively low and the p-doping becomes mandatory. This doping is usually performed with tert-butylpiridine (tBP) and the same alkaline salt, bis(trifluoromethane)sulfonimide lithium salt (Li-TFSI) used for the metal oxide.[60] These additives improve the conductivity considerably making Spiro-OMeTAD a better hole selective material.[61] However, the presence of lithium cation was demonstrated to accelerate the oxidation process as well as the degradation of iodide-based solar cells, attributing the photovoltage losses to the presence of this ion.[62,63,64] In the same way, this result came into a controversy situation due to the recent study in

bromide-based materials, suggesting different consequences in the performance of the PSCs depending on the halide compound employed.[58]

1.4.3. Space-charge accumulation zone at ESL/perovskite interface

As we mentioned in previous sections, hysteretic behaviour during electronic measurements is blocking the achievement of a real scalable and marketable perovskite solar cells. This response has been attributed to the drift of the ionic defects under the internal electric field, accumulating at the interfaces and provoking the degradation of the photovoltaic performance of the cell over the course of time.[65,66] An evidence of this feature can be described developing small perturbation techniques as impedance spectroscopy (IS) measures. The large low-frequency capacitive response usually observed under dark conditions, has been identified with ionic electrode polarization, similar to a Helmholtz double layer.[44] When a metal electrode is in contact with an electrolyte solution, the electrons remaining in the metal induce the formation of a layer of ions with opposite charge located at a *d* distance from the electrode surface, depending on their ionic radius. The negative charge of the electrons with the positive charge of the cations forms the *double electric layer*, which behaves as a capacitor due to the accumulated charge (Fig.1.23).

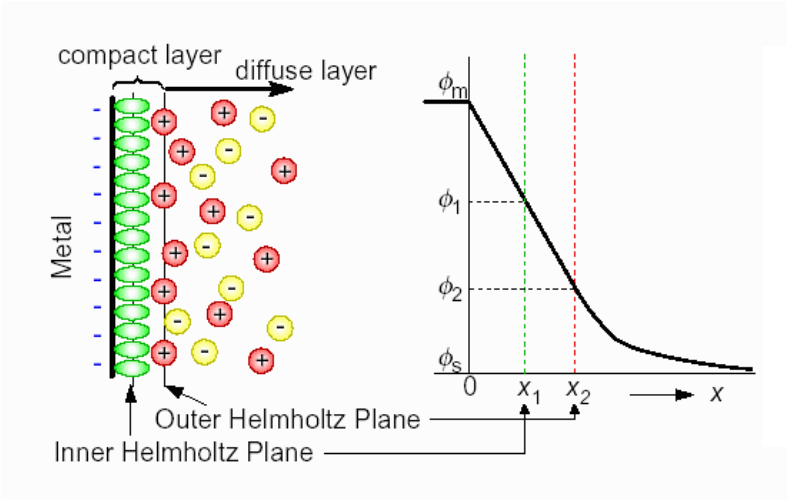

Figure 1.23. Helmholtz model for the electric double layer showing the outer and inner Helmholtz planes. The right side of the figures shows the linear drop in potential between the metal to the surface: φ_m, φ_s, respectively. Copyright https://web.nmsu.edu.

This capacitance is defined in terms of the dielectric constant of the material, ion our case, corresponding to the perovskite absorber:

$$C_H = \frac{\varepsilon\varepsilon_0}{l} \tag{22}$$

where ε is the dielectric constant of the perovskite, $\varepsilon_0$the permittivity of vacuum and l the distance between the plates of the capacitor.

However, it was also detected an increase in such low-frequency capacitance under illumination conditions (Fig.1.24a), approaching milliFarads, that cannot be explained just in terms of ionic charge accumulation at the interfaces.[43] Zarazua et.al investigated this phenomena in depth concluding that the giant capacitive response, proportionally

increased with light intensity observed in the low frequency region, should be a consequence of an electronic carriers accumulation at the metal oxide/perovskite interface, demonstrating at the same time, a direct dependence with the thickness of the absorber material (Fig.1.24b(i)). This capacitive response also involves a large photovoltage (Fig. 1.24b(ii)).[67]

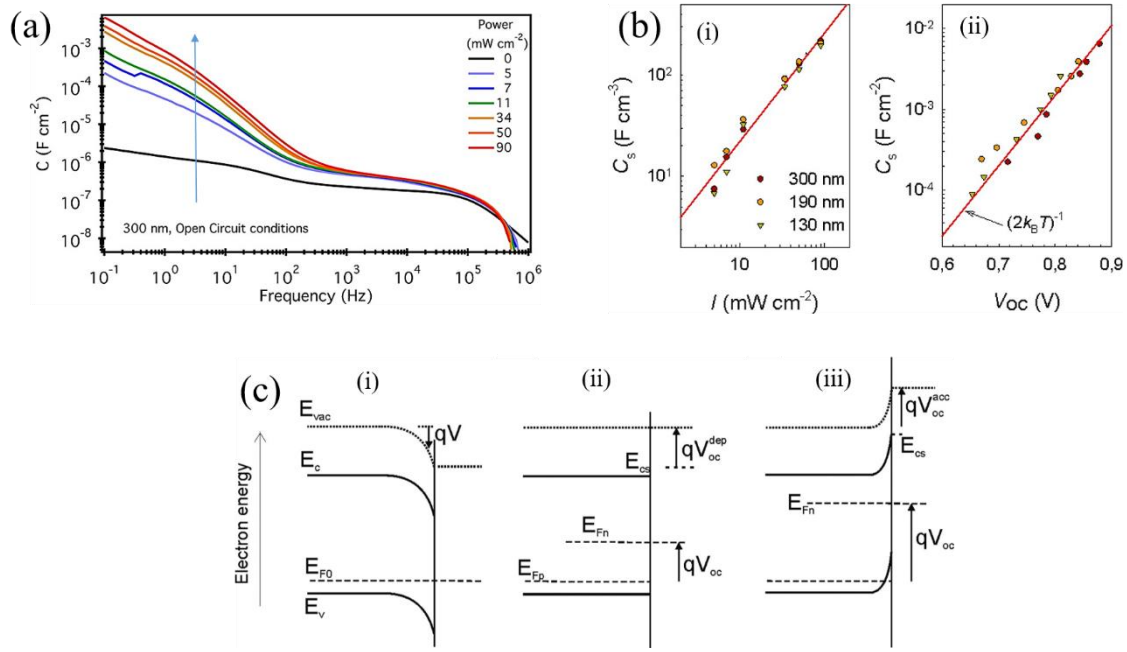

Figure 1.24. (a) Capacitance spectra of 300 nm thick perovskite measured in open-circuit conditions for different illumination intensities. (b) (i) Accumulation capacitance normalized to the absorber film thickness as a function of the light intensity showing a proportional dependence with the perovskite layer thickness and light intensity. (ii) Accumulation capacitance per unit surface as a function of the open-circuit voltage. Adapted with permission of Ref. 37, Copyright 2016, American Chemical Society.

They defined this accumulation capacitance as follows:

$$C_s = \frac{dQ}{dV} = \frac{q p_b^{1/2}}{\sqrt{2}} \left(\frac{\varepsilon_r \varepsilon_0}{k_B T}\right)^{1/2} e^{qV/2k_BT} \tag{23}$$

where Q is the charge per unit surface, q the electron charge and p_b the bulk carrier density corresponding to the p-type doping. The local separation of vacuum level from bulk value is given by qV, being V_{oc} the voltage at the contact.

The Debye length is given by $L_D^2 = \varepsilon_r \varepsilon_0 k_B T / q^2 p_b$ in terms of dielectric constant and vacuum permittivity.

When the n-i-p single heterojunction system is under dark in equilibrium at open-circuit conditions, there is a depletion layer at the ESL/perovskite interface (Fig.1.24c (i)).[68] The generation of minority carriers (electrons in the case of p-type perovskite material), provokes a flatband condition, removing the depletion region (Fig.1.24c (ii)). Under illumination at open-circuit conditions, the majority carriers (holes, in p-type) start to be collected at the accumulation zone, provoking a band bending as a consequence of

the increase of the minority carriers Fermi level, changing as well the total surface vacuum level and building up the photovoltage measured (Fig.1.24c (iii)). The photovoltage become defined as follows:

$$V_{oc} = V_{oc}^{dep} + V_{oc}^{acc} \quad (24)$$

where V_{oc}^{dep} is the voltage corresponding to the depletion layer and V_{oc}^{acc} represents the voltage of the accumulation zone. Consequently, if the accumulation zone increases, the photovoltage will also growth.

1.4.4. Surface recombination

As mentioned in section 1.4.1, the non-radiative recombination is the one limiting the maximum value achievable for open-circuit potential. The high improvement in the quality of the perovskite absorber materials has enhanced substantially the transport, leading also to a reduced bulk recombination. These achievements come to the fore the assumption that the interfacial dynamics constitute the main pathways for recombination mechanisms.

The recent PCE records of hybrid halide perovskite solar cells show density currents up to the theoretical limit, so the goal still the enhancement of the photovoltage reducing recombination. Impedance spectroscopy helps once more in the clarification of these mechanisms, being able to identify specific surface processes, directly related with phototovoltage losses. Zarazúa et.al investigated in depth the dependence of the resistive responses of perovskite devices as a function of the light intensity and voltage in two conditions: at short circuit (zero bias) and applying a voltage equal to the open-circuit potential ($V = V_{oc}$), for different illumination intensities.[69] These experiments concluded that resistive elements and accumulation capacitance perform in a proportional reverse way with irradiation intensity, suggesting the same origin for both processes. When plotting V_{oc} at each illumination, the values of geometrical capacitance C_g appears constant, while the surface capacitance C_s increase with higher illumination intensity. As detailed in previous section, this capacitive response is attributed to the light-induced accumulation zone of electronic holes in a p-type material (majority carriers). So, the proposed model relates C_s to the voltage derivative of the surface charge, p_s, stablishing a variation of C_s with the voltage thorugh the Eq.23.

In Fig.1.25, is summarized the surface recombination process and its dependence on the voltage. Here, part of the V_{oc} is built-up at the interface as a consequence of the formation of the hole accumulation zone V_{oc}^{acc}, being the rest of the photovoltage a correspondence to the suppression of the descendent band bending attained at very low light intensities.

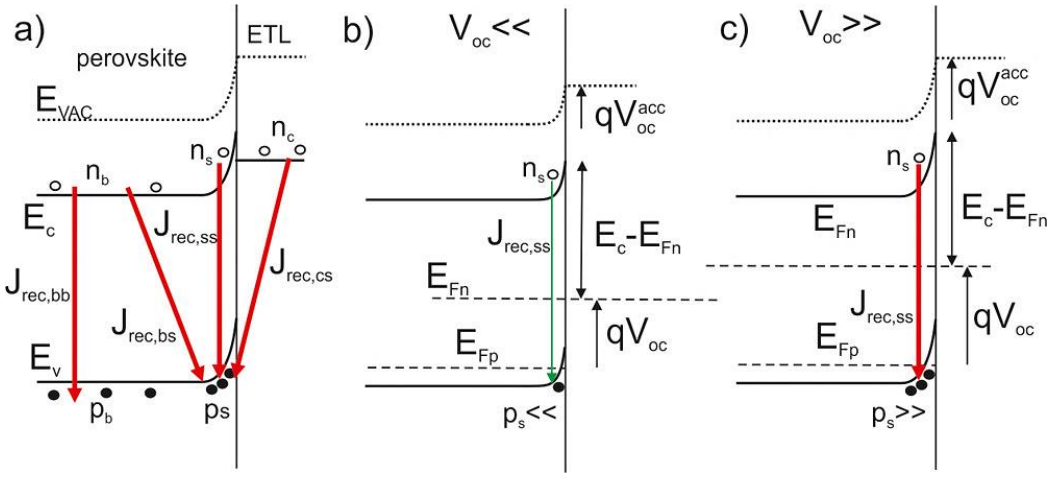

Figure 1.25. (a) Energy band diagram of the accumulation zone at the perovskite near the cathode contact (perovskite/electron transport layer) under open-circuit conditions. The schematic signals possible different electron–hole recombination routes. It is distinguished among purely bulk recombination flux $J_{rec,bb}$ (carriers located at the perovskite bulk), purely surface recombination $J_{rec,ss}$ (carriers located at the interfacial accumulation zone), mixed bulk-surface recombination $J_{rec,bs}$ (perovskite bulk electrons and interfacial holes), and mixed cathode-surface recombination $J_{rec,cs}$ (cathode material electrons and interfacial holes). Band diagram shows the formation on a majority carrier (hole) accumulation zone near the cathode contact under open-circuit conditions. In (b), the accumulation zone produces a slight upward band bending for $p_s \ll$ (slight illumination intensity producing reduced V_{oc}). In (c), larger band bending for $p_s \gg$ (high illumination intensity with $V_{oc} \gg$). Reproduced with permission of Ref.69. Copyright 2016, American Chemical Society.

Therefore, part of the open-circuit potential is built up at the interface as a consequence of the formation of a hole accumulation zone V_{oc}^{acc}.

1.5. Stability Issues in PSCs

The factors responsible for the stability issues of perovskite solar cells can be classified into two categories:

- Intrinsic: related to the bulk perovskite material and its interfacial interactions with the external selective layers, like thermal instability and ion migration.
- Extrinsic: related to environmental conditions such as light, oxygen and moisture.

1.5.1. Intrinsic factors

Regarding the intrinsic factors, the thermal instability and ion migration result in major consequences in the solar cell performance. The thermal instability is related, as previously explained, with the hydrogen interactions between the organic cation and the halides surrounding the divalent metal. Modifying the nature of the A-site cation in terms of steric size, introducing larger organic molecules as formamidinium halides shows great benefits.[70,71] However, organic hole selective contacts commonly used (e.g, Spiro-OMeTAD or PTAA) have been also demonstrated to have an important effect on this type stability. In addition, the replacement of organic HSL by complete inorganic ones, was also proved to be efficient enhancing stability, as reported by Arora et.al.[72]

1.5.1.1.Thermal instability

In addition to the great differences between $MAPbI_3$ and $MAPbBr_3$ presented in section 1.2.3.1, regarding their optical properties, the interchange of the halide atom allows also to quite interesting stability variations. Recently, Yabing Qi and co-workers reported and exhaustive photo- and thermal- degradation study comparing both structures.[73] In first place, they proposed three possible degradation pathways for the general MAPI structure:

(1) $MAPbI_3 = CH_3NH_2 + HI$ (reversible)
(2) $MAPbI_3 = NH_3 + CH_3I$ (irreversible)
(3) $MAPbI_3 = Pb^0 + I_2(g)$ (reversible)

Then, under illumination or dark conditions, the photo- and thermal-decomposition reaction proposed is:

$$MAPbI_3\,(s) \rightleftharpoons PbI_2(s) + Pb^0\,(s) + I_2(g) + CH_3NH_2(g) + CH_3I(g) + HI(g) + NH_3(g)$$

Contrary, for bromide material, the proposed chemical process is different:

$$MAPbBr_3\,(s) \rightleftharpoons PbBr_2(s) + CH_3NH_2(g) + HBr(g)$$

CH_3X and NH_3 are the thermodynamically driven products of the degradation of methylammonium cations, being irreversible to reform MA^+. Contrary, the release of $CH_3NH_2 + HX$ is considered to be reversible due to its high reactivity in neutralizing back to MA^+ and X^-as reported by Latini and coworkers (Fig1.26).[74] This could be the reason why the higher stability under operation conditions of bromide cells versus iodide-base materials.

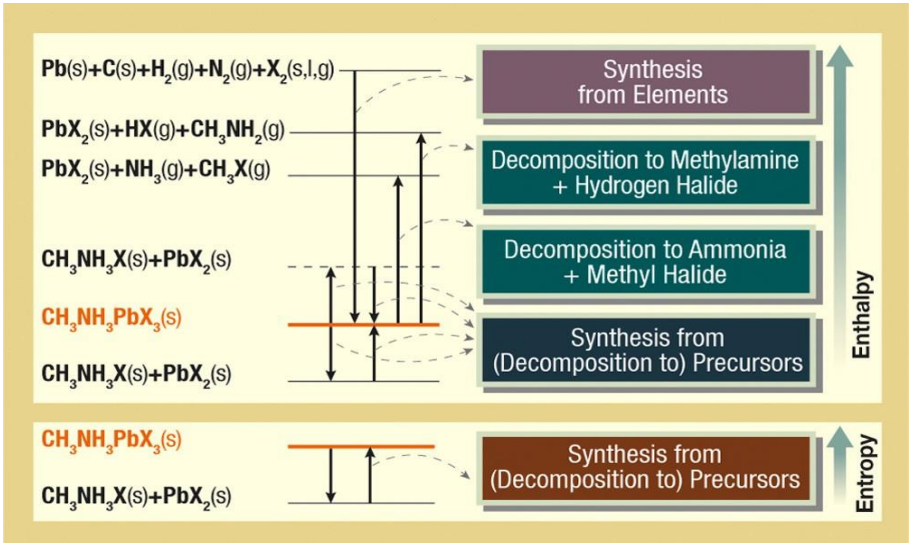

Figure 1.26. Enthalpy and entropy level scheme for possible formation/decomposition processes of $CH_3NH_3PbX_3$ perovskites. Decomposition to precursors can be both endothermic and exothermic. Enthalpy levels are not to scale. Reproduced with permission of Ref.74. Copyright 2018, American Chemical Society.

1.5.1.2.Ion migration

The consequences of ionic migration represent the major bottleneck in the achievement of real large-scale commercial PSCs, being almost inevitable in all halide perovskites configurations. In this type of devices many slow features appears during the typical physical measures as slow photoinduced response, hysteretic behaviour during JV curves and switchable photovoltaic effect.[43,75,76] This is in marked contrast to other PV technologies like silicon solar cells, where the carrier transport is as fast as no influence the transient measures. In PSCs the interactions of migrating ions with different interlayers characteristic in the general PSC configuration (fluorine-doped tin oxide (FTO)/electron selective layer (ESL)/perovskite/hole selective layer (HSL)/gold), are responsible for the slow kinetics observed, being also connected with chemical reactivity, defects sites and grain boundaries, which greatly affects the solar cell performance.[77,78]. These slow phenomena makes mandatory the establishment of a deterministic connection between the ion dynamic and the kinetic variation of the photovoltaic response. For this purpose, the quantification of the different ionic diffusion rates become mandatory in first place. Ionic diffusion rate is defined through the activation energy (E_A) (Eq.25):

$$D_m = D_0 \exp(-E_A/k_B T) \quad (25)$$

Where D_0 represent a temperature independent factor that depends on lattice vibrations and jump distance, k_B represents the Boltzmann constant and T temperature. The E_A directly depends on the structure of the crystal and the charge and radius of ions. A wide number of methods have been developed to detect and quantify the ionic diffusion rates. Photothermal induced resonance (PTIR), kelvin probe force microscopy (KPFM), ^{207}Pb NMR, ^{127}I NMR/NQR, tracer diffusion, reaction cell, doping experiments, galvanostatic measurement, impedance spectroscopy (IS) or suppression of luminescence in laterally contacted electrodes, are some of the main responsible techniques which provides evidences of ionic migration and specific values of their diffusion coefficients (Table 1). [79,80,81] A recent review published by Wang et.al. summarizes the main impacts of ion migration on the kinetics regarding working conditions in PSCs. They highlight the importance of determine which species dictate the carrier redistribution in application to external perturbation and the conductivity of those carriers, directly affected by transport resistance.[82]

Table 1. Kinetics coefficients in PSCs based in $MAPbI_3$ and $MAPbBr_3$ at room temperature and considering a crossing thickness of 100 nm. Ref. 82

Types of defects	**E_A (eV) $MAPbI_3$**	**E_A (eV) $MAPbBr_3$**	**Diffusion coefficient D ($cm^2\ s^{-1}$)**	**Transit time τ (s)**
Electron transport	-	-	0.3	10^{-9}
Extrinsic Li^+	-	-	1 x 10-7	
Organic Cation vacancy (V_{MA+})	0.46	0.56	-	10^3
Metal cation vacancy (Pb^{2+})	0.80	-	-	-
Halide interstitial (I_i)	0.08		-	-
Halide vacancy ($V_{I/Br}$)	0.08	0.09	1 x 10-8	10^{-2}

Ions accumulated at the interface	-	-	-	10^0-10^2

The quotient of conductivities is defined as follows (Eq.26):

$$\sigma_e/\sigma_i = n\mu_e/c\mu_i = 10^7\, n/c \quad (26)$$

where σ_e and σ_i corresponds to the electronic and ionic conductivities respectively, n and c are the electronic and ionic densities respectively and μ_e and μ_i the carriers mobility ($cm^2\ V^{-1}\ s^{-1}$). Through this relation, it can be consider that the current is mostly driven by the electronic current, except if the density of ions increase orders of magnitude to respect the electronic density. Focusing on ionic transport, it should be established a definite region through which the carriers diffuse, obtaining a final transit time (τ) for each type of defect or carrier. This magnitude is defined in Eq.27:

$$\tau_{diff} = d^2/D \quad (27)$$

where d^2 is the distance/ thickness to diffuse and D the diffusion coefficient. The transit time for a distance of 100 nm is detailed in Table 1.[83]

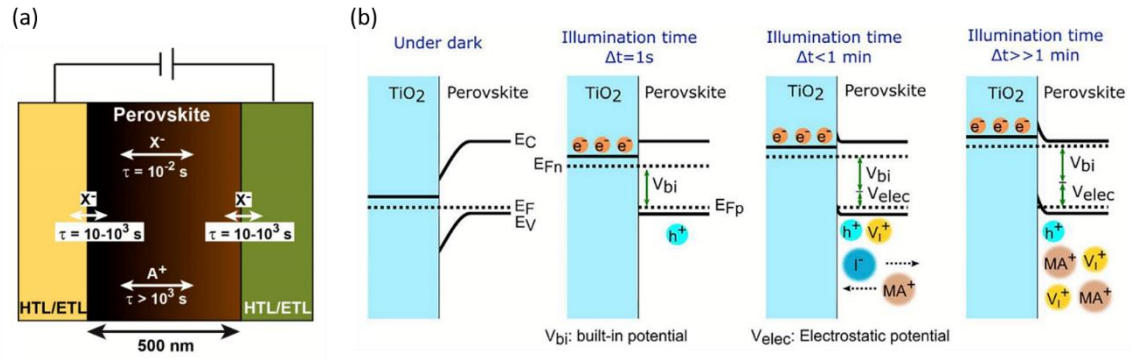

Figure 1.27. (a) Characteristic times for ionic kinetics in a general perovskite solar cell. Adapted with permission of Ref.82. Copyright 2019, Royal Society of Chemistry. (b) The energy diagram at the TiO_2/perovskite interface at four different stages: from left to right side: in the dark, at a very short illumination time of $\Delta t = 1$ s; at an illumination time close to 1 min and after a substantial illumination time of $\Delta t > 1$ min. Reproduced with permission of Ref.83. Copyright 2016, Royal Society of Chemistry.

The general conclusion strongly accepted for all the perovskite community, is that I^- anions are more likely to migrate than MA^+ and Pb^{2+} cations, as referred by the transit times of each other, directly related with the activation energy of them (Fig.1.27).[65]

In the specific case of interfacial regions between perovskite and selective contacts, the effects of the ion migration have a direct consequence in terms of photovoltage. At the ESL/perovskite interface, it was demonstrated, through specific simulations by López-Varo *et. al*, that positive carriers, e.g, holes, cation vacancies or cations itself, are accumulated at the interface under light illumination conditions, provoking a band bending which forms an electrostatic potential as a result of the electric field across the interface (Fig 1.25b).[83] The sum of this electrostatic potential to the built-in potential,

leads to an increase of the photovoltage, directly related with the light-induced accumulation capacitance already reported by Zarazua *et. al.*[67] This feature is directly related with the second main research carried out during the course of this thesis and will be further discussed in the following sections.

The harmful effects of ion migration can be significantly reduced by passivating the grain boundary, enhancing crystallinity and increasing the ion migration barrier by engineering the packing density of the crystal lattice via ion substitution.[84,85]

1.5.2. Extrinsic factors

Despite water exposure consequences, oxygen and light represents two additional degradations factors that have been widely investigated. The commercialization horizon of this technology implies the use of large areas of exposure under real operation conditions that are susceptible to be degraded. In the following section, the main effects and mechanisms reported in literature at this respect are briefly summarized.

1.5.2.1.Oxygen and light

From an operational point of view, Snaith and co-workers revealed that a reduction in solar cell efficiency was dominated by a loss in photocurrent upon oxygen exposure. They reported a process occurring through two different phases: an initial semi-reversible screening of the built-in field of the solar cell resulting as a consequence of an increased defect density and breaking down to the light-harvesting perovskite material itself with prolonged oxygen exposure. The main mechanism confirmed and accepted by the perovskite community lies in a photochemical reaction through the photogenerated electrons in the perovskite absorber. These photogenerated electrons allow a reaction between the methylammonium cation and a superoxide molecule (O_2^-), which primarily induces a fast degradation with CH_3NH_3, PbI_2, I_2 and H_2O as byproducts.[86] Aristidou *et. al* proposed the sequential mechanisms highlighting the formation of different defects consequently. In this mechanism, O_2 acts as an electron scavenger generated by light or by an external electrical bias. In addition, vacancy defects may act as molecular or charge traps, which in turn could mediate the electron-transfer reaction with oxygen. [87,88]

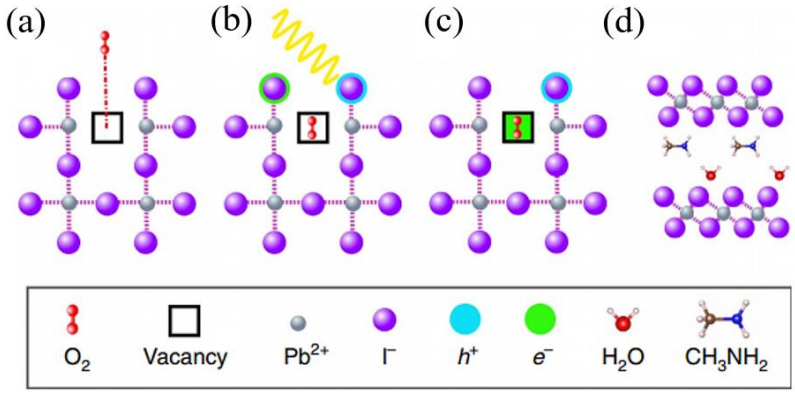

$$4CH_3NH_3PbI_3^* + O_2^- \longrightarrow 4PbI_2 + 2I_2 + 2H_2O + 4CH_3NH_2$$

Figure 1.28. **Oxygen-induced photo-degradation**. Schematic representation of the reaction steps of O_2 with $CH_3NH_3PbI_3$. (a) Oxygen diffusion and incorporation into the lattice, (b) photoexcitation of $CH_3NH_3PbI_3$ to create electrons and holes (c) superoxide

formation from O_2, and (d) reaction and degradation to layered PbI_2, H_2O, I_2 and CH_3NH_2. Reproduced with permission of Ref.87. Copyright 2017, Springer Nature Publishing AG.

However, the harmful effects related to oxygen and light not only affects at the perovskite material itself. The consequences upon the external selective layers become major in the case of organic materials as Spiro-OMeTAD, widely used as hole-selective layer. To this respect, Sánchez *et. al* reported an extensively work detailing the photoinduced degradation of Spiro-OMeTAD through absorbance spectroscopy (Fig 1.27a), demonstrating major implication during the photovoltaic performance of the cells, focusing in the increased hysteretic behaviour.[89]

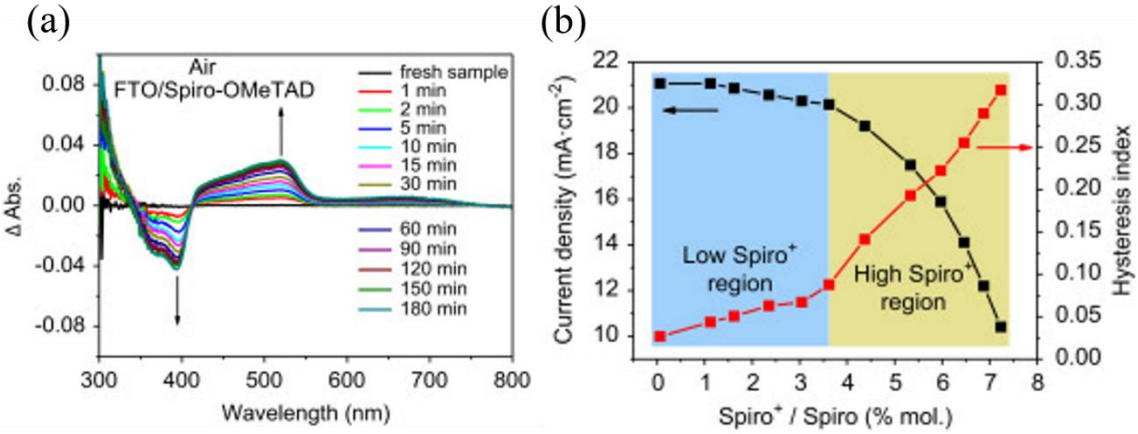

Figure 1.29. (a) Evolution of the UV–vis absorption signals of a Spiro film deposited by spin-coating on a FTO substrate at different illumination times under 1 sun. (b) Evolution of the J_{sc} (black squares) and the HI (red squares) versus the molar ratio of the $Spiro^+$. The blue and beige areas delimit the low and high Spiro doping regions. Reproduced with permission of Ref.89. Copyright 2016, Elsevier B.V.

1.5.2.2.Moisture

This section includes information of an accepted review entitled "Crystalline Clear or not: Beneficial and Harmful Effects of Water in Perovskite Solar Cells" DOI: 10.1002/cphc.201900393R1 where the PhD candidate Clara Aranda Alonso is the first author and corresponding author.

Water represents the main external factor to control during fabrication of PSCs due to the high coordination capability towards perovskite compounds. Perovskite material reacts easily with water molecules generating hydrate phases, which lead to the following chemical equilibrium (Eq.1):

$$4(CH_3NH_3)PbI_3 + 4H_2O \rightleftharpoons 4[CH_3NH_3PbI_3 \cdot H_2O] \rightleftharpoons (CH_3NH_3)4PbI_6 \cdot 2H_2O + 3PbI_2 + 2H_2O$$

(Eq. 1)

The left part of the equilibriums (black) is favoured at moderate humidity < 50%, the monohydrate phase is predominant and could be reversed by dry treatment.[90] At this stage, the presence of water can be catalogued as a beneficial factor, helping in the crystallization process of perovskite material and performing increased grain size.[91] A high crystalline

lattice perovskite material induces as well an improvement in photocurrent, photoluminescence, photovoltage and even in the stability of the perovskite devices, avoiding the inclusion of more water molecules into the structure.[92,93] However, if the equilibrium is displaced to the right (red) due to an increased concentration of water, the di-hydrated phase governs the situation. From a morphological point of view, water begins to collapse the grain boundaries of perovskite film, break their interconnectivity and generate isolating trails that increase the recombination pathways.[90] The chemical effects translate into a weaker hydrogen bond between lead halide and the organic cation (e.g, MA^+), due to the hydration. MA^+ can rapidly diffuse and separate from the PbI_6 octahedral, leading to a non-photoactive phase with a yellow-white colour, degrading completely the material by turning it back to PbI_2 and MA^+ compounds irreversibly (Fig. 1.30).[94] The consequences are optical absorption losses and major recombination processes that leads to a detriment of the photovoltaic performance of the cell.[95,90,96,97,92] In fact, a negative effect of water is also notice in other type of devices such as light-emitting diodes (LEDs). The reason behind is that water can introduce non-radiative recombination centres. As water modifies the crystalline structure of the perovskite it is expected that photoluminescence and electroluminescence properties will also be strongly affected by the inclusion of water.

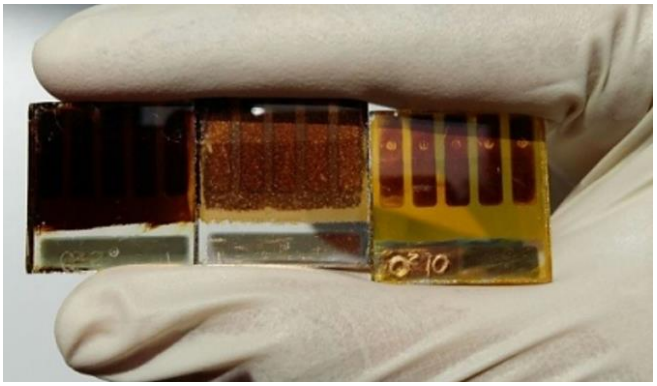

Figure 1.30. Degradation sequence of PSC. Fresh dark brown $MAPbI_3$ cell on the left and after (yellow on the right) long-term degradation by atmospheric conditions exposure with a relative humidity between 25-40 %. The cell in the middle shows an intermediate degree of degradation with yellow dots corresponding to PbI_2 compound. Reproduced with permission of Ref.94. Copyright 2017, Revista Cubana de Física.

The equilibrium displacement from one side to another represents an extremely difficult feature to control, even with the most sophisticated setups that in fact are not feasible to adopt in large-scale fabrication process. In fact, vacuum deposition process might seem like the perfect alternative to solution deposition methods to prevent water ingress during large-scale manufacturing, providing as well an extensive spectrum of possible materials to deposit within additional stability properties.[98] However, the high complexity associated with the vacuum deposition from multiple thermal sources to compete in PCE, still need to be improve and certainly increases the production costs as compared with solution process methods.[99]

Contrary, the highest PCE cells are stabilized using a mixed cations formulation in solution processes. Formamidinium iodide is included as part of the organic component of the perovskite structure due to the smaller band gap and greater spectral absorption.

However, the resultant perovskite based in FA^+ compounds, show higher instability under moisture due to the strong tendency of this cation to dissociate into ammonia and sym-triazine.[100,101] In addition, the $FAPbI_3$ materials can crystallize into two phases. The α-$FAPbI_3$ is the metastable phase at temperatures below 160 °C, converting easily to a non-perovskite δ-phase, thermodynamically more stable. This process is accelerated at high humidity and great efforts have been done to stabilize the α-$FAPbI_3$ phase, included as well in addition with MAI, which leads to an easier and adequate crystallization.[102] On the other hand, to further decrease the effects of the instability provided by the organic cations, inorganic counterparts have been added in the high efficient perovskite formulation. As Saliba and coworkers reported, the triple cation perovskite materials, including Cs^+ are thermally more stable and less affected by environmental parameters such as solvent vapours, temperature, or general working conditions. The suppression of yellow FA phase impurities and the performing of uniform perovskite grains, reduce considerably the vulnerable character of common perovskite materials based in complete organic A-site cations.[103]

Leaving a part the enormous variety of formulations that can increase the performance to high PCE solar cells, clarify the effects of water aiming in the most widely studied composition based in methylammonium iodide becomes mandatory. Shed light on the mechanisms by which these effects occurs and how to play with them to avoid any problem in the commercialization of this promising photovoltaic technology is also a main purpose. To facilitate the elucidation of a global conclusion, this review is focused in the perovskite material, differentiating between the effects of water inside the precursor formulation as an additive and as a moisture during devices fabrication and the electronic effects in the complete solar cell. As a final contribution, we remark the latest approaches reported in order to confer hydrophobic character to these solar devices.

In Fig.1.31 the main effects, mechanisms and techniques are summarized to guide the review this topic.

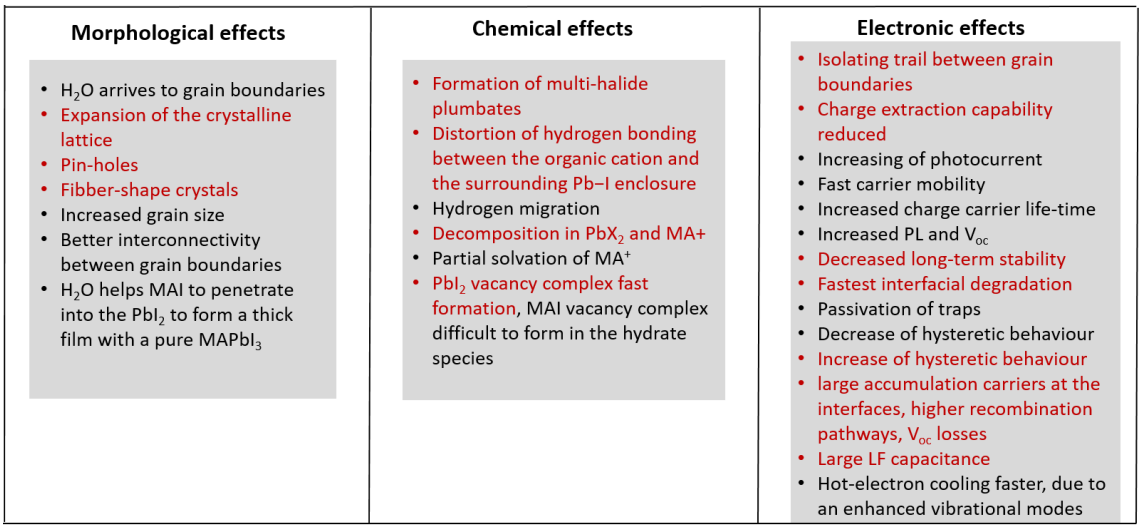

Figure 1.31. Summary of the beneficial (black) and harmful (red) effects of water in PSCs depending on the equilibrium displacement to the left (monohydrated phase) and right (di-hydrated phase).

1.5.2.3.Effect of water into the perovskite precursor solution

As mentioned earlier, water is normally regarded as a negative factor in long-term stability and lifetime of perovskite solar cells, however, it is not completely clear if it is undesirable in all the cases, or if may be even beneficial in adjusted proportions.[91,104,105,106] Yang Yang and coworkers proposed in 2014 a moisture assisted grain growth of solution process perovskite materials, obtaining high crystallinity with increased grain size, carrier mobility and charge carrier lifetime, using inverted configuration devices (p-i-n) glass/ITO/PEDOT:PSS/$CH_3NH_3PbI_{3-x}Cl_x$/PCBM/PFN/Al.[107] They also reported an improved steady-state photoluminescence (PL) and larger time resolved photoluminescence results (TRPL) for devices exposure to controlled moisture, attributing this feature to a reduction in the recombination pathways, enhancing the photovoltage and fill factor as well. Similarly, Snaith and coworkers proposed in 2015 a significantly enhanced PL and photovoltage, but this time in a regular configuration (n-i-p) PSCs glass/FTO/TiO_2/Al_2O_3/$CH_3NH_3PbI_{3-x}Cl_x$/SWCNTs/PMMA/Ag exposed to water, both in the precursor solution and in ambient atmosphere during the fabrication.[108] They concluded that the improvement of the photovoltaic performance was due to the passivation of traps after partial solvation of methylammonium precursor. Kelly and coworkers reported in 2016 parallel results developing perovskite films through a sequential deposition technique.[96] Their work highlighted the beneficial effect of a certain relative humidity amount during perovskite fabrication, investigating a final regular configuration composed by glass/ITO/ZnO_{NPs}/$CH_3NH_3PbI_3$/P3HT/Ag. They found an enhancement of perovskite device performance with higher %RH fabrication atmosphere. The larger crystal size with better inter-particle connectivity was also correlated with a reduction in the hysteretic behaviour.

From this perspective, it seems that the effect of water on the photovoltaic behaviour of PSCs is just an issue of quantity, which cannot be categorically qualified as either a beneficial or a harmful factor. However, it should be remarked that the highest PCEs are always obtained under completely dry environmental conditions, needing encapsulation techniques as an ally factor to enhance the long-term stability under real operation conditions.[109,110,111,112]

A wide wealth of literature has been reported relating different methods through which to include water directly during the perovskite crystallization.[113] In 2015, Conings *et. al* demonstrated that the addition of water into the solvent precursors up to 10% vol. slightly modified the morphology of the perovskite films, not affecting the final photovoltaic performance and relaxing as well the conditions to scale-up the fabrication technique.[114] Grätzel and coworkers proposed also the incorporation of water additives into the N,N-dimethylformamide (DMF) solvent, leading to a controllable growth of greater grain-size and highly covered perovskite absorber, attributed to the lower boiling point and the higher vapour pressure of water compared with DMF. In addition, they show an improvement in the stability cells when water was incorporated in a certain amount. They also proposed that $CH_3NH_3PbI_{3-x}Cl_x \cdot nH_2O$ hydrates generated during the annealing process could be against the corrosion of water molecules in some extent, due to the stable hydrated system.[115] Similarly, Nelson and coworkers studied in 2015 the effect of moisture in pre-formed $MAPbI_3$ films by extensive XRD and optical measurements. With the structural information they proposed the reversible hydration of perovskite single crystals and thin films showing that the monohydrate phase ($CH_3NH_3PbI_3 \cdot H_2O$) forms initially and the di-hydrate $(CH_3NH_3)_4PbI_6 \cdot 2H_2O$ phase follows upon long exposure times

to water vapour at room temperature.[90] In contrast, the presence of liquid water results in an irreversible decomposition of $MAPbI_3$ into PbI_2 (Eq.1).[116]

Monohydrate plays here as an intermediate product converting back easily to $MAPbI_3$.[117] The prolonged exposure to water vapour causes the displacement of the equilibrium to the right, becoming to appear the di-hydrate phase accompanied by the formation of lead iodide (PbI_2) and the release of two water molecules. In this study it was shown that the formation of the monohydrate followed by the di-hydrate, provokes the expansion of the crystalline lattice since the water molecules arrive to the grain boundaries. This phenomenon leads to an isolating trail between grain boundaries, reducing the charge extraction capability between them, enhancing as well the recombination pathways. In addition, the reversible process occurring during the intermediate step and after drying the film, leads to a major photovoltaic consequence: the hysteretic behaviour increases dramatically due to the augmented amount of structural defects after re-hydration (Fig.1.32a).

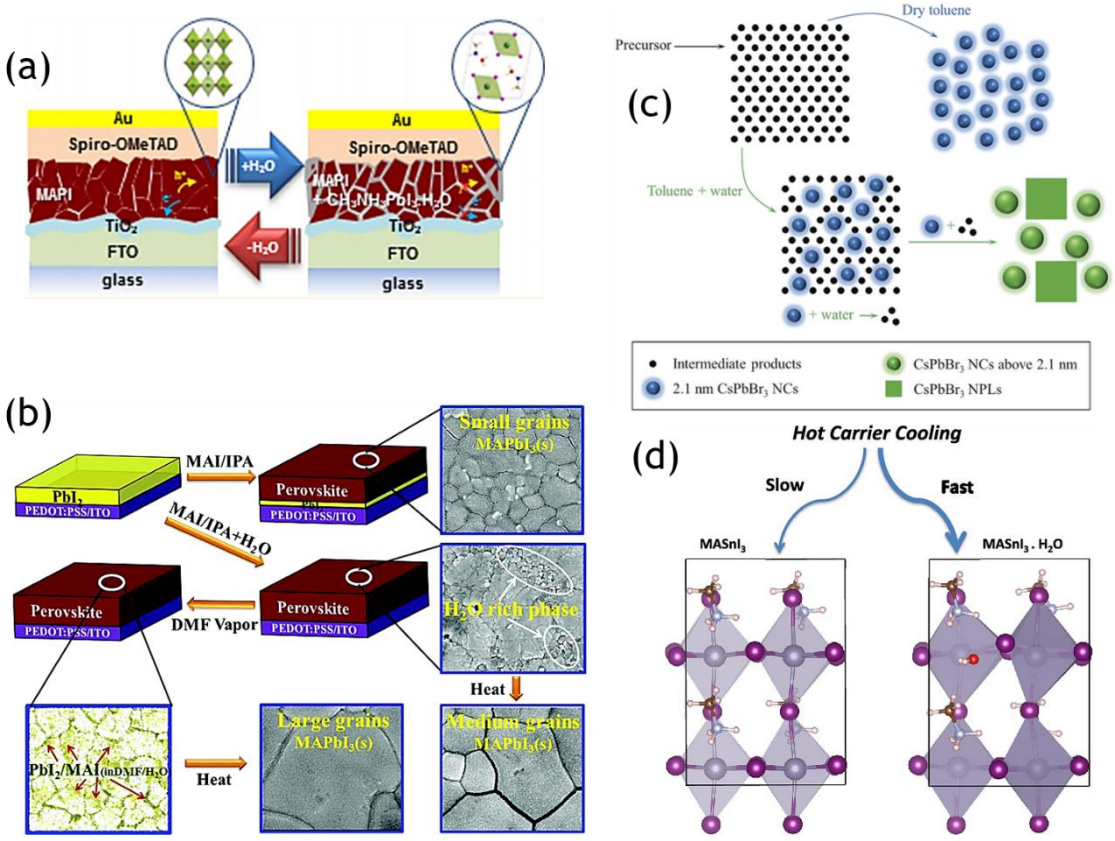

Figure 1.32. (a) Reversible hydration of perovskite material process proposed by Nelson and coworkers. Reproduced with permission of Ref.90. Copyright 2015, American Chemical Society. (b) Schematic two-step spin-coating method with water and DMF treatment proposed by Graetzel and coworkers. Reproduced with permission of Ref.115. Copyright 2017, The Royal Society of Chemistry. (c) Ligand-assisted re-precipitation method (LARP) assisted by water to grow NCs with high PLQY, proposed by Rogach and coworkers. Reproduced with permission of Ref.120. Copyright 2018, Wiley-VCH Verlag GmbH & C (d) Effect of water on the Hot–carrier cooling properties of $MASnI_3$ reported by Kachmar *et.al.* Reproduced with permission of Ref.121. Copyright 2019, American Chemical Society.

In 2017, Graetzel and coworkers reported a two-step spin coating method to grow a thick perovskite layer absorber by a synergistic effect of water as additive and DMF vapour treatment (Fig.1.32b).[115] The mechanism proposed to obtain high efficiency and stable cells under dry or environmental conditions after encapsulation, was that H_2O helps MAI to penetrate into the PbI_2 to form a thick film with a pure $MAPbI_3$ phase, producing big grains by slowing down the perovskite crystallization rate. The cooperation of water with DMF, controlling the dissolution of perovskite grains during DMF vapour post treatment, also leads to a high quality perovskite film with PCE approaching 20% in inverted configuration. However, they also noticed that when the humidity of the environment and/or in the reagents are not well controlled, the two-step method is not reproducible and a considerable amount of PbI_2 appears, extracting MAI from $MAPbI_3$.[116] In 2018 Walsh and coworkers published a complete study about the defect process in the water-intercalated iodide perovskite ($MAPbI_3$-H_2O) and monohydrated phase ($MAPbI_3 \cdot H_2O$) within a first-principles thermodynamic framework.[118] They demonstrated a PbI_2 vacancy complex fast formation, while the MAI vacancy complex is difficult to form in the hydrate species. These vacancies lead to deep charge transition levels, indicating the degradation of the perovskite material when exposed to moisture.

It seems clear that the effect of water is similar in all the cases either changing the composition of the perovskite or cell design. Recently, Rogach and coworkers proposed a water assisted method to grow size and shape controlled nanocrystals of $CsPbBr_3$.[119] Suitable amounts of water change the crystallization environment, inducing the formation of differently shaped perovskites, namely spherical colloidal nanocrystals (NCs), rectangular nano-platelets, or nanowires (Fig.1.32c). Known to be beneficial the use of a controlled amount of water during perovskite crystallization process, they proposed a modified ligand-assisted re-precipitation (LARP), widely used in the synthesis of NCs, adding a polar solvent as water to provoke a solubility equilibrium between the dissolution and crystallization of perovskite NCs.[120] The control of their growth conditions leads to form different NCs sizes and shapes with an enhanced photoluminescence quantum yield (PLQY). Kachmar *et.al* have already published the effect of water molecules onto the tin-based perovskite material ($MASnI_3$) carried out non-adiabatic molecular dynamics (NAMD) simulations.[121] They demonstrate how it affects the transport properties of the monohydrated component $MASnI_3 \cdot H_2O$ and drives hot-electron cooling faster than the pristine phase, due to an enhanced vibrational modes. It was also found an increase of the polarization and a decrease of the optical spectrum of the system, principally in the visible range (Fig.1.32d).

1.5.2.4.Effects of water exposure to films/devices

Regarding the stability issues of PSCs under real working conditions, that is, under room atmosphere and light, an intensive work had been carried out to find a useful, low cost and efficient method to obtain high PCE perovskite solar devices exposed to moisture during fabrication processes.[122,123] The large-scale horizon makes mandatory to acquire deep insight and knowledge about the ambient moisture effects on the photovoltaic performance and effective methods of fabrication under room conditions.

Lovrincic and coworkers reported in 2015 a work focused on the chemical interaction between water and the organic cation of the perovskite formulation, based in previous micro-Raman analysis.[95,124] They used infrared (IR) spectroscopy to demonstrate the fast (seconds) and reversible absorption of water into $MAPbI_3$ even with a very low %RH

(10%), prepared by co-evaporation of $PbCl_2$ and CH_3NH_3I in vacuum.[125] They proposed a model in which water has a strong influence on the hydrogen bonding between the organic cation and the surrounding Pb−I enclosure, without changes in optical absorbance (unlike the formation of the known hydrates) but with an increase in the photocurrent due to hydrogen migration. Their work highlight the strong effect of water molecules on the perovskite performance even with a very low moisture exposure. However, the most commonly used method to deposit perovskite thin films is the antisolvent method, due to its easy performance and high PCE results.[109] Thus, seems reasonable to focus on the water effect related with this deposition method perform.

A method in which the relative humidity was carefully controlled during perovskite fabrication by antisolvent method, was proposed by Kelly and coworkers.[96] Their sophisticated setup consisted in an atmospheric box of controllable RH, where dry N_2 was used as the carrier gas, flowing through a set of water bubblers into the atmospheric bag (Fig.1.33a). Through this method, they similarly observed as previously, larger perovskite crystallites at higher %RH with reduced grain boundaries and hysteretic behaviour that they attributed to a decrease in traps states.[126]

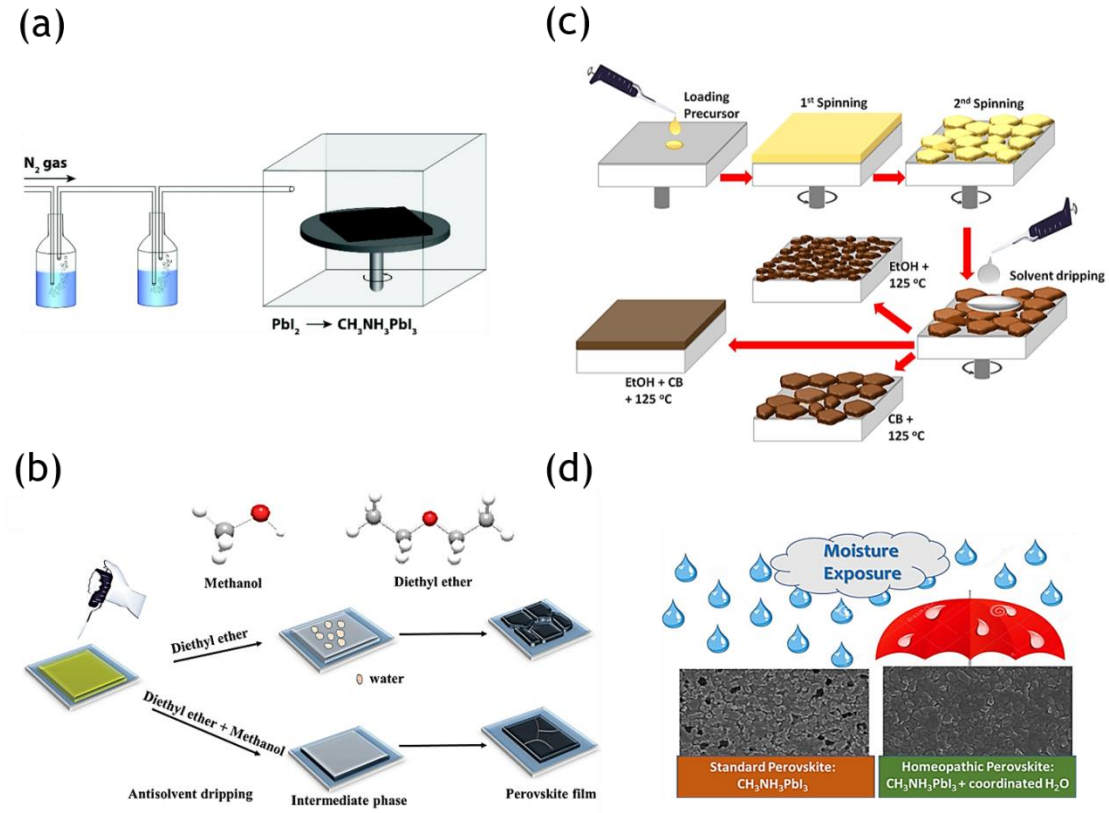

Figure 1.33. (a) Scheme of the controlled-atmosphere setup propose by Kelly and coworkers to fabricate PSCs with certain %RH. Reproduced with permission of Ref.96. Copyright 2016, The Royal Society of Chemistry. (b) Additive-antisolvent method proposed by Yang *et.al* Reproduced with permission of Ref.127. Copyright 2018, Wiley-VCH Verlag GmbH & C. (c) Solvent-antisolvent method proposed by Gedamu *et.al* using a combination of ethanol (EtOH) and chlorobenzene (CB) in various volumetric proportions. Reproduced with permission of Ref.129. Copyright 2018, Springer Nature. (d) SEM images of morphological defects appeared as a consequence of water effect,

reported by Contreras *et.al*. Reproduced with permission of Ref.93. Copyright 2018, American Chemical Society.

More recently, an additive-antisolvent method under room conditions has been proposed by Yang *et.al*., following the previous work, including large area, reported by Troughton *et. al.* [127,128] In their work, methanol is used as an additive onto the diethylether antisolvent to remove the residual water occluded in the perovskite material during first steps of crystallization (Fig.1.33b). They proposed an enhanced crystallinity lacking of pinholes and reduced hysteretic behaviour in devices prepared with their method, attributing this effect to a fast extraction of water molecules during the annealing step, as methanol has high water solubility. Once again, it is demonstrated the role of solvent additives playing a fundamental role modifying the crystallization process of perovskite material. Similarly, Gedamu *et.al* have reported also a solvent-antisolvent method to fabricate planar PSCs with good efficiency under moisture exposure.[129] In their case, (Fig.1.33c) a combination of ethanol (EtOH) and chlorobenzene (CB) in various volumetric proportions is revealed as the crucial protagonist avoiding pin-holes and obtaining controllable size of perovskite grains, improving as well the photovoltaic parameters to achieve PCE up to 14% in a planar configuration. At a similar conclusions arrived Contreras *et.al* analysing recently the effects of moisture during $MAPbI_3$ preparation.[93,130] They found that perovskite prepared under higher %RH presents more robust resistance to degradation, attributing this robustness to the retained water molecules into the perovskite structure, which avoid further invasion of moisture (Fig.1.33d).

1.5.2.5.Effects of water on photovoltaic properties

In the previous sections, we have mostly focused on the chemical and structural effects of water during perovskite preparation; both as additive or moisture form, being the literature at this respect considerable wide. However, the electronic consequences of these effects under operation conditions have not been extensively investigated. Impedance Spectroscopy (IS) has been revealed as a useful technique to determine recombination and polarization processes in PSCs.[44,131,132,133,66] The impedance (Z) measurement captures the modulated current in response to a small-amplitude modulated voltage stimulus in a wide range of frequencies. Is normally carried out on a particular steady state determined by the DC bias in specified illumination conditions. To analyse the data provided by IS measurements, two main types of representation are used: the complex impedance plot $Z'-Z''$ which reveals kinetically separated processes, showed as different arcs when the processes are well-separated with respect to frequency (time), providing resistance values by measuring the width of the arcs in the real axis. The other one is the capacitance−frequency C (F cm^{-2})−f (Hz) plot that shows the general evolution of capacitive processes, explicitly associated with the dielectric response of the perovskite layer, linked with the high frequency region (HF) and surface accumulation at the interfaces, connected with the low frequency part (LF).[134,135]

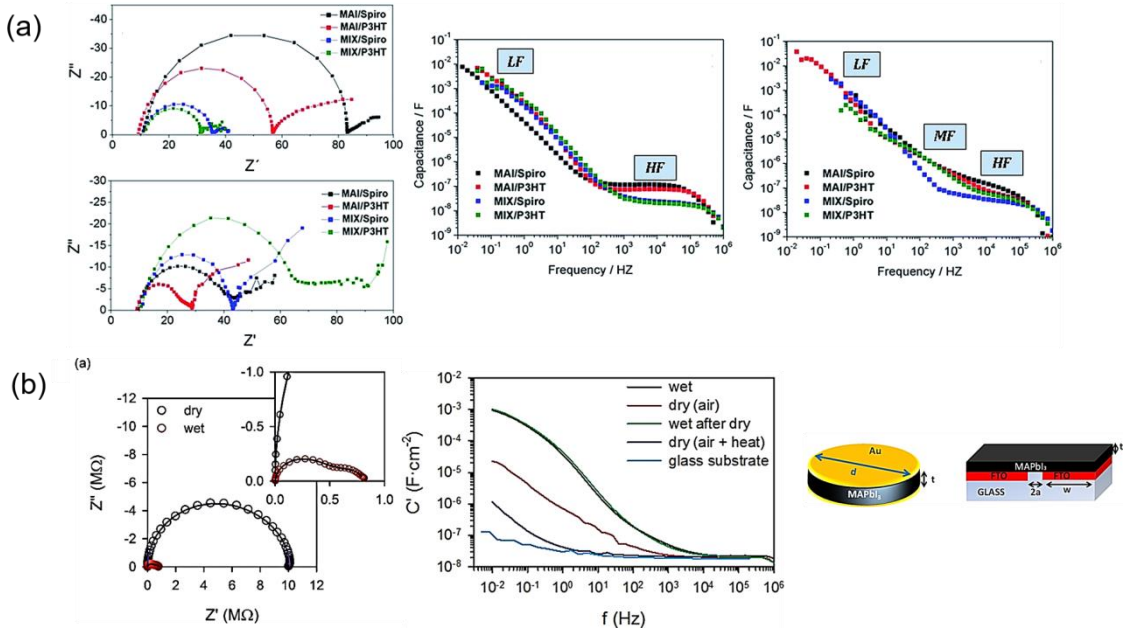

Figure 1.34. (a) Complex plane impedance spectra and capacitance-frequency response measured under open-circuit conditions and under white light illumination, showing the effects of water reported by Salado *et.al*. Reproduced with permission of Ref.136. Copyright 2017, The Royal Society of Chemistry. (b) Complex plane impedance spectra at 0V in dark of wet and dry pellets and the increase in the capacitance response at intermediate and low frequencies of the thin-film configuration device reported by García-Fernández *et.al.* and devices configurations. Reproduced with permission of Ref.137. Copyright 2018, American Chemical Society.

In 2017, Salado *et.al* proposed the first IS analysis during moisture-degradation PSCs.[136] They focused on the perovskite bulk composition and external contacts changes during fixed degradation grade. Attending to IS measurements, they found that the deterioration of the selective contacts and the appearance of more grain boundaries on perovskite layer, translate into faster recombination rate with important surface contribution that inferred from impedance analysis and capacitance-frequency response, where an intermediate frequency (IF) signal appears in the case of degraded-cells (Fig. 1.34a). Similarly, García-Fernández *et.al* developed an intensive study of the impedance response under moisture exposure of two different perovskite-based systems: polycrystalline pellet and coplanar flat thin film of $MAPbI_3$.[137] In both configurations, water performs the same effects: a huge increase in the capacitance response at intermediate and low frequencies (IF; LF respectively) coupled with an enhanced conductivity. This increased conductivity has been attributed previously to the interfacial hydrated perovskite phases formed, but may also have some contributions from partial dissolution of ions in the perovskite bulk.[95] This large capacitance was already correlated in perovskite systems with the characteristic hysteretic behaviour as well as with large accumulation carriers at the interfaces, leading to additional recombination pathways and photovoltage losses.[58] In contrast, the improvement of the conductivity, due to the presence of hydrates species, favours the transport properties of the perovskite absorber, revealing the necessity to balance the opposed contribution effects of water in PSCs in order to obtain maximized benefits (Fig.1.34b).

A part of the formulation techniques and fabrication conditions, two alternatives strategies to enhance the stability of the device itself need to be mention: the selective layers engineering and the novel synthesis of 2D-perovskites solar cells as *hydrophobic* factors. Coupling all these formulation, fabrication and hydrophobic strategies with encapsulation techniques that are summarized below, the long-term PSCs will be able to successfully being commercialized.

Regarding the selective layers, it is widely known in the literature that without the protection of the external contacts, the perovskite material is more vulnerable to degradation under ambient/working conditions.[66] Indeed, the subsequent layers required to prepare a complete device acts as a barrier layer to water and oxygen. If perovskite films are exposed to light, oxygen and moisture without any additional protection, the different degradation mechanism will be triggered. For example, hydration mechanisms of the perovskite material will be faster as compared to a complete device. For this reason, during preparation of the device, deposition of the charge extraction layers are usually completed quite fast to reduce the time exposure of the bare perovskite to ambient. However, the typical organic HSL used in n-i-p architecture, introduce additional degradation pathways regarding interfacial processes.[89] Therefore, some efforts have been done in this direction tuning the characteristics of the external contacts, becoming to rule out its use in some cases.

Han and coworkers described the use of hole-selective layer–free (HSL) configuration using conductive carbon as top contact (Fig.1.35a). They reported this material not only as an efficient collector of carriers but also as hydrophobic ally to avoid the insertion of water molecules into the perovskite material, improving the stability for over >1000 hours in ambient conditions under 1 sun (AM 1.5).[138] Unfortunately, the initial performance using this device configuration was low (~12 %) and other approaches were required. Snaith and coworkers raised the problematic hydrophilic character of Li-TFSI additive commonly used in the Spiro-OMeTAD selective layer. They proposed an alternative HSL materials based in functionalized carbazoles doped with their pre-oxidized forms (HSL^+ $TFSI^-$). This strategy added hydrophobicity to the HSL material with low contact angle of water droplets on films, as inferred from Fig. 1.35b-e.[139] Similarly, fluorine-containing hydrophobic Lewis acid dopant have been used in combination with PTAA with excellent results in terms of PCE (~19 %) and stability (>1600 h in ambient conditions).[140]

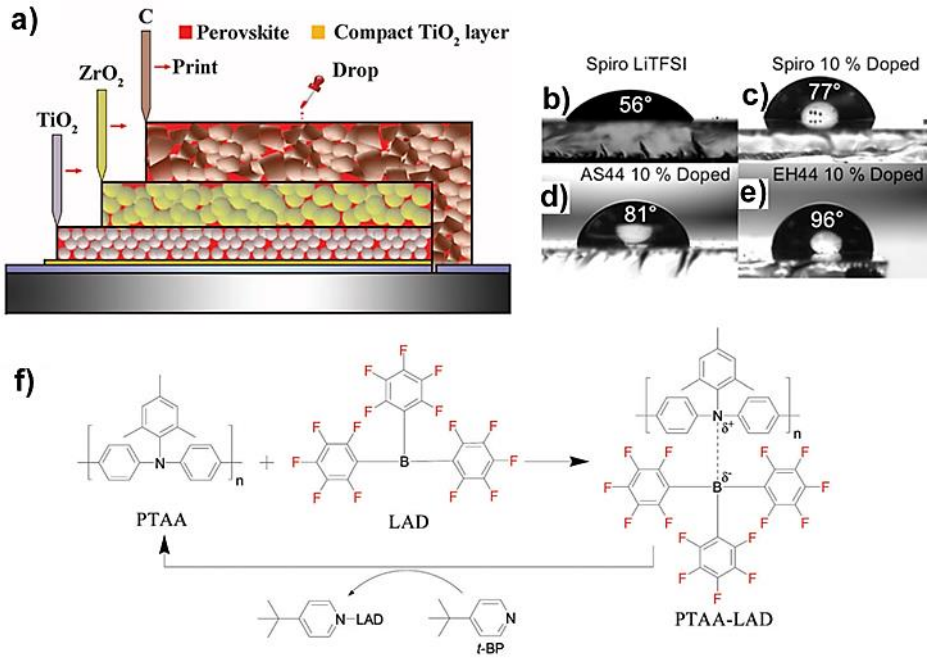

Figure 1.35. a) Device configuration of HSL-free prepared with printable carbon collector showing the cross section of the triple-layer perovskite–based mesoporous layers of TiO_2 and ZrO_2 solution. Reproduced with permission of Ref.138. Copyright 2014, American Association for the Advancement of Science. b-e) Contact angle measurements of water droplets on films of b) spiro-OMeTAD doped with Li-TFSI and c) Spiro-OMeTAD, d) AS44, and e) EH44 all doped with 10 mol % of their respective HSM^+ $TFSI^-$ salts. Reproduced with permission from Ref.139. Copyright 2016, American Chemical Society. f) Molecular structures of PTAA and LAD, and reversible formation of the adduct between Lewis basic PTAA and Lewis acid LAD in solution. Reproduced with permission from Ref.140. Copyright 2018, The Royal Society of Chemistry.

In addition to the modification of the HSL and top contact, it was also realized that the termination of the perovskite layer and its interfacial behaviour with the external contacts were determining factors. In this regards, Koocher *et al*. found that water adsorption is greatly affected by the orientation of the MA^+ cations close to the surface.[141] If the CH_3-end of MA^+ is pointing towards the contact surface, the water penetration was favoured with very low activation energies (0.023 eV). Alternatively, if the NH_3-end of the organic cation was pointing towards the external interfaces, activation energy increased up to 0.271 eV. Thus, controlling the orientation by poling the orientation or by interfacial engineering, the moisture stability could be enhanced. A more feasible approach is to modify the nature of the *A* cation (A^+) in the general perovskite formulation (ABX_3) to include the hydrophobic properties. This route has proved to be very successful with the use of cations larger than MA^+ like $HOOC(CH_2)_4NH_3I$ (AVAI), containing four methylene hydrophobic carbons, or phenethylammonium iodide (PEAI). In fact, due to the large size of A^+ cation, the perovskite structure arranges into a low dimensional material (Fig. 1.36a) that self-assembles as a thin capping layer on the top of the 3D bulk. This strategy introduce an hydrophobic surface in the perovskite absorber, succeeding one-year stability PSCs under 1 sun, at controlled temperature of 55 ºC and measured at

short circuit conditions (Fig. 1.36b).[142,106] As a final achievement, one of the recent world records of PCE 23.3% has been obtained combining a capping layer with adequate extraction materials, leading to an adequate retention of efficiencies under ambient conditions.[143]

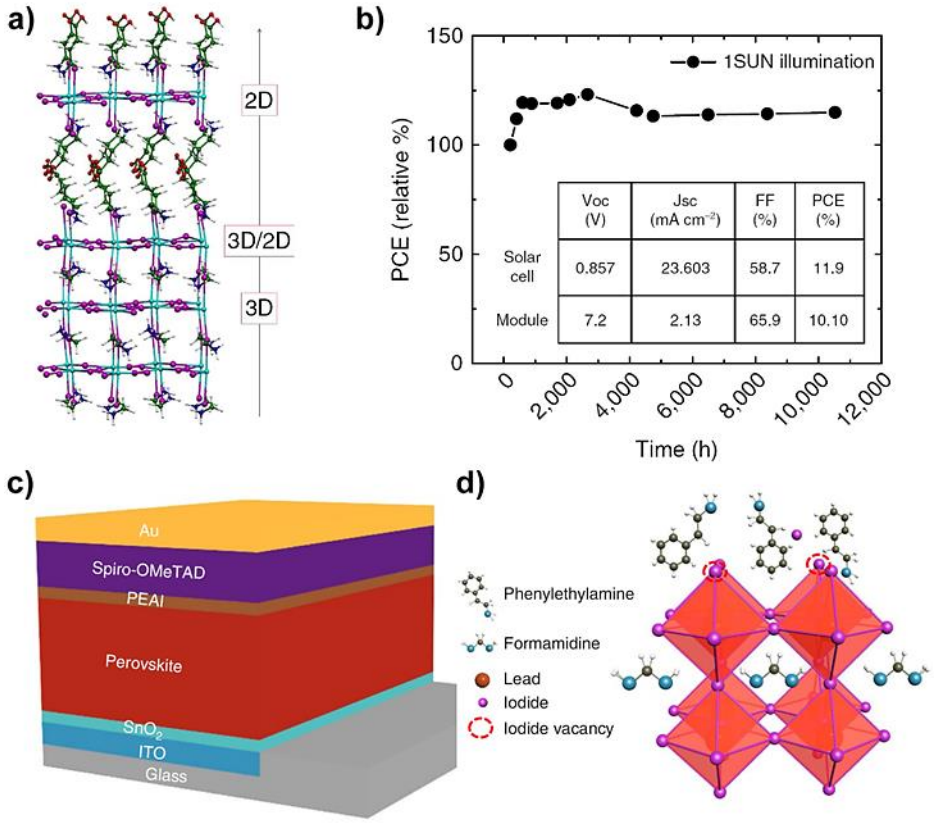

Figure 1.36. a) Interface structure with the 2D phase contacting the TiO_2 surface. b) Stability measurements done according to the standard aging conditions. In the inset, device parameters. Reproduced with permission from Ref. 142. Creative Commons Attribution 4.0 International License. http://creativecommons.org/licenses/by/4.0/ c) Device structure of the current world record, PEAI is used for post-treatment of the perovskite surface. d) Possible passivation mechanism of the PEAI layer for the perovskite film. Reproduced with permission of Ref.143. Copyright 2019, Springer Nature.

As extensively described before, even with the most sophisticated strategies to increase the stability performance of perovskite solar cells, devices without encapsulation still exhibited severe degradation under continuous illumination after several hours.[144], Therefore, a proper technology regarding the encapsulation process with advances materials become mandatory in order to achieve as longest-term PSCs for commercialization purposes. The used materials for encapsulate should match several characteristics as chemical inertness, good adhesion, high optical transmission, high dielectric constant ,mechanical strength, low water-absorptivity and high resistance to thermal oxidation and UV degradation.[145] In addition the permeation of water vapour transmission rate (WVTR) and oxygen transmission rate (OTR) needs to be two or three

orders of magnitude lower than the bare substrate, to achieve a final suitable encapsulation.[146,147] One of the most recent encapsulation technique reported is based in ultrathin plasma polymers. Anta and co-workers describe a room temperature deposition of a polymer by the remote plasma vacuum deposition of adamantine (ADA; $C_{10}H_{16}$) powder, showing an impressive stability even immersed under water.[148]

1.6. References

1. Administration, U. S. E. I. International Energy Outlook 2017 **2017**.
2. Change, T. I. P. o. C. Special report on the impacts of global warming of 1.5 °C.
3. Agency, I. R. E. Solar Energy.
4. Greenpeace, C. a. **2018**.
5. Initiative, M. E. The Future of Solar Energy: An Interdisciplinary MIT Study. . *Energy Futures* **2015**, 21–45.
6. Kojima, A.; Teshima, K.; Shirai, Y.; Miyasaka, T. Organometal Halide Perovskites as Visible-Light Sensitizers for Photovoltaic Cells. *Journal of the American Chemical Society* **2009,** *131* (17), 6050-6051.
7. Kim, H.-S.; Lee, C.-R.; Im, J.-H.; Lee, K.-B.; Moehl, T.; Marchioro, A.; Moon, S.-J.; Humphry-Baker, R.; Yum, J.-H.; Moser, J. E.; Grätzel, M.; Park, N.-G. Lead Iodide Perovskite Sensitized All-Solid-State Submicron Thin Film Mesoscopic Solar Cell with Efficiency Exceeding 9%. *Scientific Reports* **2012,** *2*, 591.
8. Lee, M. M.; Teuscher, J.; Miyasaka, T.; Murakami, T. N.; Snaith, H. J. Efficient Hybrid Solar Cells Based on Meso-Superstructured Organometal Halide Perovskites. *Science* **2012,** *338* (6107), 643-647.
9. (NREL), N. R. E. L. Best Research-Cell Efciencies https://www.nrel.gov/pv/assets/pdfs/best-research-cell-efficiencies-190416.pdf **2019**.
10. Galagan, Y. Perovskite Solar Cells: Toward Industrial-Scale Methods. *The Journal of Physical Chemistry Letters* **2018,** *9* (15), 4326-4335.
11. industry., S. T. a. S. c. c. **2019**.
12. Ke, W.; Kanatzidis, M. G. Prospects for low-toxicity lead-free perovskite solar cells. *Nature Communications* **2019,** *10* (1), 965.
13. You, J.; Meng, L.; Song, T.-B.; Guo, T.-F.; Yang, Y.; Chang, W.-H.; Hong, Z.; Chen, H.; Zhou, H.; Chen, Q.; Liu, Y.; De Marco, N.; Yang, Y. Improved air stability of perovskite solar cells via solution-processed metal oxide transport layers. *Nature Nanotechnology* **2015,** *11*, 75.
14. Cheacharoen, R.; Rolston, N.; Harwood, D.; Bush, K. A.; Dauskardt, R. H.; McGehee, M. D. Design and understanding of encapsulated perovskite solar cells to withstand temperature cycling. *Energy & Environmental Science* **2018,** *11* (1), 144-150.
15. Meng, L.; You, J.; Yang, Y. Addressing the stability issue of perovskite solar cells for commercial applications. *Nature Communications* **2018,** *9* (1), 5265.
16. Commission, I. E. INTERNATIONAL STANDARD IEC 61215 - Crystalline silicon terrestrial photovoltaic (PV) modules – Design qualification and type approval **2005**.

17. Ibn-Mohammed, T.; Koh, S. C. L.; Reaney, I. M.; Acquaye, A.; Schileo, G.; Mustapha, K. B.; Greenough, R. Perovskite solar cells: An integrated hybrid lifecycle assessment and review in comparison with other photovoltaic technologies. *Renewable and Sustainable Energy Reviews* **2017,** *80*, 1321-1344.

18. Mineralogy, H. I. o. Perovskite. *Mindat.org* **2019**.

19. Li, W.; Wang, Z.; Deschler, F.; Gao, S.; Friend, R. H.; Cheetham, A. K. Chemically diverse and multifunctional hybrid organic–inorganic perovskites. *Nature Reviews Materials* **2017,** *2*, 16099.

20. Travis, W.; Glover, E. N. K.; Bronstein, H.; Scanlon, D. O.; Palgrave, R. G. On the application of the tolerance factor to inorganic and hybrid halide perovskites: a revised system. *Chemical Science* **2016,** *7* (7), 4548-4556.

21. Varadwaj, P. R. Methylammonium Lead Trihalide Perovskite Solar Cell Semiconductors Are Not Organometallic: A Perspective. *Helvetica Chimica Acta* **2017,** *100* (7), e1700090.

22. Lee, J. H.; Lee, J.-H.; Kong, E.-H.; Jang, H. M. The nature of hydrogen-bonding interaction in the prototypic hybrid halide perovskite, tetragonal CH3NH3PbI3. *Scientific Reports* **2016,** *6*, 21687.

23. Brivio, F.; Frost, J. M.; Skelton, J. M.; Jackson, A. J.; Weber, O. J.; Weller, M. T.; Goñi, A. R.; Leguy, A. M. A.; Barnes, P. R. F.; Walsh, A. Lattice dynamics and vibrational spectra of the orthorhombic, tetragonal, and cubic phases of methylammonium lead iodide. *Physical Review B* **2015,** *92* (14), 144308.

24. Francisco-López, A.; Charles, B.; Weber, O. J.; Alonso, M. I.; Garriga, M.; Campoy-Quiles, M.; Weller, M. T.; Goñi, A. R. Pressure-Induced Locking of Methylammonium Cations versus Amorphization in Hybrid Lead Iodide Perovskites. *The Journal of Physical Chemistry C* **2018,** *122* (38), 22073-22082.

25. Milot, R. L.; Eperon, G. E.; Snaith, H. J.; Johnston, M. B.; Herz, L. M. Temperature-Dependent Charge-Carrier Dynamics in CH3NH3PbI3 Perovskite Thin Films. *Advanced Functional Materials* **2015,** *25* (39), 6218-6227.

26. Lee, J.-H.; Bristowe, N. C.; Lee, J. H.; Lee, S.-H.; Bristowe, P. D.; Cheetham, A. K.; Jang, H. M. Resolving the Physical Origin of Octahedral Tilting in Halide Perovskites. *Chemistry of Materials* **2016,** *28* (12), 4259-4266.

27. Herklotz, A.; Wong, A. T.; Meyer, T.; Biegalski, M. D.; Lee, H. N.; Ward, T. Z. Controlling Octahedral Rotations in a Perovskite via Strain Doping. *Scientific Reports* **2016,** *6*, 26491.

28. Prasanna, R.; Gold-Parker, A.; Leijtens, T.; Conings, B.; Babayigit, A.; Boyen, H.-G.; Toney, M. F.; McGehee, M. D. Band Gap Tuning via Lattice Contraction and

Octahedral Tilting in Perovskite Materials for Photovoltaics. *Journal of the American Chemical Society* **2017,** *139* (32), 11117-11124.

29. Noh, J. H.; Im, S. H.; Heo, J. H.; Mandal, T. N.; Seok, S. I. Chemical Management for Colorful, Efficient, and Stable Inorganic–Organic Hybrid Nanostructured Solar Cells. *Nano Letters* **2013,** *13* (4), 1764-1769.

30. Wakamiya, A.; Endo, M.; Sasamori, T.; Tokitoh, N.; Ogomi, Y.; Hayase, S.; Murata, Y. Reproducible Fabrication of Efficient Perovskite-based Solar Cells: X-ray Crystallographic Studies on the Formation of CH3NH3PbI3 Layers. *Chemistry Letters* **2014,** *43* (5), 711-713.

31. Baikie, T.; Fang, Y.; Kadro, J. M.; Schreyer, M.; Wei, F.; Mhaisalkar, S. G.; Graetzel, M.; White, T. J. Synthesis and crystal chemistry of the hybrid perovskite (CH3NH3)PbI3 for solid-state sensitised solar cell applications. *Journal of Materials Chemistry A* **2013,** *1* (18), 5628-5641.

32. Luo, S.; Daoud, W. A. Crystal Structure Formation of $CH_3NH_3PbI(3-x)Cl(x)$ Perovskite. *Materials (Basel)* **2016,** *9* (3), 123.

33. Jeon, N. J.; Noh, J. H.; Kim, Y. C.; Yang, W. S.; Ryu, S.; Seok, S. I. Solvent engineering for high-performance inorganic–organic hybrid perovskite solar cells. *Nature Materials* **2014,** *13*, 897.

34. Saidaminov, M. I.; Abdelhady, A. L.; Murali, B.; Alarousu, E.; Burlakov, V. M.; Peng, W.; Dursun, I.; Wang, L.; He, Y.; Maculan, G.; Goriely, A.; Wu, T.; Mohammed, O. F.; Bakr, O. M. High-quality bulk hybrid perovskite single crystals within minutes by inverse temperature crystallization. *Nature Communications* **2015,** *6*, 7586.

35. Herz, L. M. Charge-Carrier Dynamics in Organic-Inorganic Metal Halide Perovskites. *Annual Review of Physical Chemistry* **2016,** *67* (1), 65-89.

36. Leguy, A. M. A.; Frost, J. M.; McMahon, A. P.; Sakai, V. G.; Kockelmann, W.; Law, C.; Li, X.; Foglia, F.; Walsh, A.; O'Regan, B. C.; Nelson, J.; Cabral, J. T.; Barnes, P. R. F. The dynamics of methylammonium ions in hybrid organic–inorganic perovskite solar cells. *Nature Communications* **2015,** *6*, 7124.

37. Shockley, W.; Queisser, H. J. Detailed Balance Limit of Efficiency of p-n Junction Solar Cells. *Journal of Applied Physics* **1961,** *32* (3), 510-519.

38. Rühle, S. Tabulated values of the Shockley–Queisser limit for single junction solar cells. *Solar Energy* **2016,** *130*, 139-147.

39. Nayak, P. K.; Bisquert, J.; Cahen, D. Assessing Possibilities and Limits for Solar Cells. *Advanced Materials* **2011,** *23* (25), 2870-2876.

40. Nelson, J. *The Physics of Solar Cells*.

41. Shen, Q.; Ogomi, Y.; Chang, J.; Tsukamoto, S.; Kukihara, K.; Oshima, T.; Osada, N.; Yoshino, K.; Katayama, K.; Toyoda, T.; Hayase, S. Charge transfer and

recombination at the metal oxide/CH3NH3PbClI2/spiro-OMeTAD interfaces: uncovering the detailed mechanism behind high efficiency solar cells. *Physical Chemistry Chemical Physics* **2014,** *16* (37), 19984-19992.

42. Tress, W.; Correa Baena, J. P.; Saliba, M.; Abate, A.; Graetzel, M. Inverted Current–Voltage Hysteresis in Mixed Perovskite Solar Cells: Polarization, Energy Barriers, and Defect Recombination. *Advanced Energy Materials* **2016,** *6* (19), 1600396-n/a.

43. Juarez-Perez, E. J.; Sanchez, R. S.; Badia, L.; Garcia-Belmonte, G.; Kang, Y. S.; Mora-Sero, I.; Bisquert, J. Photoinduced Giant Dielectric Constant in Lead Halide Perovskite Solar Cells. *The Journal of Physical Chemistry Letters* **2014,** *5* (13), 2390-2394.

44. Almora, O.; Zarazua, I.; Mas-Marza, E.; Mora-Sero, I.; Bisquert, J.; Garcia-Belmonte, G. Capacitive Dark Currents, Hysteresis, and Electrode Polarization in Lead Halide Perovskite Solar Cells. *The Journal of Physical Chemistry Letters* **2015,** *6* (9), 1645-1652.

45. Mora-Seró, I. How Do Perovskite Solar Cells Work? *Joule* **2018,** *2* (4), 585-587.

46. Rong, Y.; Hu, Y.; Mei, A.; Tan, H.; Saidaminov, M. I.; Seok, S. I.; McGehee, M. D.; Sargent, E. H.; Han, H. Challenges for commercializing perovskite solar cells. *Science* **2018,** *361* (6408), eaat8235.

47. Zhang, Y.; Zhuang, X.; Zhou, K.; Cai, C.; Hu, Z.; Zhang, J.; Zhu, Y. Vibration treated carbon electrode for highly efficient hole-conductor-free perovskite solar cells. *Organic Electronics* **2018,** *52*, 159-164.

48. Bush, K. A.; Palmstrom, A. F.; Yu, Z. J.; Boccard, M.; Cheacharoen, R.; Mailoa, J. P.; McMeekin, D. P.; Hoye, R. L. Z.; Bailie, C. D.; Leijtens, T.; Peters, I. M.; Minichetti, M. C.; Rolston, N.; Prasanna, R.; Sofia, S.; Harwood, D.; Ma, W.; Moghadam, F.; Snaith, H. J.; Buonassisi, T.; Holman, Z. C.; Bent, S. F.; McGehee, M. D. 23.6%-efficient monolithic perovskite/silicon tandem solar cells with improved stability. *Nature Energy* **2017,** *2*, 17009.

49. Maheu, C.; Cardenas, L.; Puzenat, E.; Afanasiev, P.; Geantet, C. UPS and UV spectroscopies combined to position the energy levels of TiO2 anatase and rutile nanopowders. *Physical Chemistry Chemical Physics* **2018,** *20* (40), 25629-25637.

50. Govindasamy, G.; Murugasen, P.; Sagadevan, S. Investigations on the Synthesis, Optical and Electrical Properties of TiO2 Thin Films by Chemical Bath Deposition (CBD) method. *Materials Research* **2016,** *19*, 413-419.

51. Sandeep K. Pathak , A. A., P. Ruckdeschel , B. Roose , Karl C. Gödel , Yana Vaynzof , Aditya Santhala , Shun-Ichiro Watanabe , Derek J. Hollman , Nakita Noel , Alessandro Sepe , Ullrich Wiesner , Richard Friend , Henry J. Snaith , * and Ullrich

Steiner * Performance and Stability Enhancement of Dye-Sensitized and Perovskite Solar Cells by Al Doping of TiO2. *Advanced Functional Materials* **2014**.

52. Wang, X.; Feng, Z.; Shi, J.; Jia, G.; Shen, S.; Zhou, J.; Li, C. Trap states and carrier dynamics of TiO2 studied by photoluminescence spectroscopy under weak excitation condition. *Physical Chemistry Chemical Physics* **2010,** *12* (26), 7083-7090.

53. Berhe, T. A.; Su, W.-N.; Chen, C.-H.; Pan, C.-J.; Cheng, J.-H.; Chen, H.-M.; Tsai, M.-C.; Chen, L.-Y.; Dubale, A. A.; Hwang, B.-J. Organometal halide perovskite solar cells: degradation and stability. *Energy & Environmental Science* **2016,** *9* (2), 323-356.

54. Leijtens, T.; Eperon, G. E.; Pathak, S.; Abate, A.; Lee, M. M.; Snaith, H. J. Overcoming ultraviolet light instability of sensitized TiO2 with meso-superstructured organometal tri-halide perovskite solar cells. *Nature Communications* **2013,** *4*, 2885.

55. Wojciechowski, K.; Stranks, S. D.; Abate, A.; Sadoughi, G.; Sadhanala, A.; Kopidakis, N.; Rumbles, G.; Li, C.-Z.; Friend, R. H.; Jen, A. K. Y.; Snaith, H. J. Heterojunction Modification for Highly Efficient Organic–Inorganic Perovskite Solar Cells. *ACS Nano* **2014,** *8* (12), 12701-12709.

56. Giordano, F.; Abate, A.; Correa Baena, J. P.; Saliba, M.; Matsui, T.; Im, S. H.; Zakeeruddin, S. M.; Nazeeruddin, M. K.; Hagfeldt, A.; Graetzel, M. Enhanced electronic properties in mesoporous TiO2 via lithium doping for high-efficiency perovskite solar cells**2016,** *7*, 10379.

57. Carol L. Olson†, M. S. I., Jenny Nelson*. Defect Chemistry, Surface Structures, and Lithium Insertion in Anatase TiO2. *journal of physical Chemistry B* **2006,** *110*, 9995-10001.

58. Aranda, C.; Guerrero, A.; Bisquert, J. Ionic Effect Enhances Light Emission and the Photovoltage of Methylammonium Lead Bromide Perovskite Solar Cells by Reduced Surface Recombination. *ACS Energy Letters* **2019**, 741-746.

59. Wang, S.; Yuan, W.; Meng, Y. S. Spectrum-Dependent Spiro-OMeTAD Oxidization Mechanism in Perovskite Solar Cells. *ACS Applied Materials & Interfaces* **2015,** *7* (44), 24791-24798.

60. Hawash, Z.; Ono, L. K.; Raga, S. R.; Lee, M. V.; Qi, Y. Air-Exposure Induced Dopant Redistribution and Energy Level Shifts in Spin-Coated Spiro-MeOTAD Films. *Chemistry of Materials* **2015,** *27* (2), 562-569.

61. Schölin, R.; Karlsson, M. H.; Eriksson, S. K.; Siegbahn, H.; Johansson, E. M. J.; Rensmo, H. Energy Level Shifts in Spiro-OMeTAD Molecular Thin Films When Adding Li-TFSI. *The Journal of Physical Chemistry C* **2012,** *116* (50), 26300-26305.

62. Correa-Baena, J.-P.; Tress, W.; Domanski, K.; Anaraki, E. H.; Turren-Cruz, S.-H.; Roose, B.; Boix, P. P.; Gratzel, M.; Saliba, M.; Abate, A.; Hagfeldt, A. Identifying

and suppressing interfacial recombination to achieve high open-circuit voltage in perovskite solar cells. *Energy Environ. Sci.* **2017,** *10* (5), 1207-1212.

63. Fantacci, S.; De Angelis, F.; Nazeeruddin, M. K.; Grätzel, M. Electronic and Optical Properties of the Spiro-MeOTAD Hole Conductor in Its Neutral and Oxidized Forms: A DFT/TDDFT Investigation. *The Journal of Physical Chemistry C* **2011,** *115* (46), 23126-23133.

64. Wang, Y.; Qu, H.; Zhang, C.; Chen, Q. Rapid Oxidation of the Hole Transport Layer in Perovskite Solar Cells by A Low-Temperature Plasma. *Scientific Reports* **2019,** *9* (1), 459.

65. Azpiroz, J. M.; Mosconi, E.; Bisquert, J.; De Angelis, F. Defect migration in methylammonium lead iodide and its role in perovskite solar cell operation. *Energy Environ. Sci.* **2015,** *8*, 2118--2127.

66. Guerrero, A.; You, J.; Aranda, C.; Kang, Y. S.; Garcia-Belmonte, G.; Zhou, H.; Bisquert, J.; Yang, Y. Interfacial Degradation of Planar Lead Halide Perovskite Solar Cells. *ACS nano* **2016,** *10*, 218–224.

67. Zarazua, I.; Bisquert, J.; Garcia-Belmonte, G. Light-Induced Space-Charge Accumulation Zone as Photovoltaic Mechanism in Perovskite Solar Cells. *The Journal of Physical Chemistry Letters* **2016,** *7* (3), 525-528.

68. Guerrero, A.; Juarez-Perez, E. J.; Bisquert, J.; Mora-Sero, I.; Garcia-Belmonte, G. Electrical field profile and doping in planar lead halide perovskite solar cells. *Applied Physics Letters* **2014,** *105* (13), 133902.

69. Zarazua, I.; Han, G.; Boix, P. P.; Mhaisalkar, S.; Fabregat-Santiago, F.; Mora-Seró, I.; Bisquert, J.; Garcia-Belmonte, G. Surface Recombination and Collection Efficiency in Perovskite Solar Cells from Impedance Analysis. *The Journal of Physical Chemistry Letters* **2016,** *7* (24), 5105-5113.

70. Li, Z.; Yang, M.; Park, J.-S.; Wei, S.-H.; Berry, J. J.; Zhu, K. Stabilizing Perovskite Structures by Tuning Tolerance Factor: Formation of Formamidinium and Cesium Lead Iodide Solid-State Alloys. *Chemistry of Materials* **2016,** *28* (1), 284-292.

71. Zheng, X.; Wu, C.; Jha, S. K.; Li, Z.; Zhu, K.; Priya, S. Improved Phase Stability of Formamidinium Lead Triiodide Perovskite by Strain Relaxation. *ACS Energy Letters* **2016,** *1* (5), 1014-1020.

72. Arora, N.; Dar, M. I.; Hinderhofer, A.; Pellet, N.; Schreiber, F.; Zakeeruddin, S. M.; Grätzel, M. Perovskite solar cells with CuSCN hole extraction layers yield stabilized efficiencies greater than 20%. *Science* **2017,** *358* (6364), 768-771.

73. Juarez-Perez, E. J.; Ono, L. K.; Maeda, M.; Jiang, Y.; Hawash, Z.; Qi, Y. Photodecomposition and thermal decomposition in methylammonium halide lead

perovskites and inferred design principles to increase photovoltaic device stability. *Journal of Materials Chemistry A* **2018,** *6* (20), 9604-9612.

74. Ciccioli, A.; Latini, A. Thermodynamics and the Intrinsic Stability of Lead Halide Perovskites CH3NH3PbX3. *The Journal of Physical Chemistry Letters* **2018,** *9* (13), 3756-3765.

75. Snaith, H. J.; Abate, A.; Ball, J. M.; Eperon, G. E.; Leijtens, T.; Noel, N. K.; Stranks, S. D.; Wang, J. T.-W.; Wojciechowski, K.; Zhang, W. Anomalous Hysteresis in Perovskite Solar Cells. *The Journal of Physical Chemistry Letters* **2014,** *5* (9), 1511-1515.

76. Park, N.-G. Switchable photovoltaics. *Nature Materials* **2014,** *14*, 140.

77. Shi, L. X.; Wang, Z. S.; Huang, Z.; Sha, W. E. I.; Wang, H.; Zhou, Z. The effects of interfacial recombination and injection barrier on the electrical characteristics of perovskite solar cells. *AIP Advances* **2018,** *8* (2), 025312.

78. Fakharuddin, A.; Schmidt-Mende, L.; Garcia-Belmonte, G.; Jose, R.; Mora-Sero, I. Interfaces in Perovskite Solar Cells. *Advanced Energy Materials* **2017,** *7* (22), 1700623.

79. Senocrate, A.; Moudrakovski, I.; Kim, G. Y.; Yang, T.-Y.; Gregori, G.; Grätzel, M.; Maier, J. The Nature of Ion Conduction in Methylammonium Lead Iodide: A Multimethod Approach. *Angewandte Chemie International Edition* **2017,** *56* (27), 7755-7759.

80. Peng, W.; Aranda, C.; Bakr, O. M.; Garcia-Belmonte, G.; Bisquert, J.; Guerrero, A. Quantification of Ionic Diffusion in Lead Halide Perovskite Single Crystals. *ACS Energy Letters* **2018,** *3* (7), 1477-1481.

81. Li, C.; Guerrero, A.; Huettner, S.; Bisquert, J. Unravelling the role of vacancies in lead halide perovskite through electrical switching of photoluminescence. *Nature Communications* **2018,** *9* (1), 5113.

82. Wang, H.; Bou, A.; Guerrero, A.; AlMayouf, A. M.; Bisquert, J. Kinetic and material properties of interfaces governing slow response and long timescale phenomena in perovskite solar cells. *Energy & Environmental Science* **2019**.

83. Gottesman, R.; Lopez-Varo, P.; Gouda, L.; Jimenez-Tejada, Juan A.; Hu, J.; Tirosh, S.; Zaban, A.; Bisquert, J. Dynamic Phenomena at Perovskite/Electron-Selective Contact Interface as Interpreted from Photovoltage Decays. *Chem* **2016,** *1* (5), 776-789.

84. Zong, Y.; Zhou, Y.; Zhang, Y.; Li, Z.; Zhang, L.; Ju, M.-G.; Chen, M.; Pang, S.; Zeng, X. C.; Padture, N. P. Continuous Grain-Boundary Functionalization for High-Efficiency Perovskite Solar Cells with Exceptional Stability. *Chem* **2018,** *4* (6), 1404-1415.

85. Saidaminov, M. I.; Kim, J.; Jain, A.; Quintero-Bermudez, R.; Tan, H.; Long, G.; Tan, F.; Johnston, A.; Zhao, Y.; Voznyy, O.; Sargent, E. H. Suppression of atomic

vacancies via incorporation of isovalent small ions to increase the stability of halide perovskite solar cells in ambient air. *Nature Energy* **2018,** *3* (8), 648-654.

86. Pearson, A. J.; Eperon, G. E.; Hopkinson, P. E.; Habisreutinger, S. N.; Wang, J. T.-W.; Snaith, H. J.; Greenham, N. C. Oxygen Degradation in Mesoporous Al2O3/CH3NH3PbI3-xClx Perovskite Solar Cells: Kinetics and Mechanisms. *Advanced Energy Materials* **2016,** *6* (13), 1600014.

87. Aristidou, N.; Eames, C.; Sanchez-Molina, I.; Bu, X.; Kosco, J.; Islam, M. S.; Haque, S. A. Fast oxygen diffusion and iodide defects mediate oxygen-induced degradation of perovskite solar cells. *Nature Communications* **2017,** *8*, 15218.

88. Bryant, D.; Aristidou, N.; Pont, S.; Sanchez-Molina, I.; Chotchunangatchaval, T.; Wheeler, S.; Durrant, J. R.; Haque, S. A. Light and oxygen induced degradation limits the operational stability of methylammonium lead triiodide perovskite solar cells. *Energy & Environmental Science* **2016,** *9* (5), 1655-1660.

89. Sanchez, R. S.; Mas-Marza, E. Light-induced effects on Spiro-OMeTAD films and hybrid lead halide perovskite solar cells. *Solar Energy Materials and Solar Cells* **2016,** *158* (Part 2), 189-194.

90. Leguy, A. M. A.; Hu, Y.; Campoy-Quiles, M.; Alonso, M. I.; Weber, O. J.; Azarhoosh, P.; van Schilfgaarde, M.; Weller, M. T.; Bein, T.; Nelson, J.; Docampo, P.; Barnes, P. R. F. Reversible Hydration of CH3NH3PbI3 in Films, Single Crystals, and Solar Cells. *Chemistry of Materials* **2015,** *27* (9), 3397-3407.

91. Zhou, W.; Zhao, Y.; Shi, C.; Huang, H.; Wei, J.; Fu, R.; Liu, K.; Yu, D.; Zhao, Q. Reversible Healing Effect of Water Molecules on Fully Crystallized Metal–Halide Perovskite Film. *The Journal of Physical Chemistry C* **2016,** *120* (9), 4759-4765.

92. Byranvand, M. M.; Kharat, A. N.; Taghavinia, N. Moisture stability in nanostructured perovskite solar cells. *Materials Letters* **2019,** *237*, 356-360.

93. Contreras-Bernal, L.; Aranda, C.; Valles-Pelarda, M.; Ngo, T. T.; Ramos-Terrón, S.; Gallardo, J. J.; Navas, J.; Guerrero, A.; Mora-Seró, I.; Idígoras, J.; Anta, J. A. Homeopathic Perovskite Solar Cells: Effect of Humidity during Fabrication on the Performance and Stability of the Device. *The Journal of Physical Chemistry C* **2018,** *122* (10), 5341-5348.

94. Almora, O.; Vaillant-Roca, L.; Garcia-Belmonte, G. Perovskite Solar Cells: A brief Introduction and some Remarks. *2017* **2017,** *34* (1), 11.

95. Müller, C.; Glaser, T.; Plogmeyer, M.; Sendner, M.; Döring, S.; Bakulin, A. A.; Brzuska, C.; Scheer, R.; Pshenichnikov, M. S.; Kowalsky, W.; Pucci, A.; Lovrinčić, R. Water Infiltration in Methylammonium Lead Iodide Perovskite: Fast and Inconspicuous. *Chemistry of Materials* **2015,** *27* (22), 7835-7841.

96. Gangishetty, M. K.; Scott, R. W. J.; Kelly, T. L. Effect of relative humidity on crystal growth, device performance and hysteresis in planar heterojunction perovskite solar cells. *Nanoscale* **2016,** *8* (12), 6300-6307.

97. Huang, J.; Tan, S.; Lund, P. D.; Zhou, H. Impact of H2O on organic–inorganic hybrid perovskite solar cells. *Energy & Environmental Science* **2017,** *10* (11), 2284-2311.

98. Ávila, J.; Momblona, C.; Boix, P. P.; Sessolo, M.; Bolink, H. J. Vapor-Deposited Perovskites: The Route to High-Performance Solar Cell Production? *Joule* **2017,** *1* (3), 431-442.

99. Gil-Escrig, L.; Momblona, C.; La-Placa, M.-G.; Boix, P. P.; Sessolo, M.; Bolink, H. J. Vacuum Deposited Triple-Cation Mixed-Halide Perovskite Solar Cells. *Advanced Energy Materials* **2018,** *8* (14), 1703506.

100. Schaefer, F. C.; Hechenbleikner, I.; Peters, G. A.; Wystrach, V. P. Synthesis of the sym-Triazine System. I. Trimerization and Cotrimerization of Amidines. *Journal of the American Chemical Society* **1959,** *81* (6), 1466-1470.

101. Arabpour Roghabadi, F.; Alidaei, M.; Mousavi, S. M.; Ashjari, T.; Tehrani, A. S.; Ahmadi, V.; Sadrameli, S. M. Stability progress of perovskite solar cells dependent on the crystalline structure: From 3D ABX3 to 2D Ruddlesden–Popper perovskite absorbers. *Journal of Materials Chemistry A* **2019,** *7* (11), 5898-5933.

102. Qiu, W.; Ray, A.; Jaysankar, M.; Merckx, T.; Bastos, J. P.; Cheyns, D.; Gehlhaar, R.; Poortmans, J.; Heremans, P. An Interdiffusion Method for Highly Performing Cesium/Formamidinium Double Cation Perovskites. *Advanced Functional Materials* **2017,** *27* (28), 1700920.

103. Saliba, M.; Matsui, T.; Seo, J.-Y.; Domanski, K.; Correa-Baena, J.-P.; Nazeeruddin, M. K.; Zakeeruddin, S. M.; Tress, W.; Abate, A.; Hagfeldt, A.; Gratzel, M. Cesium-containing triple cation perovskite solar cells: improved stability, reproducibility and high efficiency. *Energ. Environ. Sci.* **2016**.

104. Hsieh, T.-Y.; Su, T.-S.; Ikegami, M.; Wei, T.-C.; Miyasaka, T. Stable and efficient perovskite solar cells fabricated using aqueous lead nitrate precursor: Interpretation of the conversion mechanism and renovation of the sequential deposition. *Materials Today Energy* **2018**.

105. He, T.; Liu, Z.; Zhou, Y.; Ma, H. The stable perovskite solar cell prepared by rapidly annealing perovskite film with water additive in ambient air. *Solar Energy Materials and Solar Cells* **2018,** *176*, 280-287.

106. Cho, K. T.; Zhang, Y.; Orlandi, S.; Cavazzini, M.; Zimmermann, I.; Lesch, A.; Tabet, N.; Pozzi, G.; Grancini, G.; Nazeeruddin, M. K. Water-Repellent Low-Dimensional Fluorous Perovskite as Interfacial Coating for 20% Efficient Solar Cells. *Nano Letters* **2018,** *18* (9), 5467-5474.

107. You, J.; Yang, Y.; Hong, Z.; Song, T.-B.; Meng, L.; Liu, Y.; Jiang, C.; Zhou, H.; Chang, W.-H.; Li, G.; Yang, Y. Moisture assisted perovskite film growth for high performance solar cells. *Applied Physics Letters* **2014,** *105* (18), 183902.

108. Eperon, G. E.; Habisreutinger, S. N.; Leijtens, T.; Bruijnaers, B. J.; van Franeker, J. J.; deQuilettes, D. W.; Pathak, S.; Sutton, R. J.; Grancini, G.; Ginger, D. S.; Janssen, R. A. J.; Petrozza, A.; Snaith, H. J. The Importance of Moisture in Hybrid Lead Halide Perovskite Thin Film Fabrication. *ACS nano* **2015,** *9* (9), 9380-9393.

109. Saliba, M.; Matsui, T.; Domanski, K.; Seo, J.-Y.; Ummadisingu, A.; Zakeeruddin, S. M.; Correa-Baena, J.-P.; Tress, W. R.; Abate, A.; Hagfeldt, A.; Grätzel, M. Incorporation of rubidium cations into perovskite solar cells improves photovoltaic performance. *Science* **2016**.

110. Uddin, A.; Upama, M. B.; Yi, H.; Duan, L. Encapsulation of Organic and Perovskite Solar Cells: A Review. *Coatings* **2019,** *9* (2), 65.

111. Brinkmann, K. O.; Zhao, J.; Pourdavoud, N.; Becker, T.; Hu, T.; Olthof, S.; Meerholz, K.; Hoffmann, L.; Gahlmann, T.; Heiderhoff, R.; Oszajca, M. F.; Luechinger, N. A.; Rogalla, D.; Chen, Y.; Cheng, B.; Riedl, T. Suppressed decomposition of organometal halide perovskites by impermeable electron-extraction layers in inverted solar cells. *Nature communications* **2017,** *8*, 13938-13938.

112. Bercegol, A.; Ramos, F. J.; Rebai, A.; Guillemot, T.; Ory, D.; Rousset, J.; Lombez, L. Slow Diffusion and Long Lifetime in Metal Halide Perovskites for Photovoltaics. *The Journal of Physical Chemistry C* **2018,** *122* (43), 24570-24577.

113. Wu, C.-G.; Chiang, C.-H.; Tseng, Z.-L.; Nazeeruddin, M. K.; Hagfeldt, A.; Grätzel, M. High efficiency stable inverted perovskite solar cells without current hysteresis. *Energy & Environmental Science* **2015,** *8* (9), 2725-2733.

114. Conings, B.; Babayigit, A.; Vangerven, T.; D'Haen, J.; Manca, J.; Boyen, H.-G. The impact of precursor water content on solution-processed organometal halide perovskite films and solar cells. *Journal of Materials Chemistry A* **2015,** *3* (37), 19123-19128.

115. Chiang, C.-H.; Nazeeruddin, M. K.; Grätzel, M.; Wu, C.-G. The synergistic effect of H2O and DMF towards stable and 20% efficiency inverted perovskite solar cells. *Energy & Environmental Science* **2017,** *10* (3), 808-817.

116. Frost, J. M.; Butler, K. T.; Brivio, F.; Hendon, C. H.; van Schilfgaarde, M.; Walsh, A. Atomistic Origins of High-Performance in Hybrid Halide Perovskite Solar Cells. *Nano Letters* **2014,** *14* (5), 2584-2590.

117. Philippe, B.; Park, B.-W.; Lindblad, R.; Oscarsson, J.; Ahmadi, S.; Johansson, E. M. J.; Rensmo, H. Chemical and Electronic Structure Characterization of Lead Halide

Perovskites and Stability Behavior under Different Exposures—A Photoelectron Spectroscopy Investigation. *Chemistry of Materials* **2015,** *27* (5), 1720-1731.

118. Kye, Y.-H.; Yu, C.-J.; Jong, U.-G.; Chen, Y.; Walsh, A. Critical Role of Water in Defect Aggregation and Chemical Degradation of Perovskite Solar Cells. *The Journal of Physical Chemistry Letters* **2018,** *9* (9), 2196-2201.

119. Zhang, X.; Bai, X.; Wu, H.; Zhang, X.; Sun, C.; Zhang, Y.; Zhang, W.; Zheng, W.; Yu, W. W.; Rogach, A. L. Water-Assisted Size and Shape Control of CsPbBr3 Perovskite Nanocrystals. *Angewandte Chemie* **2018,** *130* (13), 3395-3400.

120. Zhang, F.; Zhong, H.; Chen, C.; Wu, X.-g.; Hu, X.; Huang, H.; Han, J.; Zou, B.; Dong, Y. Brightly Luminescent and Color-Tunable Colloidal CH3NH3PbX3 (X = Br, I, Cl) Quantum Dots: Potential Alternatives for Display Technology. *ACS Nano* **2015,** *9* (4), 4533-4542.

121. Kachmar, A.; Berdiyorov, G.; Madjet, M. E.-A. Effect of Water on the Structural, Optical, and Hot-Carrier Cooling Properties of the Perovskite Material MASnI3. *The Journal of Physical Chemistry C* **2019,** *123* (7), 4056-4063.

122. Bass, K. K.; McAnally, R. E.; Zhou, S.; Djurovich, P. I.; Thompson, M. E.; Melot, B. C. Influence of moisture on the preparation, crystal structure, and photophysical properties of organohalide perovskites. *Chemical Communications* **2014,** *50* (99), 15819-15822.

123. Zhou, H.; Chen, Q.; Li, G.; Luo, S.; Song, T.-b.; Duan, H.-S.; Hong, Z.; You, J.; Liu, Y.; Yang, Y. Interface engineering of highly efficient perovskite solar cells. *Science* **2014,** *345* (6196), 542-546.

124. Grancini, G.; D'Innocenzo, V.; Dohner, E. R.; Martino, N.; Srimath Kandada, A. R.; Mosconi, E.; De Angelis, F.; Karunadasa, H. I.; Hoke, E. T.; Petrozza, A. CH3NH3PbI3 perovskite single crystals: surface photophysics and their interaction with the environment. *Chemical Science* **2015,** *6* (12), 7305-7310.

125. Liu, M.; Johnston, M. B.; Snaith, H. J. Efficient planar heterojunction perovskite solar cells by vapour deposition. *Nature* **2013,** *501* (7467), 395-398.

126. Shao, Y.; Xiao, Z.; Bi, C.; Yuan, Y.; Huang, J. Origin and elimination of photocurrent hysteresis by fullerene passivation in CH3NH3PbI3 planar heterojunction solar cells. *Nature Communications* **2014,** *5*, 5784.

127. Yang, F.; Kamarudin, M. A.; Zhang, P.; Kapil, G.; Ma, T.; Hayase, S. Enhanced Crystallization by Methanol Additive in Antisolvent for Achieving High-Quality MAPbI3 Perovskite Films in Humid Atmosphere. *ChemSusChem* **2018,** *11* (14), 2348-2357.

128. Troughton, J.; Hooper, K.; Watson, T. M. Humidity resistant fabrication of CH3NH3PbI3 perovskite solar cells and modules. *Nano Energy* **2017,** *39*, 60-68.

129. Gedamu, D.; Asuo, I. M.; Benetti, D.; Basti, M.; Ka, I.; Cloutier, S. G.; Rosei, F.; Nechache, R. Solvent-Antisolvent Ambient Processed Large Grain Size Perovskite Thin Films for High-Performance Solar Cells. *Scientific Reports* **2018,** *8* (1), 12885.

130. Aranda, C.; Cristobal, C.; Shooshtari, L.; Li, C.; Huettner, S.; Guerrero, A. Formation criteria of high efficiency perovskite solar cells under ambient conditions. *Sustainable Energy & Fuels* **2017,** *1* (3), 540-547.

131. Garcia-Belmonte, G.; Guerrero, A.; Bisquert, J. Elucidating Operating Modes of Bulk-Heterojunction Solar Cells from Impedance Spectroscopy Analysis. *J. Phys. Chem. Lett.* **2013,** *4*, 877−886.

132. Bisquert, J.; Fabregat-Santiago, F. Impedance Spectroscopy: A general Introduction and Application to Dye-Sensitized Solar Cells. In *Dye-sensitized solar cells.*, Kalyanasundaram, K., Ed. CRC Press: Boca Raton, 2010.

133. Bisquert, J.; Garcia-Belmonte, G.; Guerrero, A. Impedance Characteristics of Hybrid Organometal Halide Perovskite Solar Cells. In *Organic-Inorganic Halide Perovskite Photovoltaics: From Fundamentals to Device Architectures*, Park, N.-G.; Grätzel, M.; Miyasaka, T., Eds. Springer International Publishing: Cham, 2016; pp 163-199.

134. Bisquert, J.; Bertoluzzi, L.; Mora-Sero, I.; Garcia-Belmonte, G. Theory of Impedance and Capacitance Spectroscopy of Solar Cells with Dielectric Relaxation, Drift-Diffusion Transport, and Recombination. *The Journal of Physical Chemistry C* **2014,** *118* (33), 18983-18991.

135. Ravishankar, S.; Aranda, C.; Sanchez, S.; Bisquert, J.; Saliba, M.; Garcia-Belmonte, G. Perovskite Solar Cell Modeling Using Light- and Voltage-Modulated Techniques. *The Journal of Physical Chemistry C* **2019,** *123* (11), 6444-6449.

136. Salado, M.; Contreras-Bernal, L.; Caliò, L.; Todinova, A.; López-Santos, C.; Ahmad, S.; Borras, A.; Idígoras, J.; Anta, J. A. Impact of moisture on efficiency-determining electronic processes in perovskite solar cells. *Journal of Materials Chemistry A* **2017,** *5* (22), 10917-10927.

137. García-Fernández, A.; Moradi, Z.; Bermúdez-García, J. M.; Sánchez-Andújar, M.; Gimeno, V. A.; Castro-García, S.; Señarís-Rodríguez, M. A.; Mas-Marzá, E.; Garcia-Belmonte, G.; Fabregat-Santiago, F. Effect of Environmental Humidity on the Electrical Properties of Lead Halide Perovskites. *The Journal of Physical Chemistry C* **2019,** *123* (4), 2011-2018.

138. Mei, A.; Li, X.; Liu, L.; Ku, Z.; Liu, T.; Rong, Y.; Xu, M.; Hu, M.; Chen, J.; Yang, Y.; Grätzel, M.; Han, H. A hole-conductor–free, fully printable mesoscopic perovskite solar cell with high stability. *Science* **2014,** *345* (6194), 295-298.

139. Leijtens, T.; Giovenzana, T.; Habisreutinger, S. N.; Tinkham, J. S.; Noel, N. K.; Kamino, B. A.; Sadoughi, G.; Sellinger, A.; Snaith, H. J. Hydrophobic Organic Hole Transporters for Improved Moisture Resistance in Metal Halide Perovskite Solar Cells. *ACS Applied Materials & Interfaces* **2016,** *8* (9), 5981-5989.

140. Luo, J.; Xia, J.; Yang, H.; Chen, L.; Wan, Z.; Han, F.; Malik, H. A.; Zhu, X.; Jia, C. Toward high-efficiency, hysteresis-less, stable perovskite solar cells: unusual doping of a hole-transporting material using a fluorine-containing hydrophobic Lewis acid. *Energy & Environmental Science* **2018,** *11* (8), 2035-2045.

141. Koocher, N. Z.; Saldana-Greco, D.; Wang, F.; Liu, S.; Rappe, A. M. Polarization Dependence of Water Adsorption to CH3NH3PbI3 (001) Surfaces. *The Journal of Physical Chemistry Letters* **2015,** *6* (21), 4371-4378.

142. Grancini, G.; Roldán-Carmona, C.; Zimmermann, I.; Mosconi, E.; Lee, X.; Martineau, D.; Narbey, S.; Oswald, F.; De Angelis, F.; Graetzel, M.; Nazeeruddin, M. K. One-Year stable perovskite solar cells by 2D/3D interface engineering. *Nature Communications* **2017,** *8*, 15684.

143. Jiang, Q.; Zhao, Y.; Zhang, X.; Yang, X.; Chen, Y.; Chu, Z.; Ye, Q.; Li, X.; Yin, Z.; You, J. Surface passivation of perovskite film for efficient solar cells. *Nature Photonics* **2019**.

144. Agresti, A.; Pescetelli, S.; Cinà, L.; Konios, D.; Kakavelakis, G.; Kymakis, E.; Carlo, A. D. Efficiency and Stability Enhancement in Perovskite Solar Cells by Inserting Lithium-Neutralized Graphene Oxide as Electron Transporting Layer. *Advanced Functional Materials* **2016,** *26* (16), 2686-2694.

145. Tanenbaum, D. M.; Dam, H. F.; Rösch, R.; Jørgensen, M.; Hoppe, H.; Krebs, F. C. Edge sealing for low cost stability enhancement of roll-to-roll processed flexible polymer solar cell modules. *Solar Energy Materials and Solar Cells* **2012,** *97*, 157-163.

146. Fu, R.; Zhou, W.; Li, Q.; Zhao, Y.; Yu, D.; Zhao, Q. Stability Challenges for Perovskite Solar Cells. *ChemNanoMat* **2019,** *5* (3), 253-265.

147. Wang, R.; Mujahid, M.; Duan, Y.; Wang, Z.-K.; Xue, J.; Yang, Y. A Review of Perovskites Solar Cell Stability. *Advanced Functional Materials 0* (0), 1808843.

148. Idígoras, J.; Aparicio, F. J.; Contreras-Bernal, L.; Ramos-Terrón, S.; Alcaire, M.; Sánchez-Valencia, J. R.; Borras, A.; Barranco, Á.; Anta, J. A. Enhancing Moisture and Water Resistance in Perovskite Solar Cells by Encapsulation with Ultrathin Plasma Polymers. *ACS Applied Materials & Interfaces* **2018,** *10* (14), 11587-11594.

Chapter 2

Methods

2.1. Experimental Methods for PSCs Fabrication

In this section, the detailed steps for the fabrication of the perovskite solar cells based in iodide and bromide derivatives developed during the course of this thesis are exposed. It is divided in three subsections specifying the deposition technique of each device film: electron selective layer (ESL), perovskite material itself and hole selective layer (HSL), with a final description of the deposition of the top metal contact.

Materials

All materials were used as received: FTO glasses (25 × 25 mm, Pilkington TEC15, ~15 Ω sq−1 resistance), TiO_2 paste (Dyesol 30NRD, 300 nm average particle size), lithium bis (trifluoromethylsulfonyl) imide (Li-TFSI) from Sigma-Aldrich, CH_3NH_3I (MAI) and CH_3NH_3Br (MABr) (DYESOL/GreatcellSolar), PbI_2 and $PbBr_2$ from TCI, 99.99%, titanium diisopropoxide bis(acetylacetonate), 75% in isopropanol, from Sigma-Aldrich, and spiro-OMeTAD from Merck.

Regarding solvents materials: DMF, DMSO and GBL were purchased by Sigma-Aldrich. The antisolvents used in the crystallization process of $MAPbI_3$ and $MAPbBr_3$ were diethylether and toluene, respectively, both purchased by Sigma-Aldrich too. The properties and chemical structures of each one are summarized below.

Solvent	Molecular formula	Molecular structure	Polarity Index
Dimethylformamide (DMF)	C_3H_7NO	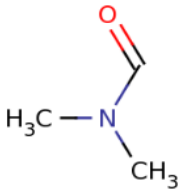	6.4
Dimethylsulfoxide (DMSO)	C_2H_6OS	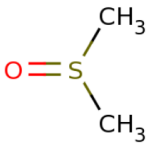	7.2
γ-butyrolactone (GBL)	C_4H6O_2	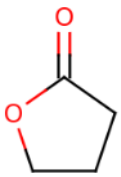	-
Diethylether	$C_4H_{10}O$	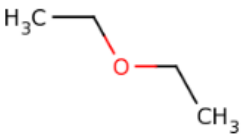	2.8

Toluene	C_7H_8	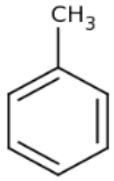	2.4

Figure 2.1. Solvents and antisolvents used in the synthesis of the perovskite materials. The molecular formula and polarity index are also shown.

2.1.1. Deposition of electron selective layer (ESL)

A titanium dioxide (TiO_2) compact layer, followed by a mesoporous layer of the same metal oxide, composed the ESL material. Prior to deposition, Fluorine-Tin-Oxide (FTO) substrates were treated and cleaned before used.

A partial etching onto the FTO with zinc powder and HCl (2 M) was done to provide a proper contact in the final solar device (Figx). A cleaner step of the substrate follows by ultra-sonication in 2% Hellmanex solution, rinsing with Milli-Q water. Additional short sonication with absolute ethanol (EtOH) during 5 minutes followed by sonication during another 15 minutes with isopropanol complete the cleaning step. A UV−O_3 treatment for 10 min was done prior to the deposition of the TiO_2 compact layer (c-TiO_2). C-TiO_2 was deposited by aerosol spray pyrolysis at 450 °C using a commercial titanium diisopropoxide bis(acetylacetonate) solution (75% in 2-propanol, Sigma-Aldrich) diluted in ethanol (1:9, v/v) as precursor, with oxygen as carrier gas. The spray was performed with a total volume of 5 mL (approx.) of the previous solution, made by 3 steps spraying of 6 s each one and waiting 30 s between steps. Mesoporous layer of TiO_2 was deposited by spin-coating at 2000 rpm for 10 s followed by 100ºC for 10 min. A 100 µl diluted paste in ethanol (1:5, weight ratio) of Dyesol 30-NRD was used. Devices were thermally treated in an oven under ambient atmosphere, using the following steps: 370ºC for 20 min with 40 min ramp time, 470ºC for 10 min with 5 min ramp time and 500ºC for 20 min.

(a) (b)

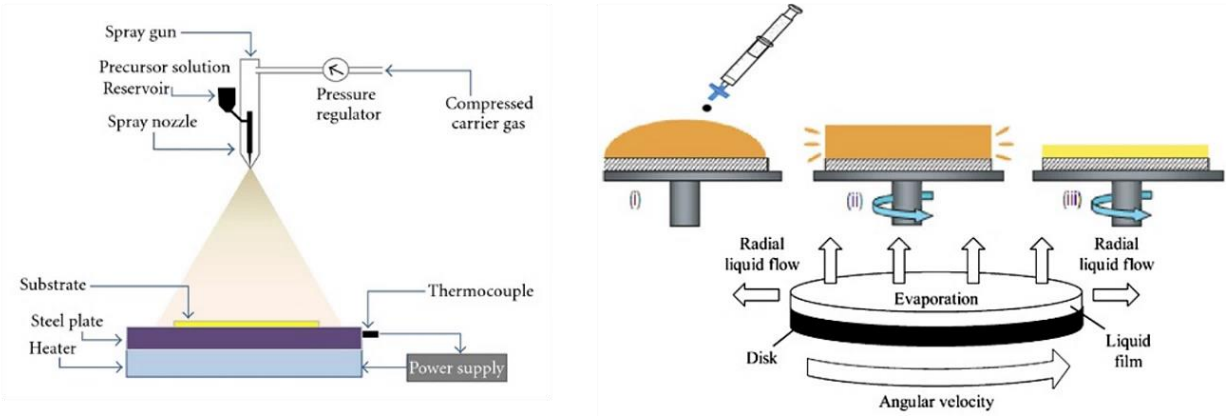

Figure 2.2. Deposition techniques for thin-film fabrication. (a) Spray pyrolysis method for c-TiO_2 layer. Copyright 2012, ISRN Nanotechnology (b) Spin coating method for m-TiO_2, Li-TFSI, Perovskite and Spiro-OMeTAD deposition. Copyright Institute of Applied Physics of Academy of Sciences of Moldova Chisinau.

2.1.2. Lithium treatment of c-TiO_2 layer

When required a lithium treatment before the deposition of perovskite films, 100 µl of a lithium bis (trifluoromethylsulfonyl) imide 35 mM solution in acetonitrile, was prepared and deposited on the top of the device by spin-coating at 3000 rpm (2000 ac) during 10 seconds, following by thermal treatment at 450ºC for 30 min.

2.1.3. Perovskite film crystallization

$MAPbI_3$

The perovskite precursor solution was prepared by mixing DMF solutions (50 wt%) containing MAI and PbI_2 (1 : 1 mol%) and MAI, PbI_2 and DMSO (1 : 1 : 1 mol%) and for different %RH the molar ratio of Pb : DMSO was modified from 0; 0.5; 0.75; 1; 1.25;1.5. The deposition was developed inside and outside a glove box using 1-step deposition method by spin coating technique with a step of 50 s at 4000 rpm, using diethylether (DETE) as antisolvent. The annealing temperature was 100ºC provided by a hot plate for thin films.

$MAPbBr_3$

$MAPbBr_3$ film was deposited, inside a glove box, using 1-step deposition method. 1.4 M $PbBr_2$ precursor solution was prepared in N,N-dimethylformamide (DMF) and dimethylsulphoxide (DMSO) without stirring at 80°C for 20 minutes until complete dissolve. After cool down at room temperature, this solution was mixed with MABr powder to obtain a final concentration of 1.4 M MABr. MAPbBr3 solution was 2 deposited by two ramps of spin coating method: 1000 rpm for 10 s and 4000 rpm for 40s, using toluene as anti-solvent during the second ramp. This was followed by annealing at 100°C for 3 min to obtain a shiny and homogenous film.

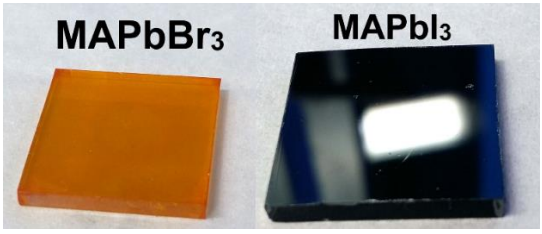

Figure 2.3. Films images of perovskite materials fabricated during the course of this thesis.

2.1.4. Deposition of Hole Selective Layer (HSL)

A solution of Spiro-OMeTAD as HTM, was prepared by dissolving 72.3 mg of (2,2′,7,7′-tetrakis(N,N′-di-pmethoxyphenylamine)-9,9′-spirobifluorene) in 1 mL of chlorobenzene, 28.8 µL of 4-tert-butylpyridine and 17.5 µL of a stock solution of 520 mg/mL of lithium bis- (trifluoromethylsulfonyl) imide in acetonitrile, as additives. Perovskite film was then covered with the HSL solution by dynamically spin coating at 4000 rpm, 800 rpm/s of acceleration for 30 s. Finally, 80 nm of gold was thermally evaporated on top of the device as a back contact, using a commercial Univex 250 chamber, from Oerlikon Leybold Vacuum. A real image of spiro-ometad layer is shown in Fig.2.4

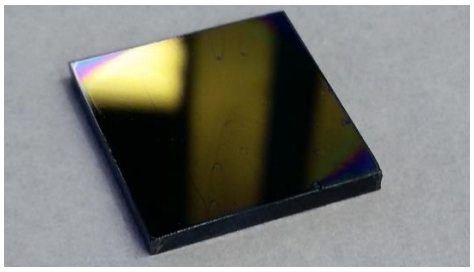

Figure 2.4. Spiro-OMeTAD film deposited onto the lead iodide perovskite material.

2.2. Optoelectronic Methods for Characterization

This section summarized the instrumental techniques used during the course of PhD thesis to characterize the synthetized materials and their optic/electronic properties to be used in solar cells.

2.2.1. Scanning Electron Microscopy (SEM)

SEM uses a focused beam of high-energy electrons to generate a variety of signals at the surface of solid specimens. The signals that derive from electron-sample interactions reveal information about the sample including external morphology (texture), chemical composition, and crystalline structure/orientation of materials making up the sample. The morphology of the different films composing the perovskite solar cells were analysed using a JEOL 7001F. SEM micrographs were further studied using the corresponding images. The equipment is equipped with an electron cannon of: 0.1-30kV, FEG and EDX detector of Si(Li) for elemental analysis.

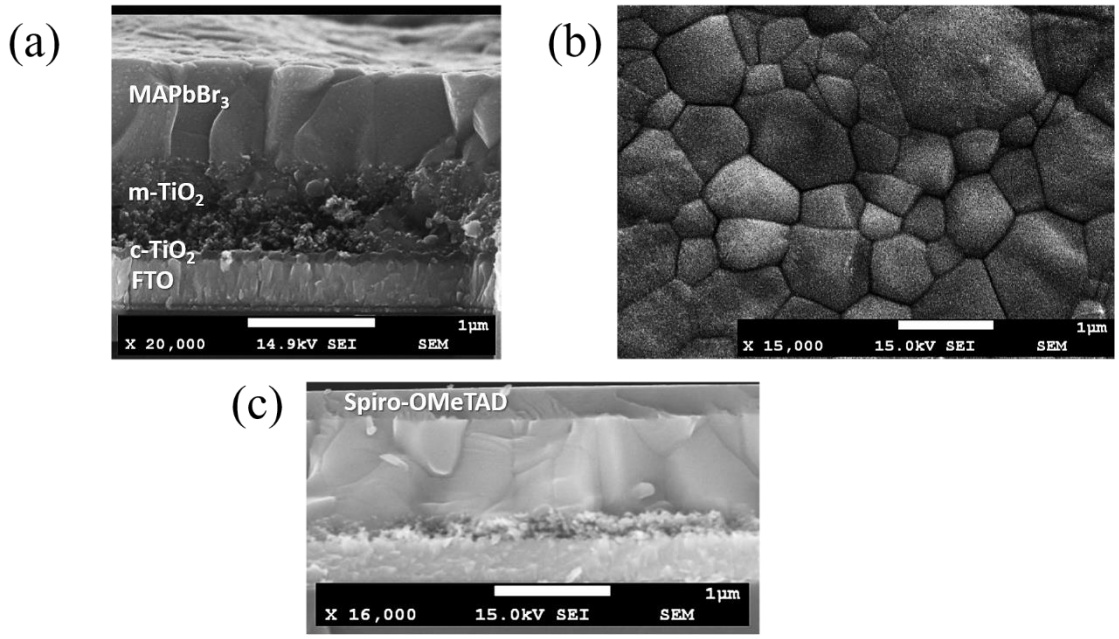

Figure 2.5. SEM images of lead bromide perovskite device. (a) Cross section without HSL on top. (b) Top view. (c) Cross section of complete device.

2.2.2. Ultraviolet-visible (UV) Absorbance Spectroscopy

This technique refers to absorption spectroscopy or reflectance spectroscopy in the ultraviolet-visible spectral region. It uses light in the visible and adjacent (near-UV and near-infrared [NIR]) ranges. The absorption or reflectance in the visible range directly affects the perceived colour of the chemicals involved, in our case, that technique brings

us information about the composition of perovskite film. The measurements were recorded by a Cary 500 Scan VARIAN spectrophotometer in the 250-800 nm wavelength range.

2.2.3. XRD diffraction

This technique relies on the dual wave/particle nature of X-rays to obtain information about the structure of crystalline materials. A primary use of the technique is the identification and characterization of compounds based on their diffraction pattern. We use this method in order to know about the crystallinity of the sample. The XRD pattern of the prepared solids were measured using X-ray diffractometer (D8 Advance, Bruker-AXS) (Cu Kα, wavelength λ=1.5406 Å).

2.2.4. Photoluminescence (PL)

To further analyse the effect of lithium doping in both selective contacts, quenching experiments of the steady state photoluminescence (PL) were carried out. The perovskite material was photo excited and the emission spectra was recorded. Photoluminescence measurements were collected by a Horiba Fluorolog 3-11, using 380 nm of excitation source and also 405 nm. Excitation measurements where carried out using the same setup in excitation mode, monitoring at 670 nm. Photoluminiscence images of our bromide films are shown in Fig.2.6.

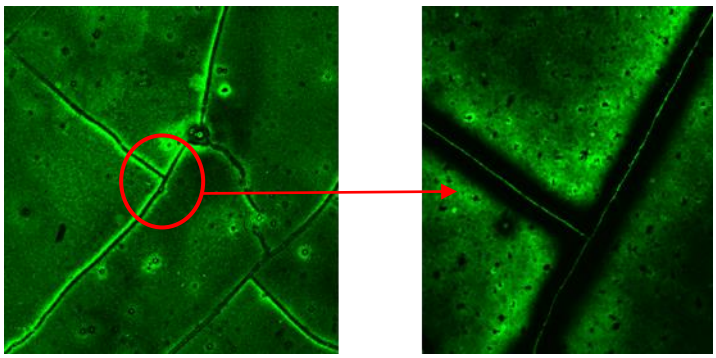

Figure 2.6. Confocal microscopy images of PL emission enhanced in the grain boundaries of $MAPbBr_3$ films.

2.2.5. Photovoltaic measures

Current density-voltage j-V curves were performed using an Abett Solar simulator equipped with 1.5 AM filter was used. The light intensity was adjusted to 100 $mWcm^{-2}$ using a calibrated Si solar cell. Devices were measured using a mask to define an active area of 0.11 cm^2 . *j-V* curves were measured in reverse and forward bias at a scan rate of 50 mVs^{-1}. Chronopotentiometry measurement were obtained using an Autolab potentiostat for 2000 seconds under 1 sun in order to studied the evolution and increasing of the V_{oc} during time under illumination.

2.2.6. Electroluminescence (EL)

Electroluminescence properties of the $MAPbBr_3$ devices were measured in a DV420A-OE CCD camera, by applying a bias voltage of 1.4 V for 20 s with a Gamry 600 potentiostat. The generated current, due to a direct injection of carriers through the external contacts of the solar device, was registered by achieving chronoamperometric profile. Electroluminiscence images of bromide cells are shown in Fig.2.7.

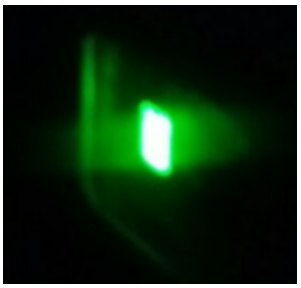

Figure 2.7. Electroluminiscence of one of our $MAPbBr_3$ solar cells by applying a bias voltage of 1.4 V.

2.3. Small Perturbation Techniques

In this subsection one of the main techniques applied during this thesis is fully described due to its relevance upon the PSC electronic characterization. The further understanding provided by this measurement in any condition, has pushed forward the field, contributing to major advances in the race to commercialization horizon.

2.3.1. Impedance Spectroscopy (IS)

Impedance spectroscopy is catalogued as a small perturbation technique because the sample of interest is perturbed but not irreversible modified during the measure, in the most of the cases. It is used to characterize energy conversion materials, as electrochemical systems and solid-state devices, usually as a function of light intensity, applied voltage, or environmental stress.[1,2]

In this technique, the response of the sample to an electrical field is monitored as a function of determined frequency ranges ω, generally between 1 MHz (microseconds) to 10 mHz (seconds) and information about energy storage, dissipation energy and relaxation processes into the system could be obtained. The amplitude of the perturbation or input signal is an AC voltage applied around a given steady-state and usually is not larger than 20 mV for perovskite solar cells.[3] The output signal is the modulated current response and the relation between the ac voltage and the output current forms the complex impedance, $Z(\Omega cm^2)$, in the frequency domain.[138] The physical meaning of impedance is the complex resistance of the sample (time-varying or frequency-dependent), defined as follows:

$$Z(\omega) = \tilde{V}(\omega)/\tilde{J}(\omega) \quad (1)$$

where the modulated voltage is defined as:

$$\tilde{V}(\omega) = V_0 e^{i\omega t} \quad (2)$$

being V_0 the amplitude of the wave, and the modulated output current as:

$$\tilde{J}(\omega) = (dj(\bar{V})/dV)\tilde{V} \quad (3)$$

where $\bar{V}$ is the corresponding steady-state voltage.[4]

The IS spectra is characterized for a Z-plane in which the real part of Z (Z') is plotted versus imaginary part of Z (Z'') over the frequencies range. To analyse the IS data, the two most common approaches are the modelling of an equivalent circuit (EC), based in the solar cell diode behaviour and the capacitive-frequency modelling. The electrical elements constituting the EC should reflect the physical mechanisms occurring in the solar

cells as carrier diffusion, recombination or charge accumulation at their corresponding time-scales. In fact, the time constants of the different physical processes can be extracted from impedance spectra. Attending to the maximum frequency of the imaginary part of the impedance plot (Z´´) (black dot of Fig.2.1), which corresponds to the inverse of the product of recombination resistance and capacitance, information about the physic mechanisms and parameters in the solar cell can be successfully achieve.[5-6]

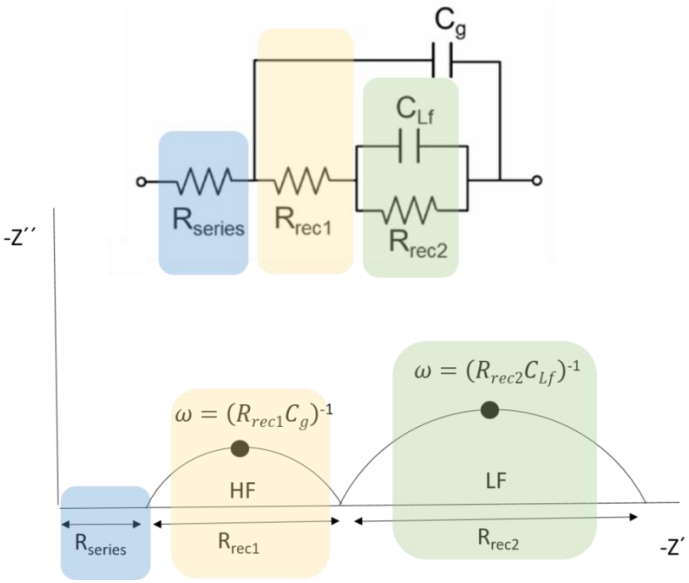

Figure 2.8. Perovskite solar cell electrical model corresponding to high frequency and low frequency regions showing series resistance, recombination resistance related with geometrical or bulk capacitance and recombination resistance related with the LF capacitance. The Z plot shows the two characteristic arcs typically observed in good PSCs.

In the EC, R_2 and C_{Lf} represent the resistance and capacitive response at low frequency regions (LF), which was already correlated with processes at the interfaces between contacts layers and perovskite material. The bulk capacitance, also called geometrical capacitance, $C_{bulk\ /g}$, connected with the dielectric properties of the perovskite, as well as the associated recombination resistance R_{rec}, are responses obtained at the high-frequency region

Regarding the capacitive-frequency modelling, three different capacitive responses are correlated with the high, intermediated and low frequency regions, C_{HF}, C_{IF}, C_{LF}; respectively.[3] The high frequency response has been already correlated with perovskite dielectric processes and series resistance contributions, while the low-frequency response is attributed to interfacial processes. (Fig.2.9)

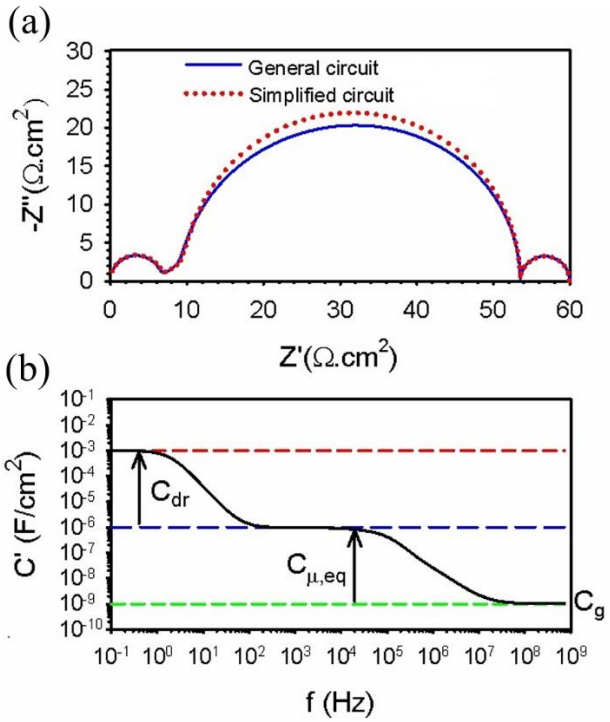

Figure 2.9. (a) Ideal impedance plot with the three differentiated regions of frequency, HF, IF and LF. (b) Capacitive-frequency plot showing the three plateaus corresponding to the geometrical capacitance, chemical capacitance and the low frequency region for interfacial processes. Reproduced with permission of Ref.3 Copyright 2014 American Chemical Society.

Mott-Schottky analysis

Another useful analysis that could be extracted from the capacitive responses are the one resulting from plotting capacitance versus voltage. This measurement is known as the Mott-Schottky analysis and consist in a voltage-modulation of the depletion layer width (w), corresponding to a Schottky barrier at the cathode. The depletion zone decreases at positive bias, increasing the capacitance response. By plotting $C^{-2}(V)$, a straight line is observed, which slope determines the p-doping density of electrical defects of an absorber material and the intercept with the x-axis provides information of flat-band potential V_{fb}. This applied voltage is the one necessary to produce flat bands in the semiconductor, depending on the energy equilibration at the contacts.[7]

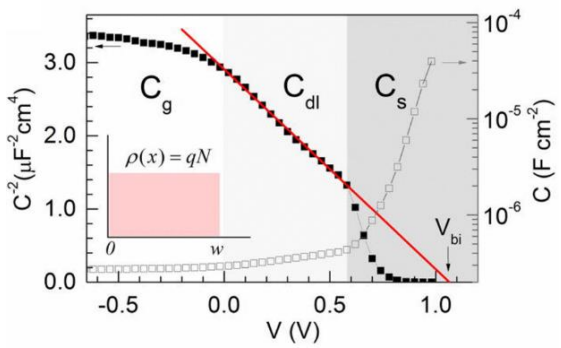

Figure 2.10. Typical Mott Schottky plot showing the three different capacitance extracted and the straight line intercepting in the flat-band potential parameter. Reproduced with permission of Ref.7. Copyright 2016, American Institute of Physics.

2.4. References

1. Bisquert, J.; Fabregat-Santiago, F. Impedance Spectroscopy: A general Introduction and Application to Dye-Sensitized Solar Cells. In *Dye-sensitized solar cells.*, Kalyanasundaram, K., Ed. CRC Press: Boca Raton, 2010.

2. Bisquert, J.; Bertoluzzi, L.; Mora-Sero, I.; Garcia-Belmonte, G. Theory of Impedance and Capacitance Spectroscopy of Solar Cells with Dielectric Relaxation, Drift-Diffusion Transport, and Recombination. *The Journal of Physical Chemistry C* **2014,** *118* (33), 18983-18991.

3. Bisquert, J.; Garcia-Belmonte, G.; Guerrero, A. Impedance Characteristics of Hybrid Organometal Halide Perovskite Solar Cells. In *Organic-Inorganic Halide Perovskite Photovoltaics: From Fundamentals to Device Architectures*, Park, N.-G.; Grätzel, M.; Miyasaka, T., Eds. Springer International Publishing: Cham, 2016; pp 163-199.

4. Garcia-Belmonte, G.; Guerrero, A.; Bisquert, J. Elucidating Operating Modes of Bulk-Heterojunction Solar Cells from Impedance Spectroscopy Analysis. *J. Phys. Chem. Lett.* **2013,** *4*, 877−886.

5. Pockett, A.; Eperon, G. E.; Peltola, T.; Snaith, H. J.; Walker, A. B.; Peter, L. M.; Cameron, P. J. Characterization of Planar Lead Halide Perovskite Solar Cells by Impedance Spectroscopy, Open Circuit Photovoltage Decay and Intensity-Modulated Photovoltage/Photocurrent Spectroscopy. *The Journal of Physical Chemistry C* **2015,** *119*, 3456–3465.

6. Almora, O.; Zarazua, I.; Mas-Marza, E.; Mora-Sero, I.; Bisquert, J.; Garcia-Belmonte, G. Capacitive Dark Currents, Hysteresis, and Electrode Polarization in Lead Halide Perovskite Solar Cells. *The Journal of Physical Chemistry Letters* **2015,** *6* (9), 1645-1652.

7. Almora, O.; Aranda, C.; Mas-Marzá, E.; Garcia-Belmonte, G. On Mott-Schottky analysis interpretation of capacitance measurements in organometal perovskite solar cells. *Applied Physics Letters* **2016,** *109* (17), 173903.

Chapter 3

Critical Overview

3.1. Problems Statements and Goals

Energetic requirements and the necessity to stop the global warming is one of the major challenges of the humanity. Solar energy has been revealed as the main promising renewable energy source, being the thermosolar and photovoltaic technologies the ones on the cusp. Photovoltaic technologies based in Silicon solar cells still capturing more than 90% of the market share. However, perovskite solar cells (PSCs) are beginning to have a major influence in the PV field, having acquired a tremendous impact combining high efficiency and low fabrication cost. The extraordinary properties of the material such as high absorption coefficient, suitable bandgap, high charge carriers mobility or diffusion lengths, have driven to an impressive enhancement in the power conversion efficiency (PCE) upon 24% in just ten years of research. The enormous potential of this technology motivates the scientific community to develop new strategies to understand in depth the scope of the possibilities in terms of basic and applied science.

Despite the important advances in the knowledge about the operation mechanisms of PSCs and the chemistry that governs their structure, some problems still need to be solved to close the gap with the theoretical maximum PCE, balancing the production costs and providing scalable conditions of fabrication with long-term stability of the devices. One of the main features still blocking the commercialization purposes is the intrinsic instability of the perovskite material against real atmospheric conditions. The hygroscopic nature of the organic part in the perovskite structure makes the exposure to ambient moisture the responsible of a substantial detriment of the perovskite properties during the solar cell operation, with the consequent diminution in the photovoltaic performance of the complete solar device. In fact, the effects of water into the perovskite devices have been described with controversy. Some authors catalogue water as a beneficial parameter during the perovskite crystallization, whereas the highest efficiencies have been reported under inert atmosphere. On the other hand, this instable photovoltaic performance is mostly evident in the appearance of the hysteretic behaviour during current-voltage *(j-V)* curves, frequently observed in PSCs, regardless of the type of device architecture. The close relationship between this behaviour with the dual nature of the carriers, electronic and ionic, makes mandatory a depth analysis of the interfacial mechanisms between the perovskite absorber and the external selective contacts, responsible of the electrical field generated by the difference among their workfunctions. The ions drift and charge collection/accumulation dynamics at the interfaces have a major impact in the photovoltage, which is one of the main photovoltaic parameters that needs improvement in the current race for the maximum PCE achievement in some perovskite formulations. In fact, for $MAPbBr_3$ there is a loss-in-potential dominated by undesired recombination mechanisms that still representing 0.4 eV loss from the theoretical value in the radiative limit. Therefore, the successful commercialization horizon could be closer if the stability issues against moisture and the photovoltage losses are solved.

This thesis addresses both challenges through bulk and interfacial engineering. The deep understanding of the effects induced by moisture exposure in perovskite materials

in first place. Secondly, a deep investigation about interfacial recombination processes through different and complementary techniques such as IS, EL and PL. For these purposes, two representative perovskite materials: $MAPbI_3$ and $MAPbBr_3$ have been optimized. For final devices, the fabrication processes to obtain high efficiency devices include the use of titanium dioxide and Spiro-OMeTAD as external selective contacts.

To facilitate the analysis of the moisture exposure effects, the most studied perovskite formulation was selected, $MAPbI_3$ in the regular n-i-p configuration. Alternatively, for photovoltage losses studies the wider band gap $MAPbBr_3$ material was selected in the same n-i-p architecture. Its band gap of 2.3 eV can theoretically provide greater open-circuit potentials (V_{oc}) and have a great potential to be used in tandem cells, light-emitting diodes (LED) and in electrochemical reactions, which increase the interest to enhance these bromide-based solar devices and its optoelectronics properties.

The followings strategies have been followed to accomplish the goals of this thesis:

- Investigate how the solvent coordination chemistry of the precursor solution affects the crystallinity of the most widely studied perovskite structure $MAPbI_3$.
- Analysis of interfacial effects of ambient factors exposure in $MAPbI_3$ devices.
- Balance the H_2O/DMSO content in the precursor solution for $MAPbI_3$ synthesis to use moisture as an ally during fabrication process.
- Study of recombination mechanisms in $MAPbBr_3$ by Impedance Spectroscopy (IS), Electroluminiscence (EL) and Photoluminiscence (PL) analysis in a wide band gap perovskite material.

These strategies have led to two important contributions in the perovskite photovoltaic field:

- ✓ Establishing a universal method for fabrication of $MAPbI_3$ PSCs under different %RH conditions with PCE approaching 19% clarifying the role of moisture exposure during crystallization process and its implications in the photovoltaic performance. The method provides an easy and scalable way to generate devices in different research labs or weather conditions and has been adopted by other research groups. Similarly, for bromide-based materials, a high quality $MAPbBr_3$ film has been developed achieving an extremely smooth and homogenous morphology, enhancing the optoelectronic properties of this material.
- ✓ Reducing recombination processes related with photovoltage losses. By interfacial engineering methods involving extrinsic ions, it is possible to minimize the surface recombination pathways. Lithium cation has been used to modify the ESL/perovskite interface leading to an enhanced open-circuit voltage up to a record value for an optimized $MAPbBr_3$ material.

Both achievements have implied the improvement of regular n-i-p perovskite architectures, enhancing the crystal quality of the absorber materials. Operation mechanisms during working conditions has been investigated by a wide range of instrumental techniques to characterize the optimized PSCs. All of the methods developed during the course of this thesis are fully described in Chapter 2.

3.2. Coordination Chemistry in the Perovskite Structure

The most facile technique to fabricate high quality perovskite thin films involves a single-step deposition method of the perovskite precursors from solution. Initially, a precursor solution was prepared with inorganic PbX_2 and organic RNH_3X reagents in polar solvents such as dimethylformamide (DMF), dimethyl sulfoxide (DMSO), γ-butyrolactone (GBL) or in a mixture of these solvents. The deposition method takes place by spin-coating technique where the speed and solution amount casted onto a conducting electrode surface govern the thickness and the quality of the film. The final annealing at low temperature (100ºC), leads to the precursor components to self-assemble into the final perovskite phase with the general ABX_3 stoichiometry. Here, A represent the organic cation, such as methylammonium ($CH_3NH_3^+$, MA^+) or formamidinium (FA^+), B the divalent metal, such as Pb^{2+} or Sn^{2+} and X the halogen that could be chlorine (Cl^-), bromine (Br^-), or iodine (I^-).

As a post-transition metal with an s^2 electronic configuration, Pb^{2+} form kinetically labile multiplied halogenated complexes, known as "plumbates". These halo-complexes undergo ligand (halogen)-metal charge transfer reactions (LMCT) where the metal-centre ion can be reduced at the same time that the oxidation of the ligand occurs.[1,2] Due to the soft Lewis-acid character of Pb^{2+} and the different Lewis-basic behaviour of the halogens, the energy of the charge-transfer transitions will be different depending on the halogen implied. In the case of iodide, a large LMCT contribution has been shown and PbI_2 is able to form high coordinated species (PbI_n^{2-n}, where n: 2-6) distinguishable by absorbance spectroscopy.[3] When the concentration of I^- increases due to the addition of the second precursor MAI, two bands corresponding to PbI_3^- and PbI_4^{2-} compounds appears (Fig.3.1), revealing a two separate complexation equilibrium (inset of Fig.3.1).

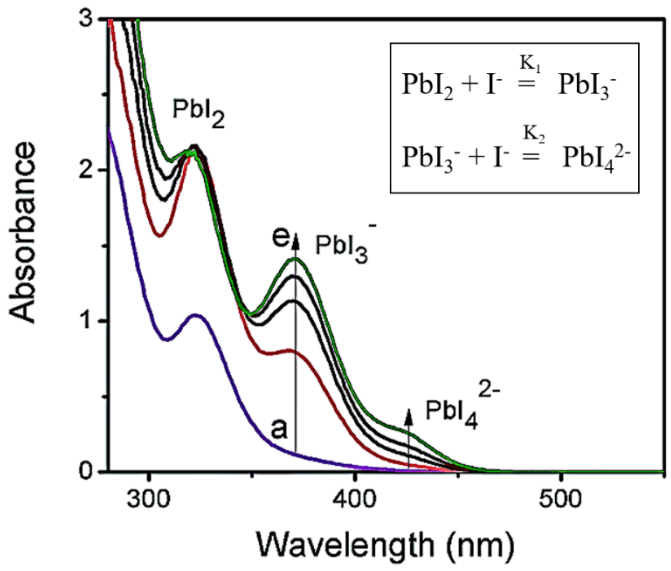

Figure 3.1. Absorption spectra of PbI_2 solution in dimethylformamide with increasing concentration of MAI. Adapted with permission of Ref.3 Copyright 2015, The Royal Society of Chemistry.

These plumbates species serve as precursors in the preliminary solution and the specific lead iodide complexes depend on the Pb: I ratio as well as on the polar character of the solvents used. As mentioned before, DMF and DMSO were two common solvents widely employed in the preparation of the perovskite material. Due to their high donor

number (D_N), they can donate a pair of electrons to form a Lewis adduct with Pb^{2+}, determining the quality of the perovskite crystal as the solvent ligands are replaced by I^- and finally removed during the annealing process. The cationic nature of methyl ammonium ($CH_3NH_3^+$) leads to assemble with the complex to form the film [PbI_n^{2-n} $(CH_3NH_3)^+$], organizing the perovskite structure in the characteristic octahedral orientation with six iodine atoms coordinating the Pb^{2+} , locating the organic cation in their interstitial sites (Fig.3.2)

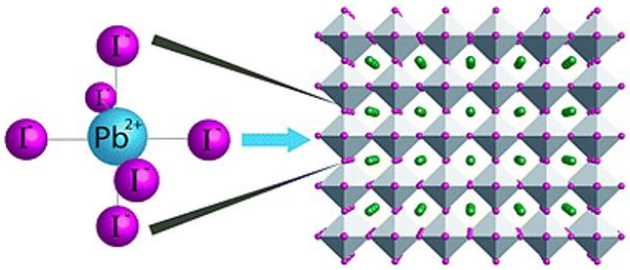

Figure 3.2. Scheme of the octahedral orientation of lead atom with six iodine ligands coordinating the sphere and the crystalline lattice. Reproduced with permission of Ref.3. Copyright 2015, Royal Society of Chemistry.

Higher quality films could be casted by the antisolvent method, facilitating the crystallization process by removing one of the solvent precursors. However, the role of the coordination ability of solvents was not really established in the literature.

As a first step clarifying the chemistry involving that coordination, the formation of polyplumbates by modification of solvents concentration, has been studied in depth during the course of this thesis. A molecular exchange takes place then between the solvents and iodide ions, stablishing the importance to be cognizant of all the various interactions that can occur between these different components and revealing the selection of solvents as a key role to improve the crystallinity of the perovskite phase to push forward the PCE of these devices. During the molecular exchange, an expanded equilibrium than the showed in the inset of Fig.3.1 dominates the complex species present in the solution, where *Solv* represents one of the mentioned solvent habitually used (Fig.3.3).

$$[Pb\ (Solv)_6]^{2+} + nI^- \rightleftharpoons [Pb\ (Solv)_{6-n}I_n]^{(2-n)} + nSolv$$

Figure 3.3. Coordinative equilibrium between solvent molecules and iodine leading to a multiiodide plumbates species.

Through absorbance spectroscopy, the coordination capability of each solvent can be analysed recording the multiiodide plumbates species formed in solution.[4]

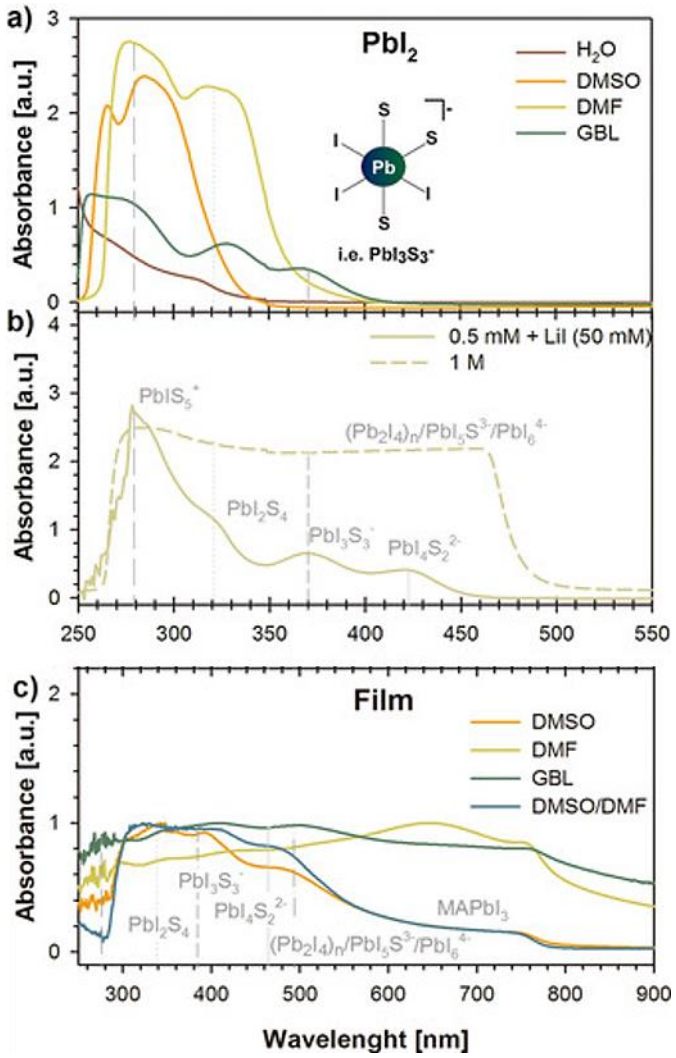

Figure 3.4. Absorption spectra of solutions containing PbI_2 (a) in a range of different solvents at a concentration of 0.5 mm and (b) at two different concentrations in DMF. The dashed line contains 100 eq. of LiI to increase the I^- concentration in the solution. Each plumbate ion is marked with a vertical line defined by their λ_{max}. (c) $MAPbI_3$ films on FTO prepared from different solvents. The signal has been normalized to the maximum value. Each plumbate ion is marked with a vertical line defined by their λ_{max}. Reproduced with permission of Ref.4. Copyright 2016, Wiley-VCH Verlag GmbH&Co.

As it is shown in Fig 3.4. when a diluted solution of PbI_2 (0.5mM) is prepared in GBL, all three species $[Pb(Solv)_5I]^+$, $[Pb(Solv)_4I_2]$ and $[Pb(Solv)_3I_3]^-$ are observed with low intensities. When the solvent used is DMF, the multiiodide plumbates formed are $[Pb(Solv)_4I_2]$ and $[Pb(Solv)_3I_3]^-$. Contrary, in DMSO solution, a higher concentration of $[Pb(Solv)_4I_2]$ is observed and just some formation of $[Pb(Solv)_3I_3]^-$ is detectable. Interestingly, when water is also tested as solvent, due to its important role during perovskite crystallization process, the absorption measurements show how H_2O rapidly coordinates Pb^{2+} to produce major concentration of $[Pb(Solv)_5I]^+$ and lower of the $[Pb(Solv)_4I_2]$ complex. These results allows stablishing a trend of coordinative affinity of the used solvents to form multiiodide-plumbates:

$$H_2O > DMSO > DMF > GBL$$

where water represents the most coordinative solvent and GBL the least.

The presence of multiplumbate ions was investigated in thin film perovskite material as a function of the solvent used during the processing to better understand the chemical and structural defects that may have an impact in photovoltaic devices. As mentioned in previous paragraphs, the final structure of a perovskite material is based on a tetragonal unit cell made of interconnected PbX_6 octahedra. For this reason, the presence of the PbI_6^{4-} complex become a requirement to favour the formation of the perovskite absorber. The analysis of the absorption spectra of films prepared with different coordinative solvents precursors, after annealing at 100ºC, revealed the presence of iodide plumbates with various degrees of coordination showing different bands intensities depending on the solvent used (Fig.3.4c). The presence of these multi-coordinate complexes in the final film dictates the type of chemical defects that impact directly on the photovoltaic performance of the solar cell due to the poor crystallinity achieve. Therefore, to favour the formation of the six-ligand coordinate lead complex and consequently, a high crystallinity of perovskite film, is necessary to balance with the coordinative capability of the solvents with the Pb:I ratio. Of course, other parameters such as temperature and deposition method are important and the antisolvent method proved to be efficient to remove the excess of coordinative solvents.

At the end of this work, it was clear that in order to prepare photovoltaic devices in ambient conditions the coordination capability between H_2O and DMSO must be controlled as it was later proved in the next achievement obtained during the development of this Thesis.

3.3. Balanced Perovskite Formulation for High PCE PSCs under Moisture Conditions.

As detail explained in section 1.2.5, the hybrid organic-inorganic nature of the perovskite structure implies an intrinsic instability of this material under light, oxygen and moisture, inducing degradation mechanisms that interferes in the photovoltaic performance of the cells. This instability represents one of the major challenges of perovskite technology, being water the main culprit of the degradation processes and the focus to develop advanced formulations and ingenious fabrication techniques to avoid its detrimental effects. These techniques were habitually designed to avoid the insertion of water molecules into the perovskite material and consequently, the displacement to the right of the Eq.1 (section 1.2.5.2.2). An enhanced photocurrent, photoluminiscence and photovoltage could appears as consequence of the first hydration stages, but the control of the equilibrium in this monohydrated phase result extremely challenging. However, the large-scale horizon makes mandatory the development of a robust method of fabrication under real room conditions keeping the low costs requirements to commercialization purposes, motivating the next research carried out in this thesis.

The knowledge acquired about the coordination capabilities of different solvents and, in particular, water and DMSO laid the groundwork to develop the method described below. During this phase of the PhD thesis, water was used as an ally to avoid the bad consequences of atmospheric exposure of perovskite material during its fabrication. Solar cells based in $MAPbI_3$ material were prepared under different % RH conditions comparing the photovoltaic response of each one. The competence between water and DMSO to coordinate lead atom and to generate the PbI_2:MAI:solvent complex was demonstrated. By SEM analysis and UV-absorbance experiments, was determined the influence on the crystal quality of the films. The investigation focus on the effect of moisture as a function of the DMSO:Pb ratio and %RH using a one-step antisolvent deposition method at room conditions, approaching a successfully 19% of PCE.[5] A clear

correlation between imbalanced ratio and morphological and chemical defects was demonstrated here. We showed that a low proportion of DMSO leads to a fiber-like morphology typical from materials fabricated from pure DMF.[6] Similarly, a large proportion of pinholes with cylindrical shape appears when the ratio of DMSO exceeds from the optimal one.

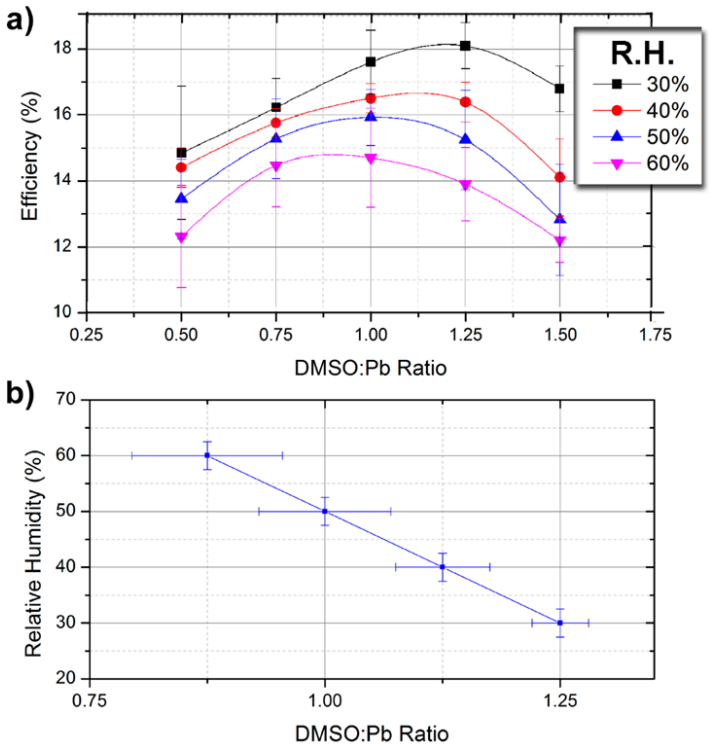

Figure 3.5. (a) Efficiency of devices fabricated under different %RH as function of the DMSO:Pb ratio used in the precursor solution. Each data point corresponds to 20 independent devices. (b) Observed maximum efficiency as a function of relative humidity and DMSO:Pb ratio, showing the linear relation between the two features. Reproduced with permission of Ref.5. Copyright 2017, The Royal Society of Chemistry.

In Fig.3.5a and 3.5b, it is clearly shown that the PCE could be controlled with this solvent engineering, balancing the DMSO:Pb ratio respect to the %RH. Up to aproximately 50% of RH, it is possible to achieve high efficiencies. However, when the moisture increases, it is most difficult to obtain good results. This is in complete agreement with formation of the di-hydrated phase $(CH_3NH_3)_4PbI_6{\cdot}2H_2O$ that governs the hydration equilibrium at humidities higher than 50% already reported in literature and explained in section 1.5.2. Then, at higher humidities, as in tropical countries in which labs the %RH is not lower than 60%, the necesity to fabricate the perovskite devices inside the glovebox or under dry atmosphere, becomes mandatory.

A formation criteria of perovskite films under atmospheric conditions optimized stoichiometry of the $PbI_2:MAI:DMSO$ adduct complex from the DMF solvent. In this solution process, an *antisolvent* was required to wash out the carrier solvent during spin coating whilst not dissolving the perovskite layer and a final thermal treatment is needed to adequate evaporation of the weakly bound polar additive, DMSO. Similar to DMSO, water is highly coordinative, The impact of this work becomes clear taken into account the number of cites until date of the corresponding publication and the fact that different

laboratories have been able to use the knowledge here reported to develop their own high efficiency PSCs, providing as well important contribution to the field.[7,8]

3.4. Kinetic Effects of Ambient Factors Exposure in PSCs.

Once the effects of water in the perovskite material itself were fully analysed and a robust method to obtain high PCE under any moisture conditions was established, the electrical characterization of complete device during light exposure was developed to further understand the interfacial mechanisms involving ion migration.[9]

A different device configuration has been investigated following an inverted planar architecture (p-i-n) based in ITO/PEDOT:PSS/$MAPbI_3$/PCBM/Metal.[10] Devices were electrically characterized using impedance spectroscopy measurements (IS) before and after degradation by biasing the device under light conditions. Different metals were used as top contact in order to understand if degradation can be avoided to some extend. Current density-voltage curves were measured using Ca, Al, Ag and Au as metal contacts. In order to avoid chemical reactivity between perovskite material and metal film their interface was covered by a thin layer of Cr_2O_3 deposited.[11] The continuous illumination brings in all of the samples without distinction, a typical S-shape in the *j-V* curve. Only in the sample covered with Cr_2O_3 the damage in the photovoltaic performance is not coupled with an S-shape curve. The detriment in the performance of the solar cell behaviour, especially in the current density values, is typically connected with degradation of the contacts.[12]

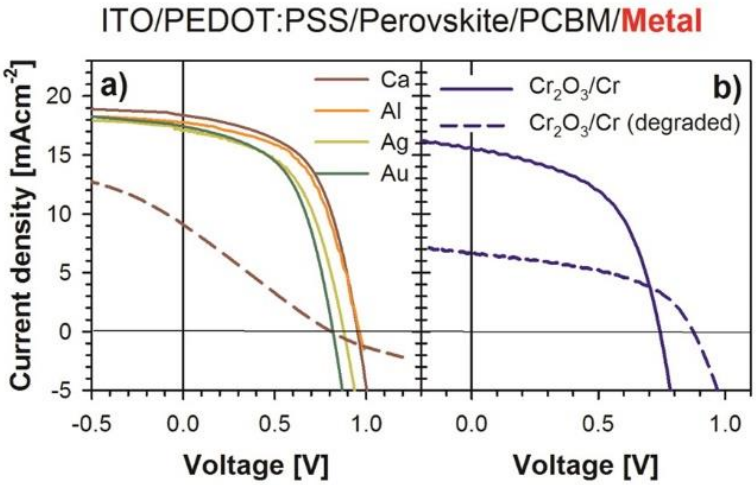

Figure 3.6. Current density–voltage curves of devices fabricated with different metal contacts measured at 1 sun light illumination. (a) Metals providing S-shape curves after degradation. (b) Contact containing Cr_2O_2/Cr does not show an S shape after degradation. Degraded devices are shown as broken lines. Adapted from Ref.10, Copyright 2016, American Chemical Society.

Scanning electron microscopy was performed to determine the cause of S-shape in the case of the top metals contact and the one protected with Cr_2O_3. The secondary electrons image revealed heavy metals (brighter zones) between perovskite and gold, coupled with delamination, while in the case of Cr_2O_3, the interface still appear quite smooth.

To fully analyse these effects, capacitance-voltage measurements through impedance spectroscopy technique, that is a *Mott-Schottky* analysis, were performed.

As previously reported and explained in the section 2.3.1. of this text, the capacitance spectrum of perovskite devices presents three areas that have been connected with different processes. The low frequency capacitance (LF) shows giant values caused by electrode polarization phenomena C_s, associated with ionic accumulation mechanisms.[13] The high frequency (HF) capacitance is affected by the series resistances, R_s, reducing the capacitive response. At intermediate frequencies (IF), a quite constant capacitance performs, governed by the polarizability of the absorber material, growing up the geometrical capacitance per unit area C_g at zero and negative bias.[14] This intermediate section could hold additional contributions related with the depletion layer capacitance C_{dl}, providing information regarding the doping densities of the absorber material, as reported previously through Mott Schottky analysis (see Methods).[15]

In the case of reactive metals (Ca, Ag, Al, Au), no modifications in doping densities are observed, while a shift in the V_{fb} is evident when comparing fresh and degraded devices. In the case of Cr_2O_3/Cr protecting layer, the doping density increases substantially when the sample is degraded, as well as a remarkable increased flat-band potential. The increasing in doping density has an effect on the energy equilibration at the cathode contact, provoking the growing of the flat-band potential. This equilibration process has a potential drop associated with two contributions: the V_{fb} in the bulk of the semiconductor, and the voltage drop at the interfacial region, producing a dipole layer (Δ/q), where Δ is the step of the vacuum level. The flat-band potential is defined as follows:

$$qV_{fb} = E_F - \Phi_c - \Delta \quad (1)$$

where E_F is the Fermi level of the active layer and Φ_c is the difference between the work functions of the contacts. In fresh devices with good solar cell performance, this dipole is relatively small. However, in the case of degraded samples, a large dipole is formed at the cathode/perovskite interface. Under illumination, the magnitude of the dipole is much larger due to the accumulation of photogenerated carriers at that interface.[16] In Fig.3.7. is represented the evolution of energy levels from fresh non-contacted, fresh contacted under dark to degraded devices under light.

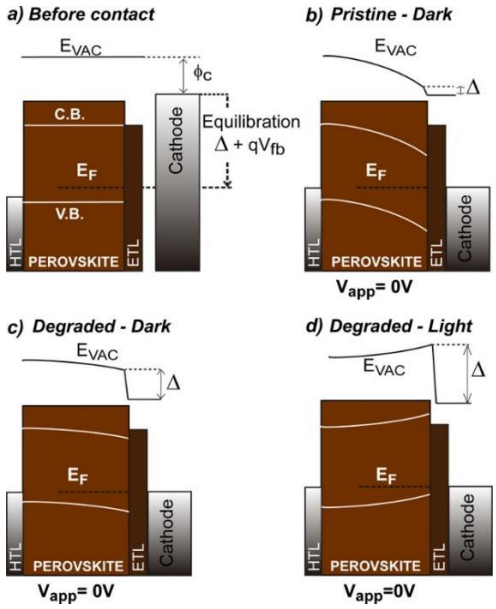

Figure 3.7. Diagram of energy levels for devices showing an S-shape *j–V* curve (a) before contact equilibration, (b) after contact equilibration for a fresh device under dark

conditions, (c) after contact equilibration for a degraded device under dark, and (d) under illumination conditions. Reproduced with permission of Ref.10. Copyright 2016, American Chemical Society.

The interfacial dipole produced in degraded devices, reduces the measured V_{fb}, provoking a reversed band in the electrical profile of the perovskite bulk. This effect blocks an efficient extraction of electrons, provoking the S-shape *j-V* curve. The magnitude of the dipole is magnified by accumulation of photogenerated carriers at the perovskite/cathode interface.

These results brings evidences of the degradation mechanisms occurring at the interfacial regions of the solar cell beyond the modifications of the perovskite material. The interfacial dynamics acquire then major attention in the race of enhanced stability and future PSCs commercialization. With this work, we established the importance of the interface between the perovskite and external interfaces and its connections with the *j-V* characteristics. We highlighted that the chemical reactivity of the contacts with migrating ions controls the *j-V* response. This was one of the first contributions in the field to highlight the relevance of migrating ions and its connection with the chemical reactivity with the contacts.

3.5. Differentiating between Bulk and Interfacial Recombination Processes.

As described in the literature review there has been much debate about the different recombination processes as measured by transition techniques. However, no clear answer was available regarding the recombination processes taking place inside the bulk and those occurring at the interfaces with the external contacts. For this reason, the next contribution look into an electrical measurement method of recombination lifetime in a complete perovskite solar cell proposing a physical model for bulk recombination specifically, performing as well IS without modifying the external contacts effect.

Therefore, as a first step defining that method, a separate analysis of pristine and cycled PSCs seems the best option to obtain information about the type of recombination governing the solar cell before and after operating conditions to separate bulk and interfacial mechanisms. Contrary, the application of the typical transient techniques as cyclic voltammetry, impedance spectroscopy, or open-circuit voltage decay (OCVD), have demonstrated to affect substantially the photovoltaic performance, inducing ion migration toward the external contacts and making more difficult the understanding of the processes involving the bulk properties of the perovskite material itself. A standard protocol of measurement becomes then mandatory to obtain information on recombination characteristics prior to applying any external perturbation that potentially modify the perovskite behaviour during measurement itself.[17] For that purpose, a 18.6% of PCE devices based in FTO/SnO_2/triple-cation perovskite/SpiroOMeTAD/Au, containing a flat conformal layer of SnO_2 deposited by atomic layer deposition (ALD), is used as the raw material to perform the different transient analysis to corroborate their influence in the processes related with the external contacts. In addition, a physical model needs to be develop to evaluate the photovoltaic parameters of the devices focused just in the bulk properties, leaving a part the influence of external contacts. Coupled with this theoretical model, that will be summarized below, a non-invasive electrical measurement based in impedance spectroscopy is carried out. IS under different light intensities and at open-circuit conditions is the selected measure to minimize the effects on the contacts, providing as well more reliable bulk properties determination.

The results of the transient techniques onto the PSCs described above, confirms structure modifications of the devices during measures. The j-V curves shows the typical hysteretic behaviour related with the ion migration in a pristine and polarized (1 sun and positive applied bias) devices. The OCVD, also shows differences between pristine and polarized, confirming previous reported data indicating that different times of light soaking experiments already modify the perovskite properties.[18] In addition, IS under 1 sun illumination and under applied bias, confirm these modifications in terms of series resistances that are originated by the external contacts. As larger positive bias applied, as larger series resistances appear. This evident instability during measurement cannot be solved just reducing the time exposure of the perturbation due to the wide differences between devices, even with the same architecture and perovskite formulation. It is more reliable then, to stablish first a physical model that fits with non-modified bulk material and check if it can be proved by the non-invasive electrical technique.

The physical model proposed is focused in a re-definition of the ideality factor, m, already described in previous sections. Assuming a homogenous distribution of carriers through the semiconductor layer of thickness, d, a non-ideality factor termed m_d is defined by a non-ideal behaviour in the *j-V* curve (Eq.17), due to a local recombination in the bulk of the active material and not to effects at the interfaces with external contacts. The recombination rate reads then as follows:

$$U_n = B_{rec} n^{2/m_d} \tag{2}$$

which re-define as well the expression of recombination resistance as:

$$R_{rec}(V) = R_{rec0} exp\left(\frac{-qV}{m_d k_B T}\right) \tag{3}$$

that takes into account just bulk recombination processes in no-polarized devices.
To check if the proposed model is in agreement with experimental results, an IS at open-circuit conditions, to do not modify the contacts, and under different light intensities needs to be performed. The impedance spectra results in two arcs, typically obtained for a device with efficient extraction layers. The fitting of these results can be obtain by considering the equivalent circuit (EC) already reported for a perovskite solar cell (Fig.3.9a).[19]

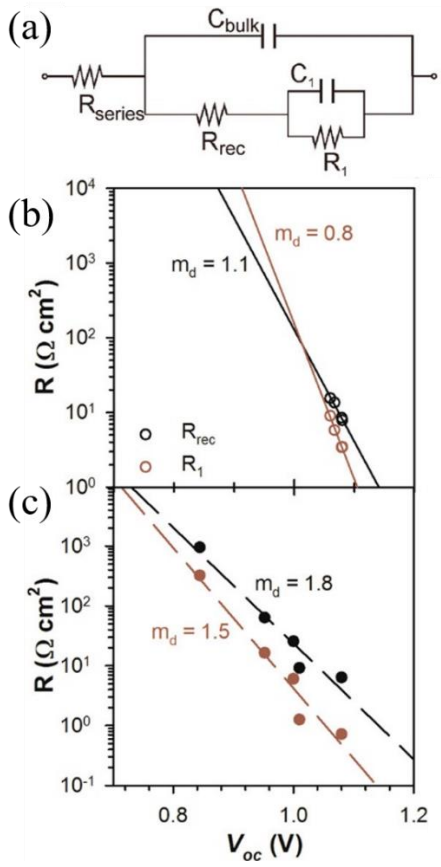

Figure 3.8. (a) Equivalent circuit considered for the fitting data from IS. (b) Fitted values for high- and low-frequency resistances in pristine (and polarized (c) devices. Adapted with permission of Ref.19. Copyright 2017, American Chemical Society-

The recombination resistance corresponding to the high frequency region, for pristine solar cell without any previous stimulus performed, is then associated with bulk recombination processes. Contrary, if the solar cell had been repeatedly perturbed by transition techniques, as a simple cyclic voltammetry, or just illuminated, the recombination resistance at HF is mainly affected by surface recombination mechanisms at the selective contacts interfaces.[20]

3.6. Reducing Surface Recombination to Enhance Photovoltage.

As can be extracted from the previous sections of this text, in the race to the highest PCE and stable PSCs, the ion migration acquires a fundamental role due to the effects activated in the solar cell performance during operation. During the course of this PhD thesis the role of migrating ions has been acquiring major attention. However, the effect of these ions present at the contacts on the recombination mechanisms was not understood at all.

As demonstrated in the previous section, IS measurements performed at open-circuit conditions avoids undesirable perturbations of the contacts, allowing to a better understanding of the processes involving the system during operation conditions.[17] Similarly, under illumination conditions, an accumulation zone of photogenerated carriers appears at the ESL/perovskite interface.[16] Due to this accumulation of holes at the perovskite side of the interface in the case of p-type doping, a surface recombination process has been proved as the main factor involved in photovoltage losses.[20,21] In addition, the intrinsic ionic contribution to the photovoltaic behaviour in PSCs, has been

correlated with the slow dynamics responsible for hysteretic response and giant capacitances under dark and light conditions indistinguishable.

For iodide-based devices, it was reported that the same lithium salt used for spiro-ometad to increase its conductivity, was also used onto the TiO_2 layer showing a beneficial effect on the photovoltaic behaviour of the PSC, specifically enhancing the current density values.[22]

Therefore, taken into account all of the premises above, an exhaustive experiment was designed focusing in the role of extrinsic ions into the bromide-perovskite devices. For that purpose, a device based in $MAPbBr_3$, with TiO_2 and Spiro-OMeTAD as contacts for simplicity, was compared with an ESL-lithium doped device (Fig 3.10).[23]

The first step in order to reduce recombination mechanisms that bring the loss-in-potential in PSCs, is minimize morphological and chemical defects, avoiding pinholes and extra-recombination pathways through them. Employing the knowledge acquired about the coordination chemistry, a very high crystalline $MAPbBr_3$ material was synthesized by antisolvent method, obtaining a smooth and thick perovskite film, with the characteristic absorbance peak at 540 nm (2.3 eV) of bromide derivatives. Current density-voltage curves were performed to compare the photovoltaic characteristic of devices with and without doping in the ESL layer.

Surprisingly, the main beneficial effect relies in the open-circuit potential, suggesting an important contribution in recombination dynamics. (Table 1)

Table 1: Photovoltaic parameters

devices	J (mA cm^{-2})	FF (%)	V_{oc} (V)	PCE (%)
without Li^+	5.3	69	1.36	4.8
with Li^+	5.5	76	1.58	6.6

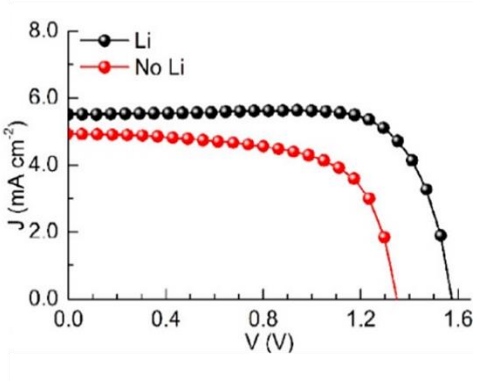

Figure 3.9. Comparison between photovoltaic parameters of non-doped and doped devices showing the enhanced open-circuit potential. Characteristic *j-V* curves measured at 50 mVs^{-1} of both type of devices. Adapted with permission of Ref. 23, Copyright 2019, American Chemical Society.

To analyse this effect, IS measurements were performed at open-circuit conditions and under different light intensities to obtain the values of recombination resistances (Fig. 3.10a) of a set of devices consecutively doped in each of the external contacts, in order to analyse if also the lithium into the Spiro-OMeTAD component also has a major effect on device properties.

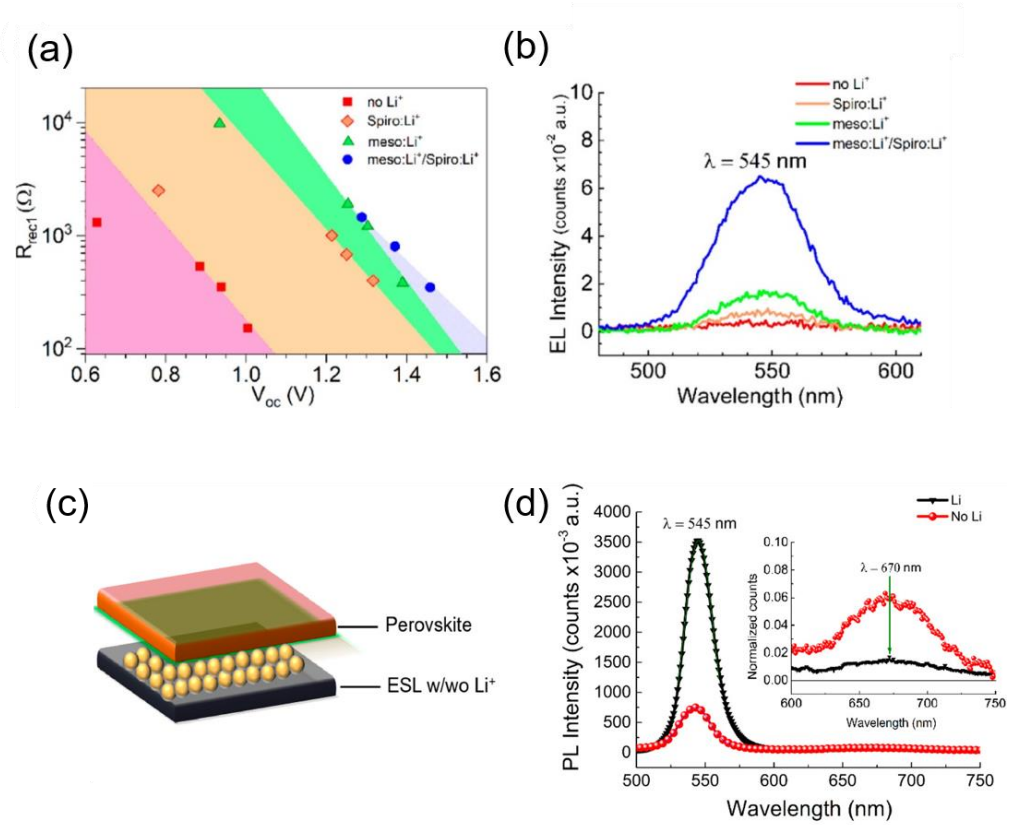

Figure 3.10. (a) Fitting results for high-frequency resistances associated with recombination processes of IS measurements under open-circuit conditions at varying irradiation intensities. Each color corresponds to a device configuration with selective contacts with different lithium salt treatments: red, FTO/*c*-TiO_2/*m*-TiO_2/PVK/spiro/Au; orange, FTO/*c*-TiO_2/*m*-TiO_2/PVK/spiro:Li/Au; green, FTO/*c*-TiO_2/*m*-TiO_2:Li/PVK/spiro/Au; and blue, FTO/*c*-TiO_2/*m*-TiO_2:Li/PVK/spiro:Li/Au. (b) EL spectra of devices shown in (a) at a forward bias of 1.4 V. (c) Schematic configuration of investigated structure by PL: FTO/*c*-TiO_2/*m*-TiO_2:Li/PVK/spiro/Au (d) ESL/$MAPbBr_3$ PL spectra obtained under continuous wave (CW) excitation (380 nm, I_{exc} = 10 mW cm^{-2}) of devices with (black) and without (red) lithium treatment at metal oxide contacts. The inset plot shows quenching of the second feature when lithium is present at the metal oxide contact. Adapted with permission of Ref. 23, Copyright 2019, American Chemical Society.

Interestingly, when plotting the recombination resistances (R_{rec}) versus open-circuit potential at different light intensities, larger R_{rec} were observed for devices with doping at both external contacts, followed by the one only treated at the ESL side (Fig. 3.10a). To confirm this slower recombination kinetic processes, that clearly allows higher photovoltages (increased in 200 mV for the doped-device) (Table 1), the recombination coefficient was calculated following the expression below, due to the previous electrical and optical history of the devices used for the IS study.[24]

$$R_{rec} = \left(\frac{dJ_{rec}}{dV}\right)^{-1} = \frac{mk_BT}{q^2 n_i^2 dB} exp\left(-\frac{qV}{mk_BT}\right) \quad (4)$$

corroborating the recombination resistance trend: reducing when the Li^+ additive is added into both external contacts, as showed below:

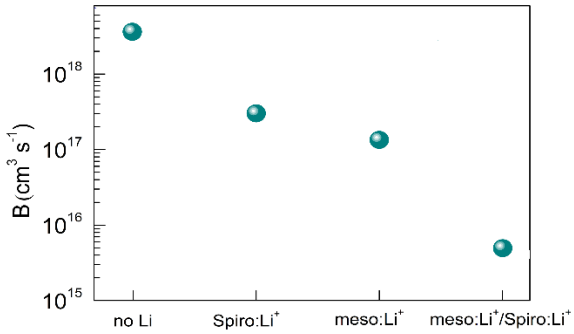

Figure 3.11. Recombination coefficient trend for the four different devices with the progressive addition of lithium to the selective contacts. Calculation made as detailed before this figure. Adapted with permission of Ref. 23, Copyright 2019, American Chemical Society.

To further analyse the nature of the recombination dynamics revealed by IS, electroluminescence (EL) experiments were carried out. Polarizing at forward bias, carriers are directly injected through the contacts. The trend (Fig.3.10b) revealed a clear influence of lithium ion in non-radiative recombination processes: as the same time as the recombination resistance increases, allowing high photovoltages, the radiative recombination through band-to-band mechanism is enhanced, indicating a reduction of non-radiative recombination pathways. In other words, in no-doped devices, the injected carriers do not recombine through the bulk, but through non-radiative recombination pathways or by radiative recombination through interfaces. In Fig. 3.10a is demonstrate that the beneficial effect of lithium ion onto the PV performance, lies mainly at the ESL/perovskite interface. Photoluminescence (PL) analysis of simpler configuration focused just in that interface, revealed the same trend observed by EL. An enhanced light emission through band-to-band pathway is the consequence of the lithium doping of the TiO_2 material. In fact, as can be observed in the inset of the same figure, when no lithium is present at that interface, a revealing emission peak at 670 nm (1.85 eV) is clearly detected, and contrary, quenched when the metal oxide is doped. This peak was identify as the radiative recombination between TiO_2 and perovskite with additional excitation experiments.

The proposed mechanism through which the lithium is reducing surface recombination and consequently, enhancing light emission and photovoltage upon record values (1.6 V), is the increasing of cation density at charge accumulation zone. The size of the space-charge layer grows, reducing the density of electronic holes, allowing higher photovoltages due to the substantial reduction of surface recombination process.

3.7. Conclusions

The main conclusions for the work carried out during the course of this thesis are set out below:

- The coordination chemistry governing the perovskite structure is highly affected by the polar character of the solvents used in precursor's solution. Depending on the coordination capability of these solvents multiiodide plumbates are formed with different coordination numbers. The desired PbI_6^{4-} moieties that conforms the characteristic octahedral disposition of perovskite structure may be substituted by these plumbate species in the films inducing a poorly crystalline structure. These species act as chemical defects detectable by UV-absorbance spectrometry. A clear coordination sequence capability is

established including water, DMSO, DMF and GBL, where the most coordinative is water and less is GBL compound, having water and DMSO similar behaviour, performing a coordination competition to surround lead atom.

- The coordinative competition between water and DMSO to form the PbI:MAI:solvent adduct controls the generation of highly crystalline perovskite structure. Controlling the H_2O:DMSO ratio during processing of the film can be used as a tool to prepare high PCE PSCs under ambient conditions in the presence of moisture. This is accomplished by balancing the DMSO:Pb ratio respect to the %RH of the working environment and efficiencies of up to PCE 19% can be achieved. For %RH > 50% the displacement to the di-hydrated phase of perovskite material forces to perform perovskite devices under protected atmosphere.

- Exposure to light intensity induces interfacial degradation in PSCs regarding chemical interactions between top metal contact and perovskite material. This chemical reactivity takes place through the interaction between migrating ions and external contacts, controlling the *j-V* response. This reactivity leads to degradation mechanisms performing as the typical s-shape of the *j-V* curve as a symptom of a poorly charge extraction capability. This is a consequence of a large interfacial dipole at the cathode/perovskite interface, which reduces the measured flatband potential, V_{fb}, provoking a reversed band in the electrical profile of the perovskite bulk. With this contribution we highlight the relevance of migrating ions and their influence in contacts reactivity.

- Electrical measures as transient techniques for photovoltaic characterization are demonstrated to modify the solar device during the measures itself. This induces the inability to distinguish recombination processes due to the bulk material or due to the external contacts. A slight modification in the non-ideal factor regarding the physical model concerning bimolecular recombination process, allows determining processes exclusively performed by bulk dynamics when a homogeneous distribution of charge is considered in a film of thickness *d*. The non-ideal factor, m_d, is proved as a good approaching performing non-invasive technique as impedance spectroscopy at open circuit conditions.

- Ionic effect onto the recombination processes is demonstrate through interfacial analysis of doped external contacts. The surface recombination is reduced by increasing cation density at hole accumulation zone. This effect reduces as well the hole density, decreasing the surface recombination at the ESL/perovskite interface. This reduction enhances light emission thought band-to-band mechanisms, allowing to perform solar cells based in $MAPbBr_3$ with record photovoltages values up to 1.6 V.

3.8. References

1. Manser, J. S.; Saidaminov, M. I.; Christians, J. A.; Bakr, O. M.; Kamat, P. V. Making and Breaking of Lead Halide Perovskites. *Accounts of Chemical Research* **2016,** *49* (2), 330-338.

2. Horváth, O.; Mikó, I. Spectra, equilibrium and photoredox chemistry of tri- and tetraiodoplumbate(II) complexes in acetonitrile. *Journal of Photochemistry and Photobiology A: Chemistry* **1998,** *114* (2), 95-101.

3. Stamplecoskie, K. G.; Manser, J. S.; Kamat, P. V. Dual nature of the excited state in organic-inorganic lead halide perovskites. *Energy & Environmental Science* **2015,** *8* (1), 208-215.

4. Rahimnejad, S.; Kovalenko, A.; Forés, S. M.; Aranda, C.; Guerrero, A. Coordination Chemistry Dictates the Structural Defects in Lead Halide Perovskites. *ChemPhysChem* **2016,** *17* (18), 2795-2798.

5. Aranda, C.; Cristobal, C.; Shooshtari, L.; Li, C.; Huettner, S.; Guerrero, A. Formation Criteria of High Efficiency Perovskite Solar Cells under Ambient Conditions. *Sustainable Energy Fuels* **2017,** *1* (3), 540-547.

6. Guo, Y.; Shoyama, K.; Sato, W.; Matsuo, Y.; Inoue, K.; Harano, K.; Liu, C.; Tanaka, H.; Nakamura, E. Chemical Pathways Connecting Lead(II) Iodide and Perovskite via Polymeric Plumbate(II) Fiber. *Journal of the American Chemical Society* **2015,** *137* (50), 15907-15914.

7. Contreras-Bernal, L.; Aranda, C.; Valles-Pelarda, M.; Ngo, T. T.; Ramos-Terrón, S.; Gallardo, J. J.; Navas, J.; Guerrero, A.; Mora-Seró, I.; Idígoras, J.; Anta, J. A. Homeopathic Perovskite Solar Cells: Effect of Humidity during Fabrication on the Performance and Stability of the Device. *The Journal of Physical Chemistry C* **2018,** *122* (10), 5341-5348.

8. Salado, M.; Contreras-Bernal, L.; Caliò, L.; Todinova, A.; López-Santos, C.; Ahmad, S.; Borras, A.; Idígoras, J.; Anta, J. A. Impact of moisture on efficiency-determining electronic processes in perovskite solar cells. *Journal of Materials Chemistry A* **2017,** *5* (22), 10917-10927.

9. Azpiroz, J. M.; Mosconi, E.; Bisquert, J.; De Angelis, F. Defect migration in methylammonium lead iodide and its role in perovskite solar cell operation. *Energy Environ. Sci.* **2015,** *8*, 2118--2127.

10. Guerrero, A.; You, J.; Aranda, C.; Kang, Y. S.; Garcia-Belmonte, G.; Zhou, H.; Bisquert, J.; Yang, Y. Interfacial Degradation of Planar Lead Halide Perovskite Solar Cells. *ACS nano* **2016,** *10*, 218–224.

11. Kaltenbrunner, M.; Adam, G.; Glowacki, E. D.; Drack, M.; Schwodiauer, R.; Leonat, L.; Apaydin, D. H.; Groiss, H.; Scharber, M. C.; White, M. S.; Sariciftci, N. S.;

Bauer, S. Flexible high power-per-weight perovskite solar cells with chromium oxide-metal contacts for improved stability in air. *Nat Mater* **2015,** *14* (10), 1032-1039.

12. Guerrero, A.; Chambon, S.; Hirsch, L.; Garcia-Belmonte, G. Light-modulated TiOx Interlayer Dipole and Contact Activation in Organic Solar Cell Cathodes. *Advanced Functional Materials* **2014,** *24* (39), 6234-6240.

13. Almora, O.; Zarazua, I.; Mas-Marza, E.; Mora-Sero, I.; Bisquert, J.; Garcia-Belmonte, G. Capacitive Dark Currents, Hysteresis, and Electrode Polarization in Lead Halide Perovskite Solar Cells. *The Journal of Physical Chemistry Letters* **2015,** *6* (9), 1645-1652.

14. Almora, O.; Guerrero, A.; Garcia-Belmonte, G. Ionic charging by local imbalance at interfaces in hybrid lead halide perovskites. *Applied Physics Letters* **2016,** *108* (4), 043903.

15. Almora, O.; Aranda, C.; Mas-Marzá, E.; Garcia-Belmonte, G. On Mott-Schottky analysis interpretation of capacitance measurements in organometal perovskite solar cells. *Applied Physics Letters* **2016,** *109* (17), 173903.

16. Zarazua, I.; Bisquert, J.; Garcia-Belmonte, G. Light-Induced Space-Charge Accumulation Zone as Photovoltaic Mechanism in Perovskite Solar Cells. *The Journal of Physical Chemistry Letters* **2016,** *7* (3), 525-528.

17. Correa-Baena, J.-P.; Turren-Cruz, S.-H.; Tress, W.; Hagfeldt, A.; Aranda, C.; Shooshtari, L.; Bisquert, J.; Guerrero, A. Changes from Bulk to Surface Recombination Mechanisms between Pristine and Cycled Perovskite Solar Cells. *ACS Energy Letters* **2017,** *2* (3), 681-688.

18. Gottesman, R.; Lopez-Varo, P.; Gouda, L.; Jimenez-Tejada, Juan A.; Hu, J.; Tirosh, S.; Zaban, A.; Bisquert, J. Dynamic Phenomena at Perovskite/Electron-Selective Contact Interface as Interpreted from Photovoltage Decays. *Chem* **2016,** *1* (5), 776-789.

19. Guerrero, A.; Garcia-Belmonte, G.; Mora-Sero, I.; Bisquert, J.; Kang, Y. S.; Jacobsson, T. J.; Correa-Baena, J.-P.; Hagfeldt, A. Properties of Contact and Bulk Impedances in Hybrid Lead Halide Perovskite Solar Cells Including Inductive Loop Elements. *The Journal of Physical Chemistry C* **2016,** *120* (15), 8023-8032.

20. Zarazua, I.; Han, G.; Boix, P. P.; Mhaisalkar, S.; Fabregat-Santiago, F.; Mora-Seró, I.; Bisquert, J.; Garcia-Belmonte, G. Surface Recombination and Collection Efficiency in Perovskite Solar Cells from Impedance Analysis. *The Journal of Physical Chemistry Letters* **2016,** *7* (24), 5105-5113.

21. Nayak, P. K.; Bisquert, J.; Cahen, D. Assessing Possibilities and Limits for Solar Cells. *Advanced Materials* **2011,** *23* (25), 2870-2876.

22. Giordano, F.; Abate, A.; Correa Baena, J. P.; Saliba, M.; Matsui, T.; Im, S. H.; Zakeeruddin, S. M.; Nazeeruddin, M. K.; Hagfeldt, A.; Graetzel, M. Enhanced electronic

properties in mesoporous TiO2 via lithium doping for high-efficiency perovskite solar cells**2016,** *7*, 10379.

23. Aranda, C.; Guerrero, A.; Bisquert, J. Ionic Effect Enhances Light Emission and the Photovoltage of Methylammonium Lead Bromide Perovskite Solar Cells by Reduced Surface Recombination. *ACS Energy Letters* **2019,** *4* (3), 741-746.

24. Bisquert, J. G.-B., G.; Mora-Sero, I. . Characterization of Capacitance, Transport and Recombination Parameters in Hybrid Perovskite and Organic Solar Cells. *Unconventional Thin Film Photovoltaics* **2016**, 57-106.

1. Manser, J. S.; Saidaminov, M. I.; Christians, J. A.; Bakr, O. M.; Kamat, P. V. Making and Breaking of Lead Halide Perovskites. *Accounts of Chemical Research* **2016,** *49* (2), 330-338.

2. Horváth, O.; Mikó, I. Spectra, equilibrium and photoredox chemistry of tri- and tetraiodoplumbate(II) complexes in acetonitrile. *Journal of Photochemistry and Photobiology A: Chemistry* **1998,** *114* (2), 95-101.

3. Stamplecoskie, K. G.; Manser, J. S.; Kamat, P. V. Dual nature of the excited state in organic-inorganic lead halide perovskites. *Energy & Environmental Science* **2015,** *8* (1), 208-215.

4. Rahimnejad, S.; Kovalenko, A.; Forés, S. M.; Aranda, C.; Guerrero, A. Coordination Chemistry Dictates the Structural Defects in Lead Halide Perovskites. *ChemPhysChem* **2016,** *17* (18), 2795-2798.

5. Aranda, C.; Cristobal, C.; Shooshtari, L.; Li, C.; Huettner, S.; Guerrero, A. Formation Criteria of High Efficiency Perovskite Solar Cells under Ambient Conditions. *Sustainable Energy Fuels* **2017,** *1* (3), 540-547.

6. Guo, Y.; Shoyama, K.; Sato, W.; Matsuo, Y.; Inoue, K.; Harano, K.; Liu, C.; Tanaka, H.; Nakamura, E. Chemical Pathways Connecting Lead(II) Iodide and Perovskite via Polymeric Plumbate(II) Fiber. *Journal of the American Chemical Society* **2015,** *137* (50), 15907-15914.

7. Contreras-Bernal, L.; Aranda, C.; Valles-Pelarda, M.; Ngo, T. T.; Ramos-Terrón, S.; Gallardo, J. J.; Navas, J.; Guerrero, A.; Mora-Seró, I.; Idígoras, J.; Anta, J. A. Homeopathic Perovskite Solar Cells: Effect of Humidity during Fabrication on the Performance and Stability of the Device. *The Journal of Physical Chemistry C* **2018,** *122* (10), 5341-5348.

8. Salado, M.; Contreras-Bernal, L.; Caliò, L.; Todinova, A.; López-Santos, C.; Ahmad, S.; Borras, A.; Idígoras, J.; Anta, J. A. Impact of moisture on efficiency-determining electronic processes in perovskite solar cells. *Journal of Materials Chemistry A* **2017,** *5* (22), 10917-10927.

9. Azpiroz, J. M.; Mosconi, E.; Bisquert, J.; De Angelis, F. Defect migration in methylammonium lead iodide and its role in perovskite solar cell operation. *Energy Environ. Sci.* **2015,** *8*, 2118--2127.

10. Guerrero, A.; You, J.; Aranda, C.; Kang, Y. S.; Garcia-Belmonte, G.; Zhou, H.; Bisquert, J.; Yang, Y. Interfacial Degradation of Planar Lead Halide Perovskite Solar Cells. *ACS nano* **2016,** *10*, 218–224.

11. Kaltenbrunner, M.; Adam, G.; Glowacki, E. D.; Drack, M.; Schwodiauer, R.; Leonat, L.; Apaydin, D. H.; Groiss, H.; Scharber, M. C.; White, M. S.; Sariciftci, N. S.; Bauer, S. Flexible high power-per-weight perovskite solar cells with chromium oxide-metal contacts for improved stability in air. *Nat Mater* **2015,** *14* (10), 1032-1039.

12. Guerrero, A.; Chambon, S.; Hirsch, L.; Garcia-Belmonte, G. Light-modulated TiOx Interlayer Dipole and Contact Activation in Organic Solar Cell Cathodes. *Advanced Functional Materials* **2014,** *24* (39), 6234-6240.

13. Almora, O.; Zarazua, I.; Mas-Marza, E.; Mora-Sero, I.; Bisquert, J.; Garcia-Belmonte, G. Capacitive Dark Currents, Hysteresis, and Electrode Polarization in Lead Halide Perovskite Solar Cells. *The Journal of Physical Chemistry Letters* **2015,** *6* (9), 1645-1652.

14. Almora, O.; Guerrero, A.; Garcia-Belmonte, G. Ionic charging by local imbalance at interfaces in hybrid lead halide perovskites. *Applied Physics Letters* **2016,** *108* (4), 043903.

15. Almora, O.; Aranda, C.; Mas-Marzá, E.; Garcia-Belmonte, G. On Mott-Schottky analysis interpretation of capacitance measurements in organometal perovskite solar cells. *Applied Physics Letters* **2016,** *109* (17), 173903.

16. Zarazua, I.; Bisquert, J.; Garcia-Belmonte, G. Light-Induced Space-Charge Accumulation Zone as Photovoltaic Mechanism in Perovskite Solar Cells. *The Journal of Physical Chemistry Letters* **2016,** *7* (3), 525-528.

17. Correa-Baena, J.-P.; Turren-Cruz, S.-H.; Tress, W.; Hagfeldt, A.; Aranda, C.; Shooshtari, L.; Bisquert, J.; Guerrero, A. Changes from Bulk to Surface Recombination Mechanisms between Pristine and Cycled Perovskite Solar Cells. *ACS Energy Letters* **2017,** *2* (3), 681-688.

18. Gottesman, R.; Lopez-Varo, P.; Gouda, L.; Jimenez-Tejada, Juan A.; Hu, J.; Tirosh, S.; Zaban, A.; Bisquert, J. Dynamic Phenomena at Perovskite/Electron-Selective Contact Interface as Interpreted from Photovoltage Decays. *Chem* **2016,** *1* (5), 776-789.

19. Guerrero, A.; Garcia-Belmonte, G.; Mora-Sero, I.; Bisquert, J.; Kang, Y. S.; Jacobsson, T. J.; Correa-Baena, J.-P.; Hagfeldt, A. Properties of Contact and Bulk Impedances in Hybrid Lead Halide Perovskite Solar Cells Including Inductive Loop Elements. *The Journal of Physical Chemistry C* **2016,** *120* (15), 8023-8032.

20. Zarazua, I.; Han, G.; Boix, P. P.; Mhaisalkar, S.; Fabregat-Santiago, F.; Mora-Seró, I.; Bisquert, J.; Garcia-Belmonte, G. Surface Recombination and Collection Efficiency in Perovskite Solar Cells from Impedance Analysis. *The Journal of Physical Chemistry Letters* **2016,** *7* (24), 5105-5113.

21. Nayak, P. K.; Bisquert, J.; Cahen, D. Assessing Possibilities and Limits for Solar Cells. *Advanced Materials* **2011,** *23* (25), 2870-2876.

22. Giordano, F.; Abate, A.; Correa Baena, J. P.; Saliba, M.; Matsui, T.; Im, S. H.; Zakeeruddin, S. M.; Nazeeruddin, M. K.; Hagfeldt, A.; Graetzel, M. Enhanced electronic properties in mesoporous TiO2 via lithium doping for high-efficiency perovskite solar cells**2016,** *7*, 10379.

23. Aranda, C.; Guerrero, A.; Bisquert, J. Ionic Effect Enhances Light Emission and the Photovoltage of Methylammonium Lead Bromide Perovskite Solar Cells by Reduced Surface Recombination. *ACS Energy Letters* **2019,** *4* (3), 741-746.

24. Bisquert, J. G.-B., G.; Mora-Sero, I. . Characterization of Capacitance, Transport and Recombination Parameters in Hybrid Perovskite and Organic Solar Cells. *Unconventional Thin Film Photovoltaics* **2016**, 57-106.

Chapter 4

Publication 1

Coordination Chemistry Dictates the Structural Defects in Lead Halide Perovskites
Rahimnejad, S.; Kovalenko, A.; Martí-Forés, S.; Aranda, C.; Guerrero, A. *ChemPhysChem*, ***2016***, *17, 2795-2798.*

CANDIDATE´S CONTRIBUTION

Nature of Contribution	Extent of Contribution
✓ Contributed to the development of perovskite precursor's solution. ✓ Synthesis of CH_3NH_3I. ✓ Preparation of perovskite films. ✓ Contributed to UV-Absorbance analysis.	20%

INTRODUCTION

This work establishes the importance of chemical and morphological defects on the photovoltaic performance of PSCs deeply analysed through UV-absorbance spectroscopy measurements. It focus in the coordinative environment of lead atom from the perovskite solution to the solid perovskite film, analysing the coordination capability of the most used solvents in order to further understanding the role of each other in the crystallinity of the absorber material, stablishing as well a coordination order between water, DMSO, DMF and GBL.

PUBLISHED MANUSCRIPT

Coordination Chemistry Dictates the Structural Defects in Lead Halide Perovskites

Sara Rahimnejad,[1,2†] Alexander Kovalenko,[1,3†] Sergio Martí Forés,[4] Clara Aranda[1] and Antonio Guerrero[1*]

1 *Institute of Advanced Materials (INAM), Universitat Jaume I, 12006 Castelló, Spain*
2 *Department of Chemistry, College of Basic science, Yadegar-e-Imam Khomeini (RAH) Shahre Rey Branch, Islamic Azad University, Tehran, Iran*
3 *Brno University of Technology, Faculty of Chemistry, Materials Research Centre, 612 00 Brno, Czech Republic*
4 *Departament de Química Física i Analítica, Universitat Jaume I, 12006 Castelló, Spain*

† *Both authors contributed equally*

Email: aguerrer@uji.es

Abstract

We show the influence of species present in precursor solution during formation of lead halide perovskite materials on the structural defects of the films. The coordination of lead by competing solvent molecules and iodide ions will dictate the type of complexes present in the films. Depending on the processing conditions all $PbIS_5^+$, PbI_2S_4, $PbI_3S_3^-$, $PbI_4S_2^{2-}$, $PbI_5S_2^{3-}$, $PbI_6^{4-}$and 1-D $(Pb_2I_4)_n$ chains are observed by absorption measurements. Different parameters are studied like polarity of the solvent, concentration of iodide ions, concentration of solvent molecules and temperature. It is concluded that strongly coordinating solvents will preferentially form species with a low number of iodide ions and less coordinative solvents generate high concentration of PbI_6^-. We furthermore propose that all these plumbate ions may act as structural defects determining electronic properties of the photovoltaic films.

Keywords: Perovskite solar cell, coordination chemistry, defects, synthesis, absorption.

Table of Content

Structural defects are created during crystallization of perovskite materials depending on coordination ability of the solvents.

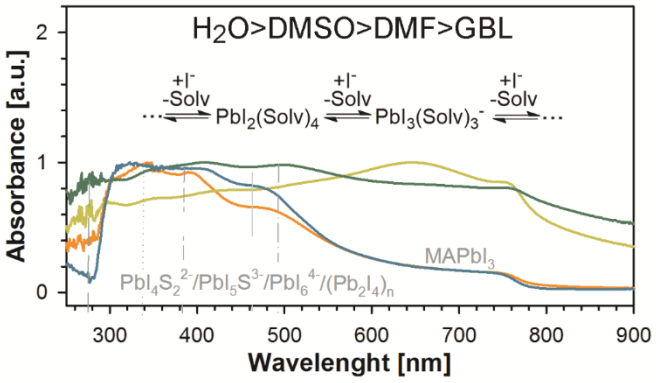

Photovoltaic devices based on lead halide perovskites have erupted as strong candidates to compete with already commercially available technologies.[1] Significant efforts have been devoted towards the achievement of high efficiencies leading to 21.0 % using derivatives of methylammonium lead triiodide perovskites. [2, 3] Solvent engineering has proved key to obtain increased crystallinity of the perovskite layer with low presence of grain boundaries and impurities, both factors limiting the device performance.[4] In spite of the great advances in this technology very little information is available on the species present in the crystallizing perovskite layer, connected with the electrical defects existent in the photovoltaic devices. Deep investigations of the species present during formation of the films are important toward the understanding of the photophysics in devices as electrical defects are known to limit the device performance.[5]

Methyl ammonium lead iodide perovskite ($MAPbI_3$) is synthesised by the reaction of PbI_2 with methyl ammonium iodide (MAI) using highly polar solvents such as Dimethylsulphoxide (DMSO), N,N-Dimethylformamide (DMF) or γ-Butyrolactone (GBL).[6,7] During this chemical reaction an equilibrium like that shown in Scheme 1 dominates the species present in solution, where S is a generic solvent. This equilibrium expands the equilibrium proposed by Kamat *et al.* who focused on the photophysic effect of having $PbI_3S_3^-$ and $PbI_4S_2^{2-}$ species in films.[8] For simplicity generation of 1-D $(Pb_2I_4)_n$ chains are not included in the equilibrium but these type of species are also expected to form during perovskite crystallization.[9] In this work we show that the coordination ability of the solvent plays a very important role and depending on the processing conditions all $PbIS_5^+$, PbI_2S_4, $PbI_3S_3^-$, $PbI_4S_2^{2-}$, $PbI_5S_2^{3-}$, PbI_6^{4-} and 1-D intermediate crystals may be present in both solution and films.

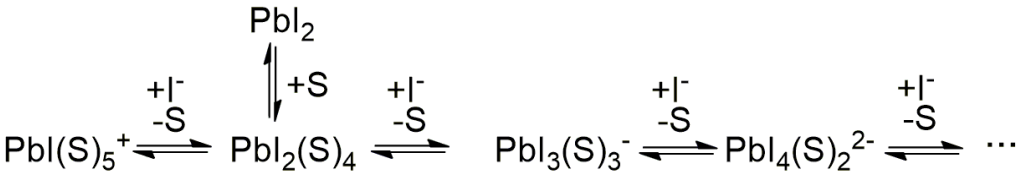

Scheme 1: Dissolution of PbI_2 in a generic solvent (S) and competitive reaction between iodide ions and solvent molecules leading to different plumbate ions.

The coordination ability of the solvent can be probed by monitoring the species present using absorption measurements of diluted PbI_2 solutions (i.e. 0.5 mM). Figure 1a shows absorption spectra of PbI_2 in a series of solvents with different coordination abilities: Water, DMSO, DMF and GBL. Depending on the solvents different proportions of plumbate ions are detected such as $PbIS_5^+$ (λ_{max} = 286 nm), PbI_2S_4 (λ_{max} = 325 nm) or $PbI_3S_3^-$ (λ_{max} = 370 nm). This is a clear evidence that the solvent is readily competing with iodine atoms to fill the octahedral coordination sphere, see for example the diagram in the inset of Figure 1a. Water is included in the series as it is known to be a key player during crystallization kinetics.[10] Absorption measurements show that H_2O readily coordinates to Pb producing mostly $PbIS_5^+$ and some PbI_2S_4. The low intensities of the bands can be taken as a clear sign that the solvent is able to fully dissociated generating Pb^{2+}. Similar results are observed for DMSO with higher concentration of PbI_2S_4 and some formation of $PbI_3S_3^-$. In DMSO covalent character between the DMSO and Pb has been described in the literature which would explain the observed λ_{max} shift and a similar effect is observed using H_2O as solvent.[2] Alternatively, in DMF higher concentration of PbI_2S_4 and $PbI_3S_3^-$ are detected than in the previous two solvents. Finally, when a less coordinating solvent such as GBL is used all three species $PbIS_5^+$, PbI_2S_4 and $PbI_3S_3^-$ are

observed with comparable intensities. Therefore we can state that the affinity to coordinate Pb of the studied solvents is as follows: H_2O>DMSO>DMF>GBL.

The equilibrium proposed in Scheme 1 can be further validated in Figure 1b by modifying the concentration of either iodide ions or solvent molecules using PbI_2 solutions in DMF. As expected for this equilibrium increasing the proportion of I^- ions

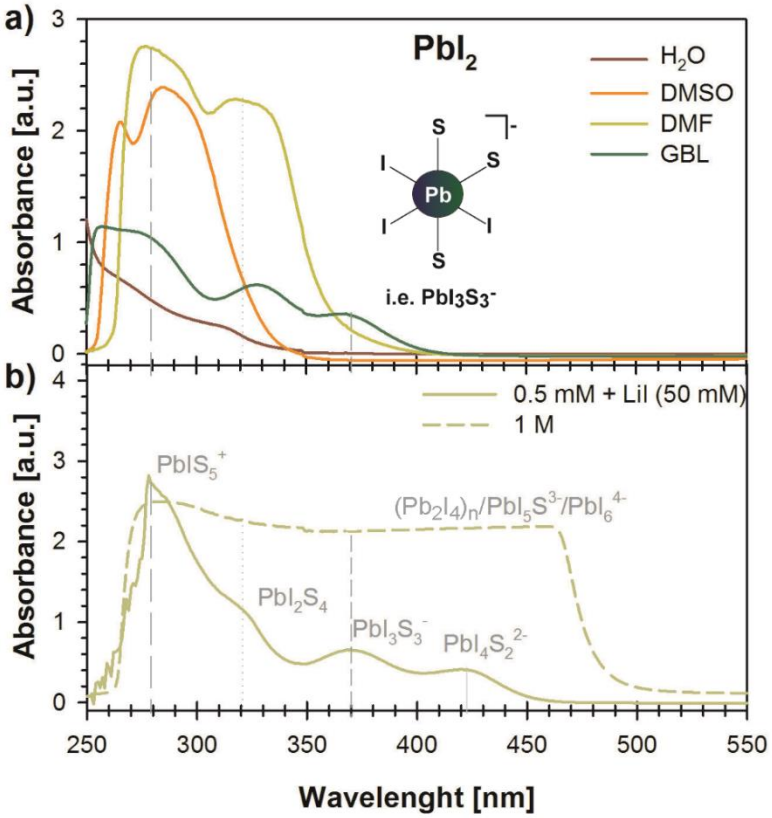

Figure 1: Absorption spectra of solutions containing PbI_2 (a) in a range of different solvents at a concentration of 0.5 mM and (b) at two different concentrations in DMF, the solid line contains 100 eq. of LiI. Each plumbate ion is marked with a vertical line defined by their λ_{max}.

using a large excess of LiI (100 eq) shifts the equilibrium towards the presence of polyiodide plumbates like $PbI_4S_2^{2-}$ (λ_{max} = 428 nm). Alternatively, increasing the PbI_2 concentration to 1 M decreases the number of solvent molecules and the absorption curve is further red shifted to reach wavelength close to λ_{max} = 490 nm, where PbI_2 films show the absorption onset due to the presence of PbI_6^{4-} moieties in the absence of the methyl ammonium cation (see supporting information).[11] We also note that 1-D $(Pb_2I_4)_n$ chains have also been reported to form and the actual absorption maximum of these type of species have not been ambiguously identified.[9, 12]

Addition of MAI to PbI_2 in these highly concentrated solutions using different solvents (Figure 2a) also show continuous absorption band covering all the range from 250 nm to 520 nm indicating that all the different multiodide plumbate species described before are present in solution ($PbIS_5^+$, PbI_2S_4, $PbI_3S_3^-$, $PbI_4S_2^{2-}$, $PbI_5S_2^{3-}$, PbI_6^{4-} and 1-D $(Pb_2I_4)_n$ chains). Although we note that the signal is saturated and the response is not linear we observe that some bands are more prominent than others depending on the solvent. For

example, whilst the band due to $PbIS_5^+$ is present in all solvents the band from PbI_2S_4 is more noticeable for DMSO in good agreement with generation of the DMSO complex during film formation.[6] Similarly, using GBL the $PbI_3S_3^-$ complex is more intense as expected for a less nucleophilic solvent than DMSO or DMF. Absorption spectra of solutions containing PbI_2 and MAI under different concentrations and solvents are shown as supporting information (Figure SI2). It is observed the generation of multiodides species containing higher proportion of I^- atoms as the amount of solvent molecule decreases.

The effect of the temperature on the competition between iodide ions and solvent has also been studied as it will pose important implications on the crystallization of bulk material. Figure 2b shows the absorption spectra of a solution containing PbI_2 and MAI (ratio 1:1, 0.05 M) in DMSO as a function of the temperature. When the temperature is increased we observe a red shift in the absorption band onset due to the presence of iodide plumbate ions containing a higher number of iodine ions. This result is in agreement with the DFT calculations shown as supporting information for DMSO where the Gibbs free energies for successive replacement of solvent molecules by iodide to obtain plumbates with a higher number of iodide ions is an endergonic process requiring energy. Then, plumbate species with high content of iodide ions will only be favoured at high temperatures. We note that the process is reversible as cooling the solution to R.T. recovers the initial spectra (see supporting information). In addition, a new band appears at a λ_{max} = 690 nm which belongs to $MAPbI_3$ species in solution as compared to the observed bands in $MAPbI_3$ films (see Figure 2c).

So far the basics of the coordination chemistry of the lead atom has been fully described in solution and now we proceed to the preparation of bulk perovskite material to understand if the acquired knowledge can be extrapolated to the synthesis of pure material. It is important to recall that in the $MAPbI_3$ crystal structure Pb is at the centre of an octahedron surrounded by six iodine atoms, one at each vertex of the octahedron. Then, the presence of PbI_6^{4-} is desired as it provides the correct environment for generation of the perovskite phase. An inverse temperature crystallization model has been proposed for crystallization of single $MAPbI_3$ crystals.[7] The model considers different solubility of the final perovskite material depending on temperature and solvent but does not account for possible variation in concentrations in the species present during crystallization. Absorption measurements shown in Figure 2b and DFT calculations suggest that the species present in solution will depend on the temperature. Therefore, the use of high precursor concentrations and high temperatures is needed for maximize the presence of PbI_6^{4-} and 1-D $(Pb_2I_4)_n$ chains.

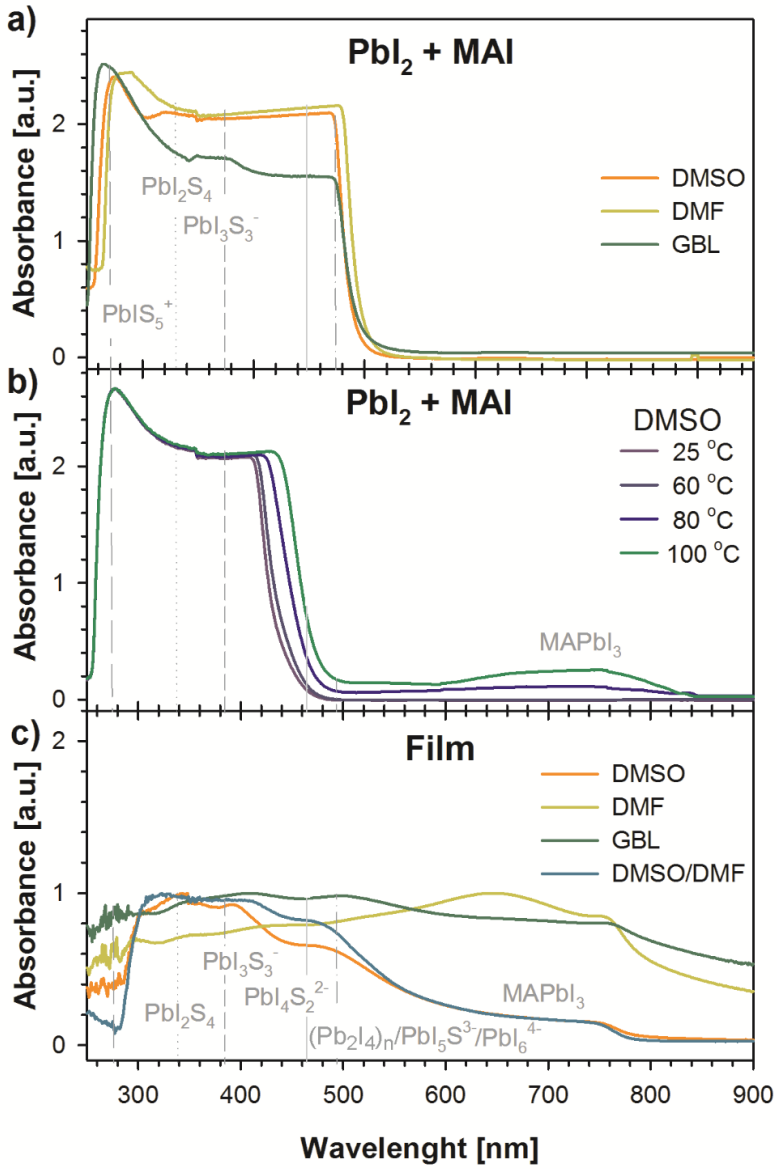

Figure 2: Absorption spectra of (a) solutions containing PbI_2 and MAI (ratio 1:1) in concentrated solution (1M) using a range of different solvents. (b) Solutions containing PbI_2 and MAI in DMSO (0.05 M) as a function of the temperature. (c) $MAPbI_3$ films on FTO prepared from different solvents, the signal has been normalized to the maximum value. Each plumbate ion is marked with a vertical line defined by their λ_{max}.

The synthesis of the bulk material is carried out by slow evaporation of the solvent in a well ventilated oven at temperatures 20 °C below the boiling point of the solvent to maintain similar evaporation kinetics amongst the solvents, full details can be found in the methods section. Interestingly, synthesis carried out in this manner provides materials with very different morphology and structure. Synthesis from DMSO (Figure 3a) generates a mixture of yellow and black powders with different morphologies as observed by SEM: black domains are needle-like and yellow domains are highly amorphous. Interestingly, the perovskite formed from DMF show crystallites with dispersion in size containing macroscopic (up to 1-2 cm) and microscopic crystallites. In general these are composed by highly aligned needles as those shown in Figure 3b. Alternatively, when GBL is used, generation of large cubic like crystallites is evident (Figure 3c). Overall the crystallinity is enhanced by using less coordinative solvents like GBL where the presences

of octahedral PbI_6^{4-} moieties are favoured. On the other hand, XRD analysis (Figure 3d) shows for DMSO a blend of PbI_2(DMSO) complex (see supporting information for reference) and $MAPbI_3$, with crystallographic planes (110), (220), (312) and (224). The additional PbI_2(DMSO) complex clearly indicates that the DMSO molecule is tightly bound to the lead.[13] On the other hand, synthesis from DMF and GBL provides quantitative yield of highly crystalline material in the tetragonal phase as compared with simulated data using monocrystalline XRD data.[14] Very importantly, crystalline defects are minimized using GBL as observed by measuring the Full width at half maximum of the peaks as compared to DMSO and DMF.

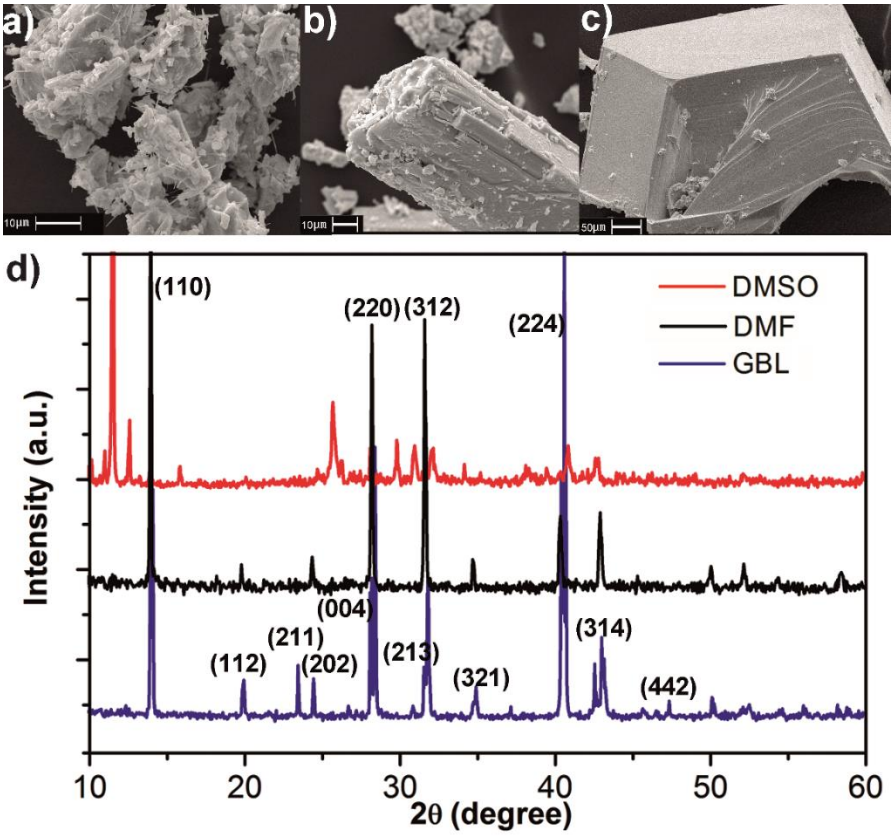

Figure 3: Representative SEM image of crystallites generated from three different solvents a) DMSO, b) DMF and c) GBL. d) XRD powder pattern of samples prepared in three different solvents. Diffraction peaks are assigned similarly to previously published results.[7]

We finalize the study with the analysis of $MAPbI_3$ films as they are representative to understand the type of structural defects present in photovoltaic devices. Figure 2c shows normalized absorption spectra of films prepared using different solvents followed by a heat treatment at 100 °C. The use of DMSO leads to films containing $MAPbI_3$ and a large proportion of all plumbate species $PbIS_5^+$, PbI_2S_4, $PbI_3S_3^-$, $PbI_4S_2^{2-}$, $PbI_5S_2^{3-}$, PbI_6^{4-} and 1-D $(Pb_2I_4)_n$ chains. The proportion of some of these plumbate ions can be modified by using the method reported by Ahn *et al.* in which diethyl ether is used during spin coating process to wash out part of the DMF and generate the PbI_2:MAI:DMSO complex.[6] Using this modification the proportion of PbI^+ and PbI_2 is reduced and PbI_3^-/PbI_4^{2-}/PbI_5^{3-}/PbI_6^{4-} are increased as expected by reducing the concentration of DMSO. The use of less coordinative solvents like DMF and GBL favour formation of the $MAPbI_3$ perovskite and this is observed in the absorption spectra with the presence of a low proportion of plumbates and by the rather flat profile of the band. We note that absorption beyond 800

nm does not reach the baseline due to voids filled with air (pinholes) inducing generation of artifacts by light scattering in the films.[15] We also highlight that the absorption spectra of $MAPbI_3$ single crystals have been reported to be rather flat in the region 400-820 nm.[7, 16] Depending on the used solvent here films show bands of different intensities at λ_{max} of 286 nm, 325 nm, 370 nm, 428 and 490 nm. Therefore, we propose that several multiodide plumbate species remain in the films.

The presence of these structural defects lead to important implications connected with the nature of electrical defects generated in photovoltaic devices which may limit the device performance. Indeed, unintentional doping like Pb, I, and MA vacancies have been reported for $MAPbI_3$.[17,18] It has also been proved that the *n*-/*p*-type can be efficiently manipulated by controlling the growth processes.[19] For example, an excess of MAI produces *p*-type character defects and excess of PbI_2 induces generation of *n*-type defects. In this respect Kamat *et al.* have detected the photoluminescence signature of PbI_3^- and PbI_4^{2-} defects in perovskite films but generation of other 1D plumbate ions chains are also expected following our absorption measurements.[8-9] Discrepancies found in the nature of the doping (n/p type) could also be the result of different presence of plumbate species. For example, it is expected that positively and negatively charge species (i.e. PbI^+ and PbI_4^{2-}) will have a totally different electrical effect in devices. In this respect our current work will need further investigations to separate the effect of each of the plumbate species and morphology of the films. i.e. It is known that DMF provide films with fibre-like morphology with a large presence of pinholes leading to shunt pathways very negative for the device performance.[20]

In summary this communication shows that coordination of lead, by competing solvent molecules and iodide ions, will dictate the species present in the precursor solution and in the final perovskite layer for photovoltaic applications. Highly polar solvents are required to dissolve the precursors but must permit the generation of PbI_6^{4-} species to provide the correct environment for perovskite crystallization. The presence of impurities is minimized by decreasing the polarity of the solvent leading to crystallization reaction into the perovskite tetragonal phase. Here we propose that all these plumbate ions may act as structural defects and these are present in films using state-of-the-art processing conditions indicating that there is still some more room to improve device efficiencies.

Supporting Information. Methods, further absorption measurements, DFT calculations and further XRD data.

Acknowledgements

We thank financial support by MINECO of Spain under project (MAT2013-47192-C3-1-R), and Generalitat Valenciana is acknowledged for financial support on the PESOL Project (ACOMP/2015/105). A. G. would like to thank the Spanish Ministerio de Economía y Competitividad for a Ramón y Cajal Fellowship (RYC-2014-16809). Serveis Centrals at UJI (SCIC) are acknowledged for the SEM measurement assistance.

Supporting Information

Coordination Chemistry Dictates the Structural Defects in Lead Halide Perovskites

Sara Rahimnejad,[1,2†] Alexander Kovalenko,[1,3†] Sergio Martí Forés,[4] Clara Aranda[1] and Antonio Guerrero[1*]

1 *Institute of Advanced Materials (INAM), Universitat Jaume I, 12006 Castelló, Spain*
2 *Department of Chemistry, College of Basic science, Yadegar-e-Imam Khomeini (RAH) Shahre Rey Branch, Islamic Azad University, Tehran, Iran*
3 *Brno University of Technology, Faculty of Chemistry, Materials Research Centre, 612 00 Brno, Czech Republic*
4 *Departament de Química Física i Analítica, Universitat Jaume I, 12006 Castelló, Spain*

† *Both authors contributed equally*

Email: aguerrer@uji.es

Methods

Materials

Materials were used as received from the suppliers: Methyl ammonium Iodide (TCI), PbI_2 (Sigma Aldrich, 99.99 %), LiI (Sigma Aldrich, 99.9%), DMSO (Sigma-Aldrich, 99.9%), DMF (Sigma-Aldrich, 99.9%) and GBL (Sigma-Aldrich, 99 %).

Synthesis of Lead Halide Perovskite in solvents

The synthesis of $MAPbI_3$ was carried by slow evaporation in three solvents DMSO, DMF and GBL. The 1:1 eq of MAI (0.954g) and PbI_2 (2.766 g) were mixed in 5 ml solvent at 60 °C in a Glove box. The solvent was slowly evaporated during 5 h by placing the solutions into a well-ventilated oven at 20-30 °C below the boiling point of the solvent. Temperatures where set at 133 °C (DMF), 169 °C (DMSO) or 174 °C (GBL). During the solvent evaporation initially a yellow solid was formed and then turned black. The solid was stirred regularly with a spatula to ensure the evaporation process of trapped solvent.

Preparation of Lead Halide Perovskite films

A 50 µL perovskite solution containing MAI and PbI2 (1:1, 1M) in either DMSO, DMF or GBL was spin coated at 4000 rpm during 50 seconds with acceleration of 4000 rpm. A transparent film is generated using DMSO and dark films with DMF and GBL. Films were annealed at 100°C for 2 minutes. For the reported process by Ahn *et al.* A 50 µL perovskite solution containing MAI (Dyesol), PbI2 (TCI, 99.999%) and DMSO (1:1:1 mol %) in a DMF solution (50 wt %) is spin coated at 4000 rpm during 50 seconds with acceleration of 4000 rpm. Non-polar diethyl ether was poured onto the spinning substrate after the initial 5-7 s to selectively wash the DMF. A transparent film generated after the spin coating and a heat treatment at 65 °C for 1 min was effective to remove the DMSO and shiny and dark brown MAPbI3 films were obtained by further annealing at 100°C for 2 minutes.

Characterization

Ultraviolet-visible absorption spectra were recorded by a Cary 500 Scan VARIAN spectrophotometer in the 250-800 nm wavelength range. The morphology of the powders

was observed using field-emission SEM using either a JEOL 7001F for powders. The XRD pattern of the prepared solids were measured using X-ray diffractometer (D8 Advance, Bruker-AXS) (Cu Kα, wavelength λ=1.5406 Å).

DFT Calculations

For geometry optimization lanl2dz double-ζ basis set was used for Pb and I atoms, and the 6-311G* basis set was applied for the solvent atoms. As a computational method an implicit Becke's three-parameter hybrid functional B3LYP containing a combination of exchange-correlation with Hartree-Fock method was applied,[21] hybrid functional has proven their accuracy for similar systems.[22] The geometry optimizations and spectral calculations were carried out without any symmetry restriction. Abovementioned combination of method and basis set has shown a good experimental correlation.[23]

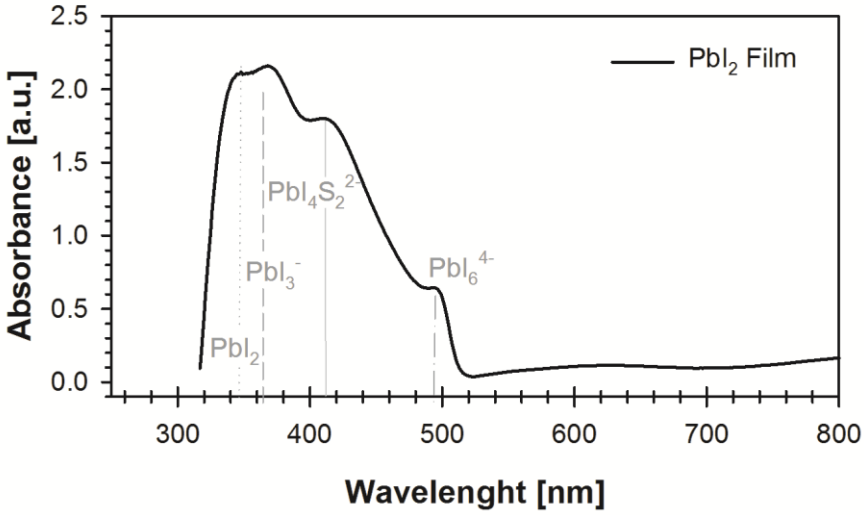

Figure SI1: Absorption spectra of a PbI_2 film. Absorption bands of species measured in solution are represented by their λ_{max} as a vertical line.

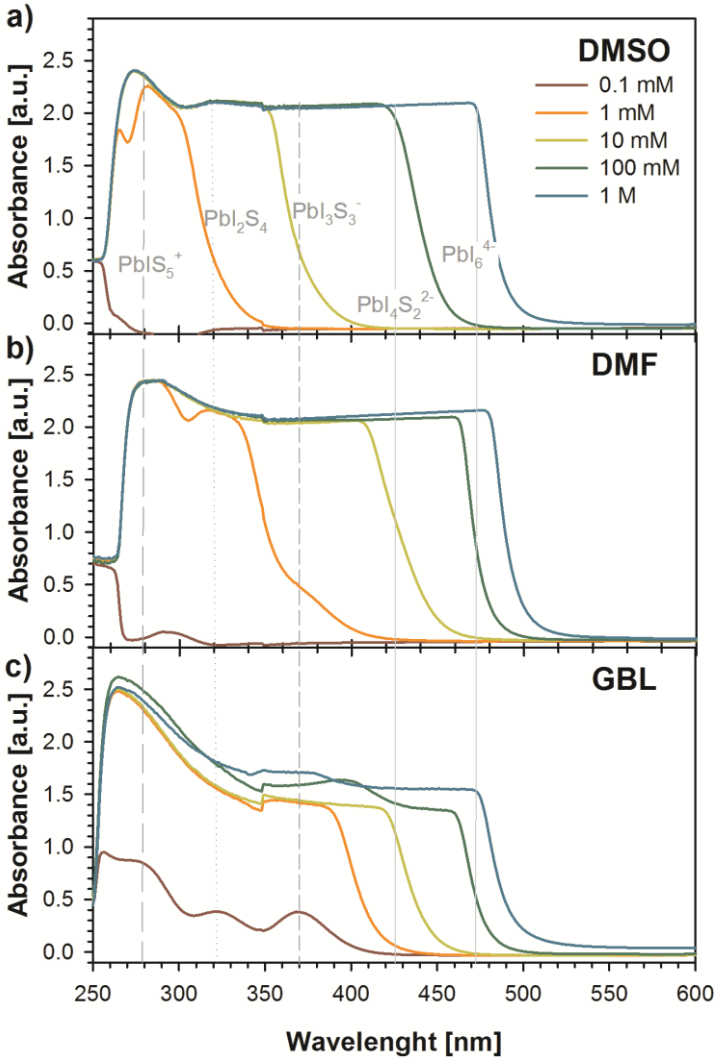

Figure SI2: Absorption spectra of solutions containing PbI_2 and MAI (ratio 1:1) using different concentrations in (a) DMSO, (b) DMF and (c) GBL. Absorption bands of species measured in solution are represented by their λ_{max} as a vertical line.

DFT calculations

In order to get a deeper insight, we have estimated the free energy of formation for the different lead complexes resulting from the successive displacement of solvent molecules by iodide (Table SI1). For this purpose, we have used the DFT formalism, combined with the use of continuous solvation models (SMD) for each of the solvents commented in the main text. Regarding the stability of hexa-coordinated complexes established between the lead and the solvent molecules, it is worth noting that the DMSO complex is the most stable, followed by the DMF and finally the GBL. Regarding the gradual replacement of solvent molecules by iodide ($PbI_xS_y + I^- \Leftrightarrow PbI_{(x+1)}S_{(y-1)} + S$) we observe that for DMSO the replacement of solvent molecules from the lead coordination sphere is not favoured, with the single exception of the $PbIS_5^+$ complex, which is slightly more stable than the hexa-coordinated complex with the solvent. Alternatively, for DMF the only species not stable in this solvent is $PbI_4S_2^{2-}$ and it is observed that PbI_2S_4 and $PbI_3S_3^-$ are degenerate in energy. In fact, according to the estimates obtained, the predominant species in DMF would be the $PbIS_5^+$ complex as observed in the absorption spectra. Finally, all the range of studied lead-iodide complexes are stable in GBL.

Table SI1. Gibbs free energies (in kcal/mol) for successive replacement of solvent molecules by iodide for the different lead complexes. The first row corresponds to the formation of the hexa-coordinated lead complex with each solvent (PbS_6^{2+}).

Complex	DMSO	DMF	GBL
PbS_6^{2+}	-35.7	-23.8	-5.0
$PbIS_5^{+}$	-0.3	-4.2	-6.6
PbI_2S_4	0.2	-0.9	-6.8
$PbI_3S_3^{-}$	3.3	-0.9	-1.1
$PbI_4S_2^{2-}$	3.0	2.4	-3.1

Besides, the partial bond order of the different interactions established between the lead and the solvent molecules (Pb-O) or with the iodide (Pb-I) have been also calculated for each complex, and they are reported in Table SI2. These bond orders are expressed as Wiberg indexes, coming from NBO calculations. The results show that the GBL present higher values of the bond orders for the Pb-I interactions than the DMF or the DMSO, being the maximum value at the PbI_3^- complex. This result also would point to a fast and preferential crystallization of the perovskite from the GBL solution, providing the formation of large crystals, as has been published recently.[7]

Interestingly, the PbI_3^- in DMSO shows similar values for the bond orders in both Pb-O and Pb-I interactions. Also, these values correspond to a strengthening in the case of the Pb-O with respect to the nearest complexes (PbI_2 and PbI_4^{2-}), but a weakening of the Pb-I interaction with respect to the same reference complexes. As a matter of fact, these results would prove the retarded crystallization of the PVK from the DMSO solution. Finally, this behaviour is also found in both the DMF and in the GBL, but the values for the Pb-I interactions are higher in magnitude respectively.

Table SI2. Bond orders for the various lead-complexes. The values correspond to an average of the Wiberg indexes between the lead cation and: the donor atom of the solvent molecules (Pb-O), and the iodide (Pb-I).

	DMF		DMSO		GBL	
Species	**Pb-O**	**Pb-I**	**Pb-O**	**Pb-I**	**Pb-O**	**Pb-I**
PbS_6^{2+}	0.120		0.131		0.117	
$PbIS_5^{+}$	0.133	0.134	0.143	0.104	0.121	0.306
PbI_2S_4	0.131	0.312	0.141	0.273	0.126	0.357
$PbI_3S_3^{-}$	0.151	0.242	0.178	0.181	0.124	0.363
$PbI_4S_2^{2-}$	0.142	0.331	0.159	0.312	0.130	0.346

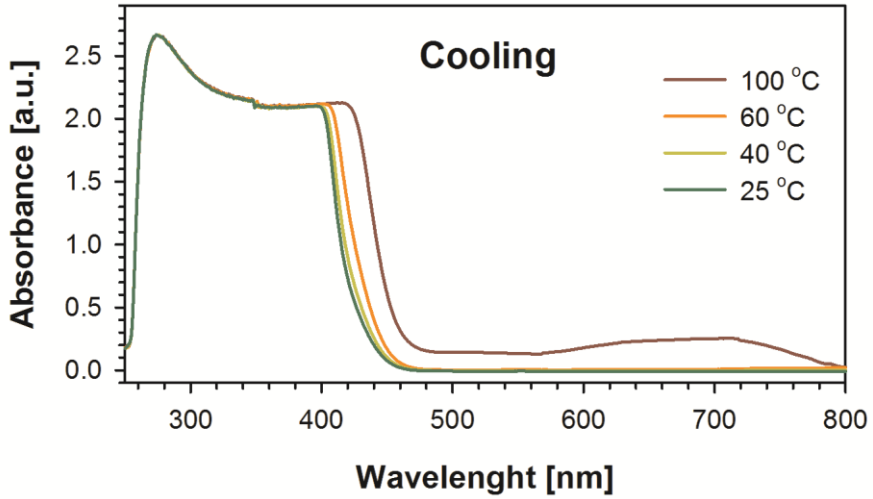

Figure SI3: Absorption spectra of solutions containing PbI_2 and MAI (ratio 1:1) in DMSO (0.05 M) as a function of the temperature during cooling of the solutions.

XRD measurements

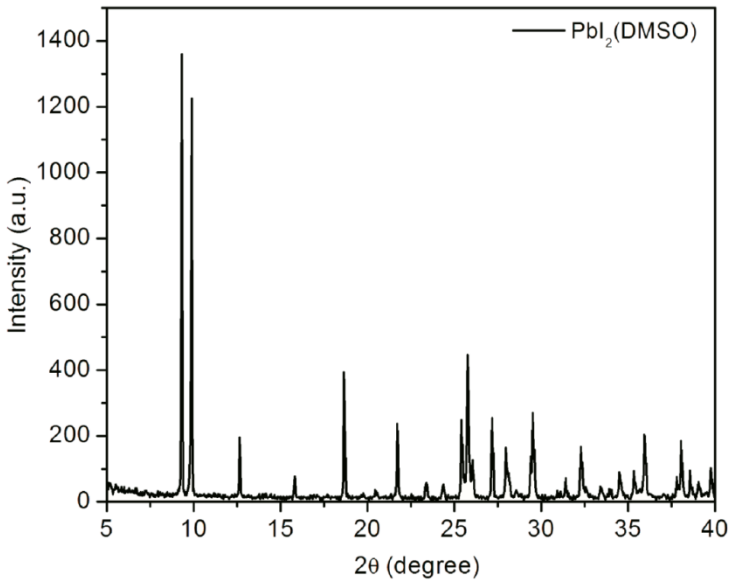

Figure SI4: XRD measurements of pure PbI_2(DMSO) synthesised as in reference [2].

References

1. Green, M. A.; Emery, K.; Hishikawa, Y.; Warta, W.; Dunlop, E. D. Solar cell efficiency tables (Version 45). *Progress in Photovoltaics: Research and Applications* **2015,** *23* (1), 1-9.

2. Yang, W. S.; Noh, J. H.; Jeon, N. J.; Kim, Y. C.; Ryu, S.; Seo, J.; Seok, S. I. High-performance photovoltaic perovskite layers fabricated through intramolecular exchange. *Science* **2015,** *348* (6240), 1234-1237.

3. Bi, D.; Tress, W.; Dar, M. I.; Gao, P.; Luo, J.; Renevier, C.; Schenk, K.; Abate, A.; Giordano, F.; Correa Baena, J.-P.; Decoppet, J.-D.; Zakeeruddin, S. M.; Nazeeruddin, M. K.; Grätzel, M.; Hagfeldt, A. Efficient luminescent solar cells based on tailored mixed-cation perovskites. *Science Advances* **2016,** *2* (1).

4. Nayak, P. K.; Bisquert, J.; Cahen, D. Assessing Possibilities and Limits for Solar Cells. *Advanced Materials* **2011,** *23* (25), 2870-2876.

5. Azpiroz, J. M.; Mosconi, E.; Bisquert, J.; De Angelis, F. Defect migration in methylammonium lead iodide and its role in perovskite solar cell operation. *Energy Environ. Sci.* **2015,** *8*, 2118--2127.

6. Ahn, N.; Son, D.-Y.; Jang, I.-H.; Kang, S. M.; Choi, M.; Park, N.-G. Highly Reproducible Perovskite Solar Cells with Average Efficiency of 18.3% and Best Efficiency of 19.7% Fabricated via Lewis Base Adduct of Lead(II) Iodide. *Journal of the American Chemical Society* **2015,** *137* (27), 8696-8699.

7. Saidaminov, M. I.; Abdelhady, A. L.; Murali, B.; Alarousu, E.; Burlakov, V. M.; Peng, W.; Dursun, I.; Wang, L.; He, Y.; Maculan, G.; Goriely, A.; Wu, T.; Mohammed, O. F.; Bakr, O. M. High-quality bulk hybrid perovskite single crystals within minutes by inverse temperature crystallization. *Nat Commun* **2015,** *6*.

8. Stamplecoskie, K. G.; Manser, J. S.; Kamat, P. V. Dual nature of the excited state in organic-inorganic lead halide perovskites. *Energy & Environmental Science* **2015,** *8* (1), 208-215.

9. Guo, Y.; Shoyama, K.; Sato, W.; Matsuo, Y.; Inoue, K.; Harano, K.; Liu, C.; Tanaka, H.; Nakamura, E. Chemical Pathways Connecting Lead(II) Iodide and Perovskite via Polymeric Plumbate(II) Fiber. *Journal of the American Chemical Society* **2015,** *137* (50), 15907-15914.

10. You, J.; Yang, Y.; Hong, Z.; Song, T.-B.; Meng, L.; Liu, Y.; Jiang, C.; Zhou, H.; Chang, W.-H.; Li, G. Moisture assisted perovskite film growth for high performance solar cells. *Applied Physics Letters* **2014,** *105* (18), 183902

11. Liu, X.; Ha, S. T.; Zhang, Q.; de la Mata, M.; Magen, C.; Arbiol, J.; Sum, T. C.; Xiong, Q. Whispering Gallery Mode Lasing from Hexagonal Shaped Layered Lead Iodide Crystals. *ACS Nano* **2015,** *9* (1), 687-695.

12. Yan, K.; Long, M.; Zhang, T.; Wei, Z.; Chen, H.; Yang, S.; Xu, J. Hybrid Halide Perovskite Solar Cell Precursors: Colloidal Chemistry and Coordination Engineering

behind Device Processing for High Efficiency. *Journal of the American Chemical Society* **2015,** *137* (13), 4460-4468.

13. Wu, Y.; Islam, A.; Yang, X.; Qin, C.; Liu, J.; Zhang, K.; Peng, W.; Han, L. Retarding the crystallization of PbI2 for highly reproducible planar-structured perovskite solar cells via sequential deposition. *Energy & Environmental Science* **2014,** *7* (9), 2934-2938.

14. Hao, F.; Stoumpos, C. C.; Liu, Z.; Chang, R. P. H.; Kanatzidis, M. G. Controllable Perovskite Crystallization at a Gas–Solid Interface for Hole Conductor-Free Solar Cells with Steady Power Conversion Efficiency over 10%. *Journal of the American Chemical Society* **2014,** *136* (46), 16411-16419.

15. Tian, Y.; Scheblykin, I. G. Artifacts in Absorption Measurements of Organometal Halide Perovskite Materials: What Are the Real Spectra? *The Journal of Physical Chemistry Letters* **2015,** *6* (17), 3466-3470.

16. Lian, Z.; Yan, Q.; Lv, Q.; Wang, Y.; Liu, L.; Zhang, L.; Pan, S.; Li, Q.; Wang, L.; Sun, J.-L. High-Performance Planar-Type Photodetector on (100) Facet of MAPbI3 Single Crystal. *Scientific Reports* **2015,** *5*, 16563.

17. Kim, J.; Lee, S.-H.; Lee, J. H.; Hong, K.-H. The Role of Intrinsic Defects in Methylammonium Lead Iodide Perovskite. *The Journal of Physical Chemistry Letters* **2014,** *5* (8), 1312-1317.

18. Guerrero, A.; Juarez-Perez, E. J.; Bisquert, J.; Mora-Sero, I.; Garcia-Belmonte, G. Electrical field profile and doping in planar lead halide perovskite solar cells. *Applied Physics Letters* **2014,** *105* (13), 133902.

19. Wang, Q.; Shao, Y.; Xie, H.; Lyu, L.; Liu, X.; Gao, Y.; Huang, J. Qualifying composition dependent p and n self-doping in CH3NH3PbI3. *Applied Physics Letters* **2014,** *105* (16), 163508.

20. Jeon, Y.-J.; Lee, S.; Kang, R.; Kim, J.-E.; Yeo, J.-S.; Lee, S.-H.; Kim, S.-S.; Yun, J.-M.; Kim, D.-Y. Planar heterojunction perovskite solar cells with superior reproducibility. *Scientific Reports* **2014,** *4*, 6953.

21. Becke, A. D. Density-functional thermochemistry. III. The role of exact exchange. *The Journal of Chemical Physics* **1993,** *98* (7), 5648-5652.

22. De Angelis, F. Modeling Materials and Processes in Hybrid/Organic Photovoltaics: From Dye-Sensitized to Perovskite Solar Cells. *Accounts of Chemical Research* **2014,** *47* (11), 3349-3360.

23. Yang, Y.; Weaver, M. N.; Merz, K. M. Assessment of the "6-31+G** + LANL2DZ" Mixed Basis Set Coupled with Density Functional Theory Methods and the Effective Core Potential: Prediction of Heats of Formation and Ionization Potentials for First-Row-Transition-Metal Complexes. *The Journal of Physical Chemistry A* **2009,** *113* (36), 9843-9851.

Chapter 5

Publication 2

Formation Criteria of High Efficiency Perovskite Solar Cells in Ambient Conditions. Aranda, C.; Cristobal, C.; Shooshtari, L.; Li, C.; Huettner, S.; Guerrero, A. *Sustainable Energy & Fuels, **2017**, 1, 540-547.*

CANDIDATE´S CONTRIBUTION

Nature of Contribution	Extent of Contribution
✓ Development of the main idea. ✓ Contribution in the design of experiments. ✓ Fabrication of PSCs. ✓ Performing of the UV-Absorbance measurements and analysis. ✓ Performing of *j-V* curves measurements. ✓ Writting part of the experimental section	85%

INTRODUCTION

This work establishes a robust method of fabrication of high PCE of PSCs based in $MAPbI_3$ materials under any atmospheric conditions. A coordinative competition between water and DMSO (polar solvent used in the synthesis of perovskite material) allows to perform an easy balance between relative humidity %RH of the ambient and DMSO:Pb ratio to adjust the amount of high coordinative solvents into the perovskite solution to enhance crystallinity properties, achieving efficiencies up to 19%. This method had been widely reproduced in several laboratories contributing with a major impact to the perovskite field.

PUBLISHED MANUSCRIPT

Formation Criteria of High Efficiency Perovskite Solar Cells in Ambient Conditions

Clara Aranda,[1] Cesar Cristóbal,[1] Leyla Shooshtari,[1,2] Cheng Li,[3] Sven Huettner,[3] Antonio Guerrero[1*]

[1] Institute of Advanced Materials (INAM), Universitat Jaume I, 12006 Castelló, Spain

[2] Institute for Nanoscience and Nanotechnology, Sharif University of Technology, Tehran, 14588-89694, Iran

[3] Organic and Hybrid Electronics, Macromolecular Chemistry I, University of Bayreuth, Universitätstr. 30, 95447 Bayreuth, Germany

Email: *aguerrer@uji.es*

Abstract

The field of lead halide perovskites for solar cell applications has recently reported impressive power conversion (PCE) above 22 % using complex mixed cation formulations. Very importantly, highest PCE have been obtained using totally dry environmental conditions increasing the processing costs (i.e. use of glovebox). In this work devices processed in air under different ambient conditions are prepared with PCE approaching 19 % for the simplest lead halide perovskite ($MAPbI_3$, MA= Methyl ammonium). It is shown that the PbI_2:MAI:additive complex needs to be generated in the correct stoichiometry (1:1:1) where additives are any highly polar molecule able to stabilize the complex (i.e. H_2O or Dimethylsulphoxide (DMSO)). At high humidity conditions H_2O is incorporated into the complex and only small concentrations of further additives are needed. Precursor formulations not adequately balanced for the humidity conditions lead to films with poor morphology as evidenced by SEM. These films show negative multiiodide plumbate chemical defects as observed by absorbance measurements. These chemical defects act as recombination centers reducing the photocurrent and Fill Factor in photovoltaic devices. In addition, it is shown the undesirable high conductivity of the perovskite hydrates ($\sigma = 8x10^{-1}$ Scm^{-1}), up to seven orders of magnitude higher than the pure $MAPbI_3$, indicating that the presence of hydrates may act as shunting pathways that can significantly reduce the open circuit potential.

Keywords: **Perovskite, coordination chemistry, defects, humidity, absorption.**

Table of Contents (TOC)

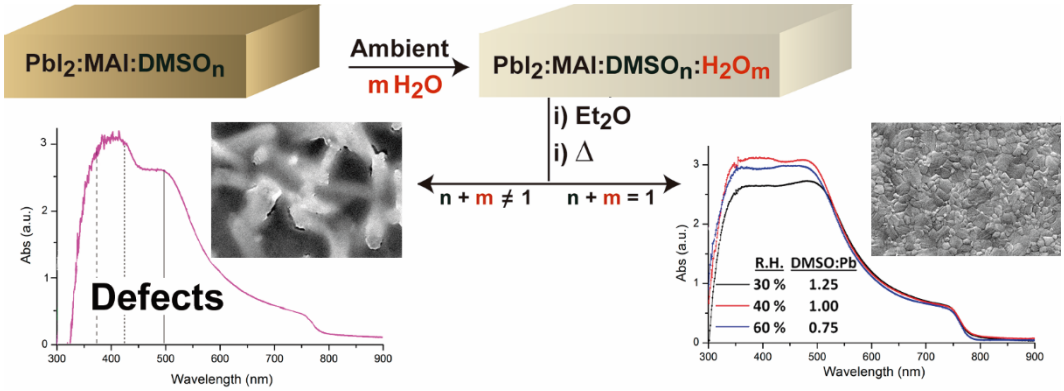

Photovoltaic devices based on lead halide perovskites have emerged as strong candidates to compete with already commercially available technologies.[1] Impressive certified power conversion efficiencies (PCE) of 21.6 % have been obtained using complex formulations where several cations are included in the basic formula ABX_3 where A is a monovalent cation (A= Cesium, Methylammonium (MA), formamidinium and rubidium), B is a divalent metal (B=Pb) and X is a halogen (X= Iodide and Bromide).[2] Alternatively, highest reported efficiencies for more simple formulations like $MAPbI_3$ is in the range of 18-19 %.[3-4] Very importantly, highest PCE are typically obtained for perovskite layers processed under totally dry conditions which would ultimately increase the costs associated to production. Unfortunately, there is not a clear answer in the field on whether the presence of environmental water is positive or negative. Indeed, the beneficial effect of environmental water has been independently reported by different authors but record efficiencies are obtained under dry conditions.[5-6] To further add complexity to the topic very often research articles do not provide details on whether the process has been carried out in a glovebox, humidity controlled laboratories or in ambient conditions. For this reason there is a need to find a robust process in ambient conditions able to provide perovskite solar cells with high efficiencies based on the good understanding of the effect of water on crystallization and physical implications.

Crystallization of $MAPbI_3$ is typically carried out from highly coordinating solvents required to dissolve the PbI_2 precursor including Dimethylsulphoxide (DMSO), N,N-Dimethylformamide (DMF) or γ-Butyrolactone (GBL).[7-11] The latest improvements in device efficiency are all connected with the production of perovskite films with few defects that show very high carriers diffusion lengths exceeding tens of micrometers.[12] Indeed, increased crystallinity of the perovskite layer is related with low presence of grain boundaries and impurities, both factors limiting the device performance.[13] Recently, the perovskite layer has been prepared highly reproducibly in a one step process by generation of the PbI_2:MAI:DMSO complex from DMF solvent.[7] The use of a solvent like Et_2O or toluene is required to wash out the carrier solvent during spin coating of the perovskite layer whilst not dissolving the perovskite layer. A final thermal treatment promotes the slow evaporation of the weakly bound polar additive (DMSO). [3, 7] Similarly, high quality perovskite layers can be produced in a two-steps method where a thin homogeneous layer of PbI_2 is prepared *via* the coordination complex with either DMSO,[14] H_2O[15] and more recently with acetonitrile.[16] In this case, the weakly bound additive is displaced by the subsequent addition of either MAI or FAI, followed by a thermal treatment.

Similarly to DMSO, water molecules are highly coordinating molecules known to be key players during degradation and crystallization of the perovskite layer. Several authors have described the effect of water during degradation of perovskite solar cells.[6, 17-20] It has been reported that water in the gas phase rapidly diffuses in perovskite films to generate hydrates *via* a two-step process starting with formation of $MAPbI_3 \cdot H_2O$ followed by $(MA)_2PbI_6 \cdot H_2O$ after prolonged exposure to moisture.[17] A perfect understanding on the actual role of water during crystallization of the perovskite layer has been more elusive due to the high complexity of the system.[21] For example, depending on the selected process a small amount of water arising from ambient moisture may be required to provide adequate film morphology.[5,22] Similarly, Snaith *et al.* described film formation under different relative humidity (R.H.) conditions and showed that the presence of water leads to less continuous morphology but significantly improved photoluminescence, film formation is faster, and showed improved device performance.[6] In the most extreme case liquid H_2O has been added to the precursor solution to generate devices with high quality of $MAPbBr_3$.[23] Unfortunately, these results are in apparent contradiction with results

obtained for top efficiency devices which are typically produced under totally dry environment.[2, 24]

Here we report the separation of effects related to water present in the ambient from that of solvent/additives (i.e. DMSO). Crystallization of $MAPbI_3$ is systematically studied as a function of the DMSO:Pb ratio and R.H. in the ambient using a one-step perovskite deposition method. Both, water and DMSO will compete to coordinate to the lead atom for generation of PbI_2:MAI:Additive complex. We correlate the presence of DMSO and H_2O during processing of the films with the final morphology of the films and generation of chemical defects. Overall, we provide a clear picture on the role of water and additives during crystallization of the perovskite layer and how the coordination chemistry will dictate the nature of chemical defects that limit the device performance.

Experimental

Materials and precursor solutions

All materials were used as received:FTO glasses (25 × 25 mm, Pilkington TEC15, ~15 Ω/sq resistance), TiO_2 paste (Dyesol 30NRD, 300 nm average particle size), CH_3NH_3I (DYESOL), PbI_2 (TCI, 99.99 %), titanium diisopropoxidebis (acetylacetonate) (75% in isopropanol, Sigma-Aldrich), spiro-OMeTAD (Merck). The perovskite precursor solution was prepared by reacting DMF solutions (50 wt %) containing MAI and PbI2 (1:1 mol %) and MAI, PbI2 and DMSO (1:1:1 mol %) and for the different humidities, the molar ratio of DMSO was changed from 0; 0.5; 0.75; 1;1.25;1.5, as is shown in figures above. The spiro-OMeTAD solution was prepared by dissolving in 1 mL of chlorobenzene 72.3 mg of (2,2′,7,7′-tetrakis(N,N′-di-p-methoxyphenylamine)-9,9′-spirobifluorene), 28.8 μL of 4-tert-butylpyridine, and 17.5 μL of a stock solution of 520 mg/mL of lithium bis-(trifluoromethylsulfonyl) imide in acetonitrile.

Interdigitated electrodes:

A perovskite layer was deposited on 20x20 mm^2 glass as described below for photovoltaic devices. A shadow mask with an interdigitated pattern and 200 □m channel length was used. Gold was thermally evaporated (60 nm) at a base pressure of 2×10^{-6} mbar. Electrodes containing the monohydrate $MAPbI_3 \cdot (H_2O)$ described in the main text was prepared by introducing interdigitated electrodes containing $MAPbI_3$ into a climate chamber (Dycomental, Model CCK) at 70 °C during 1 h.

Photovoltaic Device fabrication: All the process was carried out outside the glovebox in ambient conditions at different humidity conditons. The %RH of the lab was measured every time before the preparation of the solution with a digital hygro thermometer. Photovoltaic devices were prepared over FTO glasses, which were partially etched with zinc powder and HCl (2 M). The substrates were cleaned with soap (Hellmanex) and rinsed with Milli-Q water and ethanol. Then, the substrates were sonicated for 15 min in a solution of acetone:isopropanol (1:1 v/v), rinsed with ethanol and Milli-Q water, and dried with compressed air. After that, the substrates were treated in a $UV-O_3$ chamber for 15 min. The TiO_2 blocking layer was deposited onto the substrates by spray pyrolysis at 450 °C, using a titanium diisopropoxide bis(acetylacetonate) solution diluted in ethanol (1:9, v/v), with oxygen as carrier gas. The spray was performed in 3 steps of 6 s, spraying each time 5 mL (approx.), and waiting 30 s between steps. After the spraying process, the films were kept at 450 °C for 30 min. The mesoporous TiO_2 layer was deposited by spin coating at 2000 rpm during 10 s using a TiO_2 paste diluted in ethanol (1:5, weight ratio). After drying at 100 °C for 10 min, the TiO_2 mesoporous layer was heated at 500 °C for 30 min and later cooled to room temperature. Before the deposition of perovskite films, 100 μl of a lithium bis-(trifluoromethylsulfonyl) imide 35 mM solution in acetonitrile is prepared and deposited on the top of the device by spin-coating at 3000 rpm (2000 ac)

during 10 seconds. After that, the substrates are heated up at 450ºC during 30 min. The perovskite precursor solution (50 μL) was spin-coated at 4000 rpm for 50 s. DMF is selectively washed with non-polar diethyl ether while one-step spin- coating at 4000 rpm is carried out. After deposition, the substrate was annealed at 100 °C for 3 min. Then, the perovskite films were covered with the hole-transporting material (HTM) by dinamically spin coating at 4000 rpm for 30 s, using 50 μL of spiro- OMeTAD solution. Finally, 60 nm of gold was thermally evaporated on top of the device to form the electrode contacts using a commercial Univex 250 chamber, from Oerlikon Leybold Vacuum.

Film and Device characterization

Ultraviolet-visible absorption spectra were recorded by a Cary 500 Scan VARIAN spectrophotometer in the 250-800 nm wavelength range. The morphology of the powders was observed using field-emission SEM using either a JEOL 7001F for powders. The XRD pattern of the prepared solids were measured using X-ray diffractometer (D8 Advance, Bruker-AXS) (Cu Kα, wavelength λ=1.5406 Å). Photovoltaic devices were characterized using an Abett Solar simulator equipped with 1.5 AM filter. The light intensity was adjusted to 100 $mWcm^{-2}$ using a calibrated Si solar cell. Devices were measured using a mask to define an active area of 0.11 cm^2. Each data point shown in the graphs corresponds to an average of 20 independent devices.

Results and discussion

Effect of additives on morphology and chemical defects

During formation of the perovskite layer using the one step deposition method the correct stoichiometry of the PbI_2:MAI:additive intermediate complex needs to be generated as reported in the literature (Scheme 1).[7] Very importantly, the solution coordination chemistry of the lead atom with solvent and additives will dictate the chemical species that will be generated in the films.[25] In fact, several multiiodide plumbate ions chemical defects have been detected in films with proportions modulated by the processing conditions. For example, the effect of the solvent is key to stabilize the chemical defects and common solvents have been listed attending to the coordination ability towards PbI_2: H_2O>DMSO>DMF>GBL. As water molecules are the most coordinating molecules in the series it is clear that water present in the ambient will compete with DMSO and iodide ions present in the precursor solution during the spin coating process to generate PbI_2:MAI:Additive complex. Indeed, DMSO and H_2O additives will strongly interact with solvent molecules and iodide ions in some cases displacing iodide ions coordinating the Pb as monitored by absorbance measurements in the supporting information. As it will be shown below the total amount of additives (i.e. DMSO and H_2O) needs to be adjusted to provide the correct stoichiometry of the PbI_2:MAI:additive intermediate complex and a final $MAPbI_3$ film free of chemical defects (Scheme 1). In the reported literature procedure the initial precursor solution contains a proportion 1:1:1 with a molar DMSO value of n=1 but the process is carried out in air. Interestingly, the total molar proportion of additive molecules coordinating PbI_2:MAI is higher in the ambient due to the presence of water (m). A tentative optimum molar concentration of $n+m\approx1.5$ will lead to adequate perovskite morphologies as discussed at the end of the manuscript. If the proportion of additives is not well balanced ($n+m\neq1.5$) films will show inadequate morphology and the presence of chemical defects.

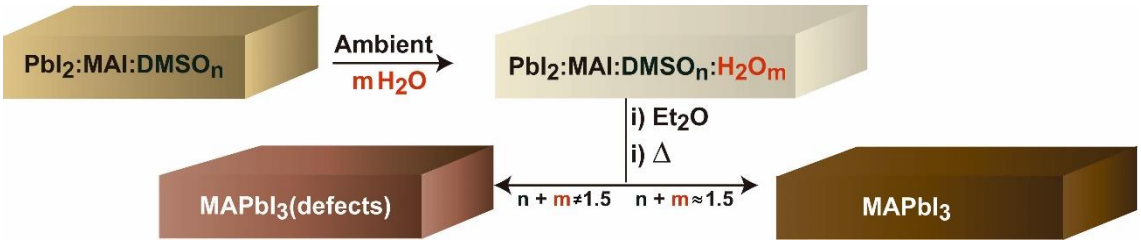

Scheme 1: Schematic representation of key steps during the one-step fabrication process that takes into account the effect of ambient water.

In order to provide understanding on the impact of additives (i.e. DMSO or H_2O) on the morphology during perovskite generation several films were prepared under different conditions and were characterized by SEM analysis and absorbance measurements. Figure 1 shows SEM images of representative films/devices fabricated using different DMSO:Pb ratios at constant R.H. (40 %). Therefore, the proportion of H_2O (m in Scheme 1) introduced in the system will be fixed. In the following discussion we refer to the DMSO:Pb ratio as a tool to modify the proportion n of DMSO in the complex as this will be the key parameter to control the crystallization as a function of the humidity conditions. The top view image (Figure 1a) of a device fabricated with a low proportion of DMSO (Ratio 0.5) clearly shows a fiber-like morphology typical from materials fabricated from pure DMF.[21, 25-26] This result not only indicates that the proportion of DMSO is insufficient to generate the PbI_2:MAI:Additive complex but also reveals the presence of uncovered electrode surface which will lead to the hole transport layer (HTL) to be in direct contact with the electron transport layer (ETL). As the DMSO proportion is increased to a DMSO:Pb ratio of 1.0 the complex is formed correctly as reported by Ahn *et al.*[7] We observe a final morphology characterized by the presence of compact films with perovskite domains in the order of 100-500 nm (Figure 1b). Therefore, the correct formation of the intermediate complex followed by the thermal treatment promotes the slow evaporation of the weakly bound DMSO providing the adequate morphology with a totally covered surface. Finally, a further increase of DMSO to a ratio of 1.5 (Figure 1c) also leads to large crystalline domains similar to those in Figure 1b. Interestingly, a large proportion of pinholes develops with cylindrical shape typical from gas evaporation from a quasi-solid state. Indeed, it is expected that the additional 0.5 mol of DMSO exceeding the adequate complex ratio will evaporate under the thermal treatment and the extra occupied volume will lead to voids in the film. It is also noted the presence of domains with large differences in contrast. Light grey domains corresponds to domains containing large proportion of heavy atoms (i.e. Pb or I) and dark domains contain larger proportion of lighter atoms such as carbon or oxygen like those expected from remaining DMSO in the films. We note that this type of morphology has recently been observed by Yang *et al.*[27] using GBL/DMSO mixtures. In that case it was shown that an additional treatment with MABr was able to recover a morphology like that shown in Figure 1b. These results point to the possibility that multiiodide plumbates with a number of iodide ions <6 are being stabilized by DMSO and the MABr treatment is able to recover the PbX_6^{4-} octahedra. The presence of bound DMSO will be confirmed below by absorption measurements. Analysis of the cross-section images (Figure 1d, 1e and 1f) is quite revealing as the presence of pinholes in the perovskite layer is observed for devices fabricated with PbI_2:DMSO ratio of 0.5 and 1.5. These pinholes will inevitably lead to the direct contact between the Spiro-OMeTAD with the mesoporous layer of TiO_2 providing

additional carrier recombination pathways, as it will be discussed in the final part of the manuscript.

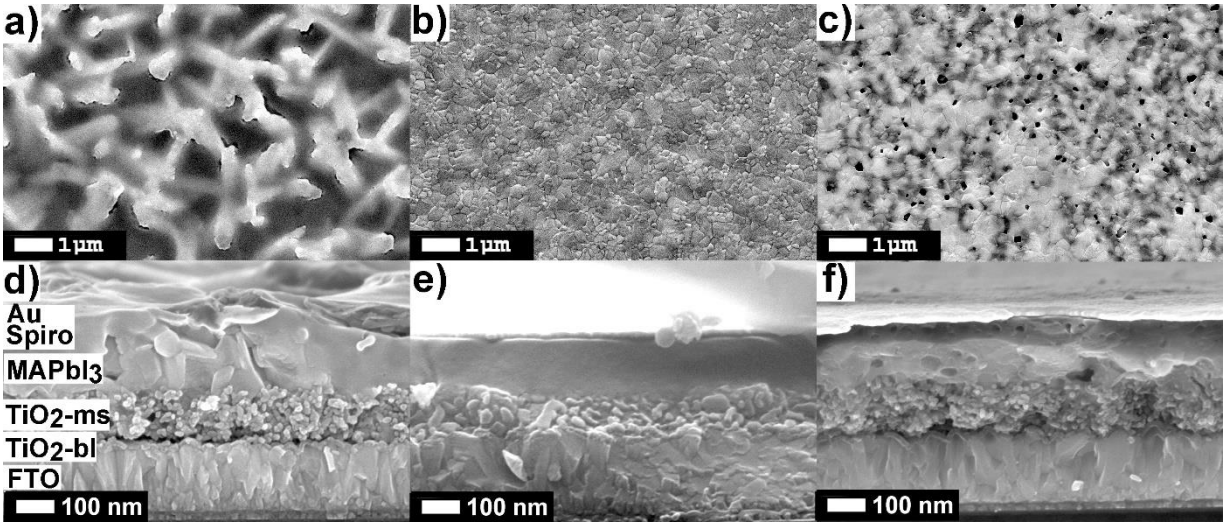

Figure 1: SEM images of devices fabricated at 40 % R.H. using different DMSO:Pb ratios: 0.5 (a and d), 1.0 (b and e) and 1.5 (d and f). Top view (a, b and c) and cross-section (d, e and f).

Alternatively, absorption measurements have proved recently useful to detect chemical defects in perovskite films. Theoretical absorption bands of pure $MAPbI_3$ are characterized by the presence of two bands at λ_{max}≈500 nm and λ_{max}≈760 nm as reported by de Angelis *et al.* using DFT calculations.[28] Alternatively, experimental absorption bands of $MAPbI_3$ films are usually more complex showing the presence of additional bands below 500 nm. Indeed, several species have been observed in films by different authors such as $PbIS_5^+$, PbI_2S_4, $PbI_3S_3^-$, $PbI_4S_2^{2-}$, PbI_5S^{3-}, PbI_6^{4-} and $(Pb_2I_4)_n$ chains all responsible for the bands in the region of ≈500 nm.[21, 29,25] Furthermore and to provide a complete picture of the absorbance response we also need to note that substrates partially covered by $MAPbI_3$ films are characterized by strong scattering >750 nm. This scattering observed when measurements are carried out using regular spectrophotometers, as opposed to optical microscopy of single crystals, leads to artifacts decreasing the intensity of bands in the range of 250-750 nm.[30]

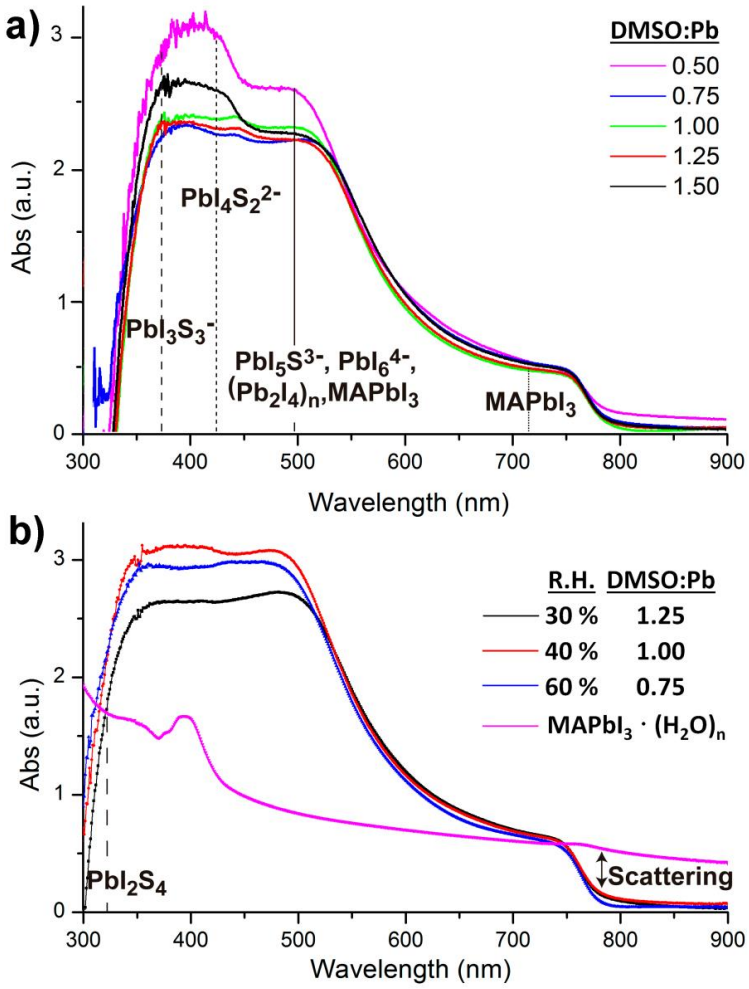

Figure 2: a) Absorption spectra of $MAPbI_3$ films measured as a function of the DMSO:Pb ratio used in the precursor solution, films fabricated at R.H.=40 %. b) Absorption measurements of $MAPbI_3$ films is studied as a function of the DMSO:Pb ratio used in the precursor solution fabricated at R.H.=40 %. λ_{max} for representative multiiodide plumbate ions are represented as vertical lines where S= solvent.

In this work, the absorption of $MAPbI_3$ films is studied as a function of the DMSO:Pb ratio used in the precursor solution fabricated at R.H.=40 %, similar conditions to those used for the SEM analysis. Figure 2a shows similar absorption band intensities in the 750 nm region for all films pointing to equal thickness of $MAPbI_3$ layer. Alternatively, absorption bands intensity in the region 350-550 nm strongly depends on the DMSO:Pb ratio. Films containing a ratio of 0.75 to 1.25 are very flat in the high energy region and are characterized by a morphology containing large crystalline domains as those shown in Figure 1b with no pinholes. Alternatively, films with a fiber-like morphology (0.5 ratio, Figure 1a) or presence of holes (1.5 ratio, Figure 1c) show bands at 350-550 nm with increased intensity, just where several multiodide plumbate species show their maximum absorbance. In particular, it appears that films containing high surface of grain boundaries do show increased intensities for multiplumbate ions such as $PbI_3S_3^-$, $PbI_4S_2^{2-}$, PbI_5S^{3-}, PbI_6^{4-} or $(Pb_2I_4)_n$. During film formation the highly coordinating DMSO is able to stabilize the species as noted in the SEM image Figure 1c where the dark domains mostly appear around the holes indicating that DMSO remains in the film rather localized in this area.

We note that a morphology presenting holes (Figure 1c) lead to short PL decay time indicating that species associated to the grain boundaries play a very important role in the recombination pathways.[27] Analysis of the precise proportion and the electrical effect of each of these species is beyond the scope of this work but in any case it appears difficult to separate physical and morphology effects.

Relative humidity effect on chemical defects and electrical properties

There are some precedents in the literature of film formation under different humidity atmospheres paying special attention to the effect on the morphology. For example, Snaith *et al.* described generation of non-continuous morphologies under high R.H. with significantly improved photoluminescence and fast film formation.[6] However, a correlation between generated species on films at humid environments and electrical properties has not been described. Here, we proceed to study the effect of water by modifying the relative humidity during processing of the devices. According to the process described in Scheme 1 and the competing displacement reactions described previously it is clear that water present in environmental humidity can be regarded as an additive which will affect crystallization of the perovskite layer. For this purpose the DMSO:Pb ratio has been modified for films fabricated at different humidity conditions and complete absorption data is shown as supporting information. Absorption results at 30% and 60% R.H. show similar trends as those observed in Figure 2a with bands with increased intensity in the 350-550 nm region when the amount of water and DMSO is not properly balanced to obtain the intermediate complex. Alternatively, it is very interesting to note that flat absorbance profiles in the region 350-550 nm is only obtained when the DMSO/H_2O concentration is controlled at given humidity conditions (Figure 2b). This certainly agrees with a competitive process to coordinate the Pb core between DMSO and H_2O. For example, as the humidity increases to R.H.=60 % a lower amount of DMSO is required to provide large crystalline domains as H_2O is acting as an additive to form the PbI_2:MAI:additive intermediate complex. Alternatively, when R.H. is reduced to 30 % increased amount of DMSO:Pb of 1.0-1.25 is required to obtain optimum morphology with reduced amount of multiiodide plumbate defects.

The electrical properties of hydrate complexes can be monitored by preparation of interdigitated electrodes containing perovskite hydrates. Here we follow a reported process to produce $MAPbI_3$ hydrates from $MAPbI_3$ films using a climatic chamber at R.H.=80 % and 60 °C during 60 min.[17] Leguy *et al.* have optically characterized $MAPbI_3{\cdot}H_2O$ using ellipsometry measurements and showed the material to form nearly colorless needles. Needles of similar morphology as previously described are obtained as observed by SEM (Figure 3a). The hydrate species generate wires of variable size but some exceeding lengths of 100 □m. A close inspection into the morphology shows that the wires are not totally compact. In addition, a picture of the film is shown as supporting information where the white colour of the perovskite hydrate can be observed. The XRD spectra shown as supporting information show some peaks which may be related to the $MAPbI_3{\cdot}H_2O$ complex (2□=25.4°, 28.4° and 31.9°) as compared with the theoretical powder spectra. In addition, some crystalline $MAPbI_3$ domains indicating that the weakly bound water molecules have been released during the XRD measurement. Finally, degradation product PbI_2 is also detected. However, other amorphous hydrate complexes may be present as well. Absorption spectra of the film is shown in Figure 2b and high degree of scattering is observed above 750 nm which will reduce the intensity of bands below this wavelength value as described before. In any case a band is observed at 400 nm typical from $PbI_3S_3^-$ or $PbI_4S_2^2$ species and higher intensity bands appear below 350

nm that extends beyond 300 nm corresponding to species with still lower amount of iodides.

The electrical properties of the hydrate were probed in an interdigitated electrode configuration (Au/ $MAPbI_3 \cdot (H_2O)n$/Au) with a 200 □m channel length on glass, see inset Figure 3b. Using similar a configuration conductivity of $MAPbI_3$ has been measured by Johansson *et al.*.[31] and Müller *et al.* noted that conductivity increases with exposure to humid ambient conditions but pure films containing $MAPbI_3 \cdot (H_2O)n$ hydrates have not been reported to this date.[18] Current-Voltage measurements were carried out in ambient conditions in the dark at scan rates of 100 mV/s. *I-V* curves of $MAPbI_3$ and $MAPbI_3 \cdot (H_2O)n$ show Ohmic behavior with higher currents for the monohydrate complex of nearly six order of magnitudes at ±1 V. We note that stability of the interdigitated electrode containing $MAPbI_3 \cdot (H_2O)n$ is low due to the large currents passing through the wires with a small diameter. Taking into account the device configuration conductivity values of the perovskite in the order of $1x10^{-8}$ Scm^{-1} and $8x10^{-1}$ Scm^{-1} are calculated, respectively. These results are in good agreement with previously reported results in interdigitated configuration and highlight that extremely sensitivity of the perovskites to moisture environment. We also note that conductivity values have been calculated attending to the geometric area defined by the gold contacts/perovskite layer. However, the real active area relevant for the calculation will be much smaller as it is defined by the hydrate wires in direct contact with the gold electrode. Therefore, the provided conductivity value of $MAPbI_3 \cdot H_2O$ only provides the low conductivity limit. In conclusion, the presence of hydrates will increase the conductivity of the perovskite layer several orders of magnitude and this will create alternative pathways for carriers to reach the contacts that may lead to shunting or a reduction of the selectivity of the contacts.

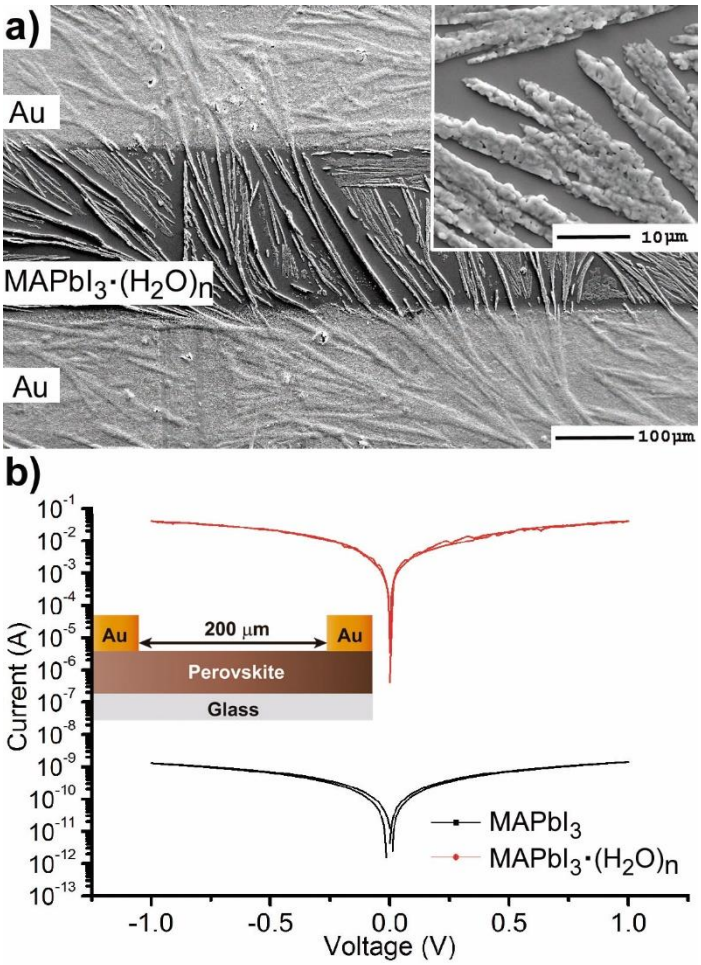

Figure 3: a) SEM image of an interdigitated electrode in the configuration Au/ $MAPbI_3 \cdot (H_2O)_n$/Au with a 200 □m channel. b) Current-Voltage curve of interdigitated electrode in the configuration shown in a) for devices containing either $MAPbI_3$ or $MAPbI_3 \cdot (H_2O)_n$.

Impact of Water and Additives on photovoltaic devices

Now that the coordination chemistry of DMSO and H_2O has been correlated with film formation morphology, absorbance and electrical properties we proceed to analyze the effect of DMSO and H_2O in photovoltaic devices. Devices are fabricated in the configuration FTO/TiO_2-bl/TiO_2-meso/$MAPbI_3$/Spiro-OMeTAD/Au where the DMSO:Pb ratio is varied under different series in humidity conditions. In order to be able to compare with the previous sections of the manuscript the same processing conditions have been used and results the same. Each data point shown in Figure 4 corresponds to an average of 20 independent devices measured under reverse bias conditions at a scan rate of 50 mV/s. Overall, device efficiency can be increased from 10.8% to 18.6% by carefully adjusting the DMSO:Pb ratio attending to the R.H.

At a given humidity conditions we observe that photocurrent (*Jsc*) of devices varies from ≈20-22 mA/cm^2 with the DMSO:Pb being higher for ratios between 0.75 and 1.25. Increased photocurrents are the result of an adequate morphology containing large crystalline domains with little presence of chemical impurities in the films. Lower photocurrents are obtained with devices at either low or high DMSO:Pb ratio as a result of inadequate morphology (Figure 1a and 1c) and presence of multiiodide plumbate species (Figure 2a). Note that absolute absorbance values are higher for films fabricated with low and high DMSO:Pb ratios (Figure 2a) but photocurrents are lower indicating

that the presence of the chemical species are related with recombination pathways. Alternatively, the highest studied humidity conditions decrease the achievable photocurrent indicating that the perovskite hydrate leads to increased recombination pathways. The open-circuit potential (V_{oc}) of the devices is rather insensitive to the DMSO:Pb ratio and seems to be more connected to the humidity conditions. Indeed, devices fabricated at R.H.=60 % show V_{oc} about 100 mV lower than those fabricated at low humidity conditions. It has been shown the highly conductive nature of the $MAPbI_3{\cdot}(H_2O)n$ hydrates. Then, it is clear that the monohydrate can act as charge carriers percolation pathways leading to shunting of the devices. This effect is more severe at low DMSO conditions (ratio of 0.5) where synthesis of the hydrate complex is maximized by reduction of competing molecules. Indeed, shunting pathways are already observed in the SEM cross-section of Figure 1d. Fill Factor (FF) of devices shows a similar trend to that of *Jsc* ranging from 60 to 78 representing depending on the processing conditions, this difference represents a 25 % increase for adequate conditions. In this regard increased DMSO and H_2O proportions during the processing conditions of the device lead to the lowest values. Therefore, it appears that not only the film morphology needs to be adequate but there should not be any excess of highly coordinating molecules as they seem to increase all recombination processes.

Very interestingly, at each humidity conditions the maximum efficiency can be maximized by tuning the DMSO:Pb ratio to obtain the correct intermediate complex stoichiometry. For example, at R.H. of 30 % the observed optimum DMSO:Pb ratio is 1.25 providing highest efficiencies in the series of 18.7% (V_{oc}= 1.05 V, J_{sc}= 22.4 mA/cm^2 and *FF*=78). At a given humidity conditions the required DMSO:Pb ratio to provide maximum efficiencies decreases as the R.H. increases. Indeed, at R.H.=60 % ratios of 0.75-1.00 offer maximum efficiencies of ≈14.5 % (V_{oc}= 1.00 V, J_{sc}= 20.5 mA/cm^2 and *FF*=72). This result clearly indicates that competition between DMSO and H_2O molecules is readily taking place following coordination chemistry reactions as those discussed previously. Interestingly, absorbance spectra of films providing the highest efficiency at each humidity conditions (Figure 2b) are flat in the range 350-550 nm indicating the presence of multiiodide plumbate ions are minimized. It is important to highlight that error bars are larger when low proportion of DMSO is used due to the presence of pinholes. The reduction in Jsc and V_{oc} in the presence of vapour water molecules is in agreement with the work by Leguy *et al.* as they observed up to a 90% drop in short-circuit photocurrent and ∼200 mV loss in open-circuit potential V_{oc} during degradation experiments.[17] In addition, extrapolation of the linear tendency observed in Figure 4b can also be used to calculate the ideal proportion of additives in a situation when no water is present (i.e. in a glovebox) providing the values n+m. =1.5 used in different parts of the manuscript.

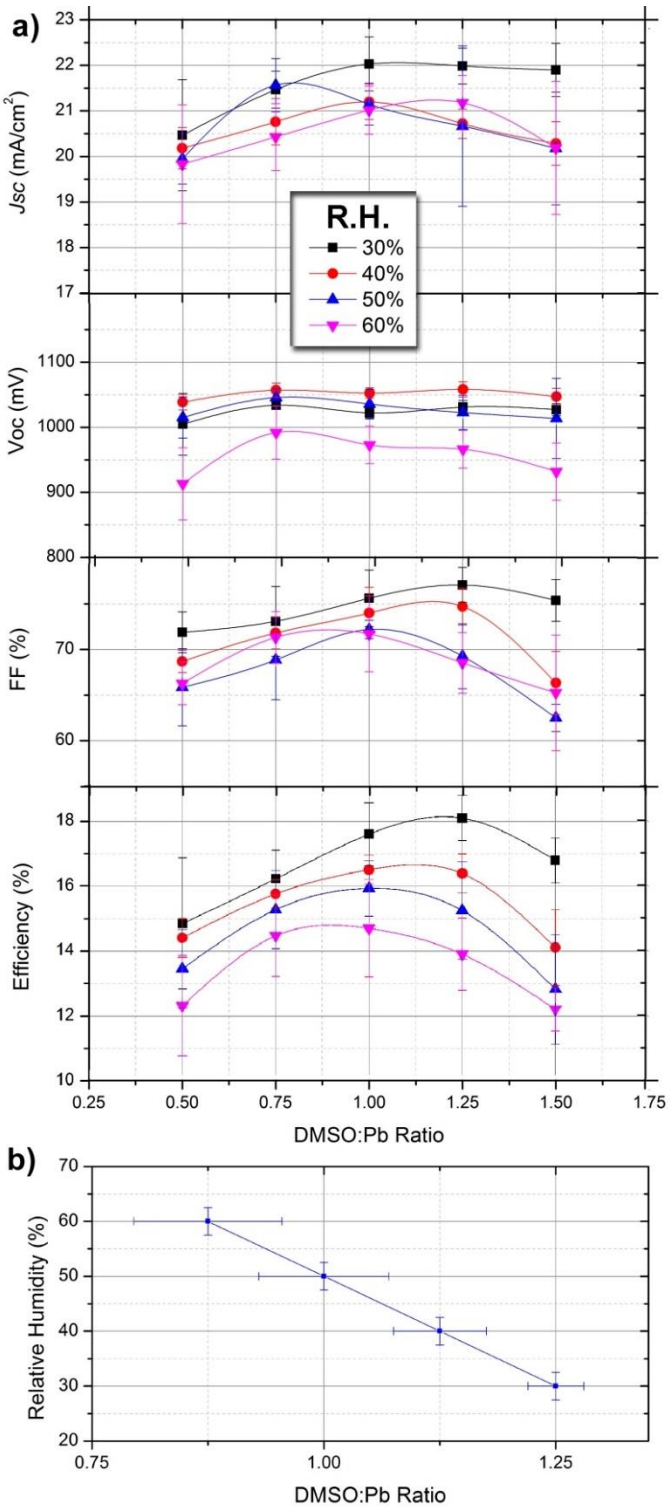

.

Figure 4: a) Efficiency parameters of devices fabricated in the configuration FTO/TiO_2-bl/TiO_2-meso/$MAPbI_3$/Spiro-OMeTAD/ as a function to the DMSO:Pb ratio used in the precursor solution fabricated under different relative humidity conditions. b) Observed maximum efficiency as a function of relative humidity and DMSO:Pb ratio.

From this data we note that the presence of water is in general negative for the final devices performance but its effect can be minimized by correctly formulating the precursor solution. Indeed, higher efficiencies are obtained for devices prepared under

low humidity conditions but in all cases DMSO:Pb ratio needs to be adjusted to provide maximum efficiencies. Very importantly, Figure 4b offers reference data for the reader to implement in their own processes taken into account different humidity conditions.

Conclusions

In the field of lead halide perovskite solar cells highest reported efficiencies are typically obtained for layers processed under a totally dry environment that ultimately increases the production costs. This manuscript presents new insights to minimize the negative effect of environmental water enabling the processing of solar cells in ambient air with high efficiencies and reproducibility. It is shown that the H_2O/DMSO ratio needs to be carefully adjusted to obtain adequate morphology and to reduce the presence of chemical defects. Both molecules compete to coordinate to the Pb atom which will limit the formation of the intermediate complex PbI_2:MAI:Additive responsible for the final properties of the films. High efficiency devices processed in air with PCE approaching 19 % can be obtained for the simplest perovskite formulation $MAPbI_3$ under different humidity conditions.

Supporting Information. Methods, further absorption measurements, XRD data.

Acknowledgements

We thank financial support by MINECO of Spain under project (MAT2013-47192-C3-1-R), and Generalitad Valenciana is acknowledged for financial support on the DISOLAR2 Project (PROMETEOII/2014/020). A. G. would like to thank the Spanish Ministerio de Economía y Competitividad for a Ramón y Cajal Fellowship (RYC-2014-16809). Serveis Centrals at UJI (SCIC) are acknowledged for the SEM measurement assistance.

Supporting Information

Formation Criteria of High Efficiency Perovskite Solar Cells in Ambient Conditions: Evidence for the Competition of Water and Additives

Clara Aranda,[1] Cesar Cristobal,[1] Leyla Shooshtari,[1,2] Cheng Li,[3] Sven Huettner,[3] Antonio Guerrero[1*]

[1] Institute of Advanced Materials (INAM), Universitat Jaume I, 12006 Castelló, Spain

[2] Institute for Nanoscience and Nanotechnology, Sharif University of Technology, Tehran, 14588-89694, Iran

[3] Organic and Hybrid Electronics, Macromolecular Chemistry I, University of Bayreuth, Universitätstr. 30, 95447 Bayreuth, Germany

Email: aguerrer@uji.es

Coordination Chemistry of the Precursor Solution

During formation of the perovskite layer using the one step deposition method the correct stoichiometry (1:1:1) of the intermediate complex PbI_2:MAI:DMSO needs to be generated. It is well established that water and DMSO are two highly polar molecules with similar coordinating properties. Then, it is clear that during device preparation in an ambient atmosphere both molecules will be competing to coordinate the Pb atom. We have recently shown that there is a direct competition between iodide ions and the solvents used in the precursor solution, clearly impacting the structural defects present in the films.[32] Scheme SI1 shows some representative equilibrium reactions that generate several multiiodide plumbate ions where all iodide ions, solvent/additive molecules (S) or other Pb atoms can coordinate to the lead and will be competing to fill the octahedral coordination sphere.

$$Pb(S)_6^{2+} \underset{-S}{\overset{+I^-}{\rightleftharpoons}} PbI(S)_5^{+} \underset{-S}{\overset{+I^-}{\rightleftharpoons}} PbI_2(S)_4 \underset{-S}{\overset{+I^-}{\rightleftharpoons}} PbI_3(S)_3^{-} \underset{-S}{\overset{+I^-}{\rightleftharpoons}} \cdots \quad \text{(Eq. 1)}$$

i.e. S=H_2O, DMSO or DMF

$$PbI_3(DMF)_3^{-} \underset{-I^-}{\overset{+DMSO}{\rightleftharpoons}} PbI_2(DMF)_3(DMSO) \quad \text{(Eq. 2)}$$

Scheme SI1: Example of competitive reactions between different solvents and additives to coordinate the lead atom.

Absorption spectra of PbI_2 dissolved in pure solvents shown (Figure SI1) confirm the equilibrium proposed in Scheme 1. Assignment of the bands that correspond to the species present under diluted conditions is provided in Figure 1 as reported previously: $PbIS_5^+$ (λ_{max}=286 nm), PbI_2S_4 (λ_{max} = 325 nm) and $PbI_3S_3^-$ (λ_{max} = 370).[32] Partially supporting this assignment the work by Kamat *el al.* described the photophysics of $PbI_3S_3^-$ and $PbI_4S_2^{2-}$ species.[33] Interestingly, the use of highly coordinating solvents like H_2O leads to

increased formation of species with a low number of iodide ions such as $PbIS_5^+$, PbI_2S_4 and possibly PbS_6^{2+} as highlighted by the increased intensity of bands in the high energy region. Alternatively, more discreetly coordinating molecules like DMF will not be so effective at displacing iodide ions from the lead coordinating sphere and species containing more iodide will be obtained (i.e. PbI_2S_4 or some $PbI_3S_3^-$).

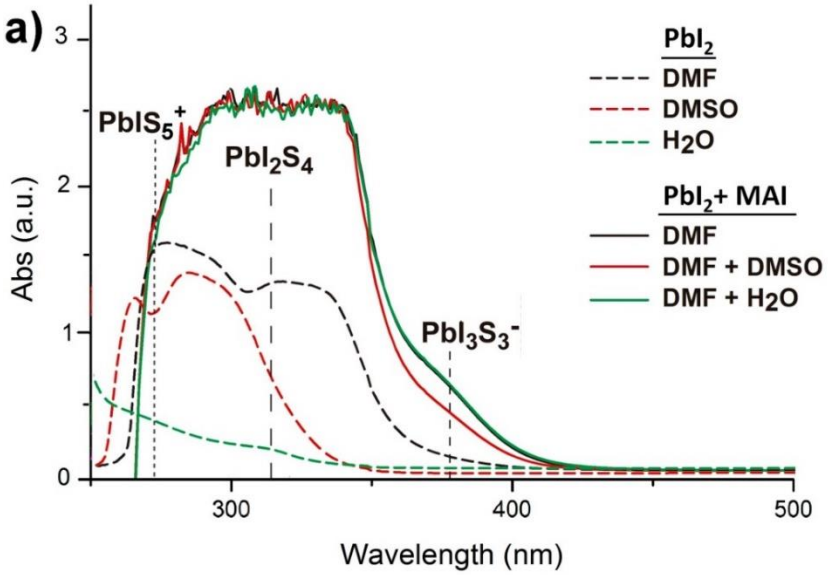

Figure SI1: Absorbance spectra of solutions containing PbI_2 (1mM) in different pure solvents (dashed line) and PbI_2 + MAI (1mM, 1:1 mol) mixtures in DMF (solid lines) either pure or with a small amount of additive (DMSO or H_2O). The proportion of additive is calculated to provide a PbI_2:MAI:DMSO ratio of 1:1:1. λ_{max} for representative multiiodide plumbate ions are represented as vertical lines where S= solvent/additives.

Furthermore, in order to study the effect of water/additive in the presence of MAI absorption measurements of solutions containing PbI_2:MAI in DMF (1 mM, 1:1 mol-ratio) are carried out. Very small amounts of either DMSO or H_2O are added to the solution which after solvent evaporation should lead to a perfect stoichiometry of the PbI_2:MAI:Additive complex (1:1:1). It is important to note that at these highly diluted conditions lead atoms are mostly surrounded by DMF molecules with a DMF/Additive mol-ratio of 25:1. However, the better coordinating ability of DMSO as opposed to DMF is evidenced by the reduction of the $PbI_3S_3^-$ absorption band intensity which indicates that DMSO will displace some Iodide ions that DMF molecules were unable to shift. This type of solvent displacement reactions is shown in Eq. 2 in Scheme SI1. Alternatively, water molecules are the most coordinating molecules in the series of solvents and if present in the precursor solution we expect a similar displacement as that shown for DMSO. Very interestingly, when H_2O is added no changes in absorption bands intensity are observed. It is well known that water molecules and DMF interact very strongly through hydrogen bonds being DMF able to breakdown the water structure by generation of $DMF{\cdot}H_2O$ dimers and aggregates ($(DMF)_m{\cdot}(H_2O)_n$).[34] Therefore, it is expected that at this small water concentration no H_2O molecules will be free to coordinate to the Pb atom. Unfortunately, at high water concentration the PbI_2 precipitates from solution and no representative data for devices can be obtained. However, a very different scenario is expected during spin coating of the precursor solution where the effect of water will be more prominent at the end of the drying process, when most of the DMF has been evaporated. Indeed, it is observed that the time of antisolvent addition will depend very

much on relative humidity (R.H.) conditions. Shiny and scattering-free films will be obtain only if antisolvent is added at the correct waiting time. Whilst at high R.H. long waiting times are required at low R.H. addition of diethyl ether will need to be fast and this is a direct consequence of the different kinetics to coordinate Pb by H_2O and DMSO molecules.

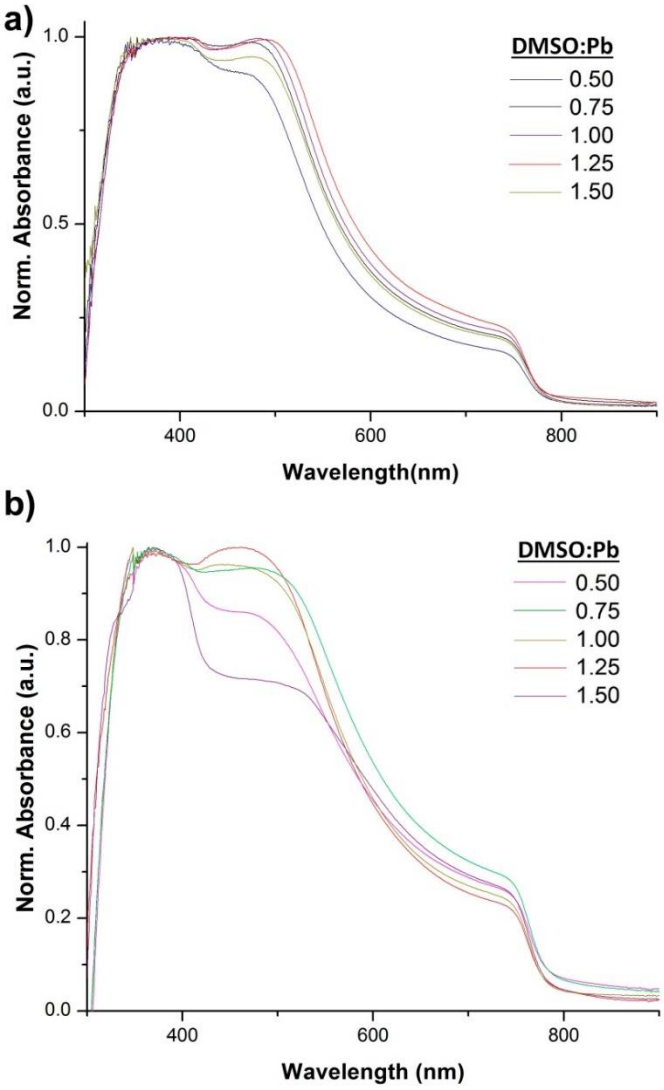

Figure SI2: a) Absorption spectra of $MAPbI_3$ films measured as a function of the DMSO:Pb ratio used under different R.H. conditions: a) R.H.= 30 % and b) R.H.= 60%.

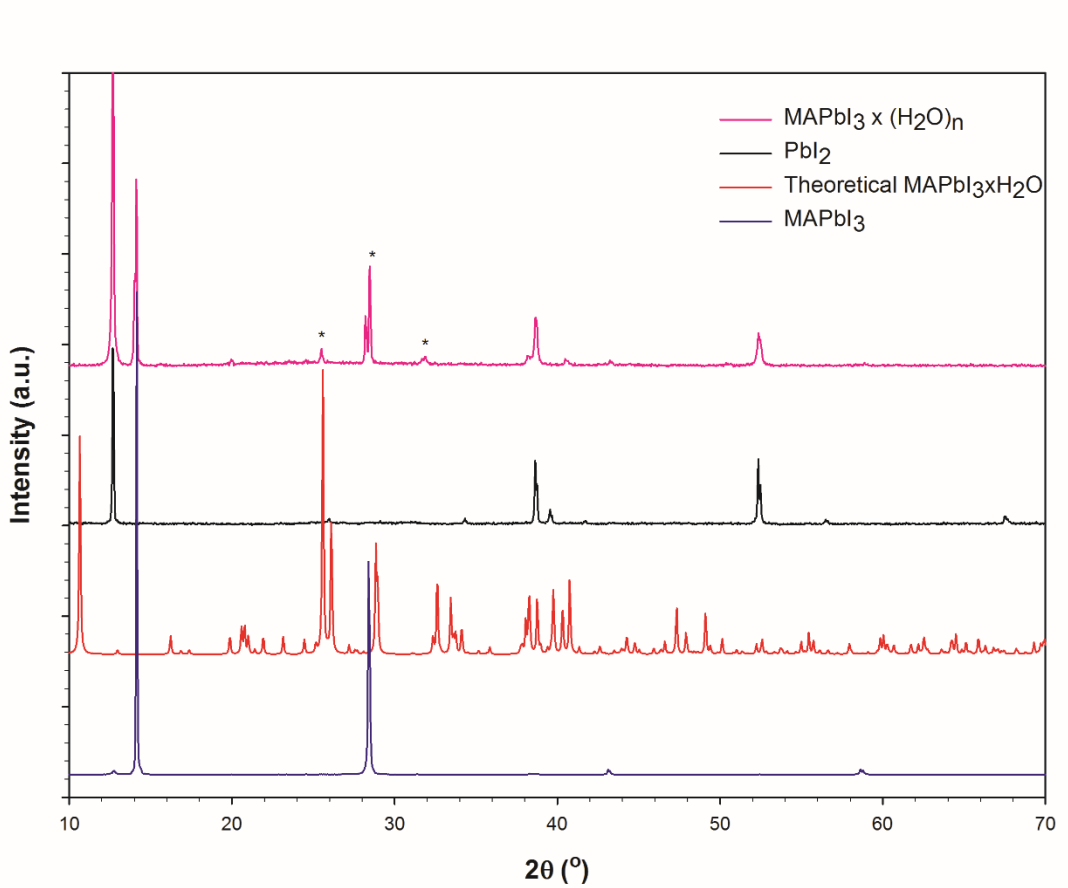

Figure SI3: Comparison of XRD difraction patterns of pure $MAPbI_3$ and PbI_2 with the theoretical powder of monohydrate $MAPbI_3 \cdot H_2O$ and the reaction product of $MAPbI_3$ in a climatic chamber at R.H.= 80 % and 60 °C during 60 min. Signals marked with asterisc may arise from the monohydrate complex.

References

1. Green, M. A.; Emery, K.; Hishikawa, Y.; Warta, W.; Dunlop, E. D. Solar cell efficiency tables (Version 45). *Progress in Photovoltaics: Research and Applications* **2015,** *23* (1), 1-9.

2. Saliba, M.; Matsui, T.; Domanski, K.; Seo, J.-Y.; Ummadisingu, A.; Zakeeruddin, S. M.; Correa-Baena, J.-P.; Tress, W. R.; Abate, A.; Hagfeldt, A.; Grätzel, M. Incorporation of rubidium cations into perovskite solar cells improves photovoltaic performance. *Science* **2016**.

3. Correa Baena, J. P.; Steier, L.; Tress, W.; Saliba, M.; Neutzner, S.; Matsui, T.; Giordano, F.; Jacobsson, T. J.; Srimath Kandada, A. R.; Zakeeruddin, S. M.; Petrozza, A.; Abate, A.; Nazeeruddin, M. K.; Gratzel, M.; Hagfeldt, A. Highly efficient planar perovskite solar cells through band alignment engineering. *Energy & Environmental Science* **2015,** *8* (10), 2928-2934.

4. Zhou, H.; Chen, Q.; Li, G.; Luo, S.; Song, T.-b.; Duan, H.-S.; Hong, Z.; You, J.; Liu, Y.; Yang, Y. Interface engineering of highly efficient perovskite solar cells. *Science* **2014,** *345* (6196), 542-546.

5. You, J.; Yang, Y.; Hong, Z.; Song, T.-B.; Meng, L.; Liu, Y.; Jiang, C.; Zhou, H.; Chang, W.-H.; Li, G. Moisture assisted perovskite film growth for high performance solar cells. *Applied Physics Letters* **2014,** *105* (18), 183902

6. Eperon, G. E.; Habisreutinger, S. N.; Leijtens, T.; Bruijnaers, B. J.; van Franeker, J. J.; deQuilettes, D. W.; Pathak, S.; Sutton, R. J.; Grancini, G.; Ginger, D. S.; Janssen, R. A. J.; Petrozza, A.; Snaith, H. J. The Importance of Moisture in Hybrid Lead Halide Perovskite Thin Film Fabrication. *ACS nano* **2015,** *9* (9), 9380-9393.

7. Ahn, N.; Son, D.-Y.; Jang, I.-H.; Kang, S. M.; Choi, M.; Park, N.-G. Highly Reproducible Perovskite Solar Cells with Average Efficiency of 18.3% and Best Efficiency of 19.7% Fabricated via Lewis Base Adduct of Lead(II) Iodide. *Journal of the American Chemical Society* **2015,** *137* (27), 8696-8699.

8. Saidaminov, M. I.; Abdelhady, A. L.; Murali, B.; Alarousu, E.; Burlakov, V. M.; Peng, W.; Dursun, I.; Wang, L.; He, Y.; Maculan, G.; Goriely, A.; Wu, T.; Mohammed, O. F.; Bakr, O. M. High-quality bulk hybrid perovskite single crystals within minutes by inverse temperature crystallization. *Nat Commun* **2015,** *6*.

9. Jeon, Y.-J.; Lee, S.; Kang, R.; Kim, J.-E.; Yeo, J.-S.; Lee, S.-H.; Kim, S.-S.; Yun, J.-M.; Kim, D.-Y. Planar heterojunction perovskite solar cells with superior reproducibility. *Scientific Reports* **2014,** *4*, 6953.

10. Liang, P.-W.; Liao, C.-Y.; Chueh, C.-C.; Zuo, F.; Williams, S. T.; Xin, X.-K.; Lin, J.; Jen, A. K. Y. Additive Enhanced Crystallization of Solution-Processed Perovskite for Highly Efficient Planar-Heterojunction Solar Cells. *Advanced Materials* **2014,** *26* (22), 3748-3754.

11. Wu, Y.; Islam, A.; Yang, X.; Qin, C.; Liu, J.; Zhang, K.; Peng, W.; Han, L. Retarding the crystallization of PbI2 for highly reproducible planar-structured perovskite solar cells via sequential deposition. *Energy & Environmental Science* **2014,** *7* (9), 2934-2938.

12. Shi, D.; Adinolfi, V.; Comin, R.; Yuan, M.; Alarousu, E.; Buin, A.; Chen, Y.; Hoogland, S.; Rothenberger, A.; Katsiev, K. Low trap-state density and long carrier diffusion in organolead trihalide perovskite single crystals. *Science* **2015,** *347* (6221), 519-522.

13. Nayak, P. K.; Bisquert, J.; Cahen, D. Assessing Possibilities and Limits for Solar Cells. *Advanced Materials* **2011,** *23* (25), 2870-2876.

14. Yang, W. S.; Noh, J. H.; Jeon, N. J.; Kim, Y. C.; Ryu, S.; Seo, J.; Seok, S. I. High-performance photovoltaic perovskite layers fabricated through intramolecular exchange. *Science* **2015,** *348* (6240), 1234-1237.

15. Wu, C.-G.; Chiang, C.-H.; Tseng, Z.-L.; Nazeeruddin, M. K.; Hagfeldt, A.; Gratzel, M. High efficiency stable inverted perovskite solar cells without current hysteresis. *Energy & Environmental Science* **2015,** *8* (9), 2725-2733.

16. Li, L.; Chen, Y.; Liu, Z.; Chen, Q.; Wang, X.; Zhou, H. The Additive Coordination Effect on Hybrids Perovskite Crystallization and High-Performance Solar Cell. *Advanced Materials* **2016**, n/a-n/a.

17. Leguy, A. M. A.; Hu, Y.; Campoy-Quiles, M.; Alonso, M. I.; Weber, O. J.; Azarhoosh, P.; van Schilfgaarde, M.; Weller, M. T.; Bein, T.; Nelson, J.; Docampo, P.; Barnes, P. R. F. Reversible Hydration of CH3NH3PbI3 in Films, Single Crystals, and Solar Cells. *Chemistry of Materials* **2015,** *27* (9), 3397-3407.

18. Müller, C.; Glaser, T.; Plogmeyer, M.; Sendner, M.; Döring, S.; Bakulin, A. A.; Brzuska, C.; Scheer, R.; Pshenichnikov, M. S.; Kowalsky, W.; Pucci, A.; Lovrinčić, R. Water Infiltration in Methylammonium Lead Iodide Perovskite: Fast and Inconspicuous. *Chemistry of Materials* **2015,** *27* (22), 7835-7841.

19. Zhou, W.; Zhao, Y.; Shi, C.; Huang, H.; Wei, J.; Fu, R.; Liu, K.; Yu, D.; Zhao, Q. Reversible Healing Effect of Water Molecules on Fully Crystallized Metal–Halide Perovskite Film. *The Journal of Physical Chemistry C* **2016,** *120* (9), 4759-4765.

20. Frost, J. M.; Butler, K. T.; Brivio, F.; Hendon, C. H.; van Schilfgaarde, M.; Walsh, A. Atomistic Origins of High-Performance in Hybrid Halide Perovskite Solar Cells. *Nano Letters* **2014,** *14* (5), 2584-2590.

21. Guo, Y.; Shoyama, K.; Sato, W.; Matsuo, Y.; Inoue, K.; Harano, K.; Liu, C.; Tanaka, H.; Nakamura, E. Chemical Pathways Connecting Lead(II) Iodide and Perovskite via Polymeric Plumbate(II) Fiber. *Journal of the American Chemical Society* **2015,** *137* (50), 15907-15914.

22. You, J.; Meng, L.; Song, T.-B.; Guo, T.-F.; Yang, Y. M.; Chang, W.-H.; Hong, Z.; Chen, H.; Zhou, H.; Chen, Q.; Liu, Y.; De Marco, N.; Yang, Y. Improved air stability of perovskite solar cells via solution-processed metal oxide transport layers. *Nature Nanotechnology* **2016,** *11*, 75–81.

23. Heo, J. H.; Song, D. H.; Im, S. H. Planar CH3NH3PbBr3 Hybrid Solar Cells with 10.4% Power Conversion Efficiency, Fabricated by Controlled Crystallization in the Spin-Coating Process. *Advanced Materials* **2014,** *26* (48), 8179-8183.

24. Domanski, K.; Correa-Baena, J.-P.; Mine, N.; Nazeeruddin, M. K.; Abate, A.; Saliba, M.; Tress, W.; Hagfeldt, A.; Grätzel, M. Not All That Glitters Is Gold: Metal-Migration-Induced Degradation in Perovskite Solar Cells. *ACS Nano* **2016,** *10* (6), 6306–6314.

25. Rahimnejad, S.; Kovalenko, A.; Martí-Forés, S.; Aranda, C.; Guerrero, A. Coordination Chemistry Dictates the Structural Defects in Lead Halide Perovskites. *ChemPhysChem* **2016,** *17* (18).

26. Horváth, E.; Spina, M.; Szekrényes, Z.; Kamarás, K.; Gaal, R.; Gachet, D.; Forró, L. Nanowires of Methylammonium Lead Iodide (CH3NH3PbI3) Prepared by Low Temperature Solution-Mediated Crystallization. *Nano Letters* **2014,** *14* (12), 6761-6766.

27. Yang, M.; Zhang, T.; Schulz, P.; Li, Z.; Li, G.; Kim, D. H.; Guo, N.; Berry, J. J.; Zhu, K.; Zhao, Y. Facile fabrication of large-grain CH3NH3PbI3-xBrx films for high-efficiency solar cells via CH3NH3Br-selective Ostwald ripening. *Nat Commun* **2016,** *7*.

28. Umari, P.; Mosconi, E.; De Angelis, F. Relativistic GW calculations on CH3NH3PbI3 and CH3NH3SnI3 Perovskites for Solar Cell Applications. *Scientific Reports* **2014,** *4*, 4467.

29. Yan, K.; Long, M.; Zhang, T.; Wei, Z.; Chen, H.; Yang, S.; Xu, J. Hybrid Halide Perovskite Solar Cell Precursors: Colloidal Chemistry and Coordination Engineering behind Device Processing for High Efficiency. *Journal of the American Chemical Society* **2015,** *137* (13), 4460-4468.

30. Tian, Y.; Scheblykin, I. G. Artifacts in Absorption Measurements of Organometal Halide Perovskite Materials: What Are the Real Spectra? *The Journal of Physical Chemistry Letters* **2015,** *6* (17), 3466-3470.

31. Sveinbjörnsson, K.; Aitola, K.; Zhang, X.; Pazoki, M.; Hagfeldt, A.; Boschloo, G.; Johansson, E. M. J. Probing Photocurrent Generation, Charge Transport, and Recombination Mechanisms in Mesostructured Hybrid Perovskite through Photoconductivity Measurements. *The Journal of Physical Chemistry Letters* **2015,** *6* (21), 4259-4264.

32. Rahimnejad, S.; Kovalenko, A.; Martí-Forés, S.; Aranda, C.; Guerrero, A. Coordination Chemistry Dictates the Structural Defects in Lead Halide Perovskites. *ChemPhysChem* **2016**, n/a-n/a.

33. Stamplecoskie, K. G.; Manser, J. S.; Kamat, P. V. Dual nature of the excited state in organic-inorganic lead halide perovskites. *Energy & Environmental Science* **2015,** *8* (1), 208-215.

34. Lei, Y.; Li, H.; Pan, H.; Han, S. Structures and Hydrogen Bonding Analysis of N,N-Dimethylformamide and N,N-Dimethylformamide−Water Mixtures by Molecular Dynamics Simulations. *The Journal of Physical Chemistry A* **2003,** *107* (10), 1574-1583.

Chapter 6

Publication 3

Interfacial Degradation of Planar Lead Halide Perovskite Solar Cells. Guerrero, A.; You, J.; Aranda, C.; Kang, Y.Soo; Garcia-Belmonte, G.; Zhou, H.; Bisquert, J.; Yang, Y. *ACS Nano, **2016**, 10, 218-224.*

CANDIDATE´S CONTRIBUTION

Nature of Contribution	Extent of Contribution
✓ Contribution in the fabrication of the PSCs. ✓ Contribution in the analysis of the results. ✓ Contribution in the performing of *j-V* curves measurements.	20%

INTRODUCTION

This work establishes the necessity of protect the perovskite/metal-top contact interface against harmful chemical reactivity inducing degradation process through illumination time effects. By IS analysis is demonstrate the origin of the typical S-shape appeared in j-V curves when devices are degraded, attributing this degradation to an ionic movement provoking the formation of a dipole at the cathode interface that modify the flatband potential impeding an efficient extraction of photogenerated carriers.

PUBLISHED MANUSCRIPT

Interfacial Degradation of Planar Lead Halide Perovskite Solar Cells

Antonio Guerrero,*[1] Jingbi You,[2] Clara Aranda,[1] Yong Soo Kang,[3] Germa Garcia-Belmonte,[1] Huanping Zhou,[2] Juan Bisquert[1,4], and Yang Yang*[2]

[1] Institute of Advanced Materials (INAM), Universitat Jaume I, 12071 Castelló, Spain
[2] Department of Materials Science and Engineering, University of California Los Angeles, Los Angeles, California 90095, USA
[3]Center for Next Generation Dye-sensitized Solar Cells, Department of Energy Engineering, Hanyang University, Seoul 133-791, South Korea
[4] Department of Chemistry, Faculty of Science, King Abdulaziz University, Jeddah, *21589*, Saudi Arabia

Email: aguerrer@uji.es, yangy@ucla.edu

Abstract

The stability of perovskite solar cells is one of the major challenges for this technology to reach commercialization with water believed to be the major degradation source. In this work, a range of devices containing different cathode metal contacts in the configuration ITO/PEDOT:PSS/$MAPbI_3$/PCBM/Metal are fully electrically characterized before and after degradation caused by steady illumination during 4 h that causes a dramatic reduction in power conversion efficiency (PCE) from values of 12 % to 1.8 %. We show that decrease of performance and generation of S-shape is associated to chemical degradation of the metal contact. Alternatively, use of Cr_2O_3/Cr as contact enhances the stability but modification of the energetic profile during steady illumination takes place significantly reducing the performance. Several techniques including capacitance-voltage, XRD and optical absorption results suggest that the properties of the bulk perovskite layer are little affected in the device degradation process. Capacitance-voltage and impedance spectroscopy results show that the electrical properties of the cathode contact are being modified by generation of a dipole at the cathode that causes a large shift of the flatband potential, that modifies the interfacial energy barrier and impedes efficient extraction of electrons. Ionic movement in the perovskite layer modify the energy profile close to the contacts modifying the energy level stabilization at the cathode. These results provide new insights into the degradation mechanisms of perovskite solar cells and highlight the importance to further study the use of protecting layers to avoid the chemical reactivity of the perovskite with the external contacts.

Keywords: **Perovskite photovoltaics, interfacial degradation, Capacitance-Voltage, impedance spectroscopy.**

Graphical Table of Contents (TOC)

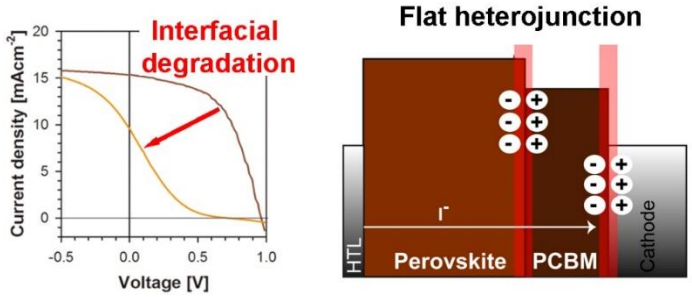

Photovoltaic applications based on perovskite materials as light-harvesters are emerging technologies which have stirred the interest of both scientific and industrial communities.[1-3] Significant efforts have been devoted towards the achievement of high efficiencies and using perovskites based on methylammonium lead triiodide ($MAPbI_3$) impressive efficiencies as high as 20.1 % have been obtained.[4] These recent developments demonstrate the enormous potential of perovskite solar cells suggesting that they may soon compete with already commercially available photovoltaic technologies. However, in order for this technology to reach maturity other aspects need to be resolved such as the long term stability.

Stability of the devices depends on many factors such as the architecture or the employed deposition method. A variety of device configurations composed of different combinations of materials layers have been proposed, and any instability arising from these materials will be critical for the device stability. Examples of architectures that have been developed are those consisting on a flat configuration based on ITO/TiO_2/Perovskite/Spiro-OMetad/Au, a variation with a porous layer of a metal oxide at the cathode contact, or an inverted configuration (ITO/PEDOT:PSS/Perovskite/PCBM/Al). Alternatively, several low cost deposition methods are currently available as those regarded as preliminary techniques towards roll-to-roll technologies *i.e.* spin coating,[3] doctor blade,[5] slot die or screen printing.[6,7] Regarding the perovskite generation this can be achieved by one-step solution coating,[2] two-steps sequential dip coating or vapour phase deposition.[1, 8]

Water is believed to be the major degradation source for degradation of this type of devices. The mechanism is not totally understood but it is clear that hybrid perovskites can react with Lewis bases such as water to irreversibly release methylammonium iodide and PbI_2. A degradation mechanism has been proposed by Frost *et al.* where a single water molecule is sufficient to degrade the material.[9] However, an excess of water is required to dissolve the HI and CH_3NH_2 byproducts. Some results indicate that instability arising from any of the layers may be critical, as indicated before. For example, Leijtens *et al.* have shown that the use of UV filters with devices containing a layer of mesoporous TiO_2 is necessary to reduce photodegradation at the oxide layer and the replacement of this layer by Al_2O_3 deliver stable photocurrents for over 41 days at 5 % efficiency from an initial PCE of 10 %.[10]

The highest reported stability results under constant illumination include the use of mesoporous TiO_2 by Burschka *et al.* using a two step deposition method where 80 % of the initial efficiency is retained after 20 days from an initial 8 %.[1] By removing spiro-Ometad and using a carbon protecting layer *Mei et al.* have reported that the stability is enhanced to reach a constant efficiency of 10.5% after 41 days of constant illumination.[7] With the exception of the work by Mei *et al.* in all reported cases there is significant

performance decay. In that work the enhanced stability is attributed to the total exclusion of water into the device thanks to the presence of a 10 μm thick carbon layer back contact. On the other side of the stability race we find flat heterojunction solar cells and in this case stability data is very scarce. Interestingly, other studies where devices have been encapsulated or have been measured in the glovebox do show significant device degradation.[10] Therefore, it is clear that other unknown degradation mechanisms different to those triggered by water are also taking place in most devices. Recently, Kaltenbrunner has reported enhanced stability with the use of Cr_2O_3 to shield the metal top contact from detrimental reactions with oxidizing and halide-forming iodide species.[11] The authors observed increased stability under ambient conditions and reduced performance decay is ascribed to water penetration into the device in the timescale of some hours.

In this work devices in the configuration ITO/PEDOT:PSS/$MAPbI_3$/PCBM/Metal are fully characterized before degradation and after degradation by simple constant illumination during 4 h in the glovebox. Two factors are responsible for device degradation: 1- Degradation of the metal contact and 2-Modification of the energy profile within the perovskite layer close to the contacts. The first factor can be suppressed by using a protective layer of Cr_2O_3. This work highlights the importance to further study how to stabilize the morphology and transport of iodide atoms through the bulk of the perovskite layer.

Results and Discussion

Current density–voltage curves

In this investigation inverted flat solar cells in the configuration ITO/PEDOT:PSS/Perovskite/PCBM/Metal have been fabricated for different reasons. First of all, degradation of perovskite solar cells has been ascribed to the moisture present in the environment and these devices work best when encapsulated.[7, 9] Secondly, the use of an inverted configuration avoids the presence of a TiO_2 layer which makes analysis more complex as electrical response will depend on the doping level and permittivity of the two semiconductor junction sides.[12] Finally, degradation features are more dramatic in the inverted configuration. A selection of different metals as cathode contacts has been tested in order to understand if degradation can be avoided.

Current density-voltage (*J–V)* curves have been measured at 1 sun light intensity conditions (1 kW/m^2). Representative curves are shown in Figure 1 and performance parameters are summarized in Table 1. As reported previously high performance devices can be prepared following a one step preparation method using CH_3NH_3I and $PbCl_2$ (3:1) as precursor using low workfunction metals such as Ca or Al.[13] Full details are described in the Experimental section. In this work efficiencies of ~12 % have been obtained for devices containing Ca or Al measured in the glovebox (J_{sc} = 18.4 mA/cm^{-2}, V_{oc} = 1.10 V and FF = 60). Slightly lower efficiencies are obtained for devices containing Ag (8.7 %), Au (7.3 %) and Cr_2O_3/Cr (7.0%) mainly due to a reduction in V_{oc} and FF.

Interestingly, in the absence of water if the device is illuminated during 4 hours at 1 sun light intensity an S-shape curve evolves for most studied metals which dramatically reduces the device efficiency providing power conversion efficiency (PCE) of <1.7 %. Selected J-V curves of degraded devices are shown in Figure 1 as broken lines. Only devices containing Cr_2O_2/Cr consistently show reduced degradation kinetics as devices retain most of the initial FF but the photocurrent is consistently reduced.

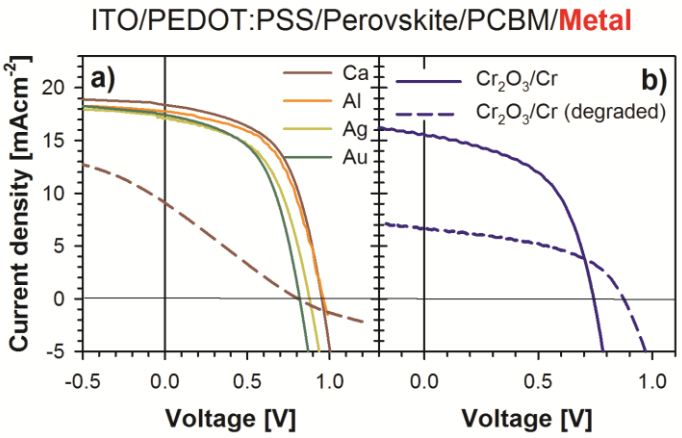

Figure 1. Current density-voltage curves of devices fabricated with different metal contacts measured at 1 sun light illumination. a) Metals providing S-shape curves after degradation b) Contact containing Cr_2O_2/Cr does not show S-shape after degradation. Degraded devices are shown as broken lines.

Table 1: Device performance parameters for devices containing different cathode contacts as a function of aging conditions and electrical parameters extracted from Capacitance-Voltage measurements under dark conditions. * Measurement carried out at 1 sun light intensity.

Contact	J_{sc} [mA/cm^2]	V_{oc} [V]	FF [%]	PCE [%]	n [x10^{16} cm^{-3}]	V_{fb} [V]	ΔV_{fb} [V]
Ca	18.39	1.10	60	12.14	1.2	1.00	-
Ca (degraded)	9.11	0.85	23	1.78	1.5	0.53	0.47
					0.9	-0.40	0.93
Al	17.79	1.11	61	12.05	0.9	1. 06	-
Ag	17.04	0.97	53	8.76	1.1	0.90	-
Au	17.46	0.82	51	7.30	2.1	0.75	-
Cr_2O_3/Cr	15.57	0.78	58	7.04	1.3	0.79	-
Cr_2O_3/Cr (degraded)	6.71	0.88	55	3.25	5.8	1.10	-0.31
					5.1*	1.03*	0.07

Bulk properties of perovskite films

Current density curves with a S-shape are typically connected to degradation of the contacts.[14] However, in order to understand if degradation is also connected to a modification of the bulk material absorption and XRD measurements of pristine and degraded films were measured (Figure 2). Films in the configuration ITO/PEDOT:PSS/Perovskite/PCBM were illuminated during 4 h in the glovebox under 1 sun light intensity conditions to simulate the degradation conditions in devices. The absorption bands of pristine and degraded films are remarkably similar. Alternatively, XRD diffraction patterns differ, modification of the XRD pattern takes place during illumination of the sample in the glovebox. In particular, the low fraction of PbI_2 peak disappears but also peak intensities and ratios change as well as the FWHM implicating a modification in the domain size.

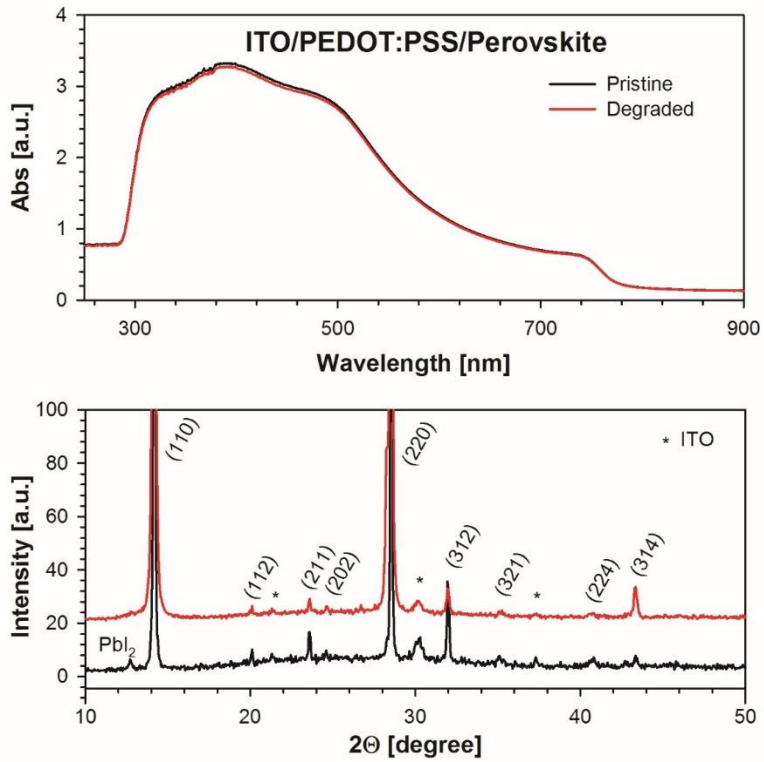

Figure 2. Bulk properties of pristine and degraded films in the configuration ITO/PEDOT:PSS/Perovskite/PCBM illuminated during 4 h in the glovebox under 1 sun light intensity conditions. (a) Absorbance spectra (b) XRD diffraction pattern.

Comparison of degraded devices by Scanning Electron Microscopy

In order to understand the origin of degradation in the absence of moisture and oxygen degraded devices were analyzed by SEM microscopy. Two selected devices are shown in Figure 3 to illustrate two configurations behaving differently electrically. Configuration based on Ca, Al, Ag or Au all provides S-shape curves and a representative image containing Au is shown in Figure 3a. From this secondary electrons image it is clear that the gold contact is not smooth as it contains coarse grains not present in fresh devices (see supporting information). In addition, it is interesting to note that the interface PCBM/Au shows signs of delamination and $MAPbI_3$/PCBM interface is rather bright pointing to high presence of heavy metal atoms at the interface. This delamination does not seem to be a cleaving effect since fresh samples do not show delamination (see supporting information). Alternatively, degraded devices containing Cr_2O_3/Cr do not show an S-shape in the *J-V* curve and relatively high FFs are obtained. A representative degraded device is shown in Figure 3b where it is clear that Cr_2O_3/Cr surface is smooth. In addition, interfaces close to the cathode are difficult to differentiate. All together suggests that Cr_2O_3/Cr clearly protects the cathode contact. For data completeness, a complete comparison of fresh and aged devices using both secondary and backscattered electrons is shown as supporting information.

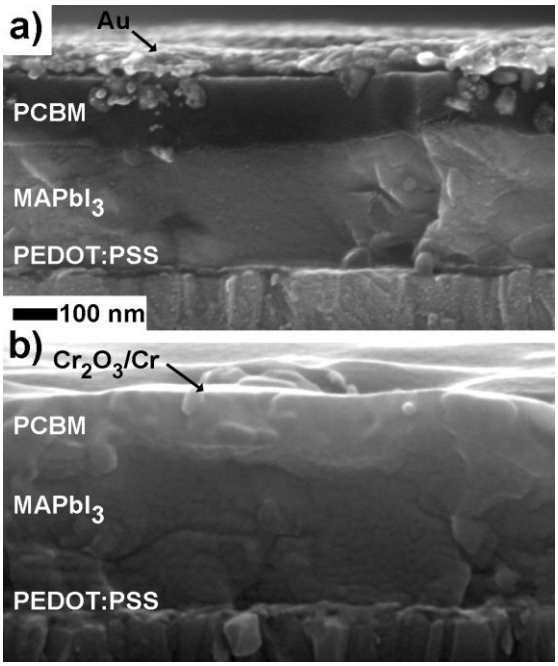

Figure 3. Scanning Electron Microscopy images of two representative degraded devices using the secondary electron detector a) shows an S-shape *J-V* curve b) Degraded device not showing an S-shape *J-V* curve.

Capacitance-voltage measurements: Mott-Schottky analysis

Capacitance-voltage measurement is a very useful technique at discerning between effects taking place at the bulk of active layer and those occurring at the interfaces with the outer contacts in photovoltaic devices.[12, 15] The reason is that measured doping densities will depend on the bulk properties of the layer and flat band potential values (V_{fb}) on energy equilibration at the contacts. In addition, capacitance measured at negative voltage under full depletion provides information on the dielectric constant of the material and this is an intrinsic property of the bulk material. In a typical measurement a DC Voltage is applied under dark conditions and a small AC perturbation (typically at 1Hz-1kHz) is over imposed. The differential current output is measured, and the DC voltage is swept over a wide range, *i.e.* –1 V to +1 V. The measured low frequency capacitance is related to the width of the depletion zone corresponding to a Schottky barrier at the cathode as supported by Kelvin Probe measurements.[12] At reverse bias full depletion occurs and corresponds to a geometric capacitance determined by the dielectric constant of the perovskite layer, Fig. 3a. Full depletion of the perovskite (300 nm) at 0 V is observed and taking into account that the thickness of the perovskite layer is about 300 nm, a relative dielectric constant for the perovskite (ε_{PVK}) of 21.2 has been found from the capacitance of fresh devices. The depletion zone decreases at positive bias voltage and as a consequence the capacitance increases, (see Figure 4a) and by plotting $C^{-2}(V)$ a straight line is observed (Figure 4).[16] The slope of the straight line is related with measurable p-doped electrical defects. In the current case we expect some differences between fresh and degraded devices since the XRD patterns change during illumination, as previously described, and morphology is related with the defect density.

Two representative case examples are shown in Figure 4 for devices showing an s-shape after device degradation containing Ca contact (Figure 4a) and other devices retaining the initial FF containing Cr_2O_3/Cr (Figure 4b). The obtained doping levels of 1

$\times 10^{16}$ cm^{-3} (Table 1) are well in agreement with our previously published results.[12] On the other hand, the intercept with the x-axis provides information on the flat band potential V_{fb}, defined as the applied voltage bias required to produce flat bands in the organic semiconductor. Note that V_{fb} is not actually the built-in potential (V_{bi}) as this last quantity also takes into account the presence of dipoles at the perovskite/cathode interface.

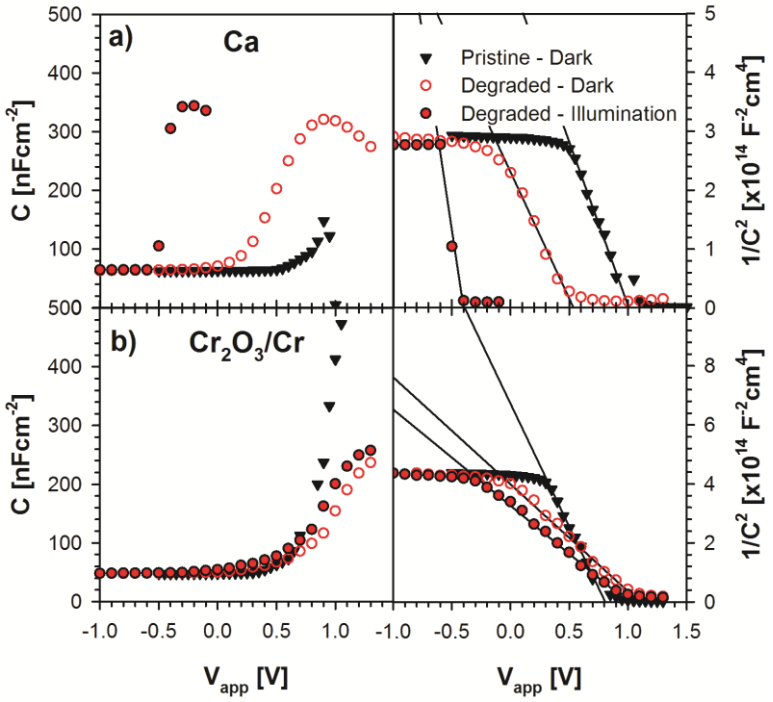

Figure 4. (a) Capacitance-voltage measurements of pristine and degraded devices carried out at 10 kHz. (b) Mott-Schottky plot of data shown in (a).

When data (Table 1) from fresh and degraded devices containing Ca metal are compared a slight increase in doping density is observed, 1.06x10^{16} cm^3 and 1.55x10^{16} cm^3, respectively. This feature suggests that the bulk properties of the perovskite layer are not significantly being modified pointing to interfacial degradation between the perovskite layer and the outer contacts for Ca containing devices. In addition, we observe that the dielectric capacitance attributed to the bulk properties of the perovskite at negative voltage remains constant. Alternatively, a shift in the V_{fb} of 0.47 V is observed for devices containing Ca towards negative values from 1.00 V to 0.53 V is a clear sign that the energetic properties at the interface between the cathode and the perovskite has dramatically been modified. More importantly, when we compare a degraded sample measured under dark conditions and under illumination a shift in V_{fb} of about 0.93V is observed that results in negative flat-band values. This is a clear sign of generation of a light induced dipole at the cathode interface as a consequence of charge accumulation of photogenerated carriers at the perovskite/cathode interface. The same effect has been previously reported for organic PCBM:P3HT solar cells.[17] Impedance spectroscopy measurements were carried out on degraded devices showing *J-V* curves with S-shape (see supporting information). An additional resistance with magnitude dependent on the applied voltage correlates with the shape of the *J-V* curve. This resistance is only observed for the degraded device and it is relatively low and constant at negative values when the photocurrent is high but sharply increases at voltages more positive than -0.2 V when the

photocurrent is low. This result points to an issue related with the extraction of carriers at the contact.

A remarkable increase in doping density is observed for degraded devices containing Cr_2O_3/Cr increasing from $1.3x10^{16}$ cm^3 and $5.8x10^{16}$ in agreement with modification of the perovskite layer (see XRD results). This increase in doping density will have an effect in the energy equilibration at the cathode contact as it will be described below. For this reason a degraded sample containing Cr_2O_3/Cr contact show an increase in V_{fb} again pointing to a modification in the energetic of all the elements involved at the cathode interface. Importantly, no shift in V_{fb} is observed when measurements in the dark and under illumination are compared. The additional resistance observed for devices containing a reactive metal is not observed for Cr_2O_3/Cr contacts.

Electrical model

A general electrical model to understand contact equilibration in photovoltaic devices needs to account for the difference in work functions between the contacts, Φ, and the Fermi level of the active layer, E_F, shown in Figure 5a. Based on previous results here we assume that the anode forms an ohmic contact with the perovskite active layer, in such a way that the energy equilibration to equalize the Fermi levels occurs predominantly at the contact $MAPbI_3$/PCBM. The potential drop associated to equilibration is generally divided into two contributions as shown in Figure 5b: a spatially extended band bending (V_{fb}) in the bulk of the semiconductor, and a voltage drop at the interface by generation of a dipole layer (Δ / q), where Δ is the step of the vacuum level. Thus the flatband potential is given by the expression[15, 18]

$$qV_{fb} = E_F - \Phi_c - \Delta \quad (1)$$

The presence of a dipole at the contact interface implies a net formation of charge separation across the interface, for example if electron charge is donated from the contact to acceptor states at the surface of the semiconductor.[18] We have previously shown using Kelvin Probe Force Microscopy (KPFM) that the magnitude of this dipole is almost negligible for highly performing perovskite solar cells.[12] The differences in work function between cathode and Fermi level of the perovskite is accommodated in the heterojunction with a depletion zone reaching about 300 nm of the perovskite layer.

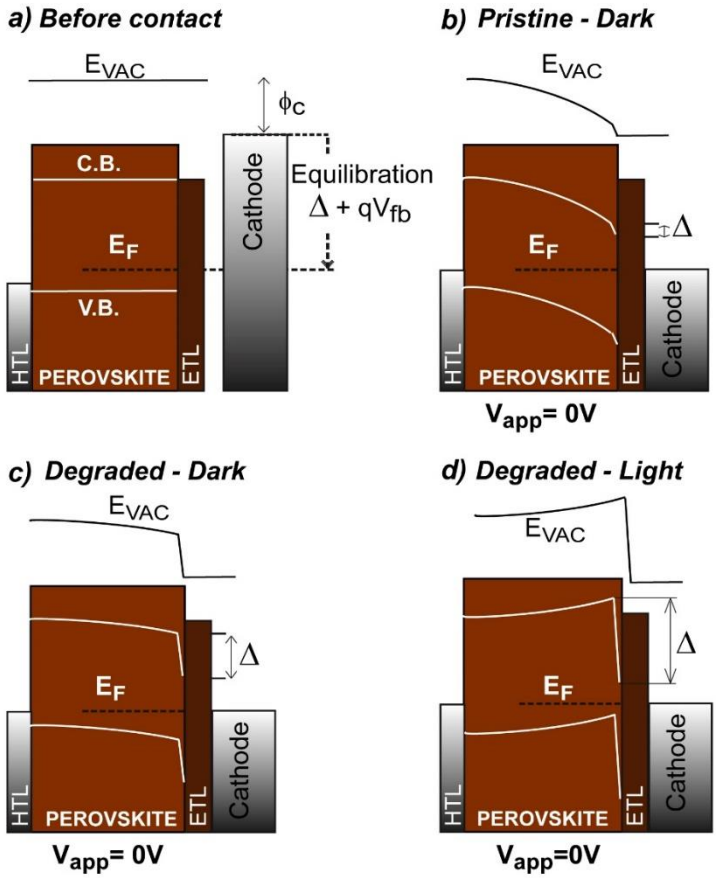

Figure 5. Energy level diagram of devices that show an S-shape *J-V* curve (a) before contact equilibration (b) after contact equilibration for a fresh device under dark conditions and after contact equilibration for a degraded device under dark (c) and illumination (d) conditions. HTL and ETL are Hole transport layer and Electron Transport layer, respectively. Formation of an interfacial dipole for the degraded device reduces the measured V_{fb} and the band in the electrical profile in the bulk of the perovskite layer is reversed hindering an efficient extraction of electrons. The magnitude of the dipole is magnified by accumulation of photogenerated carriers at the perovskite/cathode interface.

Whilst in a good performing device the dipole is very small, the evidence presented in the previous sections about the Mott-Schottky analysis and interfacial resistance, indicates that in degraded devices a large dipole is generated at the cathode/perovskite interface, and this situation is indicated in Figure 5c. The diagram shows that the presence of such a dipole reduces the required applied potential to provide flat bands and thus the measured V_{fb} is lower. From the point of view of photovoltaic operation, it is clear that the charge collection electrical field present in Figure 5b is eroded in Figure 5c. Under illumination conditions the magnitude of the dipole is magnified by accumulation of photogenerated carriers at the perovskite/cathode interface. This effect has been previously described in terms of the charging of the interface.[17] It produces an energy profile inversion which impedes efficient charge extraction by the cathode which is responsible for the S-shape curve.[14] Alternatively, for Cr_2O_3/Cr containing devices the doping density increases increasing the value of E_F and this will induce an increase in V_{fb} following eq. 1.

Origin of performance degradation

Identification of the precise interfacial reactions that actually cause the large dipole at the perovskite/cathode interface, limiting the device performance, is a complex problem of compositional analysis at the nanoscale that is beyond the scope of this work. Nevertheless the fact that the use of chromium provides a totally different degradation behavior points to corrosion of the metal contact for Ca, Al, Ag and Au as observed in SEM images in Figure 3. Importantly, recently it has been recognized that significant ionic conduction takes place in hybrid lead iodide perovskite, that gives rise to accumulation of net charge at one or both contacts.[19-21] A first principles calculation finds that that iodide vacancies and interstitials may easily diffuse across the perovskite crystal.[22] Hence under illumination the internal field shown in Figure 5c may produce the displacement of excess iodide atoms to the cathode, neutralizing the existing barrier. Ion migration as such is a reversible effect that does not account for permanent degradation, process I in Figure 6. However, metals would be prone to react with I^- ions producing irreversible degradation of the interface with generation of insulating metal-iodides materials, process II in Figure 6. In addition, the evaporated metal could also diffuse through the thin layer of PCBM and I^- would not necessarily need to diffuse thorough the entire PCBM layer. Noble metals such as Au also lead to corrosion at the interface level under oxidative stress and similar results are also observed here.[23] Note that in this case positive charges would be generated at the anode side but this would be better compensated by the PEDOT:PSS as this is a solid state polyelectrolyte. Unlike with cathode contact the effect of this additional charge on PEDOT:PSS would be to increase of the conductivity of the layer. In both cases, an insulating layer would be formed at the interface which under illumination would generate charge accumulation at the interfaces inducing the generation of a dipole either at I or II and would account for the observed measurements. Alternatively, Cr_2O_3 is known to withstand very well oxidative corrosion. Recently, it has been reported that Cr_2O_3 efficiently shields the top metal from detrimental reactions with oxidizing and halide-forming iodide species.[11] Using this protective layer the reduction in photocurrent and increase in photovoltage is related with the ion migration itself (process I) which reversibly modifies the energetic landscape at the perovskite/PCBM contact.

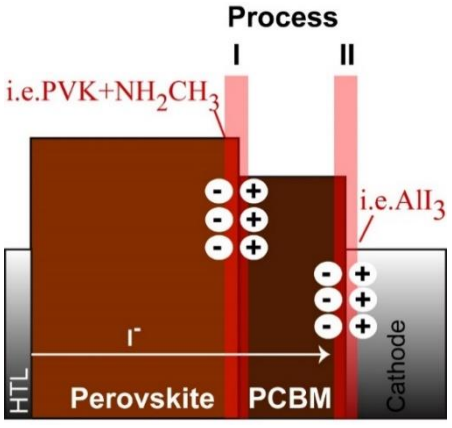

Figure 6. Feasible hypothesis which could potentially give rise to external cathode contact degradation.

Conclusions

In this work we have studied the degradation of flat heterojunction solar cells fabricated in the inverted configuration. We have demonstrated that in the absence of water, which is believed to be the major degradation source for this type of devices, reactivity of the perovskite with the cathode contact is the major degradation pathway for most metals. If the cathode contact is protected with Cr_2O_3/Cr new features appear during degradation which are due to modification of the energy bands close to the contacts. The results presented in this manuscript highlight the importance to study the use of protecting layers to avoid the chemical reactivity of the perovskite with the external contacts. Further work is needed to suppress the ionic conductivity within the perovskite layer as this modifies the performance of flat heterojunction perovskite solar cells during operation conditions.

Methods

Device preparation was carried out according to previously described methods, a brief summary is provided here.[13] A solution containing $PbCl_2$:CH_3NH_3I (1:3) in N,N-dimethylformamide (0.8M) was spin coated at 1500 rpm onto the poly(3,4-ethylenedioxythiophene) polystyrene sulfonate (PEDOT:PSS) layer. The precursor film is annealed at 90 °C for 2 h in ambient air (humidity of 35%-65%). After annealing, the perovskite films were transferred into nitrogen glove box. A 2% phenyl-C61-butyric acid methyl ester ($PC_{70}BM$) in chlorobenzene solution was coated onto the perovskite layer at 1000 rpm. Top metals were thermally evaporated with a base pressure of $6x10^{-6}$ mbar. Deposition of chromium was carried out as in ref. [11]. Efficiencies were measured using encapsulated devices in air using a solar simulator and identical devices not-encapsulated were measured by capacitance voltage in the glovebox at <0.1 ppm of O_2 and water.

J-V curves were measured using a solar simulator with the light intensity adjusted using a calibrated Si-solar cell. Measurements were carried out at a sweep rate of 50 mV/s with very small hysteresis observed. Capacitance-Voltage and impedance spectroscopy measurements were performed using an Autolab potentiostat (Model PGSTAT30) equipped with a frequency analyzer module. A small voltage perturbation (20 mV rms) is applied at frequencies from 10 kHz for Capacitance-Voltage. Capacitance-voltage measurements were carried out either in the dark or at 1 sun light illumination. Small sample to sample variation was observed in doping densities (± 0.8 $x10^{16}cm^3$) and V_{fb} (± 0.10 V) for 20 independent devices fabricated using the same process.

Films for absorption and XRD measurements were prepared as those in devices but the top contact was not evaporated. The degradation experiment for those films was carried out in a glovebox using 1 sun light intensity during a period of 4 hours. Absorption measurements were carried out with a Cary 300 Bio Spectrophotometer. Powder XRD analysis was performed with a thin film X-ray diffractometer (D4 Endeavor, Bruker-AXS) with Cu K_α radiation.

Acknowledgement

This work was partially supported by Generalitat Valenciana (project ISIC/2012/008 Institute of Nanotechnologies for Clean Energies) and the Spanish Ministerio de Economía y Competitividad (MINECO) project MAT2013-47192-C3-1-R.; and grants from US Air Force of Scientific Research (FA9550-12-1-0074) and National Science Foundation (ECCS-1509955). A.G. would like to thank the Spanish Ministerio de Economía y Competitividad for a Ramón y Cajal Fellowship (RYC-2014-16809). We thank SCIC from UJI for support on use of Scanning Electron Microscopy.

Supporting information

Supporting information containing a complete comparison of SEM images of fresh and degraded devices and additional impedance spectroscopy data. Supporting Information is available free of charge from the ACS Nano home page (http://pubs.acs.org/journal/ancac3).

Supporting information

Interfacial Degradation of Planar Lead Halide Perovskite Solar Cells

Antonio Guerrero,*[1] Jingbi You,[2] Clara Aranda,[1] Yong Soo Kang,[3] Germa Garcia-Belmonte,[1] Huanping Zhou,[2] Juan Bisquert[1,4], and Yang Yang*[2]

[1] Institute of Advanced Materials (INAM), Universitat Jaume I, 12071 Castelló, Spain
[2] Department of Materials Science and Engineering, University of California Los Angeles, Los Angeles, California 90095, USA
[3]Center for Next Generation Dye-sensitized Solar Cells, Department of Energy Engineering, Hanyang University, Seoul 133-791, South Korea
[4] Department of Chemistry, Faculty of Science, King Abdulaziz University, Jeddah, *21589*, Saudi Arabia

Email: aguerrer@uji.es, yangy@ucla.edu

SEM Analysis

A complete set of images containing fresh (Figure SI1) and aged (Figure SI2) devices are compared. Both secondary and backscattered electrons are shown to provide adequate high resolution images and compositional contrast, respectively. Fresh devices containing Au as contact do not show evident delamination at the PCBM/Au interface ruling out delamination due to a cleaving effect. This independent sample containing Au also shows bright edges at the perovskite/PCBM interface. No significant differences are observed at the interface level for fresh and degraded devices containing Cr_2O_3/Cr.

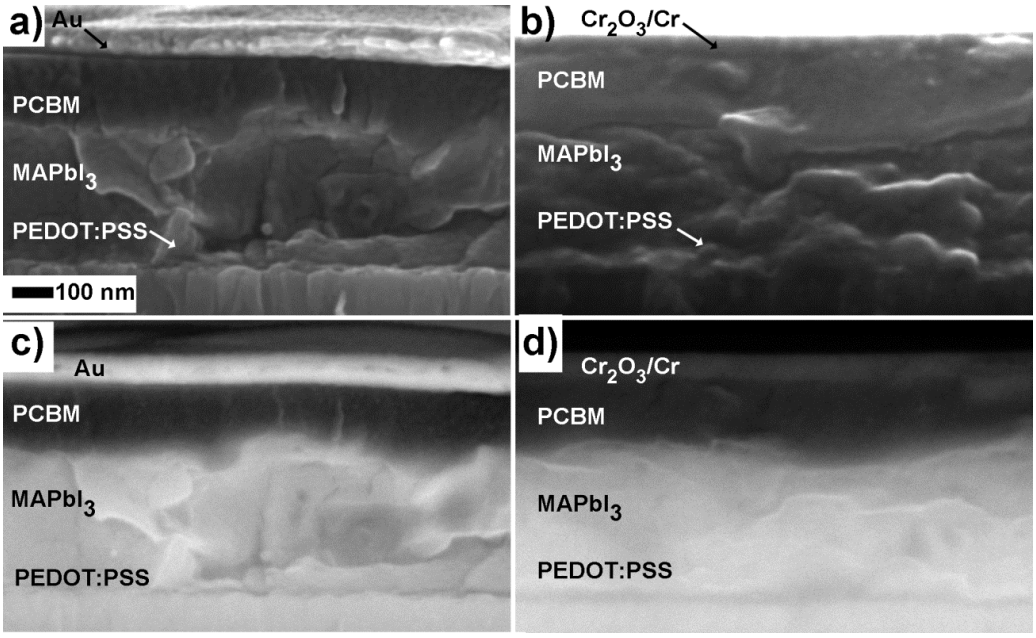

Figure SI1. Scanning Electron Microscopy images of two representative fresh devices. a) and c) Devices containing Au as contact and b) and d) Devices containing Cr_2O_3/Cr. a) and b) Secondary electrons and c) and d) Backscattered.

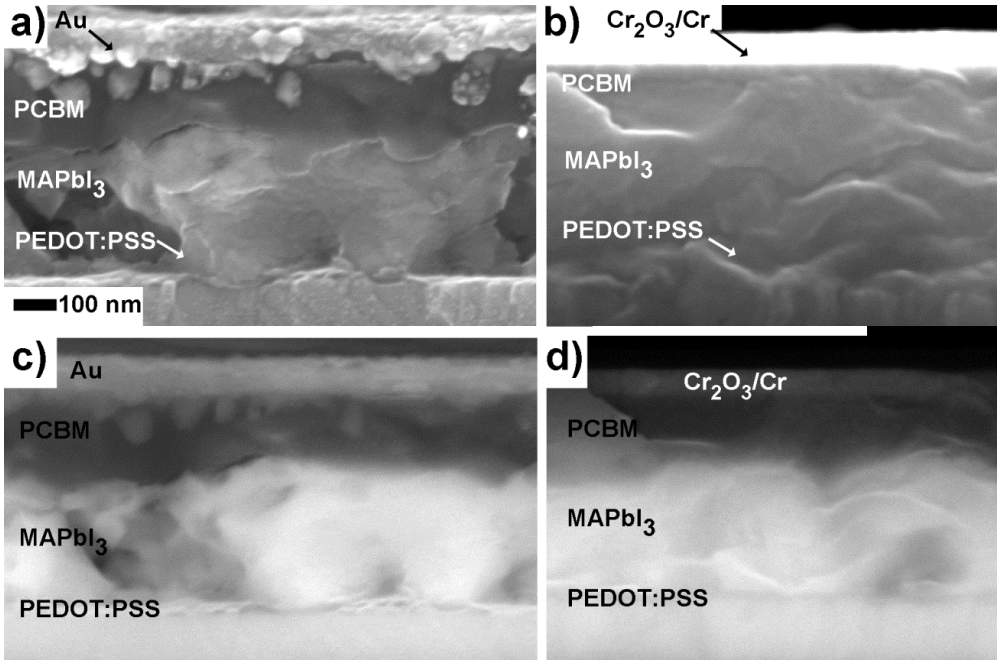

Figure SI2. Scanning Electron Microscopy images of two representative degraded devices. a) and c) Devices containing Au as contact and b) and d) Devices containing Cr2O3/Cr. a) and b) Secondary electrons and c) and d) Backscattered

Impedance Spectroscopy measurements

Impedance spectroscopy measurements have proved very useful at understanding the operation mechanism of a wide range of photovoltaic devices.[24-25] The fundamental operation principles are similar to those of capacitance-voltage but in this case at each DC voltage the applied AC perturbation is swept over a wide range of frequencies. Representation of the data in a complex impedance plot usually provides arcs (Figure SI3) and each arc is connected to a physical process taking place at a characteristic time scale. The x-axis is related to resistive processes and the y-axis to capacitive processes. Bode plots provide information on capacitance and phase information as a function of the frequency (Figure SI4)

Devices containing Al were encapsulated and measured in the frequency range between 300 kHz-200 mHz under illumination conditions. Encapsulated devices show only one contribution at high frequencies over the entire voltage range (Figure SI5). Therefore data from the encapsulated device before degradation can be fitted to a single RC circuit connected in series with R_s (the series resistance associated to external contacts and wires) as only one arc is observed. Alternatively, degraded devices clearly show two arcs at negative bias in the high frequency region (Figure SI3) and these arcs evolve as the applied bias increases. In particular the high frequency arc becomes dominant at applied voltages more positive than -0.2 V, just at the point where the photocurrent begins to decrease in the J-V curve. The high frequency part of the impedance data can be fitted to an equivalent circuit as that shown in Figure SI3b composed by two RC elements connected in series. The resistance values before and after degradation of the device are shown in Figure SI1c. Interestingly, for both degradation stages of the device R_1 shows the same shape and values but these are shifted towards negative voltage for the degraded device. On the other hand, the additional resistance only observed for the degraded device is relatively low and constant at negative values but sharply increases at voltages more positive than -0.2 V. The fact that the photocurrent of the device dramatically decreases

as R_2 increases indicates that R_2 arises from a pure source of series resistance related to contact degradation in agreement with the change of flatband potential obtained previously capacitance-voltage results. Similar results have previously been observed for organic photovoltaics in which the strength of a light induced dipole can be modulated with light at the cathode contact.[14]

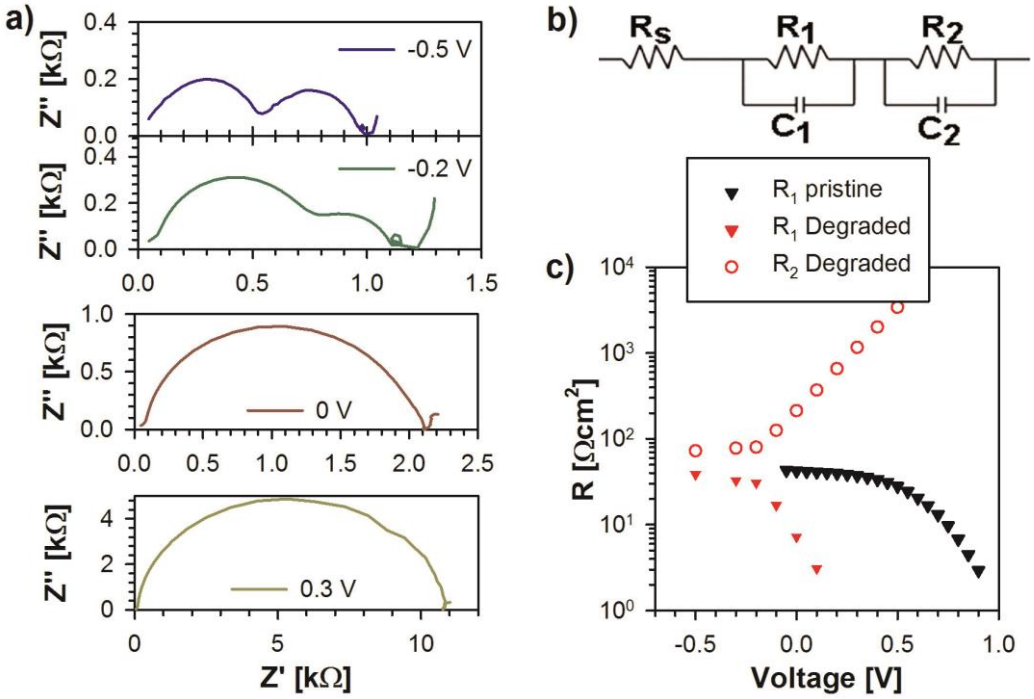

Figure SI3. a) Nyquist plots of the degraded devices measured in the dark for cathode containing Al as a function of the applied DC voltage. b) Equivalent circuit used to analyze the impedance spectroscopy data. c) Fitting results for encapsulated device before and after degradation.

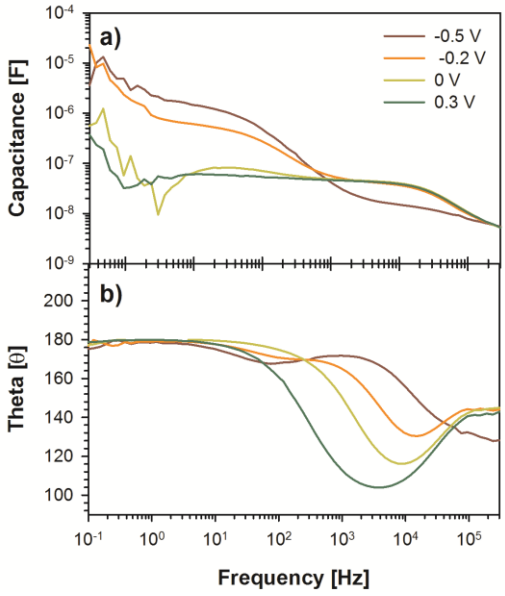

Figure SI4: Bode plots of the degraded devices containing an Al cathode contact measured in the dark. a) Capacitance b) Phase.

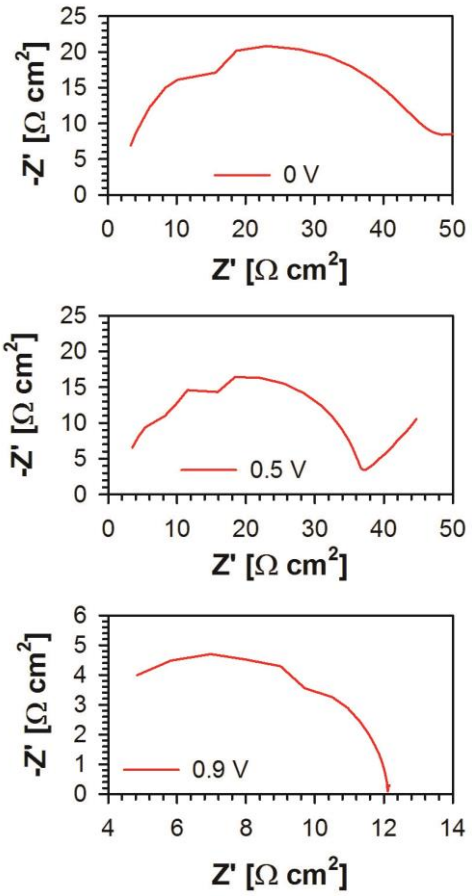

Figure SI5: a) Nyquist plots of pristine devices as a function of the applied DC voltage and high frequency region (up to 1 kHz).

References

1. Burschka, J.; Pellet, N.; Moon, S.-J.; Humphry-Baker, R.; Gao, P.; Nazeeruddin, M. K.; Gratzel, M. Sequential deposition as a route to high-performance perovskite-sensitized solar cells. *Nature* **2013,** *499* (7458), 316-319.

2. Lee, M. M.; Teuscher, J.; Miyasaka, T.; Murakami, T. N.; Snaith, H. J. Efficient Hybrid Solar Cells Based on Meso-Superstructured Organometal Halide Perovskites. *Science* **2012,** *338* (6107), 643-647.

3. Zhou, H.; Chen, Q.; Li, G.; Luo, S.; Song, T.-b.; Duan, H.-S.; Hong, Z.; You, J.; Liu, Y.; Yang, Y. Interface engineering of highly efficient perovskite solar cells. *Science* **2014,** *345* (6196), 542-546.

4. Green, M. A.; Emery, K.; Hishikawa, Y.; Warta, W.; Dunlop, E. D. Solar cell efficiency tables (Version 45). *Progress in Photovoltaics: Research and Applications* **2015,** *23* (1), 1-9.

5. Kim, J. H.; Williams, S. T.; Cho, N.; Chueh, C.-C.; Jen, A. K. Y. Enhanced Environmental Stability of Planar Heterojunction Perovskite Solar Cells Based on Blade-Coating. *Advanced Energy Materials* **2015,** *5* (4), 1401229.

6. Hwang, K.; Jung, Y.-S.; Heo, Y.-J.; Scholes, F. H.; Watkins, S. E.; Subbiah, J.; Jones, D. J.; Kim, D.-Y.; Vak, D. Toward Large Scale Roll-to-Roll Production of Fully Printed Perovskite Solar Cells. *Advanced Materials* **2015,** *27* (7), 1241-1247.

7. Mei, A.; Li, X.; Liu, L.; Ku, Z.; Liu, T.; Rong, Y.; Xu, M.; Hu, M.; Chen, J.; Yang, Y.; Grätzel, M.; Han, H. A hole-conductor–free, fully printable mesoscopic perovskite solar cell with high stability. *Science* **2014,** *345* (6194), 295-298.

8. Chen, Q.; Zhou, H.; Hong, Z.; Luo, S.; Duan, H.-S.; Wang, H.-H.; Liu, Y.; Li, G.; Yang, Y. Planar Heterojunction Perovskite Solar Cells via Vapor-Assisted Solution Process. *Journal of the American Chemical Society* **2014,** *136* (2), 622-625.

9. Frost, J. M.; Butler, K. T.; Brivio, F.; Hendon, C. H.; van Schilfgaarde, M.; Walsh, A. Atomistic Origins of High-Performance in Hybrid Halide Perovskite Solar Cells. *Nano Letters* **2014,** *14* (5), 2584-2590.

10. Leijtens, T.; Eperon, G. E.; Pathak, S.; Abate, A.; Lee, M. M.; Snaith, H. J. Overcoming ultraviolet light instability of sensitized TiO2 with meso-superstructured organometal tri-halide perovskite solar cells. *Nat Commun* **2013,** *4*, 2885.

11. Kaltenbrunner, M.; Adam, G.; Glowacki, E. D.; Drack, M.; Schwodiauer, R.; Leonat, L.; Apaydin, D. H.; Groiss, H.; Scharber, M. C.; White, M. S.; Sariciftci, N. S.; Bauer, S. Flexible high power-per-weight perovskite solar cells with chromium oxide-metal contacts for improved stability in air. *Nat Mater* **2015,** *14* (10), 1032-1039.

12. Guerrero, A.; Juarez-Perez, E. J.; Bisquert, J.; Mora-Sero, I.; Garcia-Belmonte, G. Electrical field profile and doping in planar lead halide perovskite solar cells. *Applied Physics Letters* **2014,** *105* (13), 133902.

13. You, J.; Yang, Y.; Hong, Z.; Song, T.-B.; Meng, L.; Liu, Y.; Jiang, C.; Zhou, H.; Chang, W.-H.; Li, G. Moisture assisted perovskite film growth for high performance solar cells. *Applied Physics Letters* **2014,** *105* (18), 183902

14. Guerrero, A.; Chambon, S.; Hirsch, L.; Garcia-Belmonte, G. Light-modulated TiOx Interlayer Dipole and Contact Activation in Organic Solar Cell Cathodes. *Advanced Functional Materials* **2014,** *24* (39), 6234-6240.

15. Guerrero, A.; Dörling, B.; Ripolles-Sanchis, T.; Aghamohammadi, M.; Barrena, E.; Campoy-Quiles, M.; Garcia-Belmonte, G. Interplay between Fullerene Surface Coverage and Contact Selectivity of Cathode Interfaces in Organic Solar Cells. *ACS Nano* **2013,** *7* (5), 4637-4646.

16. Boix, P. P.; Garcia-Belmonte, G.; Munecas, U.; Neophytou, M.; Waldauf, C.; Pacios, R. Determination of gap defect states in organic bulk heterojunction solar cells from capacitance measurements. *Applied Physics Letters* **2009,** *95* (23), 233302.

17. Bisquert, J.; Garcia-Belmonte, G.; Munar, A.; Sessolo, M.; Soriano, A.; Bolink, H. J. Band unpinning and photovoltaic model for P3HT:PCBM organic bulk heterojunctions under illumination. *Chemical Physics Letters* **2008,** *465*, 57-62.

18. Guerrero, A.; Marchesi, L. F.; Boix, P. P.; Ruiz-Raga, S.; Ripolles-Sanchis, T.; Garcia-Belmonte, G.; Bisquert, J. How the Charge-Neutrality Level of Interface States Controls Energy Level Alignment in Cathode Contacts of Organic Bulk-Heterojunction Solar Cells. *ACS Nano* **2012,** *6* (4), 3453-3460.

19. Xiao, Z.; Yuan, Y.; Shao, Y.; Wang, Q.; Dong, Q.; Bi, C.; Sharma, P.; Gruverman, A.; Huang, J. Giant switchable photovoltaic effect in organometal trihalide perovskite devices. *Nat Mater* **2015,** *14*, 193–198.

20. Yang, T.-Y.; Gregori, G.; Pellet, N.; Grätzel, M.; Maier, J. The Significance of Ion Conduction in a Hybrid Organic–Inorganic Lead-Iodide-Based Perovskite Photosensitizer. *Angewandte Chemie International Edition* **2015**, n/a-n/a.

21. Almora, O.; Zarazua, I.; Mas-Marza, E.; Mora-Sero, I.; Bisquert, J.; Garcia-Belmonte, G. Capacitive Dark Currents, Hysteresis, and Electrode Polarization in Lead Halide Perovskite Solar Cells. *The Journal of Physical Chemistry Letters* **2015,** *6* (9), 1645-1652.

22. Azpiroz, J. M.; Mosconi, E.; Bisquert, J.; De Angelis, F. Defects Migration in Methylammonium Lead Iodide and their Role in Perovskite Solar Cells Operation. *Energy & Environmental Science* **2015**.

23. Verdingovas, V.; Müller, L.; Jellesen, M. S.; Grumsen, F. B.; Ambat, R. Effect of iodine on the corrosion of Au–Al wire bonds. *Corrosion Science* **2015,** *97*, 161-171.

24. Bisquert, J.; Fabregat-Santiago, F. Dye-Sensitized Solar Cells. In *Impedance Spectroscopy: A General Introduction and Application to Dye-Synsitized Solar Cells*, Kalyanasundaram, K., Ed. CRC Press: Boca Raton, FL, USA, 2010.

25. Guerrero, A.; Montcada, N. F.; Ajuria, J.; Etxebarria, I.; Pacios, R.; Garcia-Belmonte, G.; Palomares, E. Charge carrier transport and contact selectivity limit the operation of PTB7-based organic solar cells of varying active layer thickness. *Journal of Materials Chemistry A* **2013,** *1* (39), 12345-12354.

Chapter 7

Publication 4

Changes from Bulk to Surface Recombination Mechanisms between Pristine and Cycled Perovskite Solar Cells. Correa-Baena, J.Pablo; Turren-Cruz, S.H.; Tress, W.; Hagfeldt, A.; Aranda, C.; Shooshtari, L.; Bisquert, J.; Guerrero, A.
*ACS Energy Letters, **2017**, 2, 681-688.*

CANDIDATE´S CONTRIBUTION

Nature of Contribution	Extent of Contribution
✓ Contribution in the electrical measurement of the PSCs. ✓ Contribution in the analysis of the results. ✓ Contribution in the development of the perovskite films onto the interdigitated devices.	20%

INTRODUCTION

This work establishes the necessity to develop a non-invasive method to electrically characterize the solar behaviour of perovskite devices to reliable distinguish between the contribution of bulk and interfaces onto the recombination processes. For that purpose, a physical model based in the re-definition of non-ideality factor,m_d, is developed with the following matching with the experimental results based in IS measurement at open-circuit conditions and under different light intensities in order to not modify the external contacts. A demonstration of the contributions of the different device layers depending on the optic and electrical history of the solar cell is clear when comparing recombination resistances of pristine and polarized PSCs.

PUBLISHED MANUSCRIPT

Changes from Bulk to Surface Recombination Mechanisms between Pristine and Cycled Perovskite Solar Cells

Juan-Pablo Correa-Baena[1], Silver-Hamill Turren-Cruz,[1] Wolfgang Tress,[1] Anders Hagfeldt,*[1] Clara Aranda,[2] Leyla Shooshtari,[2,3] Juan Bisquert,*[2,4] Antonio Guerrero*[2]

[1] Laboratory of Photomolecular Science, Institute of Chemical Sciences and Engineering, École Polytechnique Fédérale de Lausanne, CH-1015-Lausanne, Switzerland

[2] Institute of Advanced Materials (INAM), Universitat Jaume I, 12006 Castelló, Spain
[3] Institute for Nanoscience and Nanotechnology, Sharif University of Technology, Tehran, 14588-89694, Iran
[4]Department of Chemistry, Faculty of Science, King Abdulaziz University, Jeddah, Saudi Arabia

Email: anders.hagfeldt@epfl.ch , bisquert@uji.es , aguerrer@uji.es,

Abstract

Several aspects on the photophysical characterization of lead halide hybrid organic-inorganic perovskite solar cells still remain unsolved. It has been observed that ionic transport and polarization cause very slow changes that interfere transient measurements with effects that cannot be separated from recombination kinetics. Here we establish a protocol of initial measurement of the solar cell that provides information on recombination characteristics prior to any voltage by cycling. The photovoltaic device is measured by several methods: photovoltage vs. light intensity, open circuit voltage decay (OCVD) and impedance spectroscopy (IS), whilst minimizing the exposure to external voltage stimulus to avoid ionic migration to the contacts. Results are independently confirmed by the analysis of samples with interdigitated electrodes. We show that the high efficiency perovskite solar cells behave very closely to a bulk recombination ideal photovoltaic model. However, when voltage is scanned to determine current-density voltage curves and Impedance Spectroscopy at fixed illumination intensity, the cell undergoes a significant change, which we attribute to a dominance of recombination at contacts that have been modified by ionic polarization. Our method provides an effective approach to determine quantitatively the rather significant changes that occur to perovskite solar cells during standard measurements such as current-voltage curves.

Table of Content (TOC) graphic

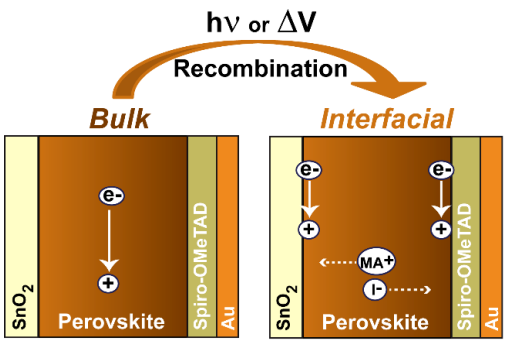

Despite the intensive advance of lead halide hybrid organic-inorganic perovskite solar cells, many important questions about the photophysical characterization still remain unsolved. Of particular importance, transient measurements are often plagued by the interference of ionic transport and polarization that cause very slow changes that cannot be separated from recombination kinetics.[1-2] One important issue impeding the proper characterization is the fact that perovskite solar cells suffer from critical device performance changes under working conditions. Certainly, the mere characterization by using different techniques appears to produce structural changes in the perovskite device. For example, it has been reported that external stimulus like light induces structural changes during photoluminescence (PL) and Raman measurements under ambient conditions.[3-6] Similarly, the use of an external electrical field during device characterization promotes ion migration towards the external contact leading to hysteretic behaviour observed during cyclic voltammetry (CV) under illumination[7-10] or in dark conditions.[11-13] Figure 1a shows a diagram that represents this ionic migration and ion built up at the external interfaces and how the charge is compensated by the contacts.

The design of measurements that minimize the dose to the external stimuli, which may provide access to the bulk electronic properties of the perovskite layer in a device with contacts, is of utmost importance. One particularly central topic concerning photovoltaic operation of the device is the determination of recombination kinetic constants and their influence on steady state performance characteristics. In previous related solar technologies, such as dye-sensitized solar cells (DSC) and organic solar cells (OSC),[14-15] it has been possible to establish unambiguously the recombination resistance. In hybrid perovskite solar cells the carrier lifetime has been described in detail using PL techniques[16-17] but the electrical measurement method of recombination lifetime in a device with contacts, which is rather common in the other types of solar cells, has not been clearly established.

In this work we present a method to study the bulk properties of the perovskite layer. We will work here with a type of lead halide perovskite solar cells that has been well described in recent publications and used for detailed IS characterization.[18-19] First, devices have been studied by using different standard transient techniques such as cyclic voltammetry, open circuit voltage decay (OCVD) and impedance spectroscopy (IS). It is shown that all these techniques involve high doses of external stimuli, which induce ion migration towards the contacts. Interestingly, using open circuit voltages (V_{oc}) under different illumination intensities during IS measurements proves to be much milder and offers information on the intrinsic properties of the perovskite layer.

Analysis by different transient techniques

Devices are prepared in the configuration FTO/SnO_2/Perovskite/Spiro-OMeTAD/Au containing a flat conformal layer of SnO_2 by atomic layer deposition (ALD). The perovskite layer presents a mixed formulation to enhance absorption and stability containing Cs/MA/FA/Pb/I/Br (Eg = 1.6 eV), where MA: Methylammonium, FA: Formamidinium.[20-21] These devices show the following performance parameters measured under reverse sweep direction: power conversion efficiency η = 18.3 %, short circuit photocurrent density j_{sc} = 22.6 mAcm^{-2}, open circuit voltage V_{oc} =1.12 V, fill factor *FF*=74%. The devices incorporate the planar configuration without mesoscopic metal-oxide contact, meaning that we do not have the perovskite infiltrated into a scaffold but a homogeneous thin film absorber layer.[19] We combine the analysis of the perovskite solar cell device with a thin film of the same perovskite on interdigitated electrodes that provides information on the conductivity as a function of light intensity.[22] This second set of devices gives access to the carrier density of perovskite layers from measurements not

dependent on photovoltaic devices. To avoid undesirable effects of ambient moisture the perovskite was protected in the interdigitated configuration with a layer of PMMA. The solar-cell devices were stable during storage for weeks in dry atmospheric conditions in the dark.

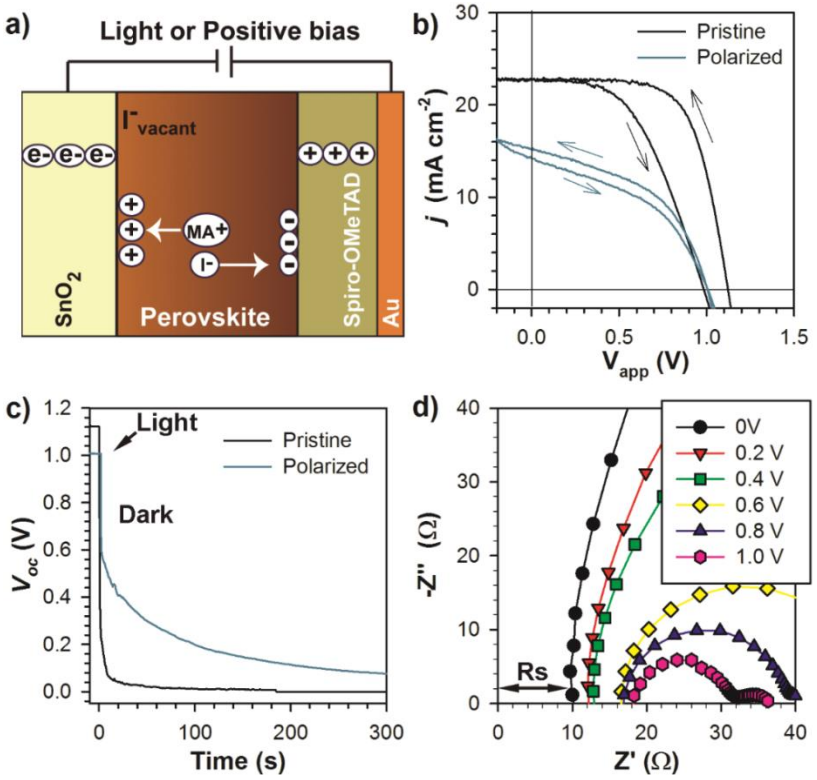

Figure 1: a) Diagram representing the ion migration under either light conditions or positive bias. b) j-V curves of a representative pristine device and a device polarized under illumination conditions for 30 min at 0 V. c) Open circuit voltage decay of a pristine and polarized device. d) Complex impedance plot of a device measured under 1 sun illumination sweeping the voltage from 0 V to 1.0 V. It is observed that the series resistance of the devices increases with the applied voltage. The pristine device is polarized by carrying out the IS measurement in d), this is 1 sun illumination conditions and different positive bias.

Transient techniques are initially tested on representative photovoltaic devices that show activated pathways for ions to migrate towards the external interfaces (Figure 1). This type of device represents the worst case scenario where most transient techniques will fail to provide reliable data. The current density-voltage (*j-V*) curves are measured at 1 sun light illumination conditions (AM1.5G) with a step of $\Delta V = 10$ mV and sweep rate of 50 mV/s. Figure 1b shows high hysteresis for a pristine device as the curves in forward and reverse direction are very different. As expected hysteresis is minimized at still lower scan rates, see supporting information Figure SI1. In addition, other devices with lower hysteresis were produced in the same batch (see supporting information Figure SI2) but the following discussion also holds for them. The same pristine sample can be studied by OCVD where the external stimulus is the light (1 sun) over a period of 10 s. After that time the source of light is switched off and the V_{oc} decay can be monitored as a function of the time. From results of the pristine sample, Fig. 1c, it is clear that the V_{oc} of the device decays very fast and values close to zero are obtained within the first 100 s. It has been reported that longer light soaking experiments in the range of minutes show significantly

different response indicating that the measurement itself is sufficient to modify the properties of the perovskite layer.[23] Another useful transient technique is Impedance Spectroscopy (IS) where a dc voltage is applied to the sample either under light or dark conditions and a small-signal ac voltage perturbation is superimposed over a wide range of frequencies. Therefore, both light and voltage are typically applied to the sample using this technique. Figure 1d shows the complex impedance plot of a device measured at 1 sun light intensity at different dc voltages starting from 0 V up to 1V. In these plots the x-axis (Z') is related to resistive elements and the y-axis (-Z'') to capacitive elements. The series resistance (R_{series}) of a device, originated by the external contacts, can be monitored using IS as a pure resistance with no capacitive elements. The value can be graphically measured from the intercept with the x-axis of the first capacitive element. The data clearly shows that the R_{series} of the device increases from 10 Ω to 18 Ω during the measurement time as the combined effect of the applied positive dc voltage and the illumination time. The increase in series resistance can be viewed as a further support for ion accumulation at the contacts as represented in Fig. 1a. It is noted that the response of the series resistance with the applied voltage is not linear. We believe that once ions are already present at the extracting interfaces a further increase in the local ion concentration is hindered as there are less available sites for ions to move. These ions will increase the recombination kinetics as well as reported elsewhere.[24] Furthermore, the presence of ions at the external interfaces can lead to chemical reactions at the interfacial level and this would modify the extraction properties of the selective contacts.[11] It is noted that the actual interfacial chemistry has been rather elusive due to the difficulty/sensitivity requirements for the characterization techniques to offer in-situ information. However, some of the previous work suggests that interfacial chemistry may be limiting the device performance. For example, iodide interactions with TiO2 has been identified to form Ti-I-Pb bond and this interaction will depend on the local iodide concentration.[25] Alternatively, it has previously been shown that iodide can also react with the oxidized form of Spiro-Ometad leading to the neutral molecule that lacks from adequate conductivity increasing the series resistance.[11] The current results suggest that the chemical reactivity is promoted by light and the required long acquisition times (≈1 h).

Polarization of the device by illumination at 1 sun at 1.2 V for 10 min totally modifies the electrical response as discussed for the IS measurements leading to a very important reduction in performance parameters as shown in j-V curve (Fig. 1b). All performance parameters are severely reduced as well as the hysteresis as most of the mobile ions have been transported towards the contacts by the induced electrical field and therefore became more immobile possibly due to chemical reactivity at the contact.[11] We note that the efficiency can be recovered as shown as supporting information and as reported previously. [26] Subsequent OCVD measurement (Figure 1c) clearly indicates that the dynamics of V_{oc} are also modified and now the decay is much slower with V_{oc} exceeding 100 mV even after 300 s. It has previously been shown that during OCVD the charging time of the interface can take several minutes and this requirement is fulfilled by polarization using the IS measuring conditions.[23] Indeed, the presence of a very large hole concentration at the interface with the electron extraction layer (i.e. SnO_2) due to accumulation conditions has been reported after using a light bias. The precise nature of ion migration and reactivity at the contacts has been dealt with in previous papers and it is still under debate.[11, 27] However, it is clear that the three discussed transient techniques (CV, OCVD and IS) persistently modify the state of the perovskite solar cell during the measurement itself. Unfortunately, it is not possible to offer a precise timescale for exposure to external stimuli upon which the electrical response is modified. Whilst some devices are very robust and can stand relatively long illumination and polarization

voltages, i.e. minutes, other devices seem to be more sensitive and dramatically modify their properties in seconds.

Physical Model

In order to develop a quantitative methodology that will allow us to assess the performance parameters of the devices, we describe a photovoltaic model for the perovskite solar cell based on standard semiconductor theory.[28-29] We are particularly interested to establish the deviation from ideality of the solar cell devices, hence we introduce in the model a specific nonideal exponent m_d and we explore the consequence of this assumption on measurable quantities. We develop the interdependence of different relevant quantities by means of a zero-dimensional model that assumes homogeneous distribution of carriers in the layer thickness d .

The voltage in the solar cell is given by the difference of electrochemical potentials (quasi Fermi levels) of electrons and holes at the respective selective contacts

$$qV = E_{Fn} - E_{Fp} \tag{1}$$

Electron and hole densities obey the following equations in terms of elementary charge q and the thermal energy $k_B T$

$$n = n_0 e^{(E_{Fn}-E_{F0})/k_B T} = N_c e^{-(E_c-E_{Fn})/k_B T} \tag{2}$$

$$p = p_0 e^{-(E_{Fp}-E_{F0})/k_B T} = N_v e^{(E_v-E_{Fp})/k_B T} \tag{3}$$

where N_c, N_v are effective densities of states in the conduction and valence band edge, respectively[29] and we have the product

$$np = n_i^{\,2} e^{qV/k_B T} \tag{4}$$

$$n_i^{\,2} = N_c N_v e^{-E_g/k_B T} \tag{5}$$

We describe the bimolecular recombination rate as a function of local carrier densities

$$U_n = B_{rec}\left[(np)^{1/m_d} - n_i^{\,2/m_d}\right] \tag{6}$$

Here the parameter B_{rec} is a kinetic recombination rate and m_d accounts for the nonideal behaviour of recombination that departs from strict bimolecular law. The recombination current is given by the integral of Eq. (6) over device thickness

$$j_{rec}(V) = j_0\left(e^{\frac{qV}{m_d k_B T}} - 1\right) \tag{7}$$

The dark diode current is $j_0 = qB_{rec} d\, n_i^{\,2/m_d}$. We remark that m_d describes nonideal behavior in the current-voltage curve, which is due to local recombination in the bulk absorber layer, and *not* to effects at the contact interfaces.

The local generation rate by absorbed light flux Φ_{ph} is

$$G = \frac{1}{d}\Phi_{ph} \tag{8}$$

The photocurrent is obtained by integration of the generation rate

$$j_{ph} \approx qGd = q\Phi_{ph} \tag{9}$$

Current voltage characteristics are described by the equation

$$j(V) = j_{ph} - j_0\left(e^{\frac{qV}{m_d k_B T}} - 1\right) \tag{10}$$

Under intense illumination the number of photogenerated carriers is larger than native doping density. Electroneutrality implies

$$n = p \tag{11}$$

From Eq. (4) the electron density depends on voltage as

$$n = n_i e^{qV/2k_B T} \tag{12}$$

We neglect the constant term in Eq. (6) and the recombination rate takes the form

$$U_n = B_{rec} n^{2/m_d} \tag{13}$$

The open circuit condition $G = U_n$, tells us that

$$n = \left(\frac{1}{d\,B_{rec}}\Phi_{ph}\right)^{m_d/2} \tag{14}$$

Open circuit voltage depends on illumination flux as

$$V_{oc} = \frac{m_d k_B T}{q}\ln\left(\Phi_{ph}\right) \tag{15}$$

An additive constant has been omitted in Eq. (15). The conductivity is

$$\sigma = q\mu_n n \tag{16}$$

where μ_n is an effective mobility. In the case of an interdigitated electrode illuminated from the top at open circuit conditions, the conductivity shows the dependence

$$\sigma = q\mu_n\left(\frac{\Phi_{ph}}{d\,B_{rec}}\right)^{m_d/2} \tag{17}$$

The recombination resistance is defined as

$$R_{rec} = \left(\frac{\partial j}{\partial V}\right)^{-1} \tag{18}$$

Thus

$$R_{rec}(V) = R_{rec0}e^{\frac{-qV}{m_d k_B T}} \tag{19}$$

So far the voltage has been associated to the splitting of Fermi levels. In the presence of a series resistance it is necessary to apply a correction to the applied voltage at the contacts:

$$V = V_{app} - jR_{series} \tag{20}$$

As mentioned above the simple model outlined here aims to capture the sources of nonideal behaviour in the current-voltage and conductivity measurements, mainly close to open circuit conditions, associated to a nearly homogeneous distribution of carriers. The model is a simple useful tool for analysing if the solar cell characteristics can be well described just by the photophysics of electron and hole carriers in the bulk, i.e. this model is determined by bulk recombination alone. We do not suggest that this is the general case. Indeed we remark below that under sustained polarization by applied bias the ionic accumulation causes a large control of recombination at the outer interface, which the above model cannot describe. For example in the case of strong inhomogeneous distribution of carriers (for example for cells with a short diffusion length) a more complex device simulation will also certainly be required.

Analysis of bulk properties of the perovskite layer

Now that a suitable physical theory has been described, we can proceed to present the measurements and analysis of the two types of devices fabricated in this work. First, in order to study the properties of bulk charge carrier densities, conductivity measurements of the perovskite material were performed on devices with interdigitated electrodes. The device configuration is shown as the inset of Figure 2a where a channel length of 50 μm is observed. The current-voltage characteristics was measured as a function of the light intensity I_0 covering the range from 0.01-100 mW/cm^2. The perovskite material clearly shows photoconductivity as previously reported[22, 30-31] and the current of the device increases more than two orders of magnitude with the incident light intensity. Conductivity can be calculated by extracting the material resistivity considering the nearly ohmic *j-V* curves and the geometrical parameters. Figure 2b shows the linear dependence of the conductivity in log scale with the light intensity. A slope of 0.45 can be calculated for data points measured at high illumination conditions and the ideality factor can be calculated from Eq. 16 with values close to unity (m_d = 0.9). Very importantly, the slope close to 0.5 from interdigitated electrodes validates the condition $n = p$ assumed in Eq. 8.

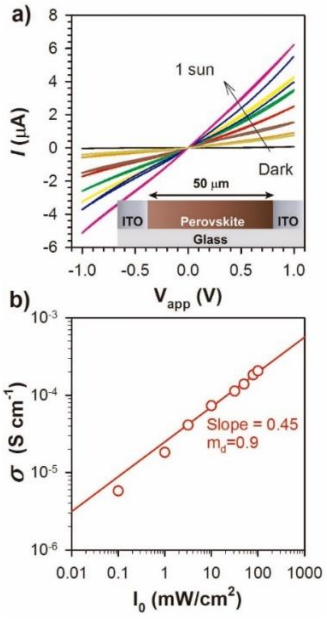

Figure 2: a) Photocurrent measurements under different illumination conditions for a sample with interdigitated electrode protected with PMMA measured at a scan rate of 50 mV/s. b) Perovskite conductivity as a function of the light intensity.

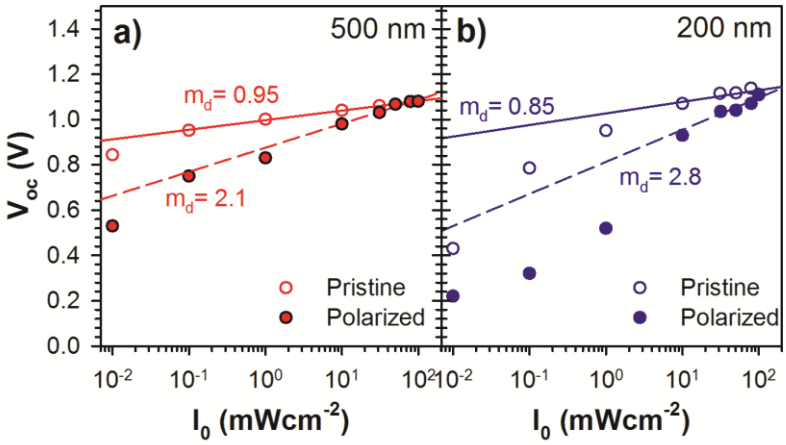

Figure 3: Comparison of V_{oc} dependence with light intensity for photovoltaic devices with different perovskite thickness (200 and 500 nm) measured when pristine and after polarization. Data has been fitted to a straight line in the range of 10-100 mWcm^{-2} light intensity.

In order to characterize recombination in the solar cell configuration we start with the V_{oc} vs. light intensity as shown in Fig. 3. The curves $V(I_0)$ show different regimes according to the light intensity as reported previously for photovoltaic devices by Zaban *et al.*[32] The presence of these regimes is better observed in Figure 2b for a thin perovskite layer (200 nm) with a polarized device. At low light intensity the curve is nearly flat most likely dominated by parasitic shunts. At intermediate light intensity the V_{oc} sharply increases and at high light intensity the V_{oc} moderately increases, which is typically observed for thin film solar cells. In perovskite solar cells it is reported that this region becomes independent of the type of contact.[32] We expect that the logarithmic dependence observed at high intensity is primarily due to bulk recombination. Here, the V_{oc} dependence has been analyzed for pristine devices and for devices that have been polarized. The data has been fitted to a straight line in the range of 10-100 mWcm^{-2} light intensity. Some representative data is shown in Figure 3 for two devices prepared with different perovskite thickness. It is observed that the $V(I_0)$ curve depends significantly on whether the device has been polarized by illumination at 1 sun at 1.2 V for 10 min. Pristine devices show V_{oc} reduction of ≈ 60 mV when the light intensity is decreased one order of magnitude, corresponding to nearly ideal behaviour of bimolecular recombination. Alternatively, polarized devices show a much more prominent dependence with a reduction of 100-180 mV under the same illumination range. This result is a clear sign that polarized devices suffer from activated recombination pathways. The ideality factor can be calculated from Eq. 14 and m_d values close to 1 are observed for pristine devices similarly to values observed for interdigitated electrodes. Alternatively, polarized devices show ideality factors exceeding 2.

Additionally, IS measurements have been performed on pristine devices to study the recombination properties. IS measurements were carried out under different light illumination conditions at V_{oc} as described above to avoid the use of external applied voltages, which could modify the external interfaces. For this reason measurement times were also minimized by restricting the lower frequency limit to avoid undesirable light induced chemical reactions with measurements starting in the dark and moving towards

high illumination conditions. At the end of the IS measurements the $j-V$ response is confirmed to be similar to that of a pristine device. By following this methodology we will show that the high frequency response is related to the recombination resistance of the bulk of the perovskite layer. Raw data on complex impedance plot and capacitance vs. frequency plots are shown as supporting information (Figure SI3) and the R_{series} does not change during the measurement as previously described. IS spectra show two arcs in the complex impedance plot as expected for a device with optimized extraction layers. Data can be fitted to the equivalent circuit previously reported (Fig. 4a).[19, 33] In this model both R_1 and C_1 are related to the perovskite/extraction layer interface and arise in the low frequency region. The capacitance C_{bulk} measured in the high frequency region is related to the dielectric properties of the perovskite layer.[19] The nature of the associated resistance (R_{rec}) leading to the high frequency arc in the complex impedance plot is not totally clear. Zarazua *et al.* have recently shown that for devices with previous electrical and optical history (i.e. previously the $j-V$ curve has been measured) the resistance is related to surface recombination processes at the external interfaces. [33] Alternatively, for pristine devices that have not been previously polarized the resistance depends exclusively on the bulk properties of the perovskite layer as it will be described below.

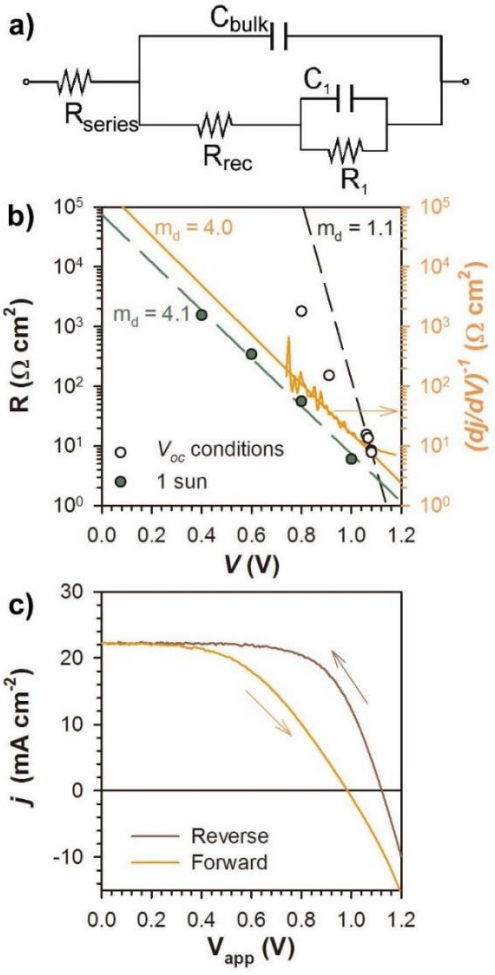

Figure 4: a) Equivalent Circuit used to fit the impedance data. b) Fitting results for the high frequency resistive response (R_{rec}) of IS measurements. Open circles correspond to measurements carried out at V_{oc} conditions under different light intensities. Green circles are obtained from measurements at 1 sun light intensity at different applied DC voltage. First derivate of current with the applied voltage is shown for comparison. The applied

voltage has been corrected to take into account the voltage drop at the external contacts due to the R_{series}. *c) j-V* response measured in the forward and reverse direction of the device analysed by impedance spectroscopy under constant illumination (1 sun) in b).

In Figure 4b it is observed that R_{rec} decreases exponentially with the light intensity providing higher V_{oc} at high light intensities. Open symbols indicate that the IS measurements have been carried out under the V_{oc} mild conditions, see experimental information. As described in Figure 3 the V_{oc} does not change much over an entire order of magnitude in light intensity. Using Eq. 18 an ideality factor approaching unity is obtained (m_d = 1.1). Very importantly, this value is very similar to that obtained in interdigitated electrodes suggesting that the resistance arises from the bulk properties of the perovskite layer. After this IS measurement the j-V curve of the device is measured and Figure 4c shows rather marked hysteresis behaviour. Subsequently, the IS response of the device is measured at constant illumination (1 sun). It has already been shown that the applied dc bias and constant light illumination used for impedance spectroscopy modifies the concentration of ions accumulated at the interfaces.[34] Indeed, variations in series resistance of devices can be observed indicating that large modifications have been induced. Interestingly, for measurements carried out at 1 sun light intensity (green circles) with applied voltage, the slope of the straight line defined by the different data points is rather different to measurements performed at V_{oc} conditions and provides an ideality factor of m_d = 4.0. It is important to note that the voltage has been corrected to account for the voltage drop that takes place at the contacts due to the series resistance of the device, Eq. 19, where the R_{series} has been obtained from fitting of the IS measurements. In any case this high frequency resistance does seem to be a real recombination resistance. Eq. 17 defines R_{rec} as the first derivative of the current density with the voltage and this function is plotted for the same device measured under 1 sun light illumination in Figure 4b (orange line). To obtain this curve, we applied direct analysis of the $j-V$ curve in Fig. 4c using Eq. 11 with correction for the series resistance for the measurement under forward conditions (orange trace). As can be observed the slope of the straight line for data points obtained from the forward scan and close to V_{oc} of the device coincides with that from the R_{rec} measured from the impedance data. Therefore, we can conclude that the resistance associated to the high frequency arc is a real recombination resistance that can provide kinetic information. The match of values indicates that this exponent directly controls the fill factor and hence the steady state performance of the perovskite cell. However, the value m_d = 4.0 is very high and indicates that the physical model outlined above in which m_d is explained by nonideal recombination, Eq. 6, is not valid when the applied voltage is inducing additional causes of nonideal behavior, that have been caused by polarization procedures. We suggest that the polarization is affecting severely the operation of contacts due to ion migration effects that lead to the nonideal exponent m_d = 4.0. In this case the proposed model based on bulk quantities does not hold due to the fact that interfacial and possibly defect-mediated recombination becomes dominant as shown by Zarazua *et al.* [33]

Finally, we can compare in Figure 5 the impedance response of pristine and polarized devices measured under V_{oc} conditions, in which the scan of dc bias is avoided, decreasing the ion migration effect. In this analysis special attention is paid to both resistive processes observed at high and low frequency. Alternatively, the ideality factor m_d can be calculated from the slopes of the straight lines defined by the resistances of the high and

low frequency regions. Pristine devices show ideality factors close to unity for both high and low resistances similar to those observed for interdigitated electrodes On the other hand, polarized devices show ideality factors considerably higher between 1.5-1.8 with values closer to those previously reported for lower efficiency devices.[33] Therefore, one can conclude that the resistances in pristine devices correspond to the recombination properties in the bulk of the perovskite layer while in pre-polarized devices recombination is taking place close to the external contacts as reported previously.

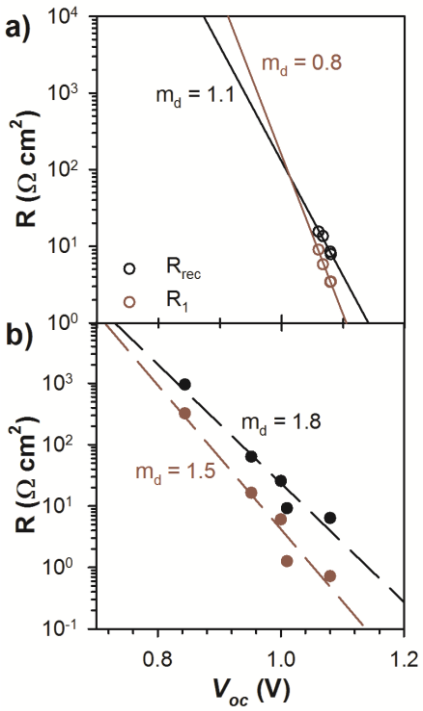

Figure 5: Fitting results for resistances associated to process in high and low frequency range for pristine (a) and polarized (b) devices.

In conclusion, we have adopted a series of characterization measurements in which a pristine, previously untreated perovskite solar cell, is under pure bulk recombination regime. A number of different measurements indicate that carrier density and open-circuit voltage are largely controlled by the bulk charge density which is established by equilibrium of generation-recombination, providing a close to ideal exponent of recombination and diode curve. However, when the solar cell is forced to establish charge extraction by applied bias voltage the contacts become modified and take a leading role in the subsequent operational properties of the solar cell. Overall we show that the electrical properties of the bulk perovskite layer can be probed by reducing the exposure of the photovoltaic device to external stimulus able to induce ion migration towards the external contacts. If the device is exposed to light or electrical field, ions will build-up at the contacts and the major electrical response will be dominated by the interfaces of the perovskite with the charge transport layers. Therefore, transient measurements will be influenced by the interference of ionic transport and polarization that cause very slow changes that cannot be separated from recombination kinetics. Alternatively, if during the measurement electrical fields are minimized, low light intensities are used and measuring times are reduced, pure electrical response of the perovskite layer appears with no interferences from the external contacts.

Methods

Electron selective layer preparation

F:SnO_2 substrates were first wiped with acetone, and then cleaned for 10 min in piranha solution (H_2SO_4/H_2O_2 = 3:1) followed by 10 min in a plasma cleaner prior to ALD deposition.

SnO_2 was deposited at 118 °C using Tetrakis(dimethylamino)tin(IV) (TDMASn, 99.99%-Sn, Strem Chemicals INC) and ozone at a constant growth rate of 0.065 nm/cycle measured by ellipsometry. TDMASn was held at 65 °C. Ozone was produced by an ozone generator ((AC-2025, IN USA Incorporated) fed with oxygen gas (99.9995% pure, Carbagas) producing a concentration of 13% ozone in O_2. Nitrogen was used as a carrier gas (99.9999% pure, Carbagas) with a flow rate of 10 sccm.

Perovskite precursor solution and film preparation

Mixed-cation lead mixed-halide perovskite solution was prepared from a precursor solution made of FAI (1 M, Dyesol), PbI_2 (1.1 M, TCl), MABr (0.2 M, Dyesol) and $PbBr_2$ (0.22 M, TCl) in a 4:1 (v:v) mixture of anhydrous DMF:DMSO (Acros). A 1.5 M stock solution of CsI (abcr GmbH) in DMSO was added to above solution in 5:95 volume ratio. The triple cation perovskite solution was deposited through a two-step spin coating program (10 s at 1000 rpm and 20 sec at 6000 rpm) with dripping of chlorobenzene as anti-solvent[35-36] during the second step, 5 s before the end. All the perovskite layers were annealed at 100°C for 45 min.

The spiro-OMeTAD (Merck) solution (70 mM in chlorobenzene) was spun at 4000 rpm for 20 s. The spiro-OMeTAD was doped at a molar ratio of 0.5, 0.03 and 3.3 with bis(trifluoromethylsulfonyl)imide lithium salt (Li-TFSI, Sigma Aldrich), tris(2-(1H-pyrazol-1-yl)-4-tert-butylpyridine)- cobalt(III) tris(bis(trifluoromethylsulfonyl)imide) (FK209, Dyenamo) and 4-tert-Butylpyridine (TBP, Sigma Aldrich), respectively.[37-39] For one experiment the Li concentration was varied from 0 to 1 molar ratio (0 to 100%). As a last step 70-80 nm of gold top electrode were thermally evaporated under high vacuum.

Interdigitated electrodes were purchased from Ossila (Code: S161). Due to the use of a bottom configuration of the interdigitated electrode the geometrical area was calculated from the contact area between the ITO and the perovskite layer ($1.50x10^{-12}$ cm^2). According to the supplied ITO thickness (100 nm) and the geometry of the electrode involves 5 fingers of each of 30 mm length.

Devices were measured under different illumination conditions using a Xe lamp (Oriel) with 1.5 AM filter in ambient at relative humidity of 30 %. The light intensity was adjusted to 100 $mWcm^{-2}$ sun light intensity using a calibrated Si solar cell. Different light conditions were generated using reflective optical filters with a wide range of neutral densities (OD = 0.1-4). Prior to the measurements devices were not exposed to any light soaking process and devices were not pre-conditioned by using an external bias. This special precaution was taken into consideration in order to avoid the effect of modification of the external interfaces due to ionic movements. Electrical measurements were carried out using a potentiostat equipped with a frequency analyzer module (Autolab PGSTAT30). Impedance spectroscopy measurements were carried out under V_{oc} conditions beginning with dark conditions and increasing the light intensity to 1 sun conditions. Experiments were carried out at a frequency range between 1MHz and 50 mHz. Using this frequency conditions each measurement at one voltage or illumination condition takes about 5 minutes. Impedance spectroscopy data was fitted using the equivalent circuit previously described in our group.[19]

ASSOCIATED CONTENT
Supporting Information
Current-voltage and impedance spectroscopy measurements

AUTHOR INFORMATION
Corresponding Authors
*E-mail: anders.hagfeldt@epfl.ch
*E-mail: bisquert@uji.es (J.B.).
Juan Bisquert: orcid.org/0000-0003-4987-4887
*E-mail: aguerrer@uji.es,
Antonio Guerrero: orcid.org/0000-0001-8602-1248
Notes
The authors declare no competing financial interest.

Acknowledgments
We acknowledge funding from MINECO of Spain under Project MAT2016-76892-C3-1-R and Generalitat Valenciana Project PROMETEOII/2014/020. A. G. would like to thank the Spanish Ministerio de Economía y Competitividad for a Ramón y Cajal Fellowship (RYC-2014-16809).

Supporting Information

Changes from Bulk to Surface Recombination Mechanisms between Pristine and Cycled Perovskite Solar Cells

Juan-Pablo Correa-Baena[1], Silver-Hamill Turren-Cruz,[1] Wolfgang Tress,[1] Anders Hagfeldt,*[1] Clara Aranda,[2] Leyla Shooshtari,[2,3] Juan Bisquert,*[2,4] Antonio Guerrero*[2]

[1] Laboratory of Photomolecular Science, Institute of Chemical Sciences and Engineering, École Polytechnique Fédérale de Lausanne, CH-1015-Lausanne, Switzerland

[2] Institute of Advanced Materials (INAM), Universitat Jaume I, 12006 Castelló, Spain
[3] Institute for Nanoscience and Nanotechnology, Sharif University of Technology, Tehran, 14588-89694, Iran
[4]Department of Chemistry, Faculty of Science, King Abdulaziz University, Jeddah, Saudi Arabia

Email: anders.hagfeldt@epfl.ch , bisquert@uji.es , aguerrer@uji.es,

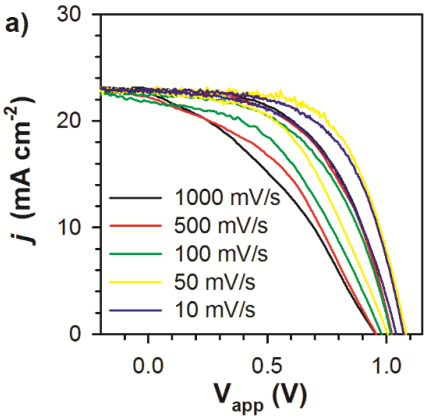

Figure SI1: *j-V* measurements carried out at 1 sun light illumination as a function of the scan rate. Hysteresis is minimized as the scan rate is reduced.

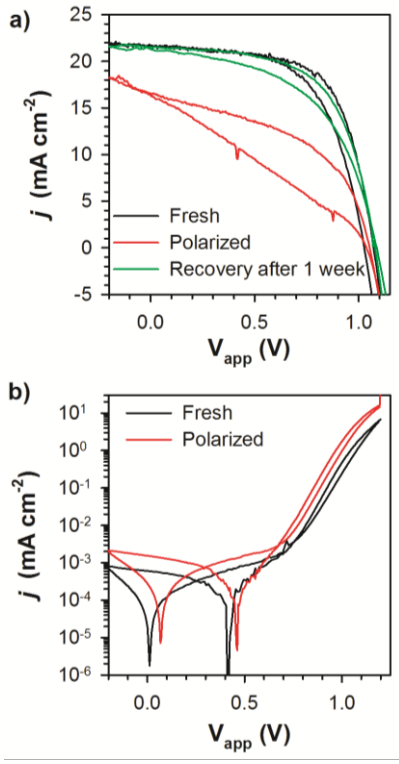

Figure SI2: a) *j-V* of a representative device prepared in the same batch that shows less hysteresis at sweep rate of 50 mV/s but similar response after polarization of the device by illumination at 1 sun at 1.2 V for 10 min. Efficiency is partially recovered after storing the device in dry oxygen in the dark. b) Comparison of *j-V* curve of fresh and polarized devices measured in the dark.

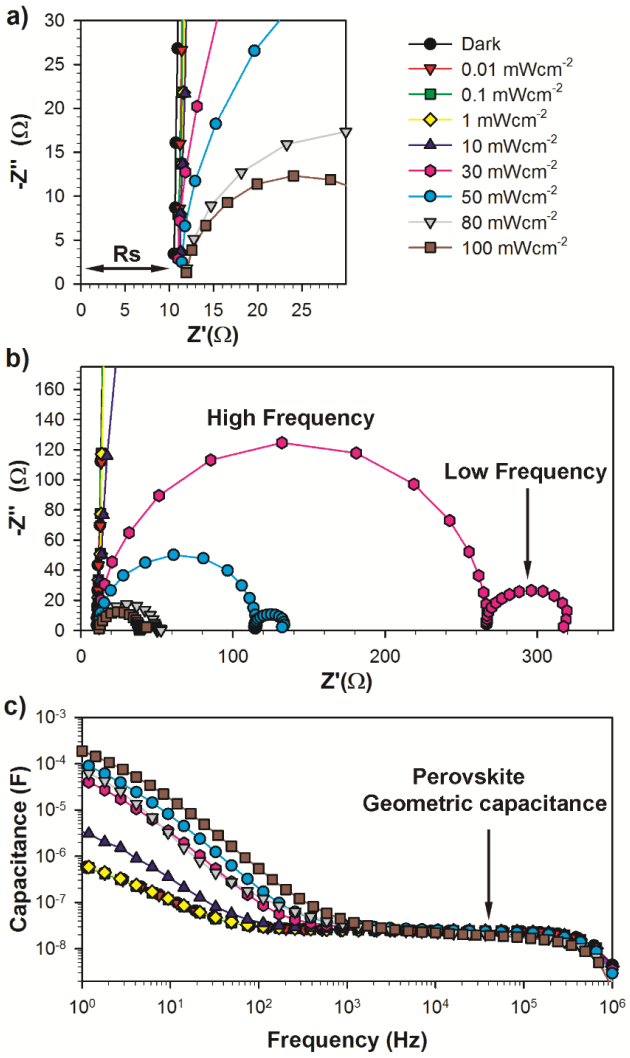

Figure SI3: Summary of impedance spectroscopy data for measurements carried out at V_{oc} conditions under different light intensities. a) Analysis of series resistance by using the complex impedance plot. The R_s remains almost constant during the measurement. b) Complex impedance plot highlighting measurements at high light intensity conditions relevant for the analysis described in the main text. Two arcs are observed as described previously in the literature c) Capacitance-frequency plot. The plateau measured at high frequencies corresponds to the bulk properties of the perovskite layer as described in the literature.[19]

References

1. Bertoluzzi, L.; Sanchez, R. S.; Liu, L.; Lee, J.-W.; Mas-Marza, E.; Han, H.; Park, N.-G.; Mora-Sero, I.; Bisquert, J. Cooperative kinetics of depolarization in CH3NH3PbI3 perovskite solar cells. *Energy & Environmental Science* **2015,** *8*, 910-915.

2. Gottesman, R.; Zaban, A. Perovskites for Photovoltaics in the Spotlight: Photoinduced Physical Changes and Their Implications. *Accounts of Chemical Research* **2016**.

3. deQuilettes, D. W.; Zhang, W.; Burlakov, V. M.; Graham, D. J.; Leijtens, T.; Osherov, A.; Bulovic, V.; Snaith, H. J.; Ginger, D. S.; Stranks, S. D. Photo-induced halide redistribution in organic-inorganic perovskite films. *Nat Commun* **2016,** *7*.

4. Galisteo-López, J. F.; Anaya, M.; Calvo, M. E.; Míguez, H. Environmental Effects on the Photophysics of Organic–Inorganic Halide Perovskites. *J. Phys. Chem. Lett.* **2015,** *6* (12), 2200-2205.

5. Zhou, Y.; Garces, H. F.; Padture, N. P. Challenges in the ambient Raman spectroscopy characterization of methylammonium lead triiodide perovskite thin films. *Frontiers of Optoelectronics* **2016,** *9* (1), 81-86.

6. Ledinský, M.; Löper, P.; Niesen, B.; Holovský, J.; Moon, S.-J.; Yum, J.-H.; De Wolf, S.; Fejfar, A.; Ballif, C. Raman Spectroscopy of Organic–Inorganic Halide Perovskites. *The Journal of Physical Chemistry Letters* **2015,** *6* (3), 401-406.

7. Unger, E. L.; Hoke, E. T.; Bailie, C. D.; Nguyen, W. H.; Bowring, A. R.; Heumuller, T.; Christoforo, M. G.; McGehee, M. D. Hysteresis and transient behavior in current-voltage measurements of hybrid-perovskite absorber solar cells. *Energy & Environmental Science* **2014,** *7* (11), 3690-3698.

8. Li, C.; Tscheuschner, S.; Paulus, F.; Hopkinson, P. E.; Kießling, J.; Köhler, A.; Vaynzof, Y.; Huettner, S. Iodine Migration and its Effect on Hysteresis in Perovskite Solar Cells. *Advanced Materials* **2016,** *28* (12), 2446-2454.

9. Snaith, H. J.; Abate, A.; Ball, J. M.; Eperon, G. E.; Leijtens, T.; Kimberly, N.; Stranks, S. D.; Wang, J. T.-W.; Wojciechowski, K.; Zhang, W.; Noel, N. K. Anomalous Hysteresis in Perovskite Solar Cells. *The Journal of Physical Chemistry Letters* **2014,** *5*, 1511–1515.

10. Tress, W.; Marinova, N.; Moehl, T.; Zakeeruddin, S. M.; Nazeeruddin, M. K.; Gratzel, M. Understanding the rate-dependent J-V hysteresis, slow time component, and aging in CH3NH3PbI3 perovskite solar cells: the role of a compensated electric field. *Energy & Environmental Science* **2015,** *8* (3), 995-1004.

11. Carrillo, J.; Guerrero, A.; Rahimnejad, S.; Almora, O.; Zarazua, I.; Mas-Marza, E.; Bisquert, J.; Garcia-Belmonte, G. Ionic reactivity at contacts and aging of methylammonium lead triiodide perovskite solar cell *Advanced Energy Materials* **2016,** *6* (9), 1502246.

12. Almora, O.; Guerrero, A.; Garcia-Belmonte, G. Ionic charging by local imbalance at interfaces in hybrid lead halide perovskites. *Applied Physics Letters* **2016,** *108* (4), 043903.

13. Garcia-Belmonte, G.; Bisquert, J. Distinction between Capacitive and Noncapacitive Hysteretic Currents in Operation and Degradation of Perovskite Solar Cells. *ACS Energy Letters* **2016**, 683-688.

14. Bisquert, J.; Fabregat-Santiago, F.; Mora-Seró, I.; Garcia-Belmonte, G.; Giménez, S. Electron lifetime in dye-sensitized solar cells: theory and interpretation of measurements. *The Journal of Physical Chemistry C* **2009,** *113*, 17278–17290.

15. Garcia-Belmonte, G.; Boix, P. P.; Bisquert, J.; Sessolo, M.; Bolink, H. J. Simultaneous determination of carrier lifetime and electron density-of-states in P3HT:PCBM organic solar cells under illumination by impedance spectroscopy *Solar Energy Materials and Solar Cells* **2010,** *94*, 366-375

16. Yamada, Y.; Nakamura, T.; Endo, M.; Wakamiya, A.; Kanemitsu, Y. Photocarrier Recombination Dynamics in Perovskite CH3NH3PbI3 for Solar Cell Applications. *Journal of the American Chemical Society* **2014,** *136* (33), 11610-11613.

17. Johnston, M. B.; Herz, L. M. Hybrid Perovskites for Photovoltaics: Charge-Carrier Recombination, Diffusion, and Radiative Efficiencies. *Accounts of Chemical Research* **2016,** *49* (1), 146-154.

18. Correa-Baena, J. P.; Steier, L.; Tress, W.; Saliba, M.; Neutzner, S.; Matsui, T.; Giordano, F.; Jacobsson, T. J.; Srimath Kandada, A. R.; Zakeeruddin, S. M.; Petrozza, A.; Abate, A.; Nazeeruddin, M. K.; Gratzel, M.; Hagfeldt, A. Highly efficient planar perovskite solar cells through band alignment engineering. *Energy & Environmental Science* **2015,** *8*, 2928-2934.

19. Guerrero, A.; Garcia-Belmonte, G.; Mora-Sero, I.; Bisquert, J.; Kang, Y. S.; Jacobsson, T. J.; Correa-Baena, J.-P.; Hagfeldt, A. Properties of Contact and Bulk Impedances in Hybrid Lead Halide Perovskite Solar Cells Including Inductive Loop Elements. *J. Phys. Chem. C* **2016,** *120* (15), 8023-8032.

20. Saliba, M.; Matsui, T.; Seo, J.-Y.; Domanski, K.; Correa-Baena, J.-P.; Nazeeruddin, M. K.; Zakeeruddin, S. M.; Tress, W.; Abate, A.; Hagfeldt, A.; Gratzel, M. Cesium-containing triple cation perovskite solar cells: improved stability, reproducibility and high efficiency. *Energ. Environ. Sci.* **2016**.

21. Anaraki, E. H.; Kermanpur, A.; Steier, L.; Domanski, K.; Matsui, T.; Tress, W.; Saliba, M.; Abate, A.; Gratzel, M.; Hagfeldt, A.; Correa-Baena, J.-P. Highly efficient and stable planar perovskite solar cells by solution-processed tin oxide. *Energy & Environmental Science* **2016,** *9* (10), 3128-3134.

22. Sveinbjörnsson, K.; Aitola, K.; Zhang, X.; Pazoki, M.; Hagfeldt, A.; Boschloo, G.; Johansson, E. M. J. Probing Photocurrent Generation, Charge Transport, and

Recombination Mechanisms in Mesostructured Hybrid Perovskite through Photoconductivity Measurements. *The Journal of Physical Chemistry Letters* **2015,** *6* (21), 4259-4264.

23. Gottesman, R.; Lopez-Varo, P.; Gouda, L.; Jimenez-Tejada, Juan A.; Hu, J.; Tirosh, S.; Zaban, A.; Bisquert, J. Dynamic Phenomena at Perovskite/Electron-Selective Contact Interface as Interpreted from Photovoltage Decays. *Chem* **2016,** *1* (5), 776-789.

24. Zarazua, I.; Han, G.; Boix, P. P.; Mhaisalkar, S.; Fabregat-Santiago, F.; Mora-Seró, I.; Bisquert, J.; Garcia-Belmonte, G. Surface Recombination and Collection Efficiency in Perovskite Solar Cells from Impedance Analysis. *The Journal of Physical Chemistry Letters* **2016,** *7* (24), 5105-5113.

25. Roiati, V.; Mosconi, E.; Listorti, A.; Colella, S.; Gigli, G.; De Angelis, F. Stark Effect in Perovskite/TiO2 Solar Cells: Evidence of Local Interfacial Order. *Nano Letters* **2014,** *14* (4), 2168-2174.

26. Tress, W.; Correa Baena, J. P.; Saliba, M.; Abate, A.; Graetzel, M. Inverted Current–Voltage Hysteresis in Mixed Perovskite Solar Cells: Polarization, Energy Barriers, and Defect Recombination. *Advanced Energy Materials* **2016,** *6* (19), 1600396-n/a.

27. Domanski, K.; Roose, B.; Matsui, T.; Saliba, M.; Turren-Cruz, S.-H.; Correa-Baena, J.-P.; Roldan Carmona, C.; Richardson, G.; Foster, J.; De Angelis, F.; Ball, J.; petrozza, a.; Mine, N.; Nazeeruddin, M. K.; Tress, W.; Gratzel, M.; Steiner, U.; Hagfeldt, A.; Abate, A. Migration of cations induces reversible performance losses over day/night cycling in perovskite solar cells. *Energy & Environmental Science* **2017**.

28. Bisquert, J. *Nanostructured Energy Devices: Equilibrium Concepts and Kinetics*. CRC Press: Boca Raton, 2014.

29. Bisquert, J.; Garcia-Belmonte, G.; Mora-Sero, I. Characterization of Capacitance, Transport and Recombination Parameters in Hybrid Perovskite and Organic Solar Cells. In *Unconventional Thin Film Photovoltaics*, Como, E. D.; Angelis, F. D.; Snaith, H.; Walker, A., Eds. The Royal Society of Chemistry: London, 2016.

30. Müller, C.; Glaser, T.; Plogmeyer, M.; Sendner, M.; Döring, S.; Bakulin, A. A.; Brzuska, C.; Scheer, R.; Pshenichnikov, M. S.; Kowalsky, W.; Pucci, A.; Lovrinčić, R. Water Infiltration in Methylammonium Lead Iodide Perovskite: Fast and Inconspicuous. *Chemistry of Materials* **2015,** *27* (22), 7835-7841.

31. Gottesman, R.; Haltzi, E.; Gouda, L.; Tirosh, S.; Bouhadana, Y.; Zaban, A.; Mosconi, E.; De Angelis, F. Extremely Slow Photoconductivity Response of CH3NH3PbI3 Perovskites Suggesting Structural Changes under Working Conditions. *The Journal of Physical Chemistry Letters* **2014,** *5* (15), 2662-2669.

32. Gouda, L.; Gottesman, R.; Ginsburg, A.; Keller, D. A.; Haltzi, E.; Hu, J.; Tirosh, S.; Anderson, A. Y.; Zaban, A.; Boix, P. P. Open Circuit Potential Build-Up in Perovskite

Solar Cells from Dark Conditions to 1 Sun. *The Journal of Physical Chemistry Letters* **2015,** *6* (22), 4640-4645.

33. Zarazua, I.; Han, G.; Boix, P. P.; Mhaisalkar, S.; Fabregat-Santiago, F.; Mora-Seró, I.; Bisquert, J.; Garcia-Belmonte, G. Surface Recombination and Collection Efficiency in Perovskite Solar Cells from Impedance Analysis. *The Journal of Physical Chemistry Letters* **2016**, 5105-5113.

34. Gottesman, R.; Lopez-Varo, P.; Gouda, L.; Jimenez-Tejada, J. A.; Hu, J.; Tirosh, S.; Zaban, A.; Bisquert, J. Dynamic phenomena at perovskite/electron-selective contact interface as interpreted from photovoltage decays. *Chem* **2016,** *1*, 776-789.

35. Jeon, N. J.; Noh, J. H.; Kim, Y. C.; Yang, W. S.; Ryu, S.; Seok, S. I. Solvent engineering for high-performance inorganic–organic hybrid perovskite solar cells. *Nat Mater* **2014,** *13* (9), 897-903.

36. Jeon, N. J.; Noh, J. H.; Yang, W. S.; Kim, Y. C.; Ryu, S.; Seo, J.; Seok, S. I. Compositional engineering of perovskite materials for high-performance solar cells. *Nature* **2015,** *517* (7535), 476-480.

37. Abate, A.; Leijtens, T.; Pathak, S.; Teuscher, J.; Avolio, R.; Errico, M. E.; Kirkpatrik, J.; Ball, J. M.; Docampo, P.; McPherson, I.; Snaith, H. J. Lithium salts as "redox active" p-type dopants for organic semiconductors and their impact in solid-state dye-sensitized solar cells. *Physical Chemistry Chemical Physics* **2013,** *15* (7), 2572-2579.

38. Abate, A.; Staff, D. R.; Hollman, D. J.; Snaith, H. J.; Walker, A. B. Influence of ionizing dopants on charge transport in organic semiconductors. *Physical Chemistry Chemical Physics* **2014,** *16* (3), 1132-1138.

39. Snaith, H. J.; Abate, A.; Ball, J. M.; Eperon, G. E.; Leijtens, T.; Noel, N. K.; Stranks, S. D.; Wang, J. T.-W.; Wojciechowski, K.; Zhang, W. Anomalous Hysteresis in Perovskite Solar Cells. *The Journal of Physical Chemistry Letters* **2014,** *5* (9), 1511-1515.

Chapter 8

Publication 5

Ionic Effect Enhances Light Emission and the Photovoltage of Methylammonium Lead Bromide Perovskite Solar Cells by Reduced Surface Recombination. Aranda, C.*; Guerrero, A.; Bisquert, J.* *ACS Energy Letters*, ***2019***, *4, 741–746.*

CANDIDATE´S CONTRIBUTION

Nature of Contribution	Extent of Contribution
✓ Development of $MAPbBr_3$ formulation. ✓ Fabrication of PSCs. ✓ Performing all the optic and electrical measurement. ✓ Analysis of the results. ✓ Preparation of figures. ✓ Writing of manuscript. ✓ Responses to the referees.	90%

INTRODUCTION

This work established the contribution of extrinsic ions in the reduction of surface recombination processes at the ESL/perovskite interface. The investigation is focused in a wide band gap material as $MAPbBr_3$ to further analyse the loss-in-potential occurring in PSCs without distinction and which is blocking the achievement of theoretical maximum PCE of these devices. Through IS analysis coupled with PL and EL measurements, it is possible to confirm that lithium ion, used as additive into the external contacts, blocks surface recombination between TiO_2/perovskite, enhancing light emission of the bulk material and pushing forward photovoltage values up to a record of 1.6 V for a n-i-p architecture using TiO_2 and Spiro-OMeTAD as selective contacts. A reduction in the hole density at the accumulation zone located at the ESL/perovskite interface, is proposed as the main mechanism thorugh the surface recombination is reduced.

PUBLISHED MANUSCRIPT

Ionic Effect Enhances Light Emission and Photovoltage of Methylammonium Lead Bromide Perovskite Solar Cell by Reduced Surface Recombination

Clara Aranda*[1], Antonio Guerrero[1], Juan Bisquert*[1]

Institute of Advanced Materials (INAM), Universitat Jaume I, 12006 Castelló, Spain

Email: caranda@uji.es bisquert@uji.es

Abstract

The achievement of optimal power conversion efficiencies (PCE) in wide band gap perovskite solar cells (PSCs) is delayed by photovoltage losses associated to the poor understanding of recombination dynamics. In this work, we use high quality methylammonium lead bromide perovskite solar cells with selective contacts treated with lithium-containing additives to investigate recombination mechanisms. By comparison of the photovoltaic performance of devices we confirm that the presence of this additive in the electron selective layer (ESL) significantly increases the open circuit potential to values of 1.58 V. Impedance spectroscopy coupled with electroluminescence and photoluminescence analysis reveals that lithium ion present at the mesoporous TiO_2 layer dramatically enhances the radiative recombination in the perovskite by reduction of undesired non-radiative and surface recombination pathways. This work highlights that the use of additives can be used to modify the electronic charge distribution at the metal oxide/perovskite interface to suppress undesired recombination mechanisms.

Table of Contents (TOC)

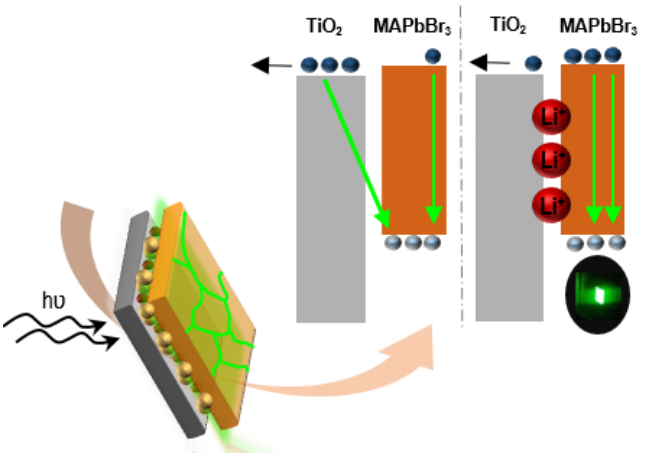

The understanding of recombination mechanisms in perovskite solar cells (PSCs) represents one of the most challenging goals in this field.[1,2] Many authors are focusing their efforts to clarify the dynamics of limiting photovoltage to achieve the maximum power conversion efficiency (PCE).[3,4] The highest PCE obtained by perovskite solar cells with the $APbX_3$ formula use a mixture of monovalent cations A (i.e. formamidinium, methylammonium (MA) and cesium) and mainly iodide derivatives (X=I) with bandgap of approximately 1.5-1.6 eV.[5] Alternatively, the perovskite solar cells based in methylammonium lead bromide material have a wider band gap of 2.3 eV and can theoretically deliver greater open-circuit voltages (V_{oc}).[6] In addition, there is high interest to improve the quality of this bromide-semiconductor film and its optoelectronics properties in complete devices as the material can be used in tandem photovoltaic devices, light emitting diodes and could be used to drive electrochemical reactions.[7,8,9,10]

The presence of undesired non-radiative recombination processes is related to a reduction in the V_{oc} of photovoltaic devices.[11] Despite the intensive work with $MAPbBr_3$ the highest reported V_{oc} is 1.61 V, yet representing 0.4 eV loss from the theoretical voltage in the radiative limit.[12] Then, this material is an excellent candidate for in depth investigations of the recombination mechanisms related with V_{oc} losses. Unfortunately, this relative success relies on the use of Ca/Al as top contact, known to be highly reactive towards perovskite and ambient conditions, and using a fullerene bis-indene adduct (ICBA) as electron selective layer (ESL).[13] Alternatively, due to the high stability of metal oxides, TiO_2 is often the preferred choice as ESL which can be used in combination with organic materials as hole selective layers (HSL).[14,9,15] Previous research with iodide perovskite derivatives has shown that Li-TFSI can be used as additive on the mesoporous TiO_2 layer to improve the photovoltaic properties of the solar cells, attributing the enhancement to a faster transport and better carrier extraction of the metal oxide.[16,17,18] However, a major gain of V_{oc} should be primarily related to a reduction of recombination mechanisms and would require further investigation.

In this work we show that the use of additives in the ESL can reduce undesired non-radiative and interfacial recombination processes leading to solar cells with increased V_{oc} and enhanced electroluminescence (EL) emission of perovskite layer. Impedance Spectroscopy measurements show that the total recombination processes are reduced when the external contacts are treated with ionic additives. Alternatively, in the absence of additives PL results clearly evidence that extraction of carriers is not efficient and emission due to $MAPbBr_3/TiO_2$ interfacial recombination processes is observed.

We developed here a 1-step process *via* the $PbBr_2$:MABr:DMSO adduct, analogue to that used for $MAPbI_3$ to prepare high quality $MAPbBr_3$ solar device.[19,20] Complete characterization of the films is shown in the Supporting Information. The high crystallinity of the $MAPbBr_3$ and absence of chemical defects and pinholes allow us to focus our attention on additive treatments studies to investigate the recombination dynamics at the interfaces. A Li-TFSI solution was spin coated onto the mesoporous TiO_2 layer followed by annealing at 450ºC to remove the organic part of the salt.[21] Figure 1a shows a scheme of the two devices configurations with and without Li-TFSI additive (w/wo Li^+). Both are composed of fluorine doped tin oxide (FTO), blocking layer of TiO_2 (60 nm) deposited by spray pyrolysis, spin-coated mesoporous layer of TiO_2 (150 nm) with and without Li^+, spin-coated $MAPbBr_3$ layer (600 nm) covered by Spiro-OMeTAD (150 nm) as HSL and gold electrode (60 nm). Both devices reached efficiencies of 4.8 % (no Li^+) and 6.6% (with Li^+), as shown by representative current-voltage curves with forward sweep under 100 mW cm^{-2} illumination (Fig. 1c). We confirm the beneficial effect of lithium additive in the ESL in the solar cell and reveal that the major difference

between the two systems is the increase of approximately 200 mV in V_{oc} (Table 1) for the device treated with Li^+.

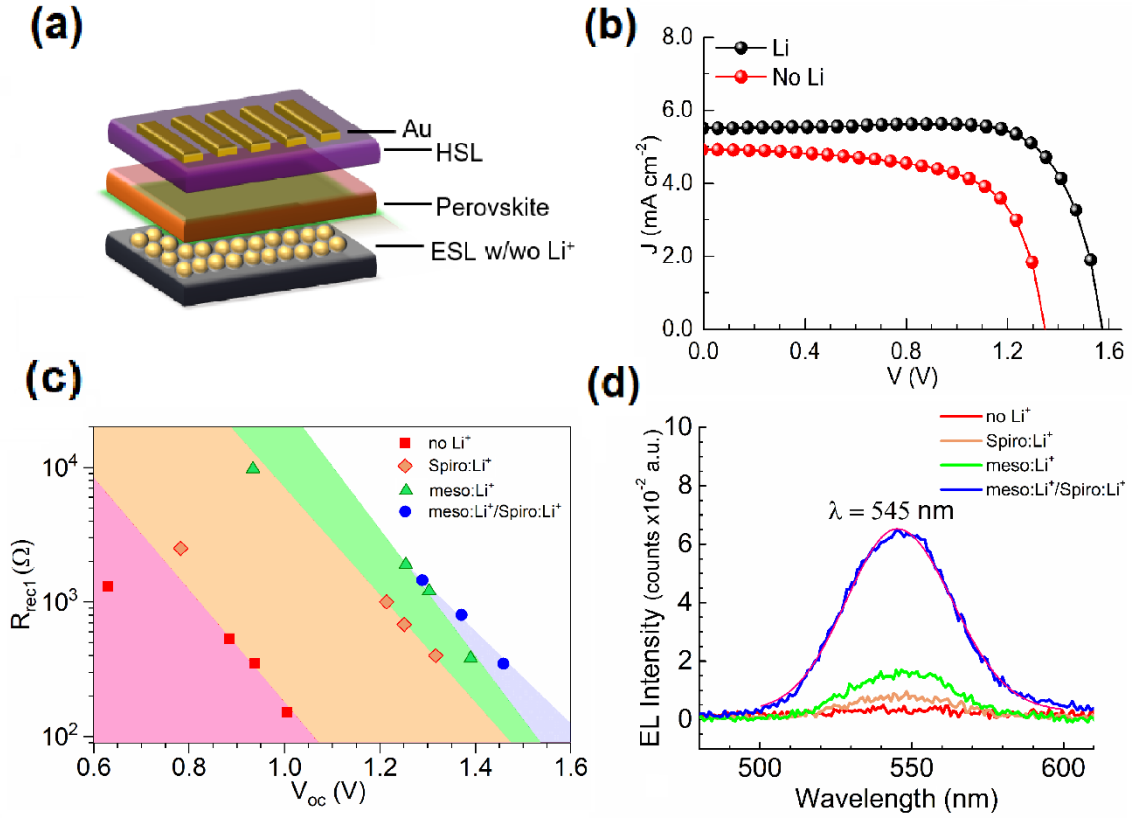

Figure 1. (a) Schematic device configuration representing the additive treatment in the mesoporous TiO_2 layer. (b) Comparison of current-voltage curves measured under 1 sun illumination (AM 1.5G) of two representative devices with and without Li^+ in the mesoporous TiO_2 layer. Only forward sweep at 50 mV s^{-1} is shown for clarity. (c) Fitting results for high frequency resistances associated with recombination processes of impedance spectroscopy measurements under open-circuit conditions at varying irradiations intensities. Each color corresponds to a device configuration with selective contacts with different lithium salt treatments: Red, FTO/c-TiO_2/m-TiO_2/PVK/Spiro/Au; Orange, FTO/c-TiO_2/m-TiO_2/PVK/Spiro:Li/Au Green, FTO/c-TiO_2/m-TiO_2:Li/PVK/Spiro/Au; Blue, FTO/c-TiO_2/m-TiO_2:Li/PVK/Spiro:Li/Au. (d) EL spectra of devices shown in c) at forward bias of 1.4 V.

Table 1. Photovoltaic parameters extracted from the JV curves shown in Fig. 1 performed at forward bias under 1 sun illumination (AM 1.5G).

Devices	**J (mA cm^{-2})**	**FF (%)**	**V_{oc} (V)**	**PCE (%)**
w/o Li^+	5.3	69	1.36	4.8
with Li^+	5.5	76	1.58	6.6

Impedance spectroscopy analysis (IS) was carried out to understand the major gain in V_{oc} as the measurements provide kinetic information of the recombination processes.[22,23] In this technique, a DC voltage is applied to the sample and a small AC voltage perturbation is added to cover a wide range of frequencies. Here, we perform IS at different irradiances (from dark to 1 sun) at open circuit conditions to avoid the use of external applied voltages, which could modify the external interfaces.[24] Complex impedance plots are shown in SI (Fig. S6). For a device with optimized ESL and HSL, IS

spectra should present two arcs in the impedance plot connected with recombination of carriers.[25] The combined radiative and non-radiative processes are probed by IS in terms of a recombination resistance (R_{rec}) which is related with the V_{oc} of the device. High values of R_{rec} are connected with favorable slow recombination kinetics. The precise origin of each resistance is not completely clear, however, it has been already related to surface recombination mechanisms at the external interfaces for devices with preceding history of optical and electrical measurements.[26] In Fig. 1c we analyze the high frequency R_{rec} of devices where no treatment with LiTFSI in any of the ESL and HSL is compared with treatment of these layers with the additive. The results show that a larger R_{rec} in a type of contact treatment is clearly associated to an increase of the photovoltage, which can be related to absolute decrease of recombination processes when Li^+ is consecutively added to each of the selective contacts, with best results in the case of both contacts treated with the additive. This reduction in the kinetics of the recombination processes is further confirmed by a calculation of the recombination coefficients presented in SI.

In order to clarify the origin of these recombination dynamics, we performed EL measures of the devices treated with LiTFSI at the contacts (Fig. 1d). In these experiments the perovskite solar cell is polarized at forward bias of 1.4 V and the emission spectra is recorded when the carriers are directly injected through the contacts. The results reveal a very interesting trend. All the devices show the distinct bromide-based perovskite peak around 545 nm which is connected to band-to-band emission in the perovskite layer. When the solar cell does not contain lithium, the band-to-band transition intensity of the perovskite emission is very weak, pointing to the presence of activated non-radiative recombination pathways. Alternatively, as the external contacts are treated with LiTFSI the intensity of bulk emission increases dramatically (blue line with treatment in both contacts). Therefore, when no lithium is used to treat the contacts, injected charges from the contacts do not recombine through the bulk *via* band-to-band emission, but rather by non-radiative recombination pathways or by radiative emission at the interfaces, as shown below. Interestingly, the presence of Li^+ increases the band-to-band radiative recombination emission at the same time that the deleterious surface recombination is reduced.

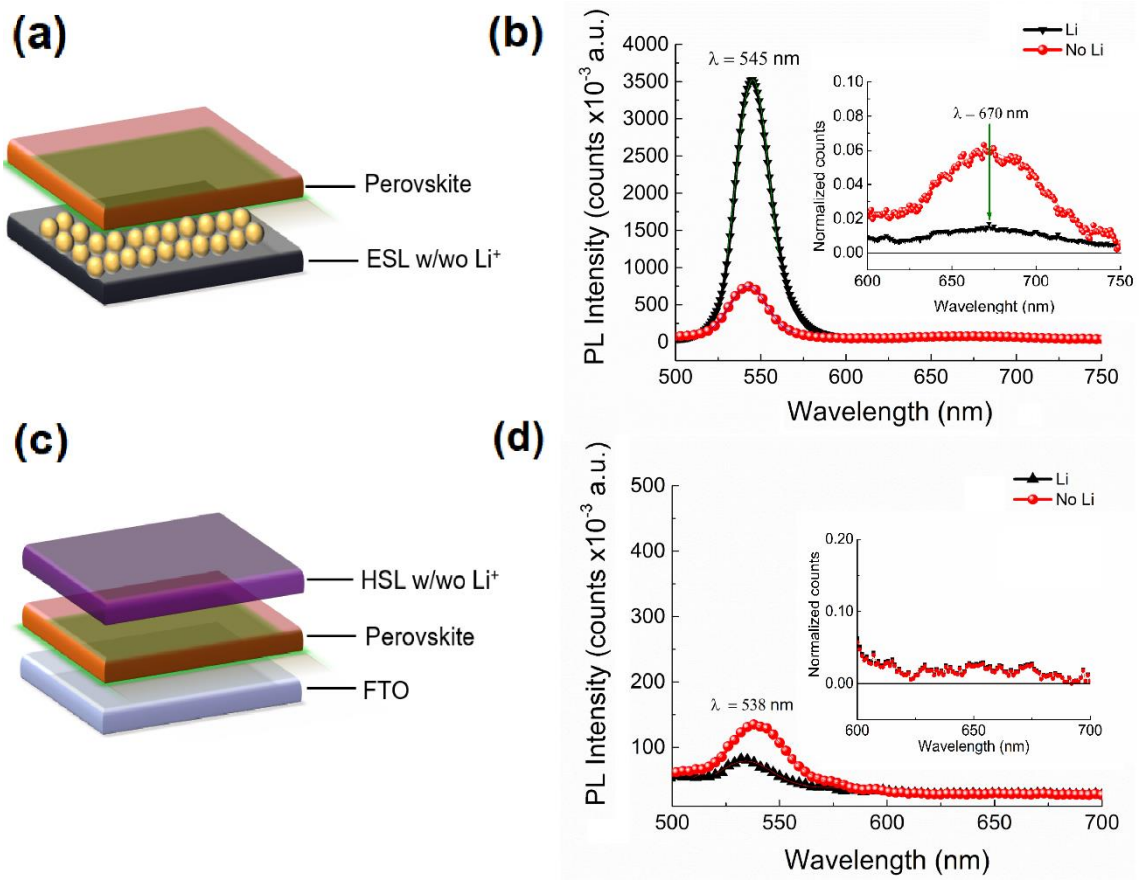

Figure 2. Photoluminescence measurements focused in both TiO_2/perovskite and perovskite/Spiro-OMeTAD interfaces showing the enhancing of perovskite emission and suppression of the interfacial emission. (a), (c) Schematic device configuration used in PL measure for ESL/$MAPbBr_3$ and $MAPbBr_3$/HSL interfaces w/wo Li^+. (b) ESL/$MAPbBr_3$ Photoluminescence spectra obtained under continuous wave (CW) excitation (380 nm, Iexc = 10 mW cm^{-2}) of devices with (black) and without (red) lithium treatment at metal oxide contact. Inset plot shows the quenching of the second feature when lithium is present at metal oxide contact. (d) $MAPbBr_3$/HSL Photoluminescence spectra obtained under same conditions as before with (black) and without (red) lithium as additive into the Spiro-OMeTAD solution.

To confirm this interpretation and to identify surface recombination features, we performed photoluminescence (PL) steady state measurement in simpler device configurations to study only one perovskite/external interface at each time. PL of perovskite films grown on mesoporous TiO_2, either containing or un-doped with Li^+ are shown in Fig. 2b. The characteristic peak emission of the perovskite bulk around 545 nm (2.3 eV of bandgap) is present when an incident monochromatic light of 380 nm excitation wavelength irradiates Li-doped (black) and un-doped (red) devices. The intensity of this emission peak follows the same trend previously showed in EL spectra: Li^+ increases light emission by band-to-band radiative recombination. But most interestingly, when the device does not contain lithium, a second low intense broad emission peak at around 670 nm (1.85 eV) is observed which is strongly quenched when TiO_2 is treated with Li^+ (inset of Fig. 2b). Previous analysis of capacitance results revealed that an accumulation layer of electronic holes, accompanied by mobile cations, is formed under illumination at the contact with TiO_2.[27] We interpret then the second feature as radiative surface recombination caused by a charge-transfer state between TiO_2 surface state located at the

conduction band of the metal oxide, and holes accumulated in the valence band at the perovskite side of the interface. The schematic diagram of the features band-to-band and interfacial recombination is shown in Fig. 3a.

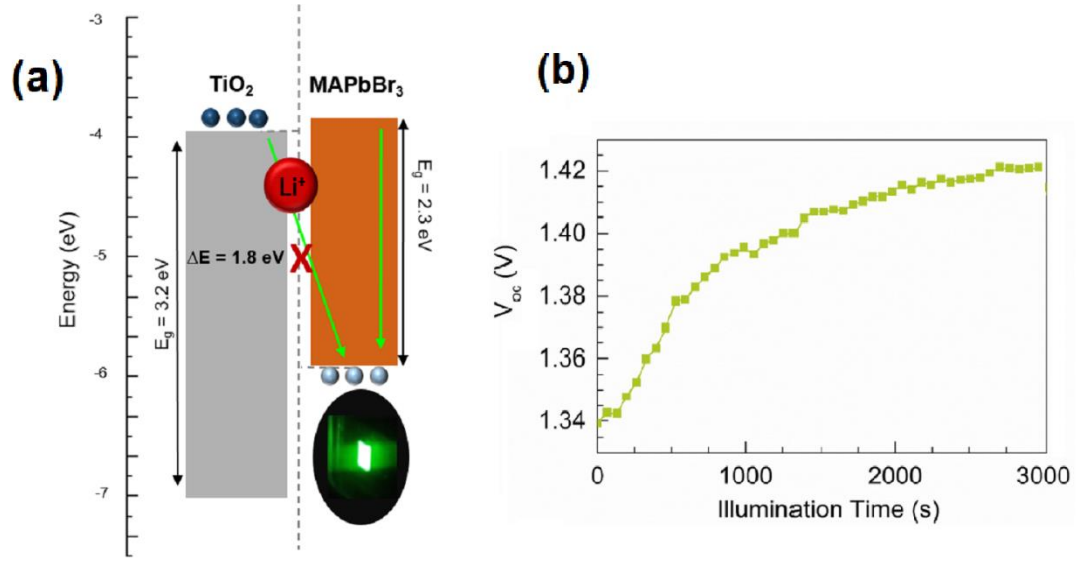

Figure 3. (a) Schematic diagram of energy levels showing the features band-to-band recombination, 545 nm and interfacial recombination from the metal oxide to the perovskite bulk, 670 nm. A real image of our perovskite emission. (b) Evolution of V_{oc} of a fresh sample under atmospheric conditions during 3000 seconds of illumination time at 1 sun.

To ratify this interpretation we performed an excitation experiment (see Fig. S5) measuring the emission intensity at a fixed wavelength, while varying the excitation wavelengths. Thus, monitoring at 670 nm we could find the source of this emission peak at 380 nm (3.2 eV) that clearly comes from the band edge of the TiO_2 material.[28] This observation confirms that the emission at 670 nm correspond to a surface recombination between ESL material and perovskite absorber. In agreement with this, we illuminated the films from the perovskite side, and the peak at 670 nm was weaker than when it is irradiate at the TiO_2 side pointing to the need of photoexcitation of the TiO_2 in order to observe the peak at 670 nm. Therefore, to observe emission at 670 nm photoexcitation in both the TiO_2 layer and the perovskite layer is required.

On the other hand, when the PL is measured in the $MAPbBr_3$/HSL interface (Fig. 2d), we note that only the band-to-band emission peak of the perovskite is observed, indicating that the presence of this additional peak is connected to the metal/oxide interface. However, this experiment confirms the necessity of the lithium as additive into the Spiro-OMeTAD in order to increase conductivity and enhance the extraction capability of this contact, as already reported in literature.[29] Note that the intensity of the perovskite emission is moderately decreased by lithium, which is a sign of enhanced charge extraction. The clear difference in perovskite emission intensity between ESL/ and /HSL PL measures is due probably of a poor crystal grain feature when perovskite is grown onto the FTO substrate instead of ESL materials.

It has been previously reported that the effect of native mobile ions in the perovskite strongly modifies the photovoltage dynamics by the contribution of ions to the space charge layer at the interface.[30] Seen from this perspective, the results in Fig. 2, coupled with the IS and EL results, show that Li^+ atoms modify the amount of hole accumulation by changing the ionic density in the accumulation zone.[31] The external Li^+ atoms increase

the cation density, increasing the size of the space charge layer, reducing therefore the surface density of electronic holes at the critical zone of the surface of the TiO_2 layer, as indicated by the decrease of charge-transfer radiative recombination observed at 671 nm and the simultaneous increase in the band-to-band emission of perovskite. In accordance with this interpretation we have observed that the dynamics of the ion redistribution upon illumination is rather slow. The V_{oc} typically increases gradually as shown in Fig. 3b corresponding to the build-up of ionic space charge[30] and consequent reduction of the non-radiative surface recombination pathways. Additional stability measurements suggest that once ions are accommodated in the interface they remain there as shown in supporting information (Fig. S7).

In conclusion, we have investigated the recombination dynamics in a high quality $MAPbBr_3$ solar cell. Radiative and non-radiative recombination channels are suppressed by treatment of the mesoporous TiO_2 layer with Li-TFSI that enhance the band-to-band emission in the perovskite layer as observed in electroluminescence experiments. We show that the major impact on the photovoltaic parameters of the cell caused by Li^+ treatment is related with an increase of the open-circuit potential, pushing it upwards approximately 200 mV respect to the device without lithium treatment. This work highlights the need to optimize ESL in perovskite solar cells containing the $MAPbBr_3$ to approach further to minimize recombination loses. The observations reported here can be connected with modification of charge accumulation at the contacts, and could be realized with different types of cations. Although Li^+ is not an ideal dopant, as it has been reported to migrate through the perovskite, further doping experiments with other materials would open a new avenue to further improve the efficiency of these devices.

Supporting Information. Experimental section, further optical and photovoltaic measurements, results of Impedance Spectroscopy, calculation of recombination coefficient.

Acknowledgements

We thank financial support by Ministerio de Ciencia, Innovación y Universidades of Spain under project (MAT2016-76892-C3-1-R). A.G. would like to thank MICINN for a Ramón y Cajal Fellowship (RYC-201416809). University Jaume I is also acknowledged for financial support (UJI-B2017-32). Serveis Centrals at UJI (SCIC) are acknowledge for the SEM measurement assistance. We are grateful to Dr. Seogjoon Yoon, for his very helpful expertise and support in the performance of the optical measures and Dr. Laxman Gouda for comments on the interpretation.

Supporting Information

Ionic Effect Enhances Light Emission and Photovoltage of Methylammonium Lead Bromide Perovskite Solar Cell by Reduced Surface Recombination

Clara Aranda*[1], Antonio Guerrero[1], Juan Bisquert*[1]
Institute of Advanced Materials (INAM), Universitat Jaume I, 12006 Castelló, Spain

Email: caranda@uji.es; bisquert@uji.es

SOLAR CELL FABRICATION

1.1 Deposition of electron selective layer (ESL)

FTO substrates were partially etch with zinc powder and HCl (2 M). Cleaned by ultra-sonication in Hellmanex detergent, rinsed with Milli-Q water and in a solution of ethanol: isopropanol (1:1 v/v). Prior to the deposition of TiO_2 compact layer substrates were treat in a UV−O_3 cleaner for 10 min. The TiO_2 blocking layer was deposited by aerosol spray pyrolysis at 450 °C, using a commercial titanium diisopropoxide bis(acetylacetonate) solution (75% in 2propanol, Sigma-Aldrich) diluted in ethanol (1:9, v/v) as precursor, with oxygen as carrier gas. The spray was performed with a total volume of 5 mL (approx.) of the previous solution, made by 3 steps spraying of 6 s each one and waiting 30 s between steps. Mesoporous layer was deposited by spin-coating at 2000 rpm for 10 s followed by 100ºC for 10 min. A 100 µl diluted paste in ethanol (1:5, weight ratio) of Dyesol 30-NRD was used. Devices were thermally treated in an oven under ambient atmosphere, using the following steps: 370ºC for 20 min with 40 min ramp time, 470ºC for 10 min with 5 min ramp time and 500ºC for 20 min.

1.2 Lithium treatment

Before the deposition of perovskite films, 100 µl of a lithium bis (trifluoromethylsulfonyl) imide 35 mM solution in acetonitrile, was prepared and deposited on the top of the device by spin-coating at 3000 rpm (2000 ac) during 10 seconds, following by thermal treatment at 450ºC for 30 min. All materials were purchased from Sigma-Aldrich and TCI.

1.3 Perovskite film deposition

$MAPbBr_3$ film was deposited, inside a glove box, using 1-step deposition method. 1.4 M $PbBr_2$ precursor solution was prepared in N,N-dimethylformamide (DMF) and dimethylsulphoxide (DMSO) without stirring at 80°C for 20 minutes until complete dissolve. After cool down at room temperature, this solution was mixed with MABr powder to obtain a final concentration of 1.4 M MABr. $MAPbBr_3$ solution was deposited by two ramps of spin coating method: 1000 rpm for 10 s and 4000 rpm for 40s, using toluene as anti-solvent during the second ramp. This was followed by annealing at 100°C for 3 min to obtain a shiny and homogenous film.

1.4 Deposition of hole selective layer (HSL) and External contact

A solution of Spiro-OMeTAD as HTM, was prepared by dissolving 72.3 mg of (2,2′,7,7′-tetrakis(N,N′-di-pmethoxyphenylamine)-9,9′-spirobifluorene) in 1 mL of chlorobenzene, 28.8 µL of 4-tert-butylpyridine and 17.5 µL of a stock solution of 520 mg/mL of lithium bis- (trifluoromethylsulfonyl) imide in acetonitrile, as additives.

Perovskite film was then covered with the HSL solution by dynamically spin coating at 4000 rpm, 800 rpm/s of acceleration for 30 s. Finally, 80 nm of gold was thermally evaporated on top of the device as a back contact, using a commercial Univex 250 chamber, from Oerlikon Leybold Vacuum.

CHARACTERIZATION

Ultraviolet-visible absorption spectra: Absorption spectra were recorded by a Cary 500 Scan VARIAN spectrophotometer in the 250-800 nm wavelength range. Scanning electron microscopy: The morphology of the films was observed using field-emission SEM using either a JEOL 7001F. SEM micrographs were further analyzed using the corresponding images. Optoelectronic measures: For photovoltaic measures, an Abett Solar simulator equipped with 1.5 AM filter was used. The light intensity was adjusted to 100 $mWcm^{-2}$ using a calibrated Si solar cell. Devices were measured using a mask to define an active area of 0.11 cm^2. *J-V*-curves were measured in reverse and forward bias at a scan rate of 50 mV/s. Impedance spectroscopy measures were performed using an Autolab potentiostat (model PGSTAT30) at open circuit conditions varying the irradiances with optical filters, from dark to 1 sun. Photoluminescence measurements were collected by a Horiba Fluorolog 3-11, using 380 nm of excitation source and also 405 nm. Excitation measurements where done using the same setup in excitation mode, monitoring at 670 nm. The electroluminescence properties of the $MAPbBr_3$ devices were measured in a DV420A-OE CCD camera, by applying a bias voltage of 1.4 V for 20 s with a Gamry 600 potentiostat. The generated current was registered by achieving chronoamperometric profile. X-ray diffraction: The XRD pattern of the prepared solids were measured using X-ray diffractometer (D8 Advance, Bruker-AXS) (Cu Kα, wavelength λ=1.5406 Å).

2.1 Characterization of perovskite films

Preparation of high quality perovskite layers plays a key role to obtain high efficiency devices, avoiding the recombination processes through pin-holes where the selective layers are in direct contact.[32] We prepared dense films of perovskite material as can be observed by cross-section scanning electron microscopy analysis (Fig. S1a), where a smooth perovskite layer with thickness approaching 600 nm is shown. The crystalline nature of the perovskite film is confirmed by XRD analysis (Fig. S1b), where the spectra reveals intense specific peaks already reported for $MAPbBr_3$.[10] The characteristic deep orange color of this kind of material is shown as well in Figure S1c. To further characterize the film, absorbance measurement (Figure S1d) was carried out, obtaining the distinctive spectra with the corresponding peak around 540 nm for bromide materials with a bandgap of 2.29 eV.

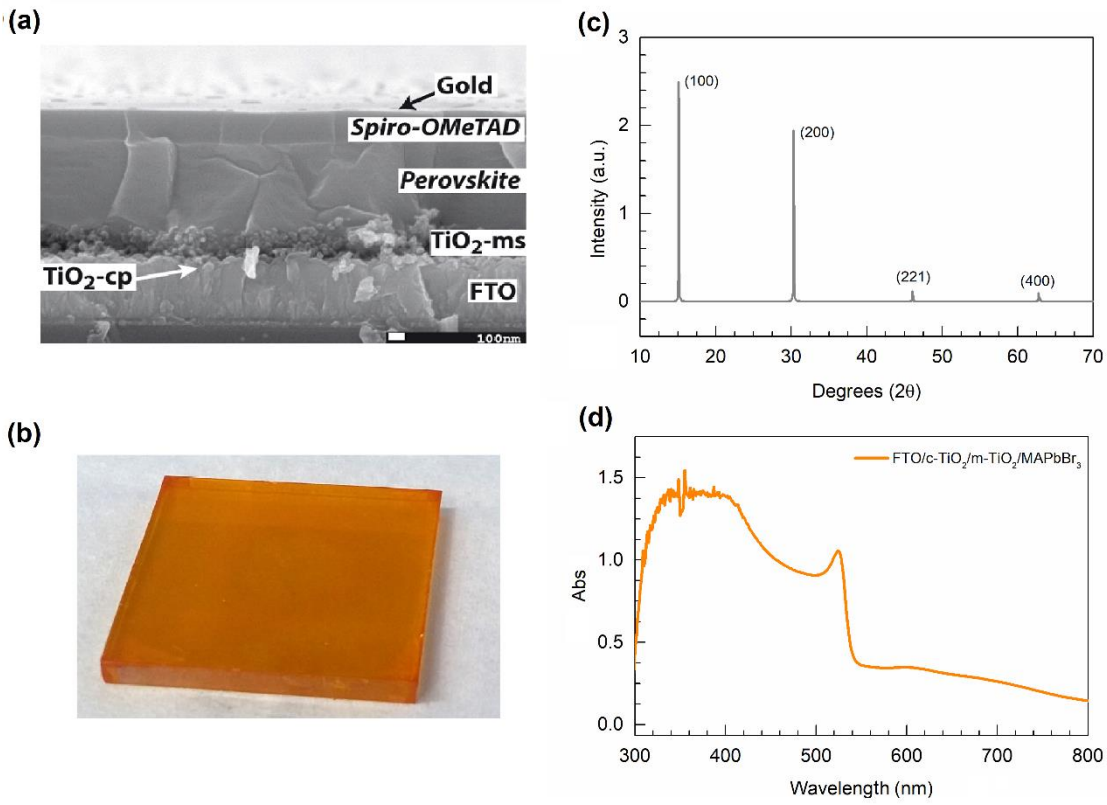

Figure S1. a) Cross-section scanning electron microscopy images of a complete device. b) Picture of a characteristic color film of $MAPbBr_3$ prepared by a 1-step deposition method. c) XRD pattern of perovskite films prepared by a 1-step deposition method. d) Absorbance spectra of films deposited on the ESL.

We confirm that no modifications in the absorbance capability of the semiconductor related to the presence of lithium in the mesoporous TiO_2 layer as can be observed in Fig. S2.

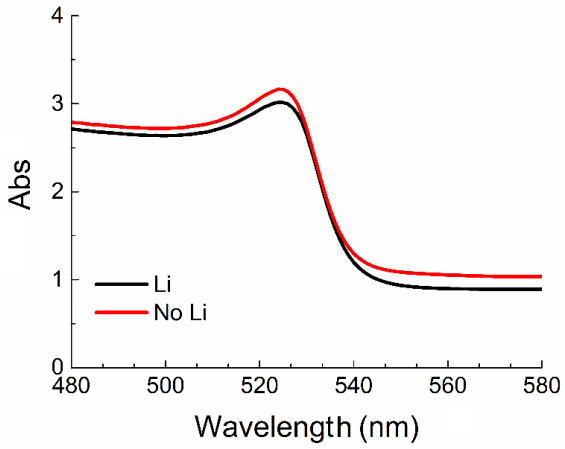

Figure S2. Absorbance spectra of $MAPbBr_3$ films fabricated onto FTO/c-TiO_2/m-TiO_2 films, with and without lithium treatment on the mesoporous layer.

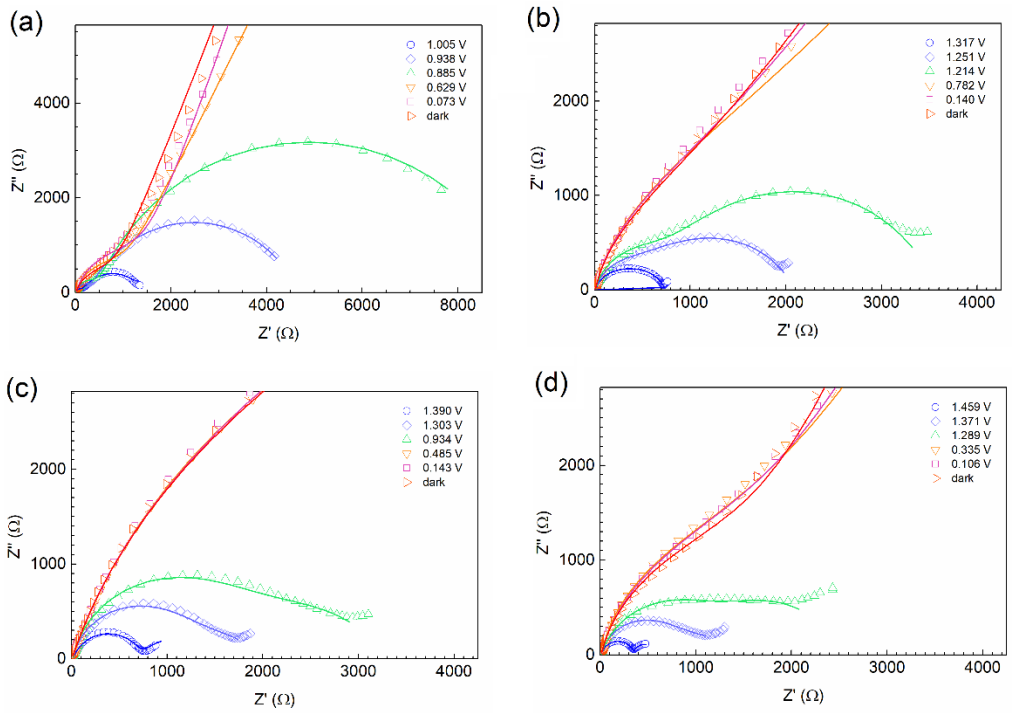

Figure S3. Impedance spectroscopy measurements at V_{oc} under 6 different irradiance intensities, from dark to 1 sun illumination, using optics filters to reduce irradiance from 40%, 30%, 10% and 5% respect of the AM 1.5G; and using a range of 40 points of frequencies from 1MHz to 20mHz. (a) no Li^+ in any contact; (b) Li^+ as additive into the spiro-OMeTAD layer; (c) Li^+ as treatment onto the mesoporous TiO_2 layer; (d) Li^+ at both external contacts.

2.2 Calculation of the recombination coefficient:

The recombination coefficient B is calculated from the recombination current (J_{rec}) according to the electrical model previously published by our group.[33] J_{rec} is related to the applied voltage (V) by the following expression:

$$J_{rec} = J_0 \exp\left[\frac{qV}{mk_BT}\right] \quad (1)$$

where q is the elementary charge, m is the ideality factor, k_BT the thermal energy, and J_0 is the diode dark current:

$$J_0 = qdBn_i^2 \quad (2)$$

$$n_i^2 = N_cN_ve^{-E_g/k_BT} = 4\left(\frac{2\pi k_BT}{h^2}\right)^3 (m_em_h)^{3/2} e^{-E_g/k_BT} \quad (3)$$

Here h is the Planck constant, d is the thickness of the layer where recombination takes place, n_i is the intrinsic carrier concentration, E_g is the semiconductor band-gap, and m_e and m_h are the effective masses of electrons and holes, respectively.

The recombination resistance unit area results from the derivative of current $i_{rec} = J_{rec}A_e$ across the electrode area A_e as

$$R_{rec} = \left(\frac{dJ_{rec}}{dV}\right)^{-1} = \frac{mk_BT}{q^2n_i^2dB}\exp\left(-\frac{qV}{mk_BT}\right) \quad (4)$$

Table S1. Evaluation parameters from Ref. [34]

Parameter	$MAPbI_3$	$MAPbBr_3$
E_g (eV)	1.69	2.34
m_e (units of m_0)	2.02	1.06
m_h (units of m_0)	0.595	0.357

Therefore, the effective recombination coefficient B can be calculated from (4) and a summary of the results are shown in Figure S4. As can be observed, the recombination coefficient reduces when the Li^+ additive is incorporated into the external contacts following the recombination resistance.

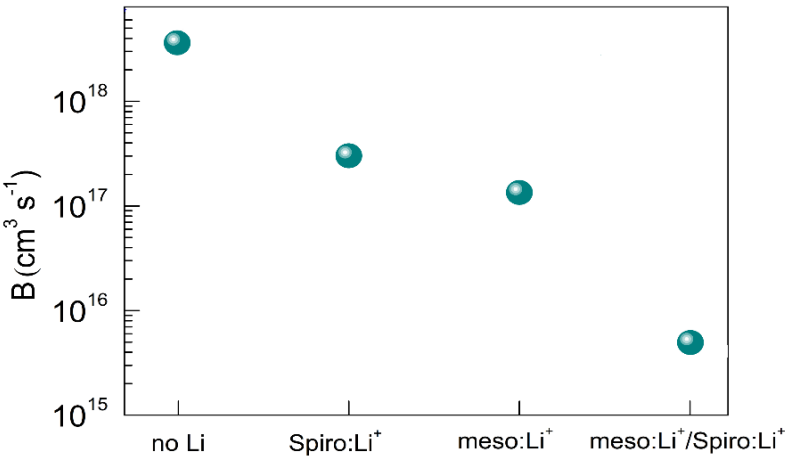

Figure S4. Recombination coefficient trend for the four different devices with the progressive addition of lithium to the selective contacts. Calculation made as detailed before this figure.

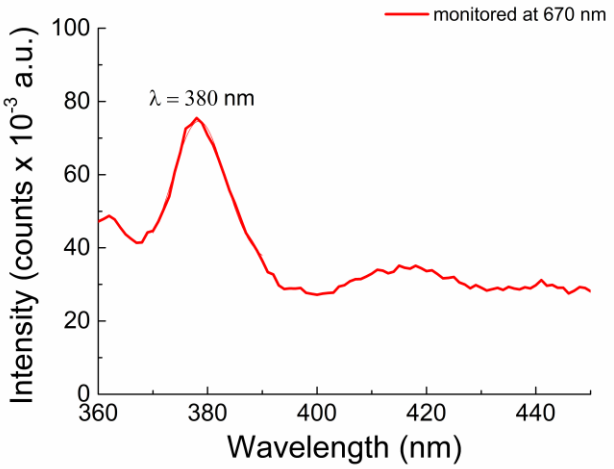

Figure S5. Excitation spectra monitoring at 670 nm. Peak at 380 nm corresponding to the 3.2 eV band edge of TiO_2.

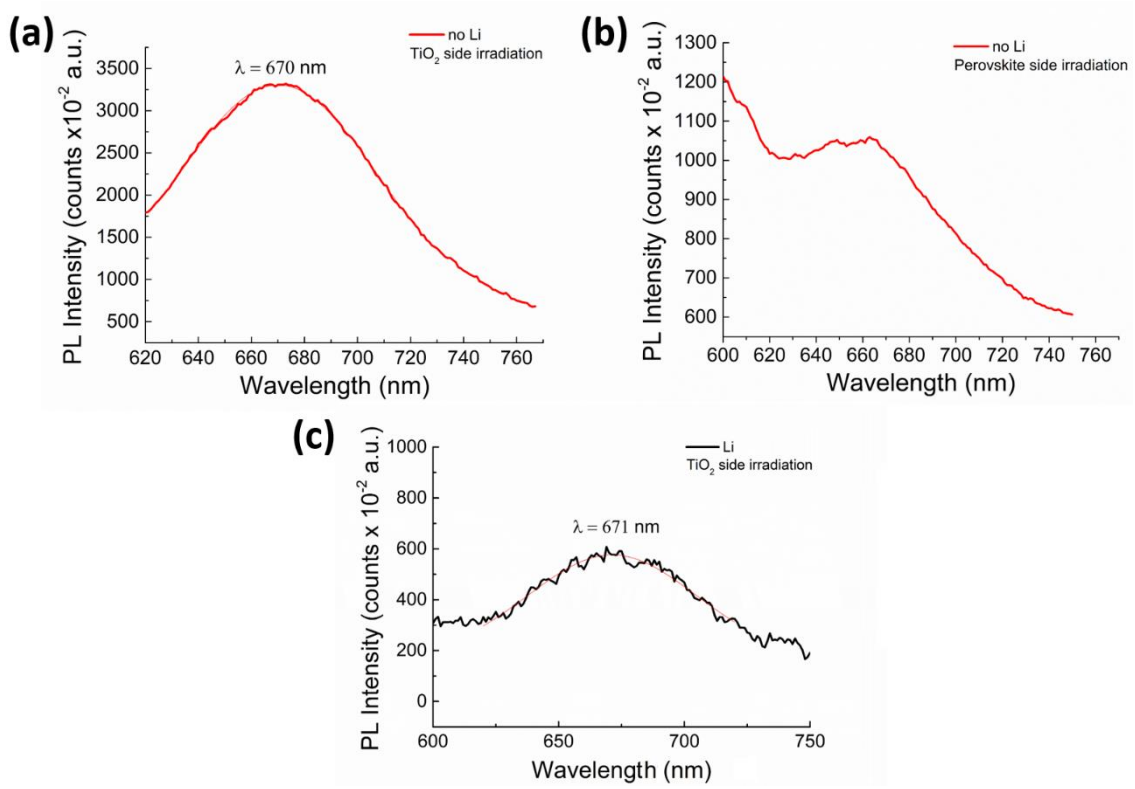

Figure S6. (a), (b) Absolute emission of the 670 nm peak recorded from the side of TiO_2 and perovskite material without lithium, respectively at 380 nm of excitation source. (c) Absolute emission of the 670 nm peak with lithium-treated TiO_2 irradiated from the metal oxide side.

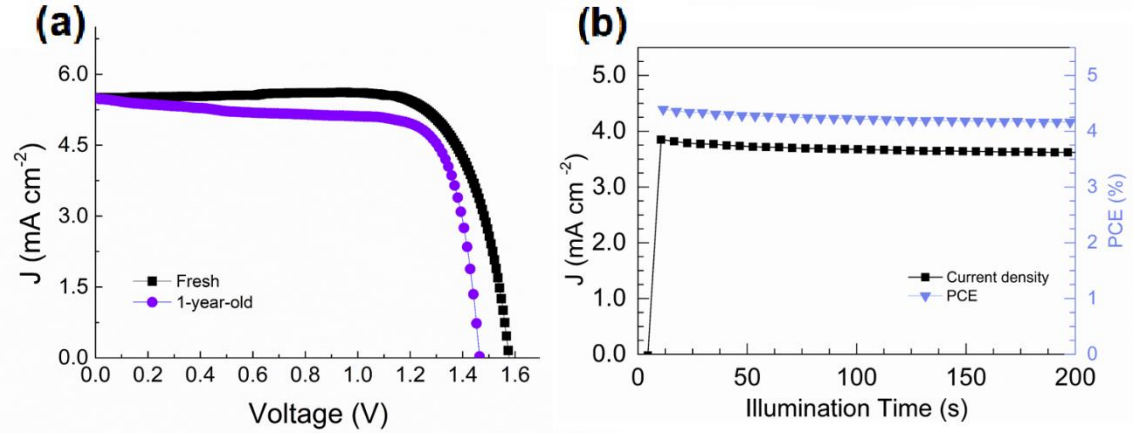

Figure S7. Further stability measures. (a) *JV* curves of fresh champion cell and 1-year-old sample cell measure under 1 sun of illumination in atmospheric conditions. (b) Evolution of density current and PCE in a chronoamperometry measure under 1 sun of illumination during 200 s.

References

1. Jiménez-López, J.; Cambarau, W.; Cabau, L.; Palomares, E. Charge Injection, Carriers Recombination and HOMO Energy Level Relationship in Perovskite Solar Cells. *Scientific Reports* **2017,** *7* (1), 6101.

2. Tress, W.; Yavari, M.; Domanski, K.; Yadav, P.; Niesen, B.; Correa Baena, J. P.; Hagfeldt, A.; Graetzel, M. Interpretation and evolution of open-circuit voltage, recombination, ideality factor and subgap defect states during reversible light-soaking and irreversible degradation of perovskite solar cells. *Energy Environ. Sci.* **2018,** *11* (1), 151-165.

3. Correa-Baena, J.-P.; Tress, W.; Domanski, K.; Anaraki, E. H.; Turren-Cruz, S.-H.; Roose, B.; Boix, P. P.; Gratzel, M.; Saliba, M.; Abate, A.; Hagfeldt, A. Identifying and suppressing interfacial recombination to achieve high open-circuit voltage in perovskite solar cells. *Energy Environ. Sci.* **2017,** *10* (5), 1207-1212.

4. Zohar, A.; Kulbak, M.; Levine, I.; Hodes, G.; Kahn, A.; Cahen, D. What Limits the Open-Circuit Voltage of Bromide Perovskite-Based Solar Cells? *ACS Energy Lett.* **2018**, 1-7.

5. Saliba, M.; Matsui, T.; Seo, J.-Y.; Domanski, K.; Correa-Baena, J.-P.; Nazeeruddin, M. K.; Zakeeruddin, S. M.; Tress, W.; Abate, A.; Hagfeldt, A.; Grätzel, M. Cesium-containing triple cation perovskite solar cells: improved stability, reproducibility and high efficiency. *Energy Environ. Sci.* **2016,** *9* (6), 1989-1997.

6. Sheng, R.; Ho-Baillie, A.; Huang, S.; Chen, S.; Wen, X.; Hao, X.; Green, M. A. Methylammonium Lead Bromide Perovskite-Based Solar Cells by Vapor-Assisted Deposition. *J. Phys. Chem. C* **2015,** *119* (7), 3545-3549.

7. Chen, Y.-S.; Manser, J. S.; Kamat, P. V. All Solution-Processed Lead Halide Perovskite-$BiVO_4$ Tandem Assembly for Photolytic Solar Fuels Production. *J. Am. Chem. Soc.* **2015,** *137* (2), 974-981.

8. Yang, M.; Zhang, T.; Schulz, P.; Li, Z.; Li, G.; Kim, D. H.; Guo, N.; Berry, J. J.; Zhu, K.; Zhao, Y. Facile fabrication of large-grain $CH_3NH_3PbI_{3-x}Br_x$ films for high-efficiency solar cells via CH_3NH_3Br-selective Ostwald ripening. *Nat. Commun.* **2016,** *7*, 12305.

9. Arora, N.; Orlandi, S.; Dar, M. I.; Aghazada, S.; Jacopin, G.; Cavazzini, M.; Mosconi, E.; Gratia, P.; De Angelis, F.; Pozzi, G.; Graetzel, M.; Nazeeruddin, M. K. High Open-Circuit Voltage: Fabrication of Formamidinium Lead Bromide Perovskite Solar Cells Using Fluorene–Dithiophene Derivatives as Hole-Transporting Materials. *ACS Energy Lett.* **2016,** *1* (1), 107-112.

10. Giesbrecht, N.; Schlipf, J.; Oesinghaus, L.; Binek, A.; Bein, T.; Müller-Buschbaum, P.; Docampo, P. Synthesis of Perfectly Oriented and Micrometer-Sized

$MAPbBr_3$ Perovskite Crystals for Thin-Film Photovoltaic Applications. *ACS Energy Lett.* **2016,** *1* (1), 150-154.

11. Nayak, P. K.; Bisquert, J.; Cahen, D. Assessing Possibilities and Limits for Solar Cells. *Adv. Mater.* **2011,** *23* (25), 2870-2876.

12. Wu, C.-G.; Chiang, C.-H.; Chang, S. H. A perovskite cell with a record-high-Voc of 1.61 V based on solvent annealed CH3NH3PbBr3/ICBA active layer. *Nanoscale* **2016,** *8* (7), 4077-4085.

13. Guerrero, A.; You, J.; Aranda, C.; Kang, Y. S.; Garcia-Belmonte, G.; Zhou, H.; Bisquert, J.; Yang, Y. Interfacial Degradation of Planar Lead Halide Perovskite Solar Cells. *ACS Nano* **2016,** *10* (1), 218-224.

14. Heo, J. H.; Song, D. H.; Im, S. H. Planar $CH_3NH_3PbBr_3$ Hybrid Solar Cells with 10.4% Power Conversion Efficiency, Fabricated by Controlled Crystallization in the Spin-Coating Process. *Adv. Mater.* **2014,** *26* (48), 8179-8183.

15. Arora, N.; Dar, M. I.; Abdi-Jalebi, M.; Giordano, F.; Pellet, N.; Jacopin, G.; Friend, R. H.; Zakeeruddin, S. M.; Grätzel, M. Intrinsic and Extrinsic Stability of Formamidinium Lead Bromide Perovskite Solar Cells Yielding High Photovoltage. *Nano Lett.* **2016,** *16* (11), 7155-7162.

16. Giordano, F.; Abate, A.; Correa Baena, J. P.; Saliba, M.; Matsui, T.; Im, S. H.; Zakeeruddin, S. M.; Nazeeruddin, M. K.; Hagfeldt, A.; Graetzel, M. Enhanced Electronic Properties in Mesoporous TiO_2 via Lithium Doping for High-Efficiency Perovskite Solar Cells. *Nat. Commun.* **2016,** *7*, 10379.

17. Jiang, Q.; Zeng, X.; Wang, N.; Xiao, Z.; Guo, Z.; Lu, J. Electrochemical Lithium Doping Induced Property Changes In Halide Perovskite $CsPbBr_3$ Crystal. *ACS Energy Lett.* **2018,** *3* (1), 264-269.

18. Chen, H.; Liu, D.; Wang, Y.; Wang, C.; Zhang, T.; Zhang, P.; Sarvari, H.; Chen, Z.; Li, S. Enhanced Performance of Planar Perovskite Solar Cells Using Low-Temperature Solution-Processed Al-Doped SnO2 as Electron Transport Layers. *Nanoscale Res. Lett.* **2017,** *12* (1), 238.

19. Ahn, N.; Son, D.-Y.; Jang, I.-H.; Kang, S. M.; Choi, M.; Park, N.-G. Highly Reproducible Perovskite Solar Cells with Average Efficiency of 18.3% and Best Efficiency of 19.7% Fabricated via Lewis Base Adduct of Lead(II) Iodide. *J. Am. Chem. Soc.* **2015,** *137* (27), 8696-8699.

20. Aranda, C.; Cristobal, C.; Shooshtari, L.; Li, C.; Huettner, S.; Guerrero, A. Formation Criteria of High Efficiency Perovskite Solar Cells under Ambient Conditions. *Sustainable Energy Fuels* **2017,** *1* (3), 540-547.

21. Detao Liua, S. L., ∗, Peng Zhanga, Yafei Wanga, Rui Zhanga, Hojjatollah Sarvarib, Feng Wanga,b, Jiang Wuc, Zhiming Wangd, Zhi David Chena,b,∗. Efficient

planar heterojunction perovskite solar cells with Li-doped compact TiO_2 layer. *Nano Energy* **2017,** *31*, 462–468.

22. Fabregat-Santiago, F.; Garcia-Belmonte, G.; Mora-Seró, I.; Bisquert, J. Characterization of nanostructured hybrid and organic solar cells by impedance spectroscopy. *Phys. Chem. Chem. Phys* **2011,** *13*, 9083–9118.

23. Garcia-Belmonte, G.; Guerrero, A.; Bisquert, J. Elucidating Operating Modes of Bulk-Heterojunction Solar Cells from Impedance Spectroscopy Analysis. *J. Phys. Chem. Lett.* **2013,** *4*, 877−886.

24. Correa-Baena, J.-P.; Turren-Cruz, S.-H.; Tress, W.; Hagfeldt, A.; Aranda, C.; Shooshtari, L.; Bisquert, J.; Guerrero, A. Changes from Bulk to Surface Recombination Mechanisms between Pristine and Cycled Perovskite Solar Cells. *ACS Energy Lett.* **2017,** *2* (3), 681-688.

25. Guerrero, A.; Garcia-Belmonte, G.; Mora-Sero, I.; Bisquert, J.; Kang, Y. S.; Jacobsson, T. J.; Correa-Baena, J.-P.; Hagfeldt, A. Properties of Contact and Bulk Impedances in Hybrid Lead Halide Perovskite Solar Cells Including Inductive Loop Elements. *J. Phys. Chem. C* **2016,** *120* (15), 8023-8032.

26. Zarazua, I.; Han, G.; Boix, P. P.; Mhaisalkar, S.; Fabregat-Santiago, F.; Mora-Seró, I.; Bisquert, J.; Garcia-Belmonte, G. Surface Recombination and Collection Efficiency in Perovskite Solar Cells from Impedance Analysis. *J. Phys. Chem. Lett.* **2016,** *7* (24), 5105-5113.

27. Zarazua, I.; Bisquert, J.; Garcia-Belmonte, G. Light-induced space-charge accumulation zone as photovoltaic mechanism in perovskite solar cells. *The Journal of Physical Chemistry Letters* **2016,** *7*, 525-528.

28. Govindasamy, G.; Murugasen, P.; Sagadevan, S. Investigations on the Synthesis, Optical and Electrical Properties of TiO2 Thin Films by Chemical Bath Deposition (CBD) method. *Materials Research* **2016,** *19*, 413-419.

29. Nguyen, W. H.; Bailie, C. D.; Unger, E. L.; McGehee, M. D. Enhancing the Hole-Conductivity of Spiro-OMeTAD without Oxygen or Lithium Salts by Using Spiro(TFSI)2 in Perovskite and Dye-Sensitized Solar Cells. *J. Am. Chem. Soc.* **2014,** *136* (31), 10996-11001.

30. Gottesman, R.; Lopez-Varo, P.; Gouda, L.; Jimenez-Tejada, J. A.; Hu, J.; Tirosh, S.; Zaban, A.; Bisquert, J. Dynamic phenomena at perovskite/electron-selective contact interface as interpreted from photovoltage decays. *Chem* **2016,** *1*, 776-789.

31. García-Rosell, M.; Bou, A.; Jiménez-Tejada, J. A.; Bisquert, J.; Lopez-Varo, P. Analysis of the Influence of Selective Contact Heterojunctions on the Performance of Perovskite Solar Cells. *The Journal of Physical Chemistry C* **2018,** *122*, 13920–13925.

32. Johnston, M. B.; Herz, L. M. Hybrid Perovskites for Photovoltaics: Charge-Carrier Recombination, Diffusion, and Radiative Efficiencies. *Acc. Chem. Res.* **2016,** *49* (1), 146-154.

33. Bisquert, J.; Garcia-Belmonte, G.; Mora-Sero, I. Characterization of capacitance, transport and recombination parameters in hybrid perovskite and organic solar cells. In *Unconventional thin film photovoltaics*, 2016; pp 57-106.

34. Feng, J.; Xiao, B. Crystal Structures, Optical Properties, and Effective Mass Tensors of CH3NH3PbX3 (X = I and Br) Phases Predicted from HSE06. *J. Phys. Chem. Lett.* **2014,** *5* (7), 1278-1282.

General Conclusions

Despite the tremendous advances achieved in perovskite PV technology, several features still need answers regarding its chemical insights and physical mechanisms. In the race to commercialization purposes, the stability issues under solar cell working conditions encompass the direction of the research. Regarding the stability, the factors involved can be catalogue as extrinsic and intrinsic.

The extrinsic ones regard to the environmental conditions simulating real work atmosphere: light, oxygen and moisture. From the three of them, water, as moisture exposure, appears as the most problematic one, inducing the fastest degradation mechanisms into the PSCs, affecting in first place to the perovskite material itself provoking the complete annihilation of its chemical structure. The second environmental factor responsible of the damage of these devices is light exposure. In this case, the most affected region of the device lies in the cathode/perovskite contact, provoking damage in the charge extraction processes.

From the different intrinsic factors, ion migration features represents a dominant influence on the particular photovoltaic behaviour observed in PSCs. Hysteretic response during current density-voltage (*j-V)* curves characterization impedes a robust establishment regarding the efficiency of the solar cell, since it depends on the conditions of measurement as applied bias, scan rate and, foremost, on the nature of external selective contacts. In addition, the very large capacitance response observed in dark and also under illumination conditions, expose the accumulation of charge at the interfaces as the main factor to control. The recombination mechanisms through radiative and non-radiative processes are also connected to ionic effects in addition to the electronic, for example via electrostatic effect, affecting the maximum achievable photovoltage to enhance PCE closer to the theoretical values.

The main goal proposed during the course of this thesis is a step forward in the solution of these extrinsic and intrinsic stability factors blocking the large-scale horizon for PSCs technology, from a bulk and interfacial engineering point of view. The extrinsic factors have been focused on the effects of water into the perovskite devices, investigating in the first place the coordination chemistry involving precursor's solvents and establishing a robust methodology to fabricate high PCE solar cells using moisture exposure as an ally to properly balance the perovskite formulation to achieve the best results.

The intrinsic factors have been faced focusing on the photovoltaic losses provoked by recombination mechanisms. In the first place, a drop in potential due to interfacial degradation caused by light exposure has been demonstrated, bringing to the fore the role of the interfaces in terms of photovoltaic parameters. A method to distinguish between bulk and interfacial recombination processes is also established using a re-definition of non-ideality factor in the bimolecular recombination model. Through this method, the necessity to develop electrical characterization techniques that minimize the modification of the system during the measures itself becomes clear. Impedance spectroscopy (IS) under open-circuit conditions appears as the most adequate option to do not perturb excessively the external contacts, which could introduce additional recombination contributions. These two previous achievements have given way to the final success of this thesis. An ionic contribution in the reduction of surface recombination processes, has allowed to reduce as well the photovoltage losses, pushing forward this photovoltaic parameter for a closer maximum theoretical value of PCE, controlling substantially the intrinsic stability issues.

The conclusions obtained through the work developed during the course of this thesis are accompanied by two important achievements in terms of photovoltaic parameters, implying important applicable contributions to the perovskite field.

First, the method of fabrication of high efficient PSCs based in $MAPbI_3$ material under moisture conditions, succeeding current density values of 23 $mAcm^{-2}$ approached to the theoretical maximum. It has been already applicate by several groups with similar results.

Second, a method to obtain record photovoltaic values up to 1.6 V for a $MAPbBr_3$ based solar cells, which has additional and important applicability in tandem devices and complementary technologies as light emitting diodes (LEDs) or electrochemical fuel production.

The main insights regarding the chemistry and physical processes obtained during the work developed in this thesis can be summarized as follows:

- The elucidation of the chemistry governing the particular structure of perovskite material results mandatory to enhance photovoltaic properties balancing stability and cost for commercialization targets.

- The influence of the solvents used in the preparation of perovskite precursors lies in their polar nature. The polar character establishes the coordination capability to form the adduct PbI_2:MAI:solvent, producing higher or poorly crystallinity of the final film; depending on the coordination number of the multiiodide plumbate species that can be formed prior to the deposition of the perovskite layer.

- A sequence in coordination capability has been established, including water as additional solvent, coupled with the most widely used: DMSO; DMF and GBL. The UV-absorbance analysis demonstrate the similar coordination capability of water and DMSO, bringing to the fore a competition between them to coordinate lead atom during the formation of octahedral structure, characteristic of lead halide perovskite materials.

- The competition between DMSO and water can be used to re-formulate the perovskite precursor solution containing DMF and DMSO, adjusting the DMSO:Pb ratio depending on the relative humidity (%RH) of the ambient. It was probed the linear dependence of this ratio with the %RH, stablishing a balance in which the higher %RH, the lower DMSO:Pb ratio is needed to proper crystallization of the absorber material. This method of $MAPbI_3$ synthesis allows to obtain PCE as high as 19% for solar cells completely fabricate under room conditions. The reliability of this methodology has been probed in several research groups achieving similar results, with the consequent contributions to the field.

- Beyond the perovskite degradation itself, external environment factors as light contribute to the interfacial degradation of complete devices. This has been proved through Mott-Schottky analysis in order to determine the density of majority carriers into the bulk material as well as the value of the flatband potential, determining the final photovoltage, which depends on the split of the Fermi levels of the external contacts. When the perovskite absorber is in direct contact with the metal top contacts, as gold, silver or even calcium, the illumination time provokes an s-shape on the *j-V* curve of the device,

evidencing a poor charge extraction capability. The damaged charge extraction of the contacts reveals as well an inverse band bending of the energy levels, which blocks the charge extraction. This effect is provoked by the accumulation of photogenerate carriers at the cathode/perovskite interface.

- The transient methods as *j-V* curves, open-circuit voltage decay (OCVD) or impedance spectroscopy (IS) under illumination or applied bias, for the electrical characterization of perovskite devices, modifies in excess the solar cell during the measurements itself. This provokes non-reliable results in terms of recombination processes caused by the bulk material or because of the external contacts. A physical model considering a non-ideal factor in the bimolecular recombination model, based in the assumption of homogeneous distribution of charge in a semiconductor of certain thickness, provides information about the recombination processes due to the bulk. IS at open-circuit potential conditions demonstrate to do not modify the external contacts, being selected as the better electrical characterization for which the model proposed matches perfectly.

- Photovoltage losses can be reduced suppressing in some extent the surface recombination processes at the ESL/perovskite interface. It can be achieve with the introduction of positive external ions, as lithium, in the cathode side of a n-i-p architecture. The density of electronic holes at the accumulation zone can be decreased by growing the density of positive cations at that side. The direct consequence is the reduction in the surface recombination process, enhancing as well the photovoltage of the solar device. The reduction in the electronic hole density favoured band-to-band recombination pathways that can be determine through electroluminescence and photoluminescence experiments. These techniques demonstrate an increased light emission from the bulk material when surface recombination is supressed. The results contribute to perform an easy method to modify surface recombination, controlling as well light emission properties. In the case of $MAPbBr_3$-based devices, a record value of photovoltage is obtained making the optimized device potentially applicable for others technologies as LEDs or for electrochemical reactions, due to its great photovoltage.